AUTOMATED WHOLE-ORGANISM FUNCTIONAL SCREENING TECHNOLOGIES AND NEUROLOGICAL DISEASE MODELS IN *C. ELEGANS*

by

Ross Charles Lagoy

A Dissertation

Submitted to the Faculty

of the

WORCESTER POLYTECHNIC INSTITUTE

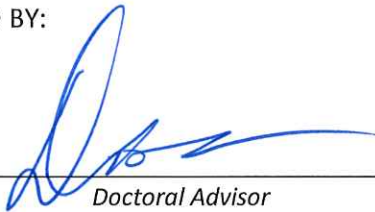in partial fulfillment of the requirements for the

Degree of Doctor of Philosophy

in

Biomedical Engineering

May 2018

APPROVED BY:

Doctoral Advisor
Dirk R. Albrecht, PhD
Worcester Polytechnic Institute
Department of Biomedical Engineering

Committee Chair
George D. Pins, PhD
Worcester Polytechnic Institute
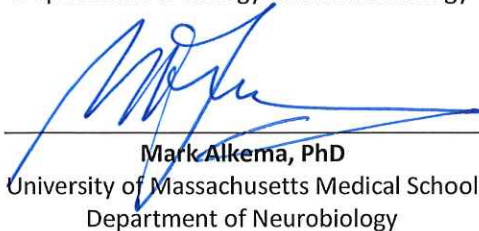Department of Biomedical Engineering

David S. Adams, PhD
Worcester Polytechnic Institute
Department of Biology and Biotechnology

Kwonmoo Lee, PhD
Worcester Polytechnic Institute
Department of Biomedical Engineering

Mark Alkema, PhD
University of Massachusetts Medical School
Department of Neurobiology

Abstract

Nearly one billion people worldwide have a neurological disease, and one out of every six adults in the United States has a mental illness. For rare and severe neurodevelopmental disorders, like Timothy syndrome (TS), exact genetic causes have been identified and studied extensively. TS is caused by a single point mutation in *CACNA1C*, a voltage-gated calcium channel (VGCC), which results in severe developmental defects, cardiac arrhythmia, and autism. Studies using patient derived cells are useful in identifying impaired cellular function, especially for TS and other neural activity-dependent disorders. Also, functional high-throughput screening assays that use disease-relevant cell types can lead to more targeted therapeutics that regulate cellular activity. Although these approaches are promising, cell-based assays do not consider the diversity of disease pathology or efficacy of broad-acting therapeutics in multi-cellular organisms. Therefore, we developed several whole-organism disease models using CRISPR-Cas9 and transgenes in the nematode *C. elegans* that harbor human VGCC mutations. We evaluated and identified behavioral, morphological, and functional phenotypes, and invented new high-throughput functional screening technologies to identify transient and potent suppressors of neural activity in these animals. We expect that these new disease models and methods will provide a pipeline for investigating activity-dependent neurological disorders in whole organisms to identify more effective therapeutics. Altogether, we aim to deepen our understanding about the brain and discover treatments for the millions of individuals that suffer from neurological disease.

Acknowledgements

I want to thank everyone that supported me in the completion of this work; my committee members, colleagues, friends and family— this would not have been possible without you.

To my committee members, advisors, and mentors: Thank you for your support and motivation. Together, you helped me become an independent scientist and discover my passion for research. Dirk, thank you for teaching me how to approach challenging technical problems and discover, prepare, and present solutions in an exceptionally thorough and complete manner.

To my colleagues: Your guidance throughout my research endeavors has been remarkable. The instruction, patients, and resources you provided me are invaluable, and I will carry these lessons and skills with me throughout my career.

To my friends: You have been there for me when I needed it the most– thank you for your encouragement and support throughout my life.

To my family:

I would not have been on this journey if it were not for you. You are my sources of inspiration and motivation. I dedicate this to you, and hope to continue to make you proud.

My successes are yours.

List of Figures

List of Tables

List of Abbreviations

Obsessive compulsive disorder	OCD
Alzheimer's disease	AD
Huntington's disease	HD
Polyglutamine	PolyQ
CaV1	*CACNA1C*
CaV2	*CACNA1A*
CaV3	*CACNA1G*
Deoxyribonucleic Acid	DNA
Interference ribonucleic Acid	RNAi
Gain-of-function	GOF
Loss-of-function	LOF
Reduction-of-function	ROF
All-*Trans* Retinal	ATR
Clustered regularly interspaced short palindromic repeats	CRISPR
CRISPR associated endonuclease 9	Cas9
Short guide RNA	sgRNA or gRNA
Single stranded oligomer	ssOligo
Protospacer Adjacent Motif	PAM
Homologous recombination	HR
Timothy syndrome	TS
Timothy syndrome type 1	TS1
Timothy syndrome type 2	TS2
Voltage-gated calcium channel	VGCC
High-throughput screening	HTS
High-content screening	HCS
NeuroTracker	NT
Dihydropyridine	DHP
Wild-type	WT
Human induced pluripotent stem cells	hiPSCs
Green fluorescent protein	GFP
Genetically encoded calcium indicator	GECI
GFP-Calmodulin Fusion Protein	GCaMP
Förster resonance energy transfer	FRET
Channelrhodopsin-2	Chr2
Site-directed mutagenesis	SDM
Nematode Growth Medium	NGM
Paralyzed arrested elongation at two-fold	Pat

Table of Contents

Chapter 1 Introduction

Human neurological diseases

Nearly one billion people worldwide are estimated to suffer from neurological disorders, which accounts for one in six adults in the United States that have a mental health condition (NIMH Mental Illness, 2018; WHO, 2006). Currently, it is only generally understood that human neurological diseases can be caused by irregular cellular function that leads to cell death. For neurological disorders like Alzheimer's and Huntington's, cells in the brain (neurons) and other parts of the nervous system degenerate and become nonfunctional (Ahmed et al., 2018). Symptoms for these disorders are most commonly developed and recognized later in life (WHO, 2006). Therefore, reliable markers for diagnosing these types of diseases usually rely on the identification of changes in behavior, while the exact causes for most neurological diseases and treatments remain largely unknown (WHO, 2006). Likewise, other neurological diseases like autism and epilepsy have no known cure or long-term effective treatments (Hyman, 2008; WHO, 2006). These diseases are also often diagnosed by irregular behavior, sporadic episodes, or by monitoring neural function. Further, severe forms of these diseases are generally referred to as neurodevelopmental disorders, since they are diagnosed at young ages sometimes causing short life expectancies or life-long symptoms. Meanwhile, symptoms for similar neural activity-dependent disorders like depression, schizophrenia, or obsessive-compulsive disorder (OCD) can sometimes be partially or completely overcome with medications or talk therapy for reasons that are also not completely understood (NAMI, 2018; Spillane et al., 2016). Altogether, neurological diseases have a wide-range of severity (acute onset trigger, or chronic and genetic)

resulting in a broad disorder classification (>600), which may impact the success of developing treatments or therapeutic methods (UCSF Medical Center, 2018).

Understanding fundamental pathology and developing therapeutic strategies for neurological diseases are major world-wide initiatives (SfN, 2018). Specifically, various case studies of rare genetic neurological diseases and genome-wide association studies have identified several genetic root causes for activity-dependent disorders, like autism and epilepsy (Heyes et al., 2015; Smoller, 2013). Some of these genes identified are not so surprising, although exciting for the development of targeted therapeutics and investigation of associated genetic pathways. In particular, these identified genes are associated with regulation of cellular function at the membrane level, like ion channels that transduce chemicals into electrical signaling which regulate important physiological function that may lead to such observable and diagnosable changes in human behavior. Therefore, rare and severe neurological disorders that have been studied in depth with known causes are extremely useful for understanding the cellular mechanisms that can cause mental disorders and extrapolating meaningful pathology for the development of effective therapeutics (Jen et al., 2016).

Electrophysiology and membrane excitation

The ability to directly measure changes in cell membrane potential led to the discovery of ion channels, a concept first conceived and pioneered throughout the 18th and 19th centuries (Verkhratsky and Parpura, 2014). During this time, the first action potential was indirectly measured using a galvanometer, followed by centuries of advancements in technology and theories about membrane excitation. These important initial technological developments and

hypotheses led to the direct recording of the membrane resting potential from a giant squid axon using improved mini-electrodes in the 1940s and throughout the following decade (Young, 1936). Results from this method implied that ion currents were the underlying reason for axon activity, then later experiments demonstrated that passive ion fluxes caused by electrochemical gradients were the source of membrane excitability due to ion channels. Further advancements in technology and understanding of fundamental biology resulted in today's gold-standard of electrophysiological methods, known as the patch-clamp technique, for directly recording both changes in membrane currents (voltage-clamp) and potential (current-clamp) by hollow glass micropipettes filled with a conductive (electrolyte) solution (Neher and Sakmann, 1976). This experimental procedure revolutionized the ability to study single ion channels and monitor electrical activity of various cell types (like neurons and muscle) *in vitro* and *in vivo*.

Ion channels

Ion channels are eukaryotic transmembrane proteins that initiate and regulate essential cellular physiological functions (Rasband, M. N., 2010). These structures provide a selectively permeable channel, or pore, enabling flow of charged particles (e.g. Na^+, Cl^-, K^+, Ca^{2+}) from the outside to the inside the cell across a concentration gradient. These pores open rapidly and close in response to mechanical or chemical stimuli, subsequently forming an electrochemical flux across the cell membrane during activation. This electrical transduction travels through the cell membrane, opening or closing additional localized ion channels that are sensitive to changes in electric potential. This transduction is rapid, requiring only milliseconds to propagate across a cell membrane. This cascade initiates the opening of subsequent voltage sensitive ion channels, selectively permeable to ions mentioned previously.

Specifically, voltage-gated calcium channels (VGCCs) are an ion channel type that open upon membrane depolarization, which allows calcium to flow into the cell by transduction of electrical signal (**Fig. 1**). Intracellular calcium is important for physiological events, like contraction, secretion, synaptic transmission, enzyme regulation, protein (de)phosphorylation, and gene transcription (Catterall, 1995, 2000, 2011). There are ten known voltage gated calcium channels, classified into three distinct subfamilies (CaVs) based on structure and function (Catterall, 2011). Minimally, all VGCC subfamilies include the pore-forming α1 subunit which is structurally comprised of four domains, each containing six transmembrane segments connected by intracellular and extracellular loop regions (**Fig. 1**). Each auxiliary subunit (i.e. α2, β, γ, and δ) provides a distinct function, together allowing entry of calcium into the cell at varying rates, and partially self-regulated by calcium and voltage-dependent (in)activation (Catterall, 2011). Altogether, VGCC subunits have evolved into seven different forms, and are expressed in different excitable cell types across vertebrate and invertebrate species (Tyson and Snutch, 2013).
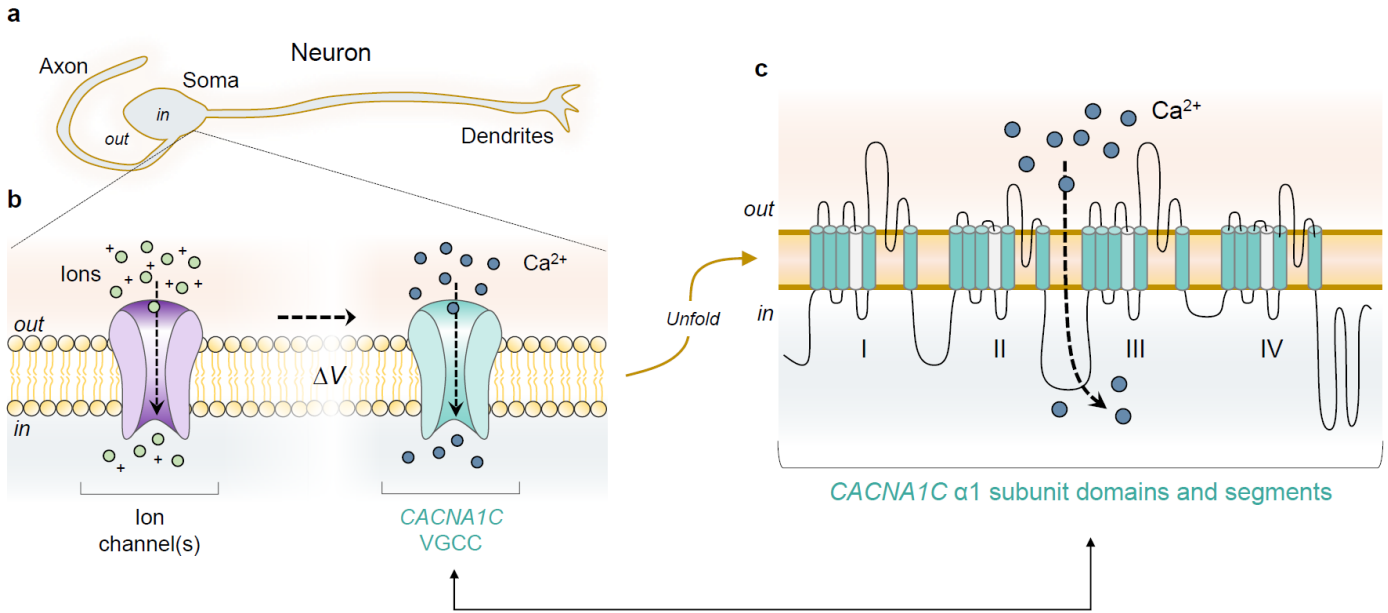
Figure 1. Illustrations of a neuron, ion channels in the cell membrane, and voltage-gated calcium channel alpha 1 subunit structure.

a. Schematic of a typical sensory neuron with a cell body (soma), axon, and sensory endings (dendrites).
b. A zoom-in of the cell membrane from a, showing two types of ion channels three-dimensional (folded) pore structures. An ion channel responsible for depolarization by influx of positively charged ions (i.e. Na$^+$, purple channel, left), which generates a propagating membrane potential (ΔV) and opens subsequent voltage-gated calcium channels (Ca^{2+}, teal channel, right). Schematic adapted from (Steinlein, 2004).
c. A topology diagram of the unfolded tertiary structure of the VGCC alpha 1 subunit (center) comprises four domains (I-IV), each with six transmembrane segments connected by loop regions. Voltage sensitive domains are shown in gray. When triggered, calcium flows through this channel from the outside to the inside of the cell (direction marked by dotted arrow). Schematic adapted from (Catterall, 2011).

The first VGCC subfamily, CaV1 (*CACNA1C*), is mainly responsible for excitation-contraction coupling in muscle, transcription in neurons and muscle, as well as secretion in endocrine cells (Catterall, 2011). Channels associated with this subfamily are termed L-type, for their 'Long lasting' and slow voltage-dependent inactivation property. Second, CaV2 channels (*CACNA1A*) are commonly denoted as P/Q-, N-, and R-type currents that initiate varying rates of fast synaptic transmission and are thus mainly expressed in neurons. Lastly, CaV3 *(CACNA1G)*, or T-type calcium channels are activated at negative potentials, with rapid voltage-dependent inactivation for rhythmic control and large calcium transients.

Cells that function with this voltage-dependent property are known as electrically excitable. Each of these cell types receive and process stimuli, triggering the electrical transduction cascade mentioned earlier. This cascade is important for facilitating cell-to-cell communication through chemical neurotransmitters released from synapses in neurons; for example, the release of acetylcholine from motor neurons produces contractile forces in muscles. Cell types also function independently based on this principle. For example, the human brain is continuously active, sending, receiving, and processing electrochemical signals across neurons through the activation of ion channels. In a general sense, these signals form all of our thoughts and behaviors. Also, the heart contracts involuntarily to regularly supply oxygen and other important nutrients throughout the body. Thus, any irregularities in ion channel structure and function in these cell types can cause severe effects in associated physiological processes, resulting in a wide variety of human disease (Adams and Snutch, 2007; Felix, 2006; Kim, 2014; Rose, 1998).

Calcium channelopathies and severe activity-dependent disorders

Channelopathies are a classification of clinically diagnosed human diseases caused by perturbations in ion channels, which can develop through genetic inheritance, or are sporadically acquired, like through other developed diseases or exposure to drugs and toxins (Kim, 2014). These mutations, or changes in the genetic DNA sequence (by deletions, duplications, inversions, substitutions, or translocations), impair ion channel gating, such as channel opening, inactivated closed (refractory period), or resting closed states (Kim, 2014) (**Fig. 2**). Generally, gain-of-function (GOF) mutations in *CACNA1C* impair channel inactivation (delayed channel closing), while loss-of-function (LOF) mutations can lead to hypoexcitability, or decreased ion flux (Kim, 2014). Reduction-of-function (ROF) channels may also exist and can cause in-between symptoms. Importantly, GOF, ROF, and LOF also have different effects depending on the ion channel type or auxiliary subunit that is affected, which could lead to similarities in overall patient symptoms (Boczek et al., 2015a; Kim, 2014; Steinlein, 2004). Since ion channels are expressed in various cell types throughout the body, dysfunction in them can cause diseases of the nervous, cardiovascular, endocrine, urinary, respiratory, and immune system (Steinlein, 2004).
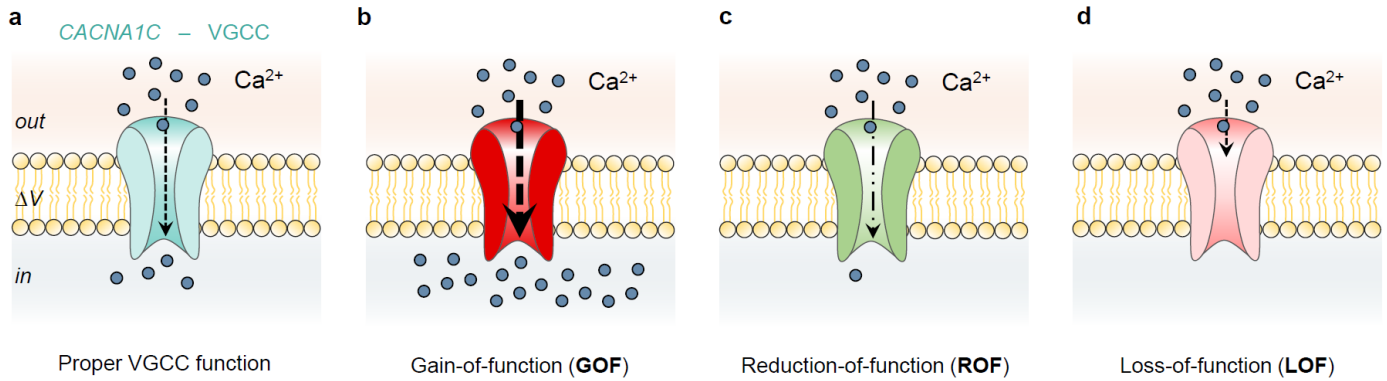
Figure 2. Different levels-of-function in ion channels, and resulting changes in transmembrane current and intracellular ion concentration.

a. An L-type voltage-gated calcium channel (VGCC) with proper channel function, allowing regular flux of calcium into the cell.
b. A gain-of-function (GOF) VGCC causes larger inward current, resulting in higher levels of intracellular calcium.
c. A reduction-of-function (ROF) VGCC causes reduced inward current, resulting in lower levels of intracellular calcium.
d. A loss-of-function (LOF) VGCC prevents channel function. Schematic adapted from (Steinlein, 2004).

8

Nervous system channelopathies are neurological disorders with a broad range of severity, known as epilepsy, migraine, and schizophrenia. Specific mutations have been detected in these diseases, identifying the pore-forming α1 subunit of voltage-gated calcium channels (i.e. *CACNA1A* and *CACNA1C*) as a major risk loci (Heyes et al., 2015; Smoller, 2013). In the human VGCC gene *CACNA1A*, up to at least 20 mutations have been identified that can lead to the GOF disorder known as familial hemiplegic migraine type 1 (FHM1) (Kim, 2014; NIH CACNA1A, 2018; Rajakulendran et al., 2010). At a cellular level, FHM1 causes increased channel activity and synaptic transmission, as these channels are highly expressed in the nervous system and responsible for neurotransmitter release. Meanwhile, GOF mutations in the L-type VGCC *CACNA1C* cause prolonged inactivation of both neural and cardiac cell types, leading to autism, cardiac arrhythmia, and severe developmental defects in humans (Landstrom et al., 2016; NIH CACNA1C, 2018). LOF conditions have also been reported in both genes, which result in decreased calcium currents or enhanced repolarization, respectively (Kim, 2014).

In particular, and consistent with clinically diagnosed symptoms, *CACNA1C* has a heterogeneous expression pattern due to mutually exclusive alternative splicing events located on chromosome 12p13.3 (Bhat et al., 2012). In humans, 80% of *CACNA1C* is highly expressed in the brain and muscle by exon 8, while 20% of *CACNA1C* is expressed by the alternatively spliced isoform exon 8A (NIH CACNA1C, 2018; NIH Timothy syndrome, 2018). One of the most characterized mutations in this gene is commonly known as Timothy syndrome (TS), in which there are two types (TS1 and TS2) with varying severity (NIH CACNA1C, 2018; NIH Timothy syndrome, 2018; Splawski et al., 2004, 2005). Less than 30 cases of TS have been reported, and TS1 is the most common (17

individuals), which are all caused by the same single GOF *CACNA1C* heterozygous missense

mutation G406R in exon 8A (Dufendach et al., 2013; Fröhler et al., 2014; Splawski et al., 2005).

Currently, four cases of the more rare and severe type 2 condition (TS2) have been reported, and

are caused be either a missense mutation G402S (three cases) or G406R (one case) in exon 8

(Fröhler et al., 2014; Splawski et al., 2005). The increase in severity is thought to be correlated to

expression pattern, and mostly all known cases of TS were acquired spontaneously (*de novo*) with

mosaic expression patterns (Splawski et al., 2004, 2005). Although the exact genetic cause is

known for this disorder, there are no currently effective therapies for these patients,

unfortunately causing a short life expectancy for several individuals with TS (average of 2.5

years). More recently, symptoms that resembled TS were reported and determined to be caused

by either missense mutation I1166T in exon 27, R518C in exon 12, R1473G in exon 38, or S643F,

all in *CACNA1C*. Each mutation was shown to have different electrophysiological phenotypes that

resemble loss-and-gain of function effects, also with varying levels of syndactyly (Boczek et al.,

2015a, 2015b; Gillis et al., 2012; Ozawa et al.). For other mutations identified in *CACNA1C* that

have symptoms not diagnosed as Timothy syndrome are sometimes referred to as Long-QT

syndrome (LQTS) (Boczek et al., 2013; Fukuyama et al., 2014; Hennessey et al., 2014), or have

been associated with schizophrenia (Hori et al., 2012). Rare genetic mutations that cause diseases

like TS are excellent case studies for investigating disease pathology, identifying how specific

genes can lead to neurodevelopmental disorders, and discovering effective therapeutic

compounds and treatment strategies for TS patients and related activity-dependent disorders.

Gold standards for human disease modeling

In 2006, researchers discovered a technique to re-program mature skin cells (i.e. fibroblasts) into an embryonic, pluripotent, state *in vitro* using select transcription factors (Takahashi and Yamanaka, 2006). These embryonic-like cells are commonly referred to as human induced pluripotent stem cells (hiPSCs). This discovery and technique enabled a new generation of research, in which scientists have been able to non-invasively obtain cells from healthy individuals or patients with diseases, and study patient specific cell-types not otherwise easily obtained in the clinic (Ardhanareeswaran et al., 2017).

For example, Yazawa *et al.* (2011) and Paşca, *et al*. (2011) both from Dr. Ricardo Dolmetsch's lab obtained fibroblasts from patients with Timothy Syndrome type 1, and generated hiPSCs for differentiation into cardiomyocytes and neuronal cell types *in vitro*, respectively (Paşca et al., 2011; Yazawa et al., 2011). Since patients with TS1 harbor the missense mutation G406R in *CACNA1C*, which is highly expressed in tissue of the heart and brain, these cell types displayed a number of phenotypes consistent with GOF-like characteristics and patient symptoms such as cardiac arrhythmia, developmental delay, and autism. Specifically, Yazawa *et al.* (2011) showed that TS1 hiPSC derived cardiomyocytes have irregular contraction and electrical activity, excess calcium influx with abnormal calcium transients, as well as prolonged action potentials (Yazawa et al., 2011). In addition, the Dolmetsch lab showed that TS1 hiPSC derived neurons and TS rodent models have defects in activity-dependent gene expression and dendritic retraction, with abnormalities in differentiation (Krey et al., 2013; Paşca et al., 2011). Heterologous and other *in vitro* model expression systems also showed similar changes in cellular activity, sometimes with

more pronounced effects (Barrett and Tsien, 2008; Boczek et al., 2015b; Dick et al., 2016; Krey et al., 2013; Landstrom et al., 2016; Splawski et al., 2004, 2005). Further, Yazawa *et al.* (2011) and Paşca, *et al.* (2011) showed that the direct incubation of these cells with Roscovitine, a cyclin-dependent kinase inhibitor and atypical L-type calcium channel blocker, can restore activity-dependent phenotypes in TS1 derived cardiomyocytes and neurons (Paşca et al., 2011; Yazawa et al., 2011). Therefore, the use of hiPSCs to study neurodevelopmental diseases has uncovered new mechanisms and provided a possible platform for the translation and development of new therapeutic compounds to treat patients with Timothy syndrome, and potentially other activity-dependent disorders (Yazawa and Dolmetsch, 2013).

Model organisms for neuroscience, human disease, and drug discovery

Although hiPSCs may be the current gold standard to elucidate novel disease pathology and evaluate therapeutic candidates, these assays may have limitations. For example, *in vitro* studies do not fully recapitulate the true heterogeneity of human diseases, nor appropriately assess off-target compound effects for use in translation (Sharma et al., 2013; Yazawa and Dolmetsch, 2013). Additionally, hiPSCs are relatively expensive, challenging to propagate, differentiate, and maintain, and experimental procedures are sometimes difficult or laborious, although protocols are constantly being developed to overcome some of these drawbacks (Khurana et al., 2015; Sharma et al., 2013; Yazawa and Dolmetsch, 2013). Heterologous systems (like transfected Xenopus oocytes, HEK, or CHO cells) yield similar results and overcome some limitations compared to hiPSC studies, but still suffer from similar translational pitfalls (Barrett and Tsien, 2008; Boczek et al., 2015b; Dick et al., 2016; Goldin Alan L., 2006; Krey et al., 2013; Landstrom et al., 2016; Senatore et al., 2011; Sharma et al., 2013; Splawski et al., 2004, 2005; Yazawa and

12

Dolmetsch, 2013). On the other hand, popular mammalian model systems, like mice, may offer a platform that includes the heterogeneity of disease and effectiveness of therapeutic compounds *in vivo* (Perlman, 2016). However, despite genetic similarities in mice to humans, their native physiological function may only be appropriate for modeling specific human disorders, while large vertebrates are not amendable to conventional genetic or compound screens (Perlman, 2016).

For example, homozygous and heterozygous genetic knock-in mouse models of Timothy syndrome type 2 are not viable (Bader et al., 2011). Thus, a homozygous knock-in (G406R) is lethal in mice, as it is in humans. For heterozygous TS2 mice, lethality is likely due to inherent differences in animal cardiophysiology (Bader et al., 2011; Bett et al., 2012). Specifically, mice have a heart rate 10X that of humans, thereby early lethality is likely due to the severity of TS heart conditions in humans (Bader et al., 2011; Bett et al., 2012; Perlman, 2016). To decrease expression of the TS2 mutant channel, an inverted neomycin cassette for TS2 in exon 8A was expressed in heterozygous TS2 mice (G406R in exon 8), yielding viable animals that also confirm autism-like behavioral phenotypes and developmental abnormalities (Bader et al., 2011; Bett et al., 2012). Also, mice expressing the homologously recombined TS G406R mutation in only the forebrain showed similar, but not all consistent, changes in specific gene expression when compared to *in vitro* hiPSC studies (Paşca et al., 2011). Despite unexpected and somewhat inconsistent results, mouse models of TS provided new understanding and insight into this rare genetic disease; however, animal models should be evaluated and selected with caution depending on the disease pathology (Perlman, 2016). Further, unexpected disease model results

are valuable pieces of knowledge, as long as they are properly characterized, explained, and shared with the community.

Currently, no other true genetic knock-in whole-organism models of Timothy syndrome exist or have been reported, even though the VGCC genetic sequence is highly conserved in other popular model systems, like nematodes (*Caenorhabditis elegans*) (**Fig. 3**), zebrafish, and the fruit fly (*Drosophila melanogaster*). Each model system offers unique opportunities for investigating TS pathology (Splawski et al., 2005). Both zebrafish and *Drosophila* have a heart and functional nervous system, which may have a more direct implication for studying systematic TS phenotypes. Models of human Long-QT syndrome (LQTS), which is sometimes associated with symptoms common in TS, but without autism, have been made and characterized in both organisms (Arnaout et al., 2007; Ocorr et al., 2007). Zebrafish harboring a human-relevant disease mutation in a potassium channel (*KCNH2*) demonstrate recapitulated human cardiac phenotypes *in vivo* (Arnaout et al., 2007; NIH KCNH2, 2018), while *Drosophila* have mutually exclusive exome splicing, similar to TS pathology (Hatje and Kollmar, 2013). Also, LQTS has been studied in *C. elegans* by observing changes in pharyngeal muscle pumping rate, similar to cardiac tissue (Schüler et al., 2015). To investigate underlying neuropathology of TS, *C. elegans* may be ideal since they have the most simple and characterized functional nervous system. Altogether, TS mutations should be generated in each of these animals, as each model organism would provide comparative and synergistic discoveries to elucidate novel genetic etiology for TS. Specifically, *C. elegans* human disease models should be developed since they are amendable to high-throughput primary screens to detect genes or compounds that rescue phenotypes and

restore irregular channel function. Then, experiments could be performed in vertebrates like zebrafish and mice, which offer a translatable platform for evaluation of both mechanistic and off-target systematic therapeutic effects in secondary compound screens.

Figure 3. Sequence alignment of CACNA1C (human) and EGL-19 (worm) and localization of conserved TS mutation loci.

a. A custom-built Needleman-Wunsch text alignment tool for input and visualization (below) of two sequences (DNA, protein, *etc*.), showing *CACNA1C* (*Sequence A*) and *EGL-19* (*Sequence B*). Domain I, section 6 (IS6) is highlighted by the black box. A green box represents a match (=), and blue is a mismatch (!). Evaluation variables: mismatch = 1, gap = 2, and skew = 1. http://users.wpi.edu/~rosslagoy/nwunsch.html

b. The alpha 1 subunit of *CACNA1C/EGL-19* showing the mutation loci and amino acid change(s) in TS patients (black) and the worm (blue). IS6 is boxed with zoom-in. TS1 loci is marked in red and TS2 in black.

c. The protein sequence alignment of *CACNA1C* and *EGL-19* for the TS mutation loci produced by the online tool in a, highlighting the well-conserved IS6 protein sequence for the TS mutation loci (green box and underline).

C. elegans *as a model organism for studying human diseases*

Caenorhabditis elegans (*C. elegans*) is a simple model organism to study neuroscience and development, originally discovered by Sydney Brenner and colleagues in the late 1950s (Brenner, 1974). Ever since, these natural soil-dwelling and transparent invertebrate animals led to the first whole genome sequence from a multi-cellular organism (C. elegans Sequencing Consortium, 1998), the only fully mapped nervous system containing just 302 neurons in an adult hermaphrodite (White et al., 1986), and the first and only complete map of timing and direction of every cell lineage (of 959 somatic cells) from egg to adult (Sulston et al., 1983). Notably, the worm has also been invaluable for the discovery of fundamental biological pathways involved in apoptosis (programmed cell death) (Ellis and Horvitz, 1986), interference RNA (RNAi) (Fire et al., 1998), and transgenic expression of green fluorescent protein (GFP) (Chalfie et al., 1994), all of which have been recognized with Nobel prizes. Additionally, worm strains are cheaply available through the *Caenorhabditis* Genetics Center (CGC), and RNAi libraries are also commercially available. It is also now straightforward to introduce mutations into the *C. elegans* genome, in single cells or multiple cell types, by microinjection (Mello et al., 1991); therefore, *C. elegans* became useful for the study of human disease and fundamental biological questions.

Using standard transgenic techniques, human neurological diseases have been modeled in *C. elegans*, like Huntington's disease (HD) and Alzheimer's disease (AD) (Faber et al., 1999; Hornsten et al., 2007; Kim et al., 2016; Link, 1995; McCormick et al., 2013). In humans, Huntington's disease is caused by excessive repeated copies of CAG in the HD gene that encodes for polyglutamine (polyQ) and results in progressive neurodegeneration (Faber et al., 1999). Transgenic expression

17

of the longest 150 residue ployQ tract in a subset of sensory neurons in *C. elegans* leads to progressive cell degeneration, mortality, and protein aggregates (Faber et al., 1999). Shorter polyQ residues, or less severe disease types in humans, also had minor or no effects in the observed neuron, although were estimated to have the same expression levels (Faber et al., 1999). Similarly, a worm model of AD that expresses human tau in all neurons, exhibits neurodegeneration and aggregates, both characteristic of the disease pathology. Also, some AD and other human disease orthologs are conserved in *C. elegans*, and can yield similar consistent pathological differences through GOF, LOF, and reduction-of-function (ROF) genomic backgrounds (Hornsten et al., 2007; Link, 1995). Together, these two examples demonstrate that it is possible to model human diseases in *C. elegans* through transgenic heterologous approaches.

Another approach for generating human disease models in *C. elegans* uses a prokaryotic-derived genome modification system, known commonly as CRISPR-Cas9, short for c̲lustered, r̲egularly i̲nterspaced, s̲hort p̲alindromic r̲epeats (CRISPR) with RNA-guided Cas9 endonuclease (CRISPR-Cas9) (Hsu et al., 2014; Jinek et al., 2012). When expressed in the germline of *C. elegans* using standard microinjection techniques, the CRISPR-Cas9 complex localizes to genomic DNA *via* a short guide RNA (sgRNA) and introduces double stranded breaks that are endogenously repaired through homologous recombination (**Fig. 4**), causing either random insertions or deletions (indels) (Friedland et al., 2013). As a first example and proof-of-concept, Dickenson *et al.* (2013) showed that it is possible to make targeted insertions by supplying a DNA repair template (donor) during cutting events, referred to as CRISPR-Cas9 homology directed repair (CRISPR-Cas9 HR), with up to ~20% efficiency (Dickinson et al., 2013). The efficiency of CRISPR-Cas9 derived cuts

and HR-directed insertions largely depend on user-defined conditions, like desired insertion loci, knock-in sizes, or HR positive screening methods. Fortunately, user guides and workflows have recently been published and are freely accessible to assist in experimental design and gene editing considerations (Dickinson and Goldstein, 2016). Also, multiple co-CRISPR strategies have been established to improve screening efficiency for positive HR events that might otherwise be difficult to identify, like the insertion of single gain-of-function point mutations (Arribere et al., 2014; Kim et al., 2014).
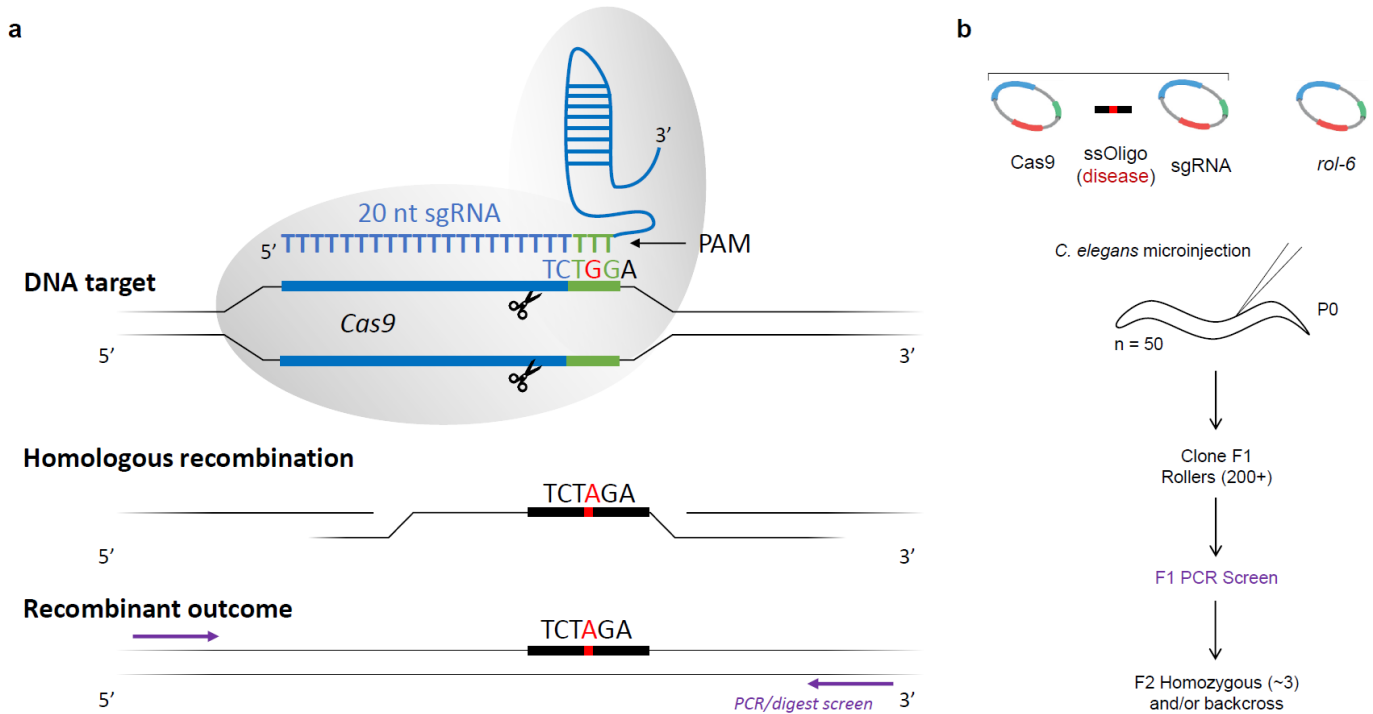
Figure 4. Schematic of CRISPR-Cas9 HR for directed insertion of point mutations in genomic DNA of C. elegans.

a. The CRISPR-Cas9 complex localizes to the region of DNA to induce a double stranded DNA break directed by a short guide RNA sequence (sgRNA). For this version of Cas9, an NGG PAM sequence is required for proper localization of the Cas9 endonuclease complex. After successful cleavage, typical DNA repair mechanisms recombine nearby DNA to mend the broken sequence. Taking advantage of this native cellular mechanism, the system can repair the cut region with a non-native DNA donor sequence that may contain desired mutations (TS1 loci and mutation shown in red). The donor sequence must also contain a mutated PAM site such that the complex does not mistakenly target the donor sequence, leading to unsuccessful donor-induced HR. In this example, both the TS1 and PAM mutation provide overlapping functions, simplifying design. Finally, successful HR events are detectable in animals expressing the recombinant outcome by PCR sequencing, sometimes compatible with restriction digests to more rapidly identify insertions (as shown here, TCTAGA is XbaI). Schematic adapted from (Friedland et al., 2013).

b. The generation of such recombinant outcomes in *C. elegans* is accomplished by microinjection (~ 50 animals) of a mixed solution in the germline containing the Cas9 endonuclease, sgRNA, single-stranded donor oligo (ssOligo), and *rol-6* translational marker. Homozygous animals can be generated through subsequent cloning steps, which also eliminates off-target effects. If targeted genes are essential, then the use of proper balancer strains may be required for maintenance and propagation.

20

Taken together, transgenic expression and knock-in mutations using CRISPR-Cas9 in *C. elegans* enable rapid, effective, and economical approaches for investigating structure-function relationships of human disease genes in a whole-organism. However, transgenic approaches do not always accurately model human diseases, as expression levels may vary in individuals and could lead to gene silencing and unwanted heterogeneity, but these are more traditional than CRISPR-Cas9. Meanwhile, CRISPR-Cas9 genome editing offers an approach to develop accurate models of human diseases with more control and greater confidence in results, directly linking endogenous gene function to phenotype in model organisms.

Tools and techniques for monitoring and stimulating cellular activity in C. elegans

As briefly mentioned above, transgenes are also useful for expressing heterologous fluorescent proteins (like green fluorescent protein, GFP) to visualize physical features, like cellular structures and protein localization, and monitor dynamic processes, like changes in cellular activity using genetically encoded calcium indicators (GECIs) (Akerboom et al., 2012; Chen et al., 2013; Nakai et al., 2001; Tian et al., 2009, 2012). In general, GECIs are derived from GFP (or proteins with other fluorescent wavelengths) and modified by fusion of a calmodulin (CaM) domain. The CaM domain binds to intracellular free calcium, which causes a conformational change in the molecule, becoming proportionally brighter in its presence (**Fig. 5**). These sensors are bright, photostable, and biostable, and known commonly as GCaMPs, for GFP-Calmodulin Fusion Proteins (Nakai et al., 2001). All GECIs are based on the same calcium binding property, while some (e.g. Cameleon) require Förster resonance energy transfer (FRET), and often require more complicated optical configurations with lower signal-to-noise, and either high calcium affinity or fast intramolecular dynamics (Tian et al., 2012). Also, dye-based (non-genetically encoded)

calcium indicators can be used for *in vitro* preparations and function similarly, but are usually difficult to target to specific cell types, and loading procedures are low-throughput and can be damaging, which can hinder and complicate imaging in specific cell types especially for long-term durations (Paredes et al., 2008).
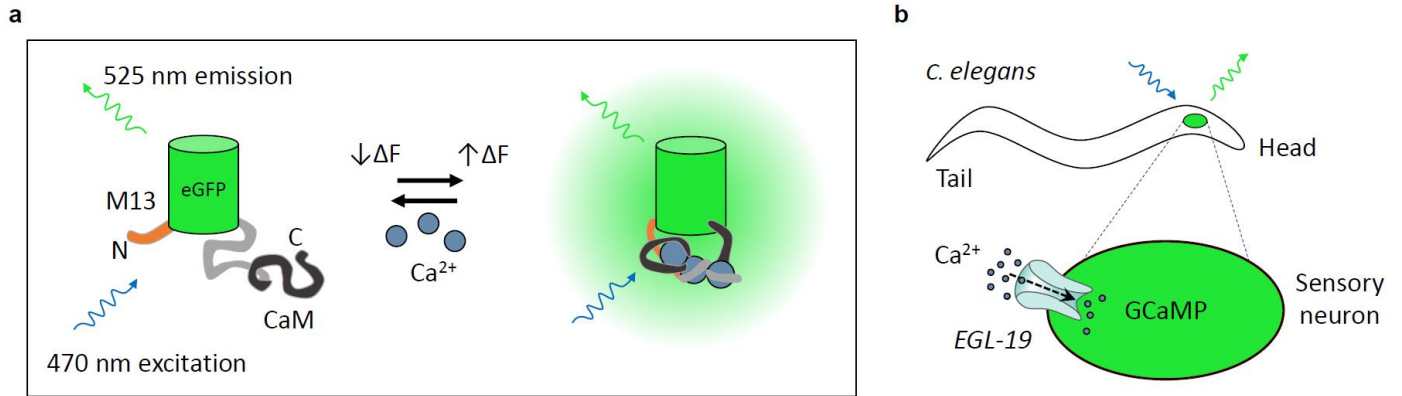
Figure 5. Genetically encoded calcium indicators are molecules that increase brightness in the presence of calcium, which can be expressed in living organisms to monitor calcium dynamics.

a. The GECI known as GCaMP is an enhanced-GFP fused to M13 at the N-terminus and a calcium binding domain (CaM) at the C-terminus. In the presence of calcium, the protein complex undergoes a conformational change and increases in fluorescence ($\uparrow\Delta F$). A blue excitation wavelength (~470 nm) is used to emit green baseline fluorescence (~525 nm) in the GECI (GCaMP) shown. Schematic adapted from (Pérez Koldenkova and Nagai, 2013).

b. GECIs can be genetically expressed in single cells of whole living organisms, like a *C. elegans* sensory neuron (shown), to monitor changes in intracellular calcium dynamics proportional to voltage-gated calcium channel function.

23

C. elegans were one of the first *in vivo* model systems used for evaluating single-wavelength genetically encoded calcium sensors (GCaMPs) that can be expressed in single or multiple cells and cell types using standard transgenic techniques (Tian et al., 2009) (**Fig. 5**). Since its initial demonstration, GCaMPs have become brighter and faster, with larger dynamic range and higher affinity to calcium binding, but sometimes compromises baseline fluorescence with a shift towards red wavelength excitation (485 nm for GCaMP2.2, and above for GCaMP3) (Akerboom et al., 2012; Chen et al., 2013). In worms, GCaMPs have been used to monitor changes in compartmentalized single cellular activity of neurons (i.e. axons, dendrites, and somas), muscle, or multi-cellular brain-wide recording in intact living animals (Hendricks et al., 2012; Kato et al., 2015; Kerr et al., 2000; Schrödel et al., 2013). Further, researchers have been able to monitor neural activity at both scales (single neurons or brain-wide) in freely behaving worms and zebrafish (Kim et al., 2017; Larsch et al., 2013; Nguyen et al., 2015). These studies reveal both detailed *in vivo* sub-cellular function and brain-behavior states not before possible using conventional electrophysiological techniques (Hendricks et al., 2012; Kato et al., 2015). Additionally, GECIs are extremely useful for investigating scientific questions and hypothesis specifically related to calcium, especially in *C. elegans* where VGCCs are responsible for facilitating large changes in membrane potential (Gao and Zhen, 2011; Lockery and Goodman, 2009; Lockery et al., 2009; Mellem et al., 2008). In this regard, GECIs report second-messenger cellular activity (calcium), while fluorescent genetically encoded voltage indicators would provide measurements of membrane potential and cellular activity, of which are currently being improved in attempt to match the patch-clamp gold standard technique with similar benefits to GECIs *in vivo* (Pakhomov et al., 2017; Peterka et al., 2011). It is possible to record

electrophysiological signals in *C. elegans* using traditional patch-clamp techniques in disassociated preparations; however, not as commonly practiced in worms and typically limited to large cell types (like muscle) due to technical difficulties in recording from neurons and processes (can be <2 µm) (Goodman et al., 2012; Lockery and Goodman, 1998). Importantly, methods to stimulate cellular activity in cells and whole organisms, like *C. elegans*, have also been developed to investigate behavioral and mechanistic cause and effect in whole-animals at the cellular and systemic levels.

Heterologous expression of light-gated cation channels derived from green algae, known as microbial opsins, or channelrhodopsins, is one artificial way to stimulate cellular activity in cells and whole organisms, like *C. elegans* and mice (Nagel et al., 2002, 2003). The channelrhodopsin-2 (Chr2) channel opens rapidly (with millisecond resolution) after absorption of photons in the presence of the All-*Trans* Retinal (ATR) chromophore, which allows monovalent and divalent cations to flow into the cell (Nagel et al., 2003). This ion flux depolarizes the cell membrane, and generates strong and measureable currents simply by illumination using traditional GFP filters (450-490 nm), first observed using the patch-clamp technique in heterologous systems, like neurons (Boyden et al., 2005; Nagel et al., 2003). When a modified GOF Chr2 channel (H134R) is expressed in only *C. elegans* muscle cells or mechanosensory neurons with exogenous treatment of ATR, strong simultaneous contractions and reversal responses (typical of touch) are induced, and changes in muscle cell membrane excitability were measured by patch-clamp electrophysiology (Nagel et al., 2005). Other microbial opsins can also hyperpolarize cells in heterologous systems, known as halorhodopsins, which function by similar properties like Chr2.

However, these opsins differ in which ions flow through its transmembrane pore (i.e. Cl^-) and the wavelength of activation (Leifer et al., 2011; Schobert and Lanyi, 1982; Zhao et al., 2008). Light-evoked responses in cells and organisms also seem to be transient, without noticeable habituation in response signal depending on cell type and conditions (Boyden et al., 2005). These optogenetic techniques have also been applied to other model systems and vertebrates (Anikeeva et al., 2011; Gunaydin et al., 2014), empowering the experimental control of orthogonal cellular stimulation to induce behavioral responses and study involved neural circuits. These highly specific and targeted stimulation approaches are also being used to treat activity-dependent disorders (Albert, 2014; Gradinaru et al., 2009; Gunaydin et al., 2014; Towne and Thompson, 2016; Vann and Xiong, 2016).

Recently, researchers identified a red-light shifted channelrhodopsin (Chrimson) to independently activate co-cultured cell populations with blue-light excitation Chr2 variants (Klapoetke et al., 2014). The excitation wavelength separation spectra of Chrimson and Chr2 (and GCaMPs) has also found use for simultaneous stimulation and monitoring of calcium activity using only light in whole organisms (Larsch et al., 2015; Schild and Glauser, 2015) (**Fig. 6**). Alternatively, it is possible to use red light to monitor calcium activity (RCaMP, using mRuby-CaM, or R-GECO1) with blue light to stimulate (Chronos) with even greater wavelength spectra separation; however, RCaMP has not been as completely developed and characterized as the GCaMP families, but there have been a few promising recent advancements (Akerboom et al., 2013). Taken together, the established spectrum of fluorophores and light-activate microbial opsins offer unique combinations for monitoring, stimulating, and inhibiting multiple

independent cell types *in vitro*, like brain slices and cell populations, and *in vivo*, using transparent

whole organisms (e.g. *Drosophila*, zebrafish, and *C. elegans*) or fiber-optics to deliver light deep

within vertebrate brains (Anikeeva et al., 2011; Tian et al., 2009).
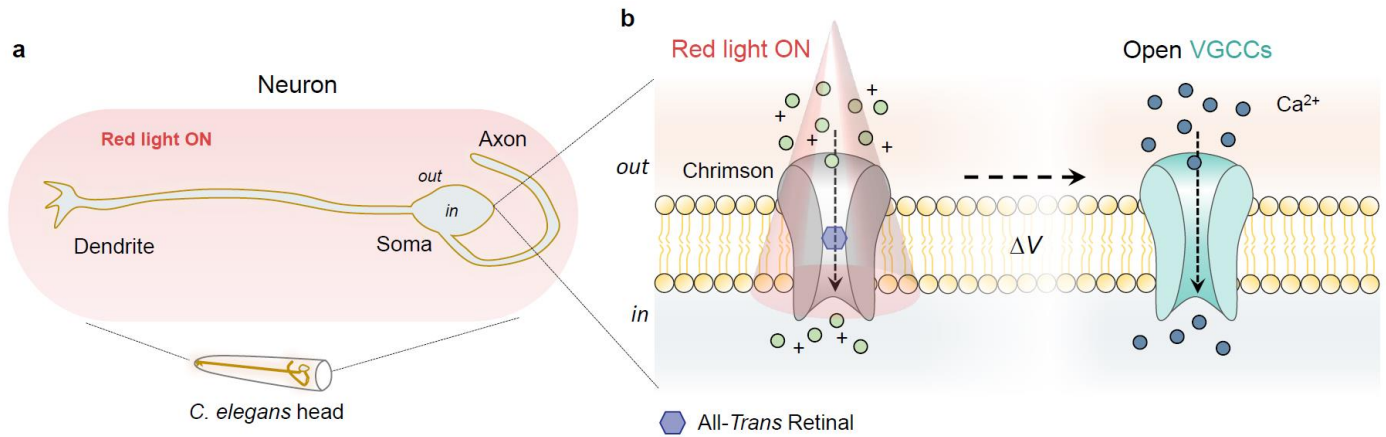
Figure 6. Expression Chrimson in a single neuron in the C. elegans *head stimulated by red light opens local and subsequent voltage-gated calcium channels.*

a. A single neuron expressing the channelrhodopsin Chrimson in the head of *C. elegans* (zoom-in from below) with the red light excitation (~617 nm).
b. An illustration of the neuron cell membrane zoom-in from a showing the ion channel Chrimson opening to red light stimulation in the presence of the All-*Trans* Retinal chromophore (gray channel with red shading and purple molecule, left), allowing influx of positive ions, depolarizing the cell membrane (ΔV), and opening subsequent local voltage-gated calcium channels (teal channel, right).

Additionally, since *C. elegans* are small (~1 mm) and can survive in liquid environments, microfluidic devices have become increasingly popular for more natural odor-based stimulation and observation of population behavior in a highly controlled setting (Albrecht and Bargmann, 2011; San-Miguel and Lu, 2013). Fluid dynamics at this micrometer scale is laminar and highly predictable (Blow, 2007; Lee et al., 2011; Whitesides, 2006), which provides the unique opportunity to generate well-defined spatiotemporal chemical patterns that house freely behaving animals (Albrecht and Bargmann, 2011). These behavioral microfluidic devices also allow for long-term observation (hours) of hundreds of animals in a single experiment, while smaller-scale higher-magnification devices enable the recording of stimulated cellular activity in either single animals with high-resolution, or up to 20 or more animals at once with different genetic backgrounds in a single experiment with wide-field microscopy (Chronis et al., 2007; Larsch et al., 2013). These higher-resolution devices have also been shown to be compatible with neural imaging, since typical GCaMP excitation is independent of stimulation with liquid-borne odors (Chronis et al., 2007; Larsch et al., 2013). Microfluidic experiments can also be automated, delivering pulses of the same, or different, natural odor stimuli for hours at well-defined time points and patterns (Albrecht and Bargmann, 2011; Larsch et al., 2013). These experiments are highly reproducible with many different applications. Altogether, these optogenetic and microfluidic tools can be used synergistically for multiplexed experiments to probe the function of excitable cells within different aqueous environments, and to investigate changes in behavior or activity-dependent function caused by specific mutations in whole organisms.

Using C. elegans *to study human channelopathies*

In *C. elegans*, there are three identified orthologous VGCCs: *EGL-19* (L-type), *UNC-2* (P/Q/R/N type), and *CCA-1* (T-type) (Lee et al., 1997; Schafer and Kenyon, 1995; Shtonda and Avery, 2005). Specifically, *egl-19* was discovered through a traditional forward genetic screen using ethyl methanesulfonate (EMS) in which mutants (all missense point-mutations) were initially identified as egg-laying defective with abnormal forward speed and elongated or short body phenotypes (Trent et al., 1983). Since then, *egl-19* has been characterized as the pore-forming α1 subunit through an additional EMS screen, further genetic mapping, and non-complementation screens against other known *egl-19* mutations, like the ROF *egl-19(n582)* (R899H in IIIS4) allele (Lee et al., 1997). From one study, two myotonic and increasingly severe GOF mutations *egl-19(ad695)* (A906V in IIIS4) and *egl-19(n2368)* (G365R near IS6) were identified to cause pharyngeal pumping defects, short (dumpy) body phenotypes, constitutive egg laying, and cold temperature sensitivity (for *egl-19(n2368)* only) (Lee et al., 1997). Also, these GOF mutations showed prolonged action potentials in terminal bulb muscle measured by patch-clamp and electropharyngeograms, while the ROF mutation also showed slower kinetics during the depolarization phase, consistent with VGCC function (Lee et al., 1997; Schüler et al., 2015; Tang et al., 2014). The *egl-19* gene was also cloned and identified as having high residue homology (19 of 23) found in the IIIS5-S6 and IVS5-S6, where sensitivity to dihydropyridines (DHP), the hallmark of the α1 subunit in VGCCs, was first implicated and later confirmed (Jospin et al., 2002; Kwok, 2013; Kwok et al., 2006, 2006; Lee et al., 1997; Tang et al., 2014). Transgenic rescue of *egl-19* in the ROF mutant background was also enough to restore body structure and pharyngeal pumping phenotypes (Lee et al., 1997). Further, an *EGL-19::GFP* transgenic fusion construct showed

protein localization to body wall muscle in early embryonic development and in several head neurons (Lee et al., 1997). A true *egl-19* null, or complete genetic knockout (LOF) in *C. elegans*, has been attempted, but is not maintainable since *egl-19* is believed to be an essential gene (Lee et al., 1997).

Since these initial studies, *egl-19* has been further characterized in *C. elegans* and heterologous systems. In addition to pharyngeal bulb membrane excitation defects in the worm, body wall muscles also have decreased inactivation, reduced desensitization, a more negative half-activation potential shift, and an increased sensitivity to voltage in GOF mutants, while ROFs require stronger depolarization to activate intracellular calcium rise, all measured by patch-clamp and simultaneous calcium imaging in muscle of dissected animals (Jospin et al., 2002). These electrophysiological results suggest reason for the resulting differences in whole-organism body morphology, where hypertonic muscle structure is observed in GOF animals, while more flaccid and longer morphology (hypotonic) than wild-type in ROF (Lainé et al., 2014). Additionally, a severe ROF mutant *egl-19(ad995)* exhibits an early developmental arrest (Pat, paralyzed arrested elongation at two-fold) phenotype (Jospin et al., 2002; Kwok et al., 2006; Lee et al., 1997; Tang et al., 2014; Williams and Waterston, 1994). Further, the increasingly severe hypertonic *egl-19(ad695)* and *egl-19(n2368)* phenotypes are also proportional to a shift in voltage dependency (towards more negative potentials) measured by *in situ* electrophysiological recordings, which has been associated with a decrease in inactivation rate (Jospin et al., 2002; Lainé et al., 2014).

31

The location of mutations and missense residue properties of these alleles can also partially explain observed changes in muscle electrophysiology. For example, the ROF *egl-19(n582)* mutation loci segment (IIIS4) has been associated with voltage sensing, and could explain the depolarization defects, as well as elucidate implications in a related human disease that is also associated in this specific voltage-sensitive channel region (Lainé et al., 2014). The ROF R899H missense mutation replaces the wild-type residue to a larger hydrophobic one, which has been show to alter the channel's half-activation potential, voltage sensing, and inactivation kinetics in sodium channels (Lainé et al., 2014). Since the GOF 365R mutation is localized to the start of the IS6 intracellular loop region, such observed recordings may be due to close proximity binding of auxiliary subunits that regulate inactivation kinetics, as shown in potassium channels (Lainé et al., 2011, 2014; Shtonda and Avery, 2005). By chance, the *egl-19(n2368)* mutation is similar to the human TS2 causing loci, in that their location is exactly the same, however, the resulting amino acid is change different (an arginine instead of serine in TS2), but yield similar slowed channel inactivation measured by simultaneous patch-clamp and calcium imaging in stimulated *C. elegans* muscle (Lainé et al., 2014). Therefore, although not directly linked to the human TS1 or TS2 genotypes, these mutations may assist in the investigation of channel properties for Timothy syndrome and other human channelopathies.

To some extent, yet not as thoroughly characterized, the orthologous auxiliary subunits *unc-36* and *ccb-1* (α2/δ and β, respectively) of *egl-19* have been investigated in *C. elegans* and shown to localize near and directly to the channel, and regulate voltage dependence, activation kinetics, and calcium current conductance in body muscle (except for possibly redundant α2/δ and β

subunits) (Lainé et al., 2011, 2014; Shtonda and Avery, 2005). It has also been reported that *egl-19* is mislocalized in GOF mutants when using an α2/δ subunit binding GFP construct, especially in the more severe *egl-19(n2368)* allele, which may explain the decrease in maximal conductance of body wall muscles (Lainé et al., 2014). Also, traditional heterologous systems, like transfected Xenopus oocytes or HEK cells show that similar GOF and ROF mutations have comparable electrophysiological properties, which implies that transgenic expression of mutant VGCCs might yield associated results in other model systems (Morrill and Cannon, 1999; Zhang et al., 1994). In many of these studies, researchers have also shown that dihydropridines, like the addition of nifedipine (Jospin et al., 2002) or nemadipine (Lainé et al., 2011) to dissected animals, can (partially) inhibit the peak of calcium dependent activation by patch-clamp, while developing therapeutics that target the auxiliary subunits could also indirectly lead to effective treatments for VGCC channelopathies (Budde et al., 2002; Song et al., 2017).

High-throughput screening with C. elegans

C. elegans are an ideal model system for genetic and chemical screens due to their small size as adults (up to 1 mm), nearly 200-300 clonal progeny per adult hermaphrodite, rapid developmental timeline (3 days from egg to adult), and cost effectiveness (Leung et al., 2008; Lucanic et al., 2018; O'Reilly et al., 2014; O'Rourke et al., 2009). Albeit tedious, traditional forward genetic screens using *C. elegans* have proven to be important for the discovery of specific genes and pathways with particular functions, like for identifying the function of *egl-19.* In these screens a chemical mutagen (EMS) causes hundreds to thousands of phenotypes that can lead to a single (or few) causal gene(s), which could take up to months of genetic mapping by manual labor (Jorgensen and Mango, 2002; Kutscher and Shaham, 2014). In another compound-based

approach, genetically identical animals can be treated with hundreds to thousands of chemical compounds to identify a single (or few) phenotypic effects in wild-type animals (over days to weeks) that also led to a single or few causal gene(s) also by laborious genetic mapping (Burns et al., 2006a; Kutscher and Shaham, 2014). Further, a more direct two-fold screening approach could be used to identify compound targets that restore specific disease phenotypes, which in comparison, may still take up to months to map and identify a single compound target gene (Burns et al., 2006a; Kwok et al., 2006). Therefore, the bottleneck in these conventional screening approaches is the manual labor of genetic mapping to identify causal genes or therapeutic targets, while identification of phenotypes (at least for compound-based screens) can be automated by image-based data analysis (Burns et al., 2006a; Partridge et al., 2017). Alternatively, whole-genome sequencing of *C. elegans* is possible to identify target genes with less human labor, yet not always available or the most economical option (Hillier et al., 2008). However, identifying more specific effects in disease models could improve the efficiency of mapping causal interactions through somewhat biased forward genetics.

Kwok *et al.* (2006) demonstrated one of the first chemical and subsequent genetic screening approaches, which led to the discovery of a new class of compounds that inhibit *egl-19*, the only L-type VGCC in *C. elegans* (Burns et al., 2006a; Kwok et al., 2006). In this study, two to three wild-type animals (L3-L4 stage) were added to each well of a 24 well plate on standard nematode growth medium (NGM) containing 25 µm of different compounds, and allowed to grow five days with food (OP50 *E. coli*). At three, four, and five days, still images were recorded automatically, then phenotypes were scored automatically or by manual observation of the animals in each

well. From still images, only body size defects and population growth phenotypes were detected automatically, while the detection of irregular movement required manual observation. Once compounds were identified as primary "hits" for causing impaired phenotypes, P0 animals were mutagenized and F1 progeny were distributed to each well of a multiwell plate containing the same hit compound. Candidate target genes were then identified either manually or automatically by suppression of the original phenotype during compound exposure, then exact genetic loci were mapped. Employing this strategy and screening nearly 14,100 compounds, a family of 1,4-dihydropyridines (DHPs), one of which they named nemadipine-A, was discovered to antagonize the alpha 1 subunit of VGCCs directly in worms (*egl-19*), while other FDA-approved DHPs failed to have robust responses (Kwok et al., 2006). Among the FDA-approved DHPs, felodipine was the only compound that accumulated to the same extent in the animal body like nemadipine-A, causing only a mild population growth defect phenotype (Gro). This screen showed that it is possible to identify compounds that have broad effects on animal morphology, which can lead to the isolation of specific and disease relevant genetic targets in *C. elegans*.

By combining plate-based compound screening approaches with mutant animals, direct compound targets may be identified in a more efficient manner. Therefore, this combinatorial chemical-genetic screening strategy was used to identify azaperone, and an associated class of antipsychotic compounds that decreased aggregated tau and neural degeneration in a *C. elegans* model of Alzheimer's disease (McCormick et al., 2013). The primary screen identified general hits that suppressed tau-induced movement defects in AD worms, followed by testing more precise rescue phenotypes, like decreased levels of insoluble tau, and decreased neuronal loss by

increased cell count using a GFP reporter. These hits were further characterized in heterologous systems, revealing similar restorative effects which, together, suggest a new mechanism for suppression of tau pathology (McCormick et al., 2013). Although this workflow was successful, screening fluorescent reporter signal in human disease models first could more efficiently identify hits or other direct targets. To this end, such a screen poses a technical challenge that is primarily keeping large populations of animals immobilized during high-resolution imaging while exposed to compounds, especially for HTS in the nervous system of whole organisms (Kinser and Pincus, 2017).

Recently, Mondal *et al.* (2016) developed an automated image-based technology to screen for compounds that effect fluorescent disease-model phenotypes in *C. elegans* (Mondal et al., 2016). In their first compound screen, Mondal *et al.* (2016) used fluorescent protein aggregation as a measurable phenotype for a worm model of Huntington's disease (HD). First, *C. elegans* HD models expressing the fluorescent reporter were grown by liquid culture in 96 well plates, of which each well contained ~40 age-synchronized animals and a different compound or control buffer. Worms were then removed from compound exposure, kept separated by treatment, and transferred to a large 96-well format microfluidic trap array device for immobilization during imaging. Using this method, 983 FDA approved compounds were screened, of which they identified 17 hits that reduced the mean aggregate numbers lower than three standard deviations (99%) of the control group(s). Of the 17 compounds, four were statistically significant, and only one compound known as Dronedarone showed a strong dose-dependent reduction in protein aggregates. A similar fluorescent-phenotyping screen strategy was also recently used to

identify norbenzomorphans that reduced neurodegeneration in a *C. elegans* Alzhimer's disease model using the same method (Mondal et al., 2018). Other new methods with greater throughput (>23,500 compounds) and also based a similar GFP-reporter phenotyping approach identified inhibitors of cell death in *C. elegans* (Schwendeman and Shaham, 2016). Together, technological improvements in conventional phenotyping methods and fluorescent reporter-based assays expand HTS in *C. elegans*, which may lead to identifying more direct targets for human diseases.

It is becoming increasingly clear that research efforts are directed towards reducing manual labor while improving the identification of more direct effects in whole organisms and patient-derived human disease models. This generally requires the automation of liquid handling, sample preparation and immobilization, automated collection of data, and streamlined highly-accurate analysis and visualization. Further, new disease models should be developed in parallel with new screening technologies to expand the discovery of effective treatments for humans suffering from disease. Specifically, disease models of human activity-dependent disorders, as well as new functional screening technologies in whole organisms using new technologies should be developed to both deepen our understanding of neurological disease and to discover new and effective therapeutic targets. Also, new methods and systems should be cheap, easy to use, and widely adaptable, allowing for rapid adoption, reproducibility, and amenability to screen large compound libraries (>100,000 compounds) with minimal manual effort. With these values, and strong rationale, new method development and technologies will advance the biological

understanding of and lead to effective treatments for a larger class of human neurological disorders.

Long-term goal and specific aims

The <u>long-term goal</u> of this dissertation is to advance the understanding of human neurological diseases toward the discovery of new effective treatments (**Fig. 7**). My <u>objective</u> is to develop *C. elegans* models of human neurological disorders, characterize phenotypes, and invent new functional screening technologies to identify modulators of cellular activity *in vivo*. I <u>hypothesize</u> that human neurological disease models in *C. elegans* will elucidate novel genetic causes, and compounds that modulate cellular activity *in vivo* will be identified through new functional screening technologies. It is expected that, through achieving the <u>three specific aims</u> (below), this thesis will significantly contribute to further the understanding of human neurological diseases and lead to treatments for the millions of individuals who suffer from them.

1. ***Establish a pipeline*** for modeling and quantifying phenotypes in *C. elegans* models of human channelopathies.

2. ***Develop and characterize*** a microfluidic screening technology for the identification of short-term modulators of cellular activity *in vivo*.

3. ***Develop and characterize*** a screening method to identify compounds that modulate neural activity *in vivo* over long-term durations.

Long-term goal

To advance the understanding of human neurological diseases toward the discovery of new effective treatments.

Objective

To develop *C. elegans* models of human neurological disorders, characterize phenotypes, and invent new functional screening technologies to identify modulators of cellular activity *in vivo*.

Hypothesis

Human neurological disease models in *C. elegans* will elucidate novel genetic causes, and compounds that modulate cellular activity *in vivo* will be identified through new functional screening technologies.

AIM I
Establish a pipeline for modeling and quantifying phenotypes in *C. elegans* models of human channelopathies.

AIM II
Develop and characterize a microfluidic screening technology for the identification of short-term modulators of cellular activity *in vivo*.

AIM III
Develop and characterize a screening method to identify compounds that modulate neural activity *in vivo* over long-term durations.

Expected outcomes

C. elegans models of human channelopathies and evaluation of phenotypes *in vivo* will elucidate novel genetic causes.

New functional screening platforms will identify subtle, short- and long-term calcium channel modulators *in vivo*.

Figure 7. Flow diagram of thesis dissertation, with long-term goal, objective, hypothesis, specific aims, and expected outcomes.

39

Chapter 2 Establish a pipeline for modeling and quantifying phenotypes in *C. elegans* models of human channelopathies

I formed a collaboration with H. Kim in Dr. Craig Mello's lab at the University of Massachusetts Medical School (UMMS) in the Program of Molecular Medicine, supported by the Howard Hughes Medical Institute. H. Kim and I designed and developed the TS CRISPR-Cas9 and constructs, H. Kim did the injections, and we both screened for HR positive mutants. H. Kim developed the *EGL-19::GFP* animals and attempted to generate an *egl-19* null using CRISPR-Cas9. I also collaborated with T. McDiarmid, in Dr. Catharine Rankin's lab at the University of British Columbia (UBC) in Vancouver, BC. T. McDiarmid performed all plate-based behavioral experiments. The *egl-19p::egl-19cDNA* line and construct was obtained from Dr. Yasunori Saheki for cloning, crosses, and site-directed mutagenesis. Other original constructs were obtained from Dr. Cori Bargmann's lab at The Rockefeller University in NYC, NY. Additional mutant strains were obtained from the CGC for the generation of imaging lines.

Abstract

One in every six adults in the United States has a mental health disorder, in which there are currently no known cures or effective treatments. The diversity of symptoms and indirect measures of possible causes in humans has hindered the development of treatments for such a broad class of diseases. Timothy syndrome (TS) is a rare and severe neurodevelopmental disorder with a known genetic cause. TS patients have a single missense mutation in the voltage-gated calcium channel gene *CACNA1C* that results in prolonged channel inactivation and causes autism, cardiac arrhythmia, and severe developmental arrest. Animal models of TS and other activity-dependent disorders are either lacking, or do not fully recapitulate human symptoms, although they can provide insight into disease pathology. In this Chapter, we aim to establish a pipeline for modeling human neurological disorders affecting calcium activity in *C. elegans*. We used the TS mutation as a proof-of-concept to test multiple disease modeling approaches, as well as quantify changes in behavior, morphology, and *in vivo* calcium imaging in neurons of intact whole organisms. Our results indicate that it is indeed possible to directly mimic the genetic cellular defects in human diseases like TS using CRISPR-Cas9 HR and detect measureable differences in animal behavior, morphology, and calcium activity in *C. elegans*. I expect that this disease modeling pipeline will be useful for modeling and characterizing other channelopathies like TS to deepen our understanding of disease pathology that may lead more effective therapeutics and treatment strategies.

Introduction

Mental health disorders are one of the most common illnesses for humankind with no known cures (NIMH Mental Illness, 2018; WHO, 2006). The complexity of these disorders result in a wide variety of diagnoses (>600), ranging from anxiety and depression (triggered onset and acute), to epilepsy and schizophrenia (developmental and chronic) (UCSF Medical Center, 2018). Regardless of the severity, behavioral tests are the most common ways to diagnose these illnesses, but these do not identify individual underlying causes. Therefore, the main causes leading to most mental health disorders remains unknown, making it challenging to develop accurate animal models, as well as identify therapeutic targets to discover effective treatments.

Investigating rare neuropsychiatric and developmental disorders have led to the identification of underlying genetic causes (Jen et al., 2016). Patients with Timothy syndrome type 1 (TS1) harbor a GOF missense mutation G406R in the L-type voltage-gated calcium channel (VGCC) *CACNA1C*, which causes severe autism, irregular development, and cardiac arrhythmia (Splawski et al., 2005). Also, studying large populations of individuals with mental illness yielded the same gene, *CACNA1C*, as a potential risk loci for epilepsy and schizophrenia (Heyes et al., 2015; Hori et al., 2012; Smoller, 2013). This gene is also expressed in many cell types, but mostly in neurons and muscle, and coordinates the influx of calcium into the cell (Akerboom et al., 2013; NIH CACNA1C, 2018). Calcium is essential for cellular function, thus dysfunction caused by TS results in abnormal cellular activity, which has been shown extensively in patient derived cells and animal models (Bader et al., 2011; Paşca et al., 2011; Yazawa et al., 2011). Although this rare disorder and corresponding animal models have provided insight into TS and mutations in ion channels in

general, a broad range of disease models and pipelines for the discovery of effective therapeutics in activity-dependent disorders have not yet been developed, especially using whole organisms.

In this Chapter, I aim to establish this pipeline for *C. elegans* and highlight important considerations for investigating human channelopathies, or diseases caused by mutations in ion channels, in this organism. I show here that this approach requires (1) techniques to accurately generate human disorders in a living organism, and (2) methods to measure changes in development, behavior, and cellular activity. *C. elegans* are ideal animals for developing this pipeline due to available methods to engineer human mutations, as well as their cost effective maintenance, rapid clonal development, behavioral repertoire, and transparent bodies compatible with imaging techniques for monitoring cellular activity in whole living animals.

To generate human disease models in *C. elegans*, we used the CRISPR-Cas9 homology directed repair complex to induce the human TS1 mutation in the *C. elegans* genome, since the VGCC ortholog *egl-19* sequence is highly conserved (Splawski et al., 2005). We developed additional cell-specific and genome-wide channelopathy models in *egl-19*, which have quantifiable differences in neuronal activity. Further, we found that a selection of these mutants have quantifiable differences in behavior and body morphology using a high-throughput plate-based assay. Finally, we describe the overall success of our pipeline and future possibilities towards screening for therapeutic treatments, and highlight important considerations when generating new human disease models in model organisms. We expect that these results and ideas will provide a new platform for modeling human activity-dependent disorders in *C. elegans*, by

inducing disease-associated mutations using CRISPR-Cas9 or transgenes in these animals, then quantify resulting changes in animal development, behavior, and cellular activity. We also expect that this pipeline will be extendable to additional channelopathies in other VGCC genes or ion channels related to neuropsychiatric diseases, which altogether, will accelerate the discovery of novel therapeutic targets for translational medicine.

Results

An genome-wide TS mutation causes early developmental arrest in C. elegans

Using CRISPR-Cas9 homologous-recombination (CRISPR-Cas9 HR) (Kim et al., 2014), we developed the first whole-organism model of Timothy syndrome type 1 (TS1) in *C. elegans* (**Fig. 8**). Using standard microinjection technique (Mello et al., 1991), the orthologus mutation in the human TS1 condition, G406R, was inserted at the homologous position in *C. elegans*, G369R, at ~2% efficiency (55 animals injected, 210 animals screened, 3 HR positive events detected) (**Fig. 8a-c**). Heterozygous (TS1/+) animals were first detected by PCR screening young adults, while homozygous (TS1/TS1) animals were first observed on the plate and confirmed by PCR and sequencing (**Fig. 8b-c**). Homozygous TS1 animals were severely arrested at the L1 stage, compared to healthy adult wild-type animals (**Fig. 8d-e**). To maintain TS1 animals and develop a strain that could be used with conventional calcium imaging techniques, the genetic balancer Dnt1 was used since its genomic locus is within 0.18 map units of *egl-19* (**Fig. 8f**). After a second series of crosses, homozygous TS1 (and TS/Dnt1, not shown) animals expressing GCaMP in the AWA sensory neuron pair were developed with expression confirmed by fluorescence (**Fig. 8g**).
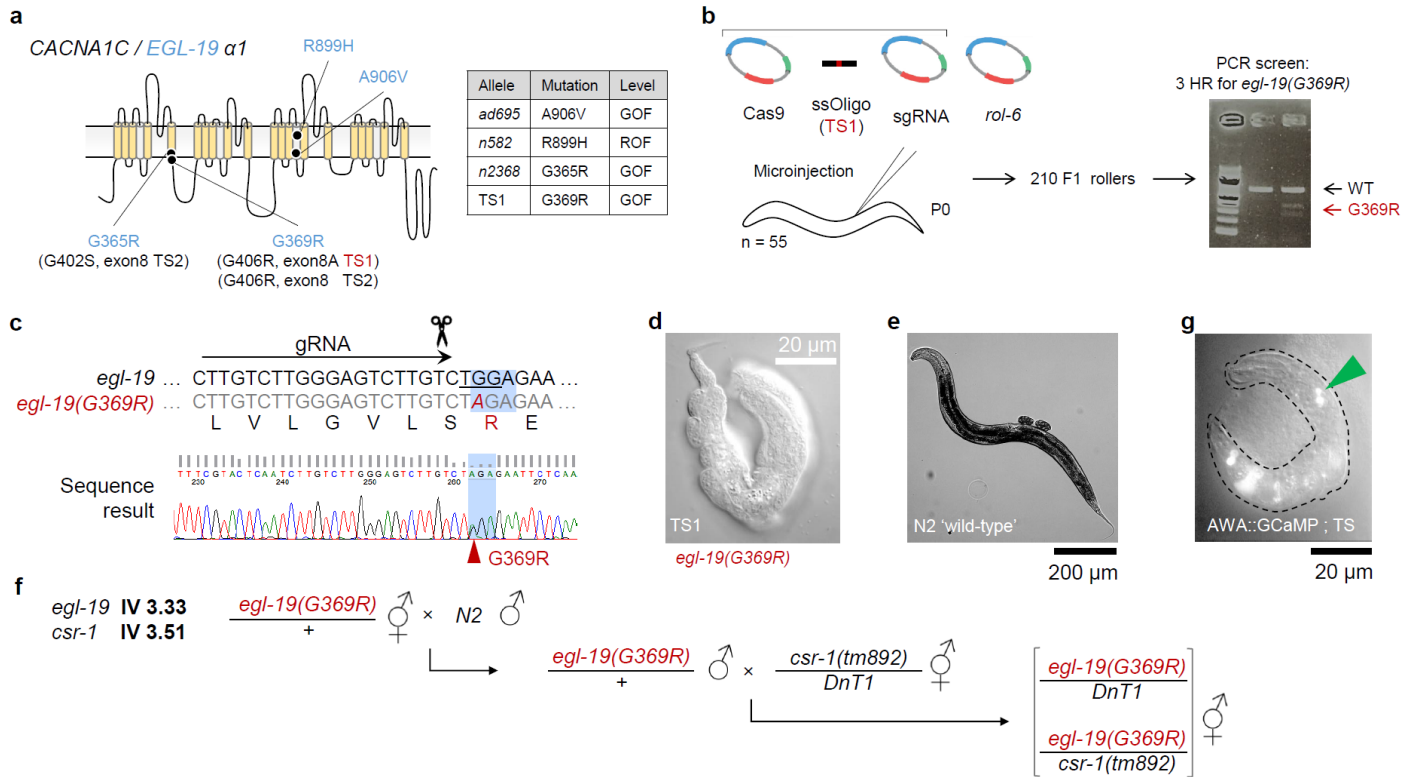
Figure 8. A Timothy syndrome mutation in the orthologus voltage-gated calcium channel in C. elegans *causes a severe developmental arrest phenotype by CRISPR-Cas9 homology directed repair.*

a. The VGCC alpha 1 subunit *CACNA1C* ortholog in *C. elegans* is *EGL-19*. Several isolated *C. elegans* mutant strains are available from an EMS screen: A906V and G365R are gain-of-function (GOF) and R899H is a reduction-of-function (ROF). G369R is expected to be GOF and the mutation site for TS1 (G406R in humans).

b. The CRISPR-Cas9 injection mix with custom designed sgRNA and ssOligo TS1 donor was injected in 55 young adult *C. elegans*, 210 F1 progeny were selected having the roller phenotype and cloned. Of the 210 F1 roller progeny, 3 were heterozygous HR positive for the TS1 insertion. PCR and XbaI confirmed the TS1 insertion in TS1/+ animals.

c. The sequence alignment results from successful CRISPR-Cas9 HR of TS1 in *C. elegans*. WT gene is above, and mutated below (red *A*). The resulting mutated protein sequence at codon position for G369R (TS1) is below and highlighted in blue. PAM sequence is underlined, and 20 nucleotide sgRNA is beneath the arrow. The raw sequence result trace shows the heterozygous double A/G peak at position 262 where the TS1 insertion was made (red arrow).

d. A fully developed homozygous TS1 animal generated by CRISPR-Cas9 HR is arrested at L1 stage. Image taken at 100X DIC.

e. A fully developed wild-type adult *C. elegans* with two eggs laid on a standard NGM plate (right).

f. The genetic location of *egl-19* is within 0.18 map units of *csr-1* on chromosome IV, for which the genetic balancer Dnt1 can be used to successfully maintain and propagate TS1 homozygotes and heterozygotes. TS1 animals are maintained as TS1/Dnt1, and can be used for subsequent crosses (as in g).

g. A fully developed homozygous TS1 animal expressing GCaMP in the AWA chemosensory neuron pair (green arrow) generated by a sequence of crosses, initiated by the balancer cross outlined below and explained in f. Fluorescent image taken at 100X DIC.

45

A model to explain genetic causes of the TS phenotype in C. elegans

The resulting homozygous TS phenotype in *C. elegans* generated by CRISPR-Cas9 HR resembles a previously reported ROF phenotype and pharmacologically blocked channel (Kwok et al., 2006; Lee et al., 1997). This inspires several possibilities for function of the *egl-19(G369R)* gene in *C. elegans*, which is expected to be a GOF mutation (as in humans and heterologous systems). In healthy worms (wild-type) and embryos, *egl-19* is transcribed, translated, and transported to the cell membrane for proper VGCC function, possibly by *calf-1* (**Fig. 9a**) (Saheki and Bargmann, 2009). In homozygous TS animals (TS/TS), the chromosome or *egl-19(G369R)* allele is either not transcribed, folded, transported, or functional at the cell membrane, leading to the severe developmental arrest (Pat) phenotype, resembling early reports of a likely *egl-19* null (**Fig. 9b**). Further, the β subunit (*ccb-1*) interacts with the G369R location, which may also affect proper channel function if *EGL-19(G369R)* is translocated properly, leading to severe calcium influx and decreased inactivation, like the human condition. The overabundance of calcium in the cell could also affect gene expression or the translocation process (Catterall, 2011). Also, *C. elegans* that are heterozygous for TS (TS/+) develop properly and look like healthy animals, suggesting that the TS mutation is autosomal recessive (requires both copies), and either not expressed or is terminated at either translocation stage (**Fig. 9c**). Other GOF mutations are semi-dominant (like *egl-19(n2368)* and *egl-19(ad695)*), while ROF heterozygotes have not been as carefully observed, but seem to also be semi-dominant (personal observation for *egl-19(n582)*). Each of these possibilities seem reasonable, and should be examined further to clarify the exact genetic function of the TS mutation in *C. elegans*. Once a cause is identified, then suppressors could be screened for to restore proper translocation, channel function, or gene expression in *C. elegans*.
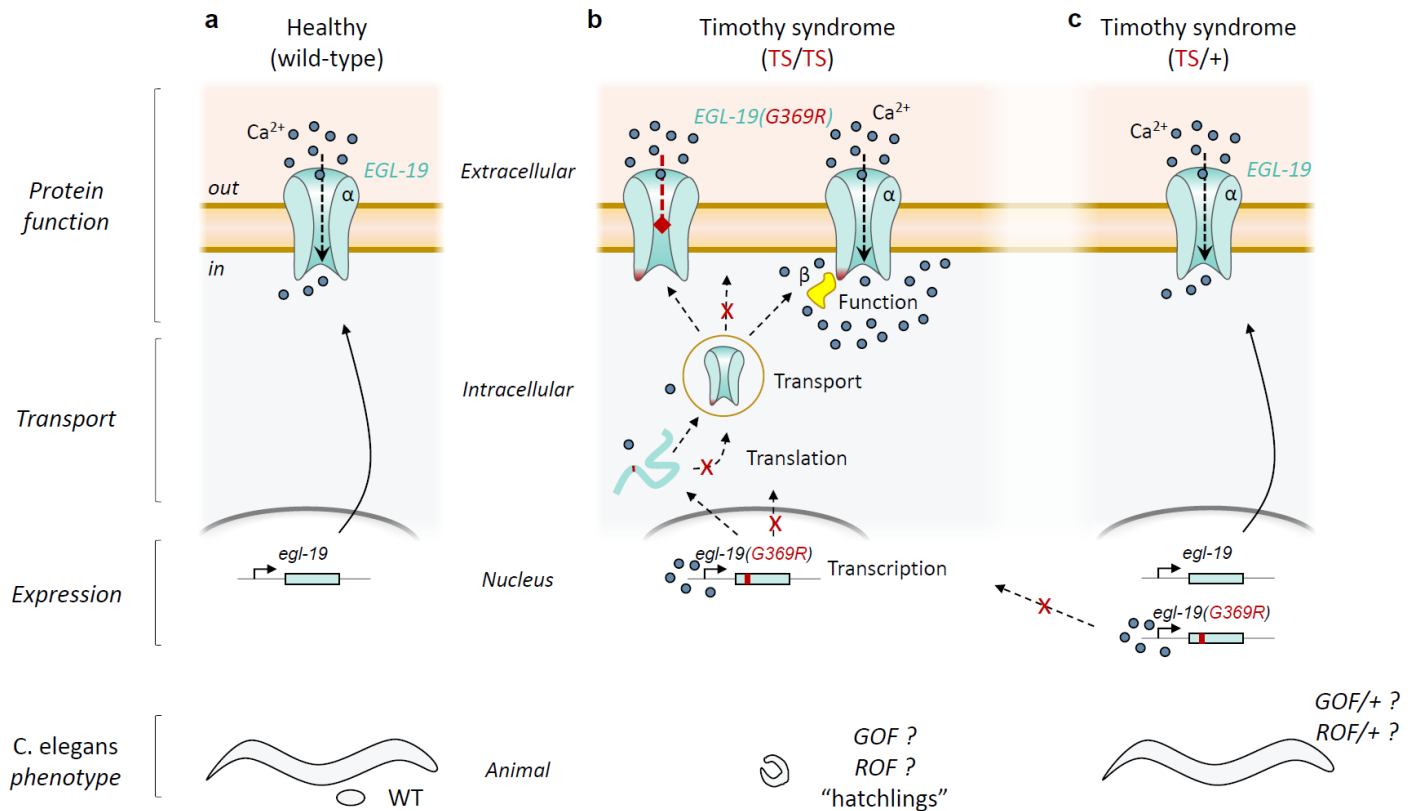
Figure 9. A model to explain potential genetic causes for the severe TS phenotype in C. elegans.

a. In healthy (wild-type) animals, *egl-19* is properly expressed and translocated to the cell membrane for function.

b. In homozygous TS/TS animals, the severe developmental arrest phenotype is likely caused by irregular expression, translation, transport, or function of *EGL-19* at the cell membrane (severe ROF, left; or GOF, right). Red X's represent possible stages at which proper *egl-19* function is terminated, although not confirmed. Interestingly, a severe homozygous ROF mutation causes a similar developmental arrest phenotype, while parents can develop into adults that are long and flaccid (Kwok et al., 2006; Lee et al., 1997). Also, blocked *EGL-19* VGCCs using nemadipine-A cause a similar arrest phenotype (Kwok et al., 2006). Therefore, evidence suggests that if *EGL-19* is not functional, then the severe ROF developmental phenotype is caused. However, since the reason for this phenotype has not been identified (as in expression and translocation by *calf-1*), then it remains to be discovered how the level-of-function is responsible for an expected GOF, ROF, or null-like (Pat) phenotype.

c. A heterozygous TS/+ animal looks healthy and develops normally. Therefore, the TS allele is likely autosomal recessive, or becomes non-functional during expression or translocation as in b.

47

EGL-19 *expression localizes to neurons and muscle in early larval development*

A similar CRISPR-Cas9 HR strategy was used to insert a green fluorescent protein (GFP) at the 3'

C-terminus end of *EGL-19* at ~1% efficiency (**Fig. 10a-b**) (Kim et al., 2014). A single homozygous

EGL-19::GFP animal was identified by PCR screening and maintained as wild-type, with no

apparent effects on development or morphology. High-magnification DIC fluorescence imaging

was used to identify the location of the *EGL-19* protein in the head of L1 animals (**Fig. 10c**).

Fluorescence was detected at the cell membrane in more than half a dozen neurons in the head,

as well as the pharynx and body wall muscle (green outlines, **Fig. 10c-d**), and was fairly consistent

among the population (**Fig. 10d**). No GFP expression was observed in N2 controls using the same

camera exposure settings and fluorescence intensity (black outline, **Fig. 10e**).
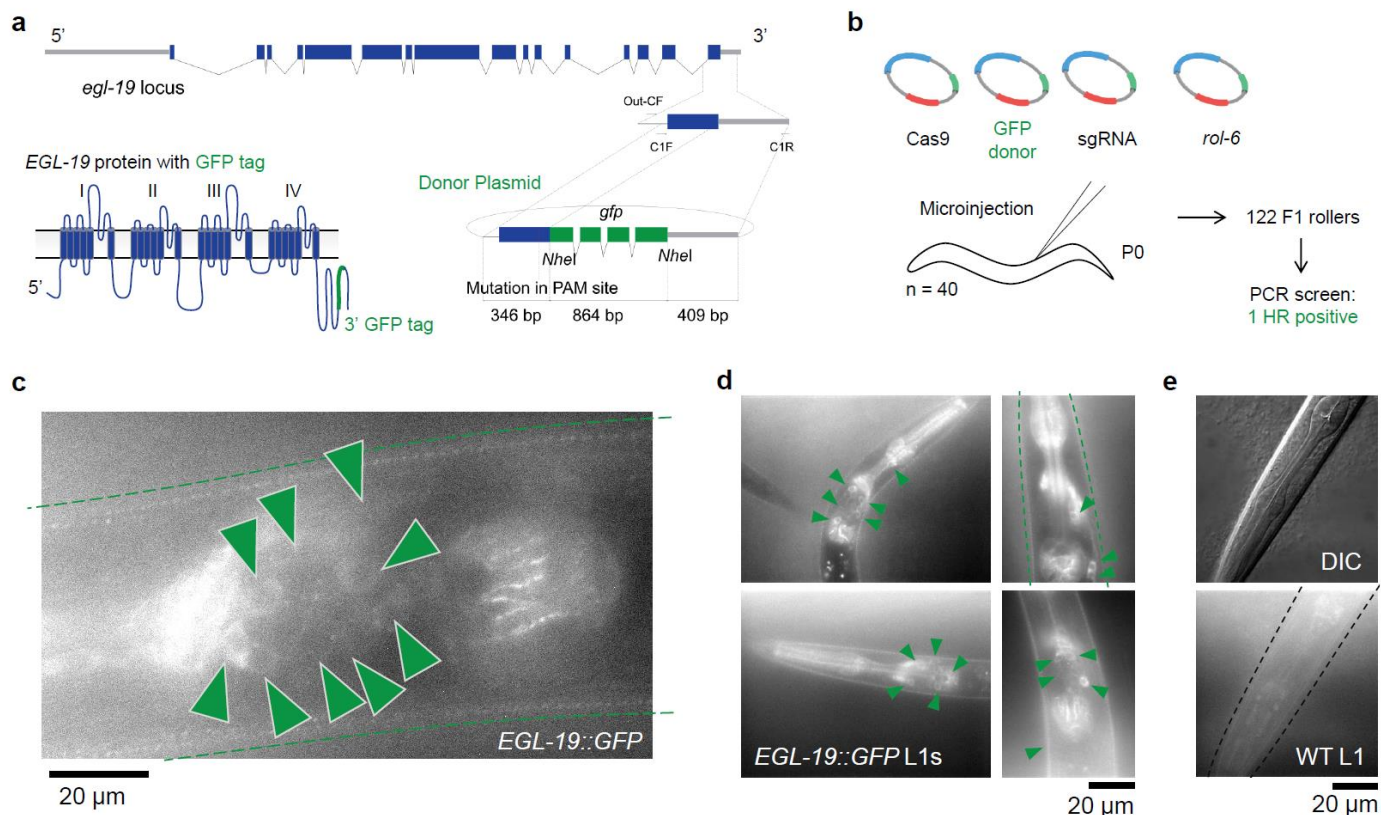
Figure 10. An EGL-19::GFP *knock-in generated by CRISPR-Cas9 HR reveals protein expression and cellular localization of* EGL-19 *during early development.*

a. A GFP tag was designed for insertion at the C-terminus of the *EGL-19* gene. The donor plasmid was constructed to contain *egl-19* homology flanking the GFP for successful genomic insertion using CRISPR-Cas9 HR.

b. An injection mix containing all constructs shown were injected into 40 young adult *C. elegans*. Of 122 F1 rollers, 1 *EGL-19::GFP* HR positive animal was identified.

c. An L1 stage *EGL-19::GFP* animal imaged using 100X DIC. The cell membrane of more than half a dozen head neurons, as well as the pharynx and body wall muscle (green arrows and dotted outline).

d. Four L1 stage *EGL-19::GFP* animals imaged using 100X DIC. Green arrows point to GFP expression in neurons, body wall muscle, or pharyngeal muscle.

e. Wild-type N2 L1 animals imaged using 100X bright field DIC (top) did not show GFP expression (below).

49

A possible strategy to identify EGL-19 *mislocalization in GOF and ROF mutants*

Now that it is possible to identify the exact endogenous location of *EGL-19* by tagged GFP, these animals can be used to observe the location of *EGL-19* in GOF and ROF animals, which is hypothesized to either be mislocalized, over- or under-expressed in these genotypes leading to all reported phenotypes. Healthy, wild-type animals show proper expression and translocation of *EGL-19* to cell membranes and various cell types by GFP signal, but should be further characterized in the embryo and other developmental stages (L2-L4s and adults) as well as throughout the body (tail, head, dorsal and ventral) (**Fig. 11a**). If the TS mutation is knocked into the *EGL-19::GFP* animals, it is expected that GFP signal will be mislocalized to the cytoplasm of neurons and muscle with variable levels of expression at the cell membrane and less overall brightness (**Fig. 11b**). If the TS/TS animals resemble a null, then expression of EGL-19 might only be observed at the embryonic stage (1-1/2 fold embryo nuclei) as previously reported in wild-type animals or not at all (Lee et al., 1997). Others have reported that the α2/δ subunit is mislocalized in GOF young-adult animals (*egl-19(ad695) and egl-19(n2368)*); therefore, inducing these mutations in the *EGL-19::GFP* reporter strain using CRISPR-Cas9 HR could confirm this result with higher specificity to *EGL-19* location independent of subunit mislocalization. Further, co-expression of *unc-2* and *cca-1* using mCherry or another independently excitable wavelength (either by CRISPR-Cas9 HR or transgenes) in *EGL-19::GFP* animals would be useful in identifying the distribution of VGCCs throughout the body of *C. elegans* at various developmental stages and different levels-of-function, which has not yet been thoroughly characterized.
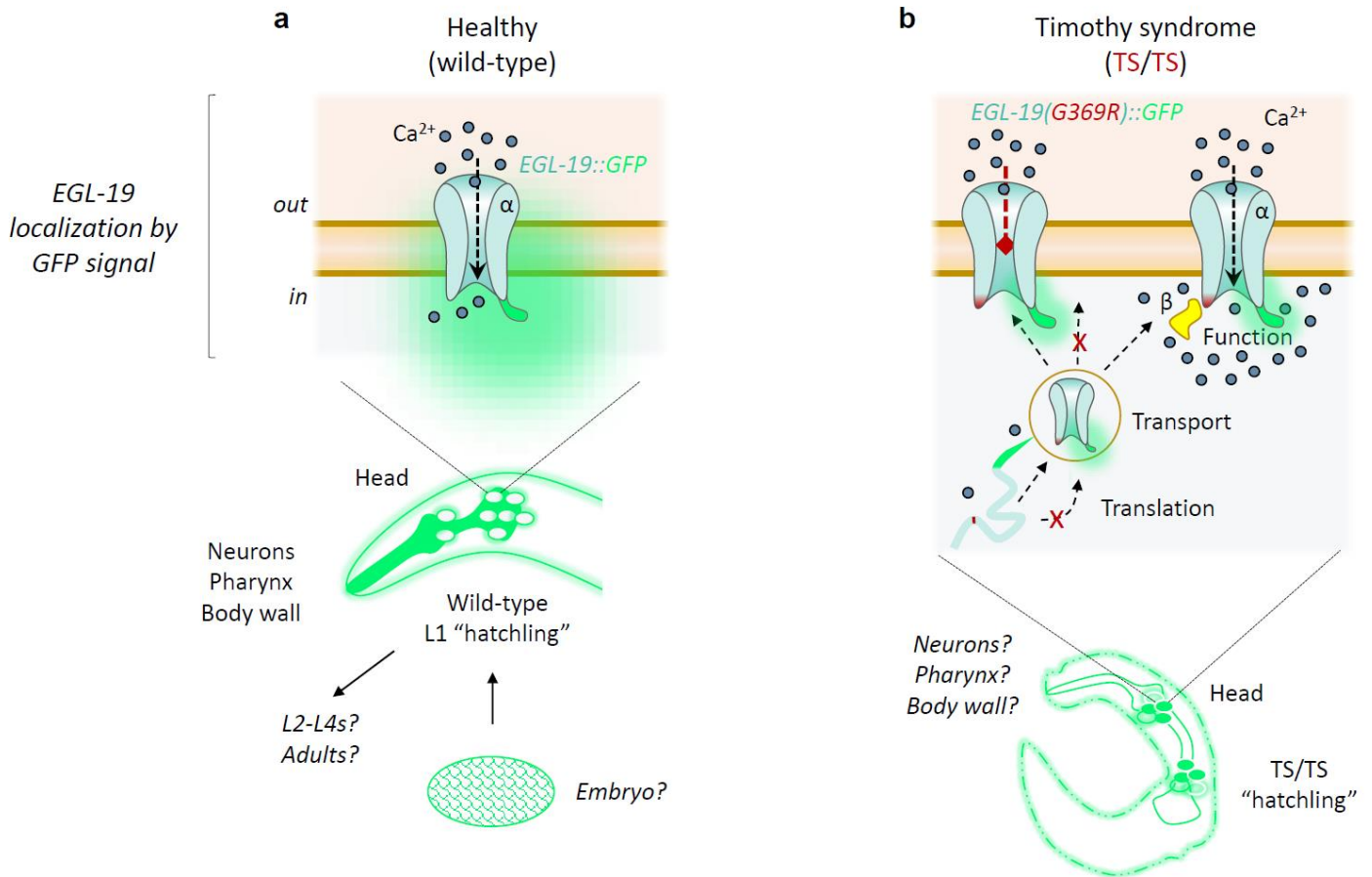
Figure 11. A model for identifying the location of EGL-19 in various level-of-function genetic backgrounds in C. elegans.

a. Wild-type *C. elegans* with an *EGL-19::GFP* tag show expression in some head neurons and muscle cell types, particularly the pharynx and body wall muscle. This GFP signal is directly linked to *EGL-19* localization since it was knocked-in using CRISPR-Cas9 HR at the endogenous genomic locus. Other developmental stages (as well as throughout the body) should be observed for GFP expression, like in embryos or L2-L4s and adult animals.
b. In homozygous TS/TS animals, it is expected EGL-19 is either under- or over-expressed and likely mislocalized to the cytoplasm or nuclei of various cell types due to the severely arrested developmental phenotype.

High-throughput plate-based recording reveals differences in C. elegans channelopathy model behavior and morphology

A high-throughput plate-based quantification method was used to investigate whether various level-of-function mutations in *egl-19* affect behavior and morphology in *C. elegans* (Swierczek et al., 2011). Videos of adult animals freely-behaving on standard NGM plates were recorded for ten minutes for all genotypes, and post-processed to automatically quantify midline length (animal outline), forward speed (blue-purple track), and reversal duration across all genotypes (**Fig. 12a**). Detailed representations of body morphology and plate dispersal area for each genotype are produced by the tracking software, which show noticeable qualitative differences in size and total plate area tracked after ten minutes of recording behavior on the plate (**Fig. 12b-f**). As expected, the midline-length of two severe gain-of-function mutations *egl-19(ad695)* and *egl-19(n2368)* were significantly shorter than wild-type, while the reduction-of-function *egl-19(n582)* animals had significantly longer midline lengths (**Fig. 12g**). Further, an endogenously expressed *egl-19cDNA* transgene rescued midline-length to wild-type levels when expressed in *egl-19(n582)* animals (**Fig. 12g**). Also, baseline speed during ten minutes of locomotion was significantly reduced in the most severe GOF mutation, while a reduction in baseline speed was apparent in the *ROF* animals, and slightly rescued in the transgenic animals, but to significance (**Fig. 12h**). Lastly, a brief mechanical tap was delivered to the plate after ten minutes of baseline recording to induce a synchronized reversal response. The duration of the reversal response was significantly faster for both GOF mutants and longer in the ROF mutant, while the transgenic animals were rescued to wild-type response levels (**Fig. 12i**). Reversal speed was not different among all genotypes (data not shown).
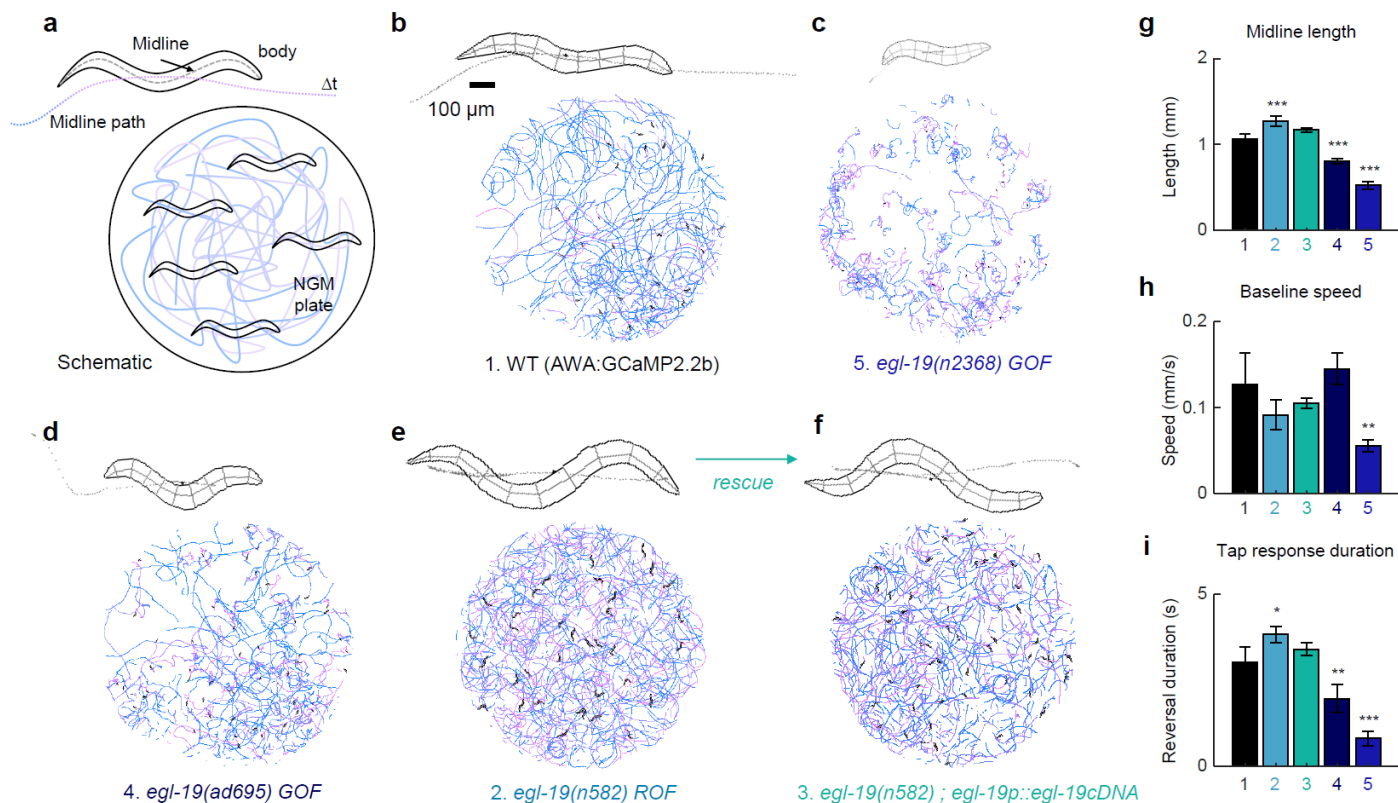
Figure 12. Morphological and behavioral phenotypes in C. elegans *models of calcium channelopathies by plate-based high-throughput recording.*

a. A schematic of the worm body outline, midline, and midline path. Below is a schematic of the plate containing animals with the midline path from blue to pink corresponding to time elapsed. Traces represent individual animal tracks for ten minutes of video recording.

b. Actual representation of the body outline for a wild-type (WT) animal with midline, midline path, and segmentation produced using the plate-based recording tracker software. Below are animal dispersal tracks during ten minutes of video recording. This format is consistent for the following panels, c–f. Scale bar for b-f, 100 µm.

c. The gain-of-function *egl-19(n2368)* mutant strain resulting in a severely short body morphology and corresponding animal tracks with less total dispersal area compared to WT.

d. The gain-of-function *egl-19(ad695)* mutant strain with short body morphology, animal tracks, and less total dispersal area compared to WT.

e. The reduction-of-function *egl-19(n582)* mutant strain with longer body morphology and more total dispersal area compared to WT.

f. An *egl-19(n582)*; *egl-19p::egl-19cDNA-mChr* rescue strain with slightly restored body morphology and restored total dispersal area compared to WT.

g. Bar graph representation of the mean for each genotype midline length (mm). Bar colors and number labels correspond to genotypes from panels b–f. Error bars represents SD of four plate averages for g-i Symbols represent significance (*** $p < 0.001$, ** $p < 0.01$, * $p < 0.05$) after a one-way ANOVA with Bonferroni's correction, as compared to wild-type (1).

h. Bar graph representation of the average baseline speed (mm/s) for each genotype and comparison across all genotypes, colors and statistics as in g.

i. Bar graph representation of the average reversal duration after a single mechanical tap (s), quantified for and compared across all genotypes, colors and statistics as in g and h.

53

High-throughput calcium imaging reveals functional differences in channelopathy models

To probe for differences in intracellular calcium activity in neurons of these channelopathy models, animals harboring genome-wide *GOF* and *ROF* mutations in *egl-19* were crossed into integrated animals expressing the genetically encoded calcium sensor in the chemosensory AWA neuron (AWA::GCaMP2.2b). Since homozygous TS1 animals were not directly compatible with conventional calcium imaging methodologies, a transgenic construct harboring the TS1 mutation in *egl-19cDNA* for cell-specific expression in the AWA chemosensory neuron was developed by site-directed mutagenesis (SDM) and standard microinjection techniques (**Fig. 13a-b**). The construct was then directly microinjected into AWA::GCaMP animals, and array positives were selected and confirmed to express both GCaMP and the TS1 construct in AWA, by visualization of the mCherry translational marker, when immobilized in a microfluidic device and compared to wild-type (**Fig. 13c-f**). These animals did not exhibit any obvious behavioral or morphological phenotypes compared to wild-type. This line was also crossed into the *egl-19(n582)* ROF mutant to determine whether cell-specific GOF TS1 rescue is sufficient to restore proper calcium signaling in subsequent assays, assuming the GOF *egl-19(G369R)* transgene is expressed and functional. These animals looked similar to the ROF *egl-19(n582)* phenotype (data not shown).
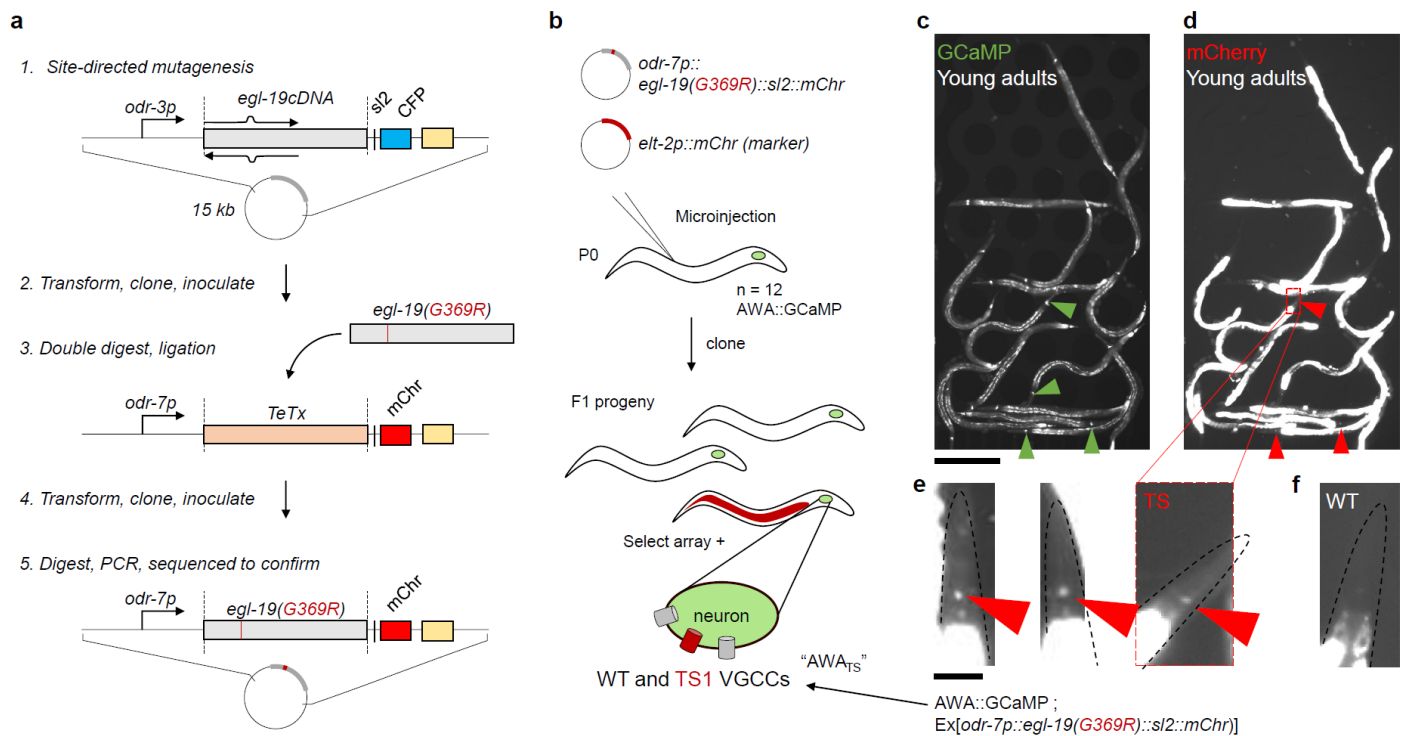
Figure 13. Generation of a transgenic TS single sensory neuron C. elegans *model by site-directed mutagenesis.*

a. Schematic outline of the procedure used for developing the *egl-19(G369R)* TS1 construct. Site-directed mutagenesis was performed by a single 15 kb PCR cycle using a primer pair that contained a single point mutation (notched arrows). In later steps, the TS1 mutation insert was ligated into a plasmid containing an AWA specific promoter and mCherry translational marker.

b. The *egl-19(G369R)* TS1 construct and red intestine co-injection marker was mixed and injected into the gonads of 12 young adult *C. elegans* expressing GCaMP in the AWA neuron (integrated). F1 progeny containing the mCherry co-injection maker were selected and maintained.

c. Wide-field fluorescent imaging of ~15 young adult TS1 animals from b paralyzed in a microfluidic device with blue-light excitation (green emission) showing GCaMP expression in the AWA chemosensory neuron (green arrows). Scale bar, 400 μm.

d. The same filed-of-view as shown in c with green-light excitation (red emission), showing mCherry expression in the AWA chemosensory neuron (red arrows). Scale bar, 400 μm from c.

e. Magnified view of three animals from d, showing positive mCherry expression in the cell body of AWA. Scale bar for e-f, 50 μm.

f. An array negative AWA::GCaMP animal showing no mCherry expression in AWA prepared similarly as described in c.

A slightly modified high-throughput microfluidic device was used to precisely deliver a 100 s pulse of 1.15 µM diacetyl odor to two different *egl-19* genotypes expressing GCaMP in AWA in a single experiment (Lagoy and Albrecht, 2018; Larsch et al., 2013). This odor-neuron pair was chosen since the g-protein coupled receptor (GPCR) *odr-10* is expressed in AWA that detects the odorant diacetyl for chemosensation (Sengupta et al., 1996). All individual response traces across all genotypes are shown by the heat map, with average response traces for each represented below (blue traces, **Fig. 14a-b**). Animals with peak response times longer than 10 s after the pulse start were observed (red traces, **Fig. 14b**). Subsequent plots and calculations were performed on filtered traces with a peak time less than 10 s after the pulse start (black traces, **Fig. 14b-l**). Several calcium response traces were overlaid and resized to emphasize the qualitative differences in calcium response kinetics (**Fig. 14c**), like area under the curve (**Fig. 14d**), and second-degree polynomial fitted decay (**Fig. 14e**).

Average peak $\Delta F/F_0$ calcium responses were compared to wild-type (WT) across all genotypes (**Fig. 14f**). A significant reduction in peak response was detected in the ROF genotype, as well as the AWA-specific TS1 rescue in the same ROF background and the endogenously expressed wild-type *egl-19* rescue (**Fig. 14f**). Co-expression of an *unc-2(zf35)* GOF transgene in the AWA::GCaMP chemosensory neuron seemed to significantly reduce the peak response. The time it takes for each genotype to reach its maximum peak response (or time-to-peak) was calculated, with only the same or faster response times observed as compared to wild-type (**Fig. 14g**). The most prominent difference was observed between wild-type and the most severe GOF *egl-19(n2368)* mutant population, as well as the mixed balancer strain population(s), which served as a control

for the TS1 mixed population animals (**Fig. 14g**). Additionally, the area under the curve showed no significant differences across all genotypes after multiple comparisons (**Fig. 14h**); however, only the first four genotypes were of particular interest to compare because these resembled the most direct models of human channelopathies as genome-wide mutations. When comparing only these mutants together, a significant increase in area under the curve was observed for the less-severe GOF mutant, as also observed qualitatively (**Fig. 14d, i**). Likewise, average peak $\Delta F/F_0$ calcium responses were of specific interest between WT, the ROF, and ROF rescue genotype populations. When these genotypes were compared selectively, there was a significant increase in average peak $\Delta F/F_0$ calcium response, but still significantly reduced when compared to wild-type animals (**Fig. 14j**). No significant differences were detected across all genotypes for the time it takes to reach half the maximum peak ($t_{1/2}$, or referred to as desensitization) (**Fig. 14k**). However, the initial rate of decay (λ) was significantly faster for the more-severe GOF mutant (**Fig. 14l**). Finally, balanced heterozygous TS1/Dnt1 animals mixed with Dnt1 homozygotes showed no differences in kinetics when compared to a Dnt1/+ and homozygous mixed population, with only slight noticeable differences in time-to-peak response, but not as prominent as the other *egl-19* GOF mutations (**Fig. 14g**, **h**).
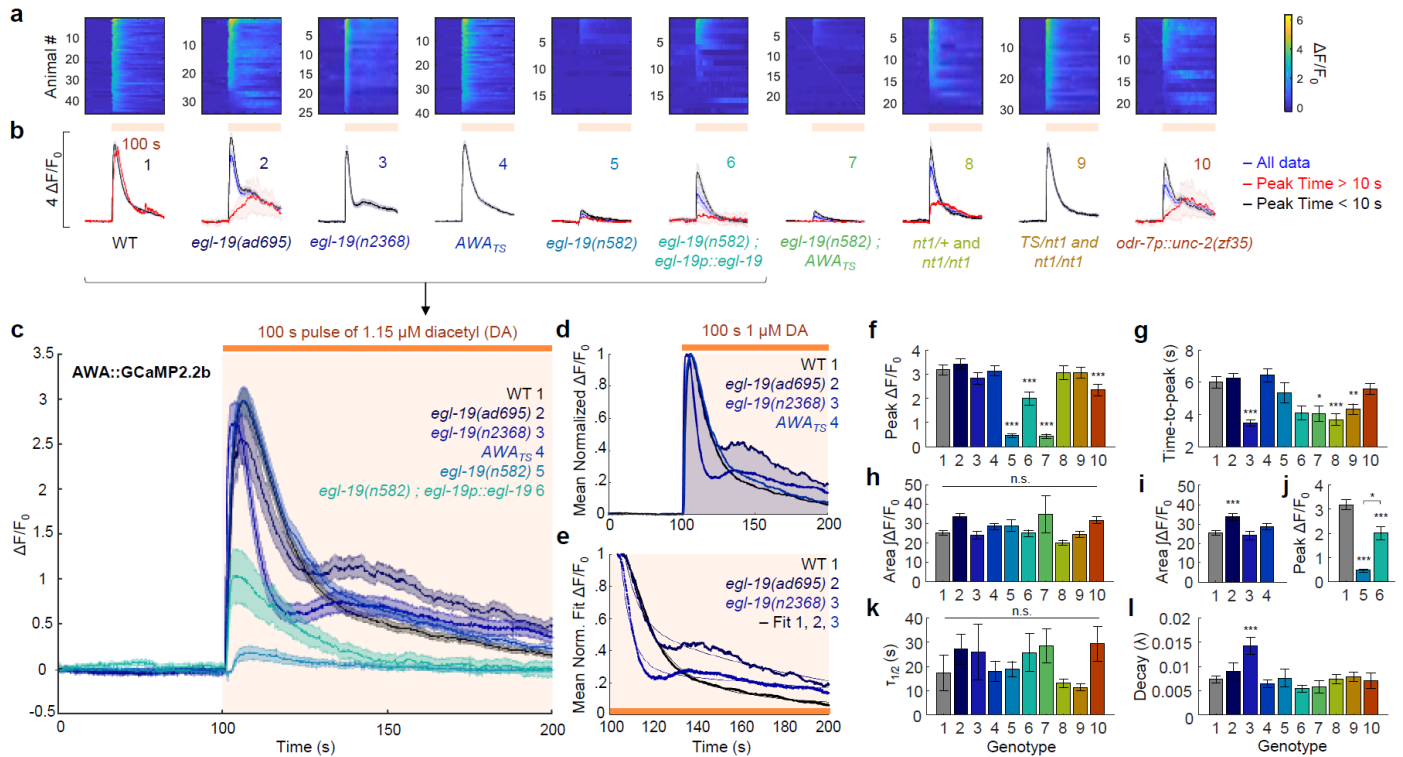
Figure 14. Odor-evoked calcium activity in C. elegans *models of VGCC channelopathies have altered calcium kinetics.*

a. Heat maps represent all individual calcium traces across ten independent genotypes, corresponding to labels in b, with a 100 s pulse exposure to 1.15 µM diacetyl (orange bar, below). Sample sizes (individual animals) are shown along the y-axis.

b. Average $\Delta F/F_0$ calcium response traces for all genotypes and data traces (blue), corresponding to individual heat maps in a. Animals that took longer than 10 s to reach their maximum peak response are averaged and shown in red. Filtered traces that do not include red traces are shown in black, which are used for all subsequent quantifications. Corresponding trace shading represents SEM.

c. Mean $\Delta F/F_0$ calcium response traces overlaid for the first six genotypes corresponding to b show altered calcium response kinetics. Orange fill represents the presence of 100 s of 1.15 µM diacetyl pulse. Corresponding trace shading represents SEM.

d. Average normalized $\Delta F/F_0$ calcium response traces for the first four genotypes from b and c. Orange fill represents presence of odor stimulus. Shading under the curve (#2) represents area calculated for one genotype *egl-19(ad695)* from these plots.

e. Mean normalized $\Delta F/F_0$ calcium response traces from d with a second degree polynomial decay fit (thin lines) for each of the first three genotypes. Orange fill represents presence of odor stimulus.

f. Mean peak $\Delta F/F_0$ calcium responses for all ten genotypes, corresponding to label color and left-to-right order in b. Error bars represent SEM, for f-l. Symbols represent significance (*** $p < 0.001$, ** $p < 0.01$, * $p < 0.05$) after a one-way ANOVA with Bonferroni's correction.

g. Time-to-peak quantification of individual $\Delta F/F_0$ calcium responses across all ten genotypes.

h. Area under the normalized $\Delta F/F_0$ calcium response curves across all ten genotypes. No significance (n.s.).

i. Bar plot from h for only the first four genotypes.

j. Bar plot from f for only WT, ROF, and ROF rescue genotypes. Error bars represent SEM.

k. Desensitization ($t_{1/2}$) for all genotypes from mean normalized $\Delta F/F_0$ calcium response traces.

l. The decay rate (λ) for all genotypes from mean normalized $\Delta F/F_0$ calcium response traces.

58

Methods & Materials

C. elegans *maintenance*

Animals were grown at 20°C on OP50 *E. coli* bacteria seeded on standard NGM plates following standard protocols (Brenner, 1974). For all microfluidic experiments, animals were selected as L4s the day prior and tested as young adults the next day (Larsch et al., 2013). For all behavior experiments, animals were tested as adults (Swierczek et al., 2011). For specific strain information, see *Supplemental Information—Strains*.

CRISPR-Cas9 homologous-recombination and PCR screen of TS1 point mutation insertion in C. elegans

Plasmid-based CRISPR-Cas9 homologous-recombination was successfully completed by following previous protocols (Kim et al., 2014). First, a protospacer adjacent motif (PAM) site was selected closest to the desired mutation site. Custom designed forward and reverse short guide oligomers were ordered (IDT), prepped (5 μL of 100 μM each, 10 μL water), annealed (95°C for 2 min, 85°C for 10 s, 75°C for 10 s, 65°C for 30 s, 55°C for 30 s, 45°C for 30 s, 35°C for 10 s, 35°C for 10 s, 25°C for 10 s, 4°C ∞), diluted 1:100, and ligated 2:1 using NEB Quick Ligase into a cut sgRNA plasmid backbone (pRB1017, cut with BsaI-HF for 2 hr at 37°C and gel purified) (Arribere et al., 2014). The ligated product was transformed to DH5α on LB AMP plates, mini/midi-prepped (Qiagen, no. 12143), purified, and confirmed by sequencing using the M13 primer. An 80-nucleotide single stranded oligomer was custom designed and ordered (IDT) to contain the G369R missense mutation, which also co-acted as a silent PAM-site mutation and introduced the XbaI restriction enzyme site to detect the insertion for more efficient PCR screening (**Fig. 8b-c**).

59

The final plasmid injection mix contained 50 ng/µL each of Cas9 vector, *pRF4::rol-6(su1006)*, sgRNA vector, and ssOligo donor (**Fig. 8b**). A total of 55 wild-type animals were injected, and 210 animals were cloned and PCR screened (2 animals/50 µL reaction) using the *EGL-19_TS_fwd* and *EGL-19_TS_rev* primer pair, followed by a restriction enzyme digestion (20 µL reaction, 3 µL each PCR product, 2 µL 10X CutSmart, 0.3 µL XbaI, 14.7 µL H$_2$O) This screen yielded three independent lines with successful HR heterozygous events detected by three PCR fragments on a 1% Agarose gel (**Fig. 8b**). The G369R allele was maintained by the Dnt1 genetic balancer strain (LGIV), since homozygous TS1 animals were arrested at an early developmental stage and unable to produce offspring (**Fig. 8d**).

CRISPR-Cas9 homologous-recombination and PCR screen for the EGL-19::GFP *tag*

To introduce the GFP coding sequence in the 3' end of the endogenous *egl-19* locus, we used a plasmid-based CRISPR-Cas9 mediated HR injection mix (Kim et al., 2014). First, we selected a PAM site near the stop codon of the endogenous *egl-19* locus (**Fig. 10a**). Following the sgRNA protocol described above, new custom designed forward and reverse oligomers were ordered (IDT), annealed, diluted, and ligated into a cut sgRNA plasmid backbone (pRB1017) following previous methods (Arribere et al., 2014). To build the GFP donor, *egl-19* genomic sequence (LGIV: 7,417,562-7,418,315) was amplified from N2 genomic DNA with *C1F* and *C1R* and inserted into the pCR^{tm}-Blunt II-TOPO$^{®}$ vector (Invitrogen, K2800-20) (**Fig. 10a**). A NheI site was introduced by PCR sewing immediately before the stop codon in this fragment of *egl-19*. A silent mutation was introduced to disrupt the PAM site in the HR donor also by PCR sewing. The final PCR product was cloned into the pCR^{tm}-Blunt II-TOPO$^{®}$ vector. Finally, the GFP fragment from pPD95.75 (Addgene) was inserted to the NheI site (**Fig. 10a**).

60

The final plasmid injection mix contained 50 ng/μL each of Cas9 vector, *pRF4::rol-6(su1006)*, sgRNA vector, and GFP donor (**Fig. 10b**). For the Cas9 expression vector, the *Peft-3::Cas9-SV40_NLS::tbb-2* 3'UTR was excised from the pUC57 plasmid backbone (Friedland et al., 2013) and inserted into the pCR^tm-Blunt II-TOPO® vector (Invitrogen, K2800-20) digested with EcoRI and HindIII since shared homology regions between co-injected plasmids increased HR efficiency (data not shown). A total of 40 N2 animals were injected, and 122 F1 rollers were cloned and PCR screened using primers that flanked the homology arm (*out-CF*) and inside (*C1R*) (**Fig. 10b**). From this screen, one HR event was identified and the homozygous *EGL-19::GFP* animals were healthily maintained (**Fig. 10b-d**).

High-magnification DIC bright field and fluorescence imaging

Wild-type (N2), homozygous TS1, homozygous TS1; AWA::GCaMP, and homozygous EGL-19::GFP animals at the L1 developmental stage were carefully transferred to 1% Agarose pads. A small drop (1 μL) of 25 mM sodium azide in H_2O was added on top of animals for immobilization during imaging and cover-slipped. An inverted differential interference contrast (DIC) microscope with fluorescence was used to image at 100X using an oil immersion lens. Due to low GFP expression levels for *EGL-19::GFP* animals, a 4 s camera exposure time was used to capture localized GFP signal. The fluorescence source was only present while images were captured to prevent photobleaching and phototoxicity.

PCR and sequencing of egl-19 genetic crosses into AWA::GCaMP

Genomic lysis samples were prepared using single animals or starved plates (1 μL of animal pellet) in 10 μL lysis buffer as previously described (Ahringer, 2006). For plate lysis, only 1 μL of DNA solution was used, 2.5 μL for single worm lysis with adjusted water volumes per 50 μL reaction. PCR followed the hot start protocol (Genesee Scientific Apex^{tm} blue, #42-145) for amplification (95°C for 5 min; 95°C for 30 s, T_m°C for 2 min or 2:30 min, 75°C for 30 s, repeated 35x; then 75°C for 5 min, 4°C ∞). Next, a 1% agarose gel (1X TAE) electrophoresis (1 hr) was used to visualize 25–50 μL PCR bands, then cut, purified, and point mutations in DNA confirmed by sequencing (GENEWIZ). All primers and annealing temperatures (T_m) are listed under *Supplemental Information—Primers*.

High-throughput plate-based recording of mutant animal behavior

All data collection, mechanosensory stimulation, and representation storage were performed using the Multi-Worm Tracker platform (Swierczek et al., 2011) (**Fig. 12**). For each genotype, about four plates containing ~60–80 age synchronized adult animals were recorded on the same day (~150–200 behaving animals per genotype). First, ten minutes of baseline behavior was recorded to measure and quantify the average body length and forward speed for each genotype (**Fig. 12b-h**). A push solenoid was used to deliver a mechanical tap to the plate after the ten minutes of baseline recording to measure and quantify the average reversal duration for each genotype (**Fig. 12i**).

Site-directed mutagenesis for generation of a transgenic TS C. elegans model

A modified QuikChange site-directed mutagenesis (SDM) protocol was developed to insert a point-mutation (G369R) in a plasmid containing wild-type *egl-19cDNA* (**Fig. 13**). A ~15 kb *odr-3p::egl-19cDNA::sl2::CFP* construct was used for SDM. A 50 µL reaction containing template DNA (1 µL of 50 ng/µL), 10X buffer (5 µL), forward and reverse primers (1.25 µL of 100 ng/µL each), dNTPs (1 µL), diH$_2$O (to 48 µL), 100% DMSO (1 µL), and Pfu polymerase (1 µL) was prepared, with the following cycle parameters (95°C for 30 s; 95°C for 30 s, 55°C for 1 min, 68°C for 1min/kb, cycled 20-40X; 68°C for 10 min, 4°C ∞). Primers were designed using a free online QuikChange Primer Design platform (Agilent). The next day, DpnI (1 µL) was added to the reaction at 37°C for 2 hrs, then centrifuged for 15 s. Next, 5 µL of this reaction was used for transformation to XL-10 super competent cells (from the Dempski Lab, WPI) and plated on standard LB plates. For all inoculation steps, *egl-19* plasmids were grown at 25°C for two days due to slow transformation rates. Colonies were selected, inoculated (25°C overnight), mini prepped, and sequenced using *EGL-19_TS_fwd* to confirm the mutated insertion. Using the successfully generated TS1 construct from SDM, two double digests and ligation reactions were performed to insert *egl-19(G369R)* into a construct containing the AWA specific promoter *odr-7* and *mCherry* translational marker (from *odr-7p::TeTx::sl2::mChr*). A 20 µL NEB CutSmart NheI/FseI reaction protocol was used for both constructs, then gel purified to ligate at a ratio of 3:1 following the NEB T4 ligase protocol at 16°C overnight. Next, 7 µL of the above reaction was used to transform then plated on AMP resistant LB plates grown at 25°C for 2 days. Various sized colonies were selected, inoculated, mini prepped, and digested to confirm insert size, then sequenced to confirm proper promoter and insertion sequences.

About 12 young-adult AWA::GCaMP animals were injected with 50 ng/µL *odr7p::egl-19(G369R)::sl2::mChr* and 10 ng/µL *elt-2p::mChr* co-expression intestine marker for array positive selection (**Fig. 13b**). Independent array positive animals were selected and maintained. Co-expression and co-localization of *mCherry* was confirmed in animals tested after calcium imaging (**Fig. 13c-e**).

Microfluidic solution preparation

Diacetyl (2,3-butanedione, Sigma) odor dilutions were prepared on the day of the experiment beginning with a 30 mL 1:1000 (10^{-3}, 11.5 mM) dilution vortexed for 1 min in paralysis buffer (S. Basal buffer without cholesterol containing 1 mM acetylcholine agonist (—)-tetramisole hydrochloride), and serially diluted to 1.15 µM (10^{-7}, 1.15 µM). Stock 1 mg/mL fluorescein was prepared in paralysis buffer and made to a final concentration of 200 ng/µL in the control flow, with 100 ng/µL in the odor to visualize the stimulus pulse. While dilutions were prepared, up to ~20 animals of each genotype were loaded into separate arenas, and exposed to paralysis buffer flow for 1 hour prior to odor delivery to keep animals stationary during recording. Acquisition of at least 200 s (10 fps, 100 ms exposure, 10 ms blue light pulse, 10 ms delay, 2x2 binning) began with a precise 100 s odor pulse delivered from 100 s to 200 s.

Microfluidic calcium imaging and data analysis

Methods followed those described previously (Lagoy and Albrecht, 2015, 2018; Larsch et al., 2013). A modified high-throughput microfluidic imaging device optimized for 4X magnification with two physically separated arenas was used for imaging experiments (Lagoy and Albrecht, 2018). Optical configurations were customized using an ASI RAMM frame and commercially

available components for low-magnification wide-field GCaMP excitation (4X/0.28 NA), with high-resolution (1024x1024), 10 fps image acquisition by a sCMOS Hammamatsu Orca Flash 4 (Lagoy and Albrecht, 2018). Custom scripts were used for quantifying neuron (soma) fluorescence (NeuroTracker ImageJ macro) as previously described (Lagoy and Albrecht, 2018; Larsch et al., 2013), and MATLAB17a was used for data analysis and visualization. Change in fluorescence (ΔF/F$_0$) was calculated as $(F - F_0)/F_0$ where F$_0$ is mean fluorescence of each frame during the first 100 s before stimulation, then each genotype trace was averaged across individuals with several independent repeated trials (**Fig. 14a-b**). Peak ΔF/F$_0$ was calculated by finding the mean maximum from the pulse start until 10 seconds later, and time-to-peak was calculated for every animal (**Fig. 14f-g, j**). All baselines and peaks were normalized from zero to one, respectively, and the area under the pulse duration curve was calculated (**Fig. 14d, h, i**). Using individual normalized traces, rate of inactivation (λ) and average desensitization (t$_{1/2}$) was also quantified for each genotype using a second degree polynomial decay curve fit ($y = ae^{(b \times x)} + ce^{(d \times x)}$), where λ = |b|, and $t_{1/2} = |\ln(2)/\lambda|$ to the normalized fluorescence traces (**Fig. 14k-l**).

Statistical comparisons

MATLAB2017a was used for all statistical comparisons shown (**Fig. 12g-i, Fig. 14f-l**). A one-way analysis of variance (ANOVA1) was used to compare differences across genotypes with Bonferroni's correction method for multiple comparisons (* $p < 0.05$, ** $p < 0.01$, *** $p < 0.001$). Sample sizes correspond to individual animals (as shown in **Fig. 14a**), since they are treated as independent measurements (Larsch et al., 2013). Nonparametric comparisons of data in **Fig.14f-**

l using Kruskal-Wallis with Bonferroni's correction yielded similar statistical conclusions, and may be more appropriate moving forward as not all quantifications were normally distributed.

Discussion

In this Chapter, we established a pipeline for generating human channelopathy mutations in *C. elegans* to assess quantifiable differences in three levels of conserved organismal physiology: morphology, behavior, and calcium activity. Human mutations have been previously modeled in *C. elegans* through heterologous or transgenic approaches (Faber et al., 1999; McCormick et al., 2013), while advances in genome engineering using CRISPR-Cas9 have broadened the approach and ability to study the effects of genome-wide modifications (Arribere et al., 2014; Dickinson et al., 2013; Friedland et al., 2013; Kim et al., 2014). For our first approach, we decided to follow-up on previous well-established channelopathy disease modeling work by generating the first genome-wide *C. elegans* model of Timothy Syndrome type 1 using CRISPR-Cas9 homology directed repair. Consistent with the human and mouse model TS symptoms, this human GOF mutation causes a severe developmental arrest phenotype in *C. elegans*, where animals were not able to develop past the L1 stage (Bader et al., 2011; Splawski et al., 2005). Surprisingly, this phenotype is similar to severe hypomorphic reduction-of-function morphology shown by the *egl-19(ad995)* allele, or by specifically antagonizing *EGL-19* channel function pharmacologically with nemadipine-A (Kwok et al., 2006; Lee et al., 1997). Therefore, the *egl-19(G369R)* TS mutation is recapitulating a severe non-functional ROF Pat phenotype (null-like) (Williams and Waterston, 1994), or the channel is indeed being expressed and the expected GOF prolonged opening is causing the severe arrest stage (**Fig. 9**).

It is also important to consider that generating mutations in essential genes requires careful observation and appropriate follow-up strategies to maintain successful genomic modifications, like using balancer strains. Interestingly, in this study a genetic balancer enabled successful propagation and continued maintenance of our otherwise lethal TS1 *C. elegans* model. This is the proper expectation and use of genetic balancer strains in *C. elegans*, yet intriguing that a mixed chromosome pair can successfully rescue the TS1 phenotype. Likewise, heterozygous TS1/+ *C. elegans* developed normally, and were morphologically similar to wild-type. This is also striking, as all reported human cases of TS are believed to be heterozygous and have mosaic expression patterns (NIH Timothy syndrome, 2018; Splawski et al., 2005), which still cause severe developmental phenotypes, while we observe the exact opposite in our heterozygous *C. elegans* animal model (**Fig. 9**). Therefore, the TS1 allele in *C. elegans* must be autosomal recessive, while it is autosomal dominant in humans and mice. Further, this example highlights that phenotypes discovered from generating human mutations in *C. elegans* may be unexpected, and thus not directly compatible with conventional analysis or intended methods, like calcium imaging. Further, follow-up suppressor screens for genes or compounds that restore normal morphology in these animals to wild-type levels should be completed. Specifically, the TS1 strain is an excellent candidate for genetic or therapeutic suppressor screens due to its strong phenotype, such that any positive hits should show drastic restoration in morphology and overall development. Further, any follow-up discoveries involving this strain could potentially yield novel therapeutics and conserved genetic pathways related to human Timothy syndrome pathology.

To investigate *egl-19* expression patterns in *C. elegans*, we generated a GFP tag at the C-terminus of *EGL-19* using CRISPR-Cas9 HR. To somewhat of a surprise, these *EGL-19::GFP* animals developed normally, especially since it has been shown that the 3' end of the human ortholog *CACNA1C* encodes a transcription factor that regulates neurite extension and inhibits CaV1.2 expression (Gomez-Ospina et al., 2013). Therefore, this function might not be interfered with or conserved in *C. elegans*. Also, unlike previous *EGL-19::GFP* fusion or GFP auxiliary-binding strains (Lainé et al., 2014; Lee et al., 1997), this endogenous modification approach may reduce variability across individuals, yielding a more specific and less variable survey of *EGL-19* localization and expression levels. It would also be interesting to cross our *EGL-19::GFP* strain into *UNC-2::RFP* or *CCA-1::RFP* animals to survey sub-cellular co-localization and distribution of all VGCCs in *C. elegans*, and make mutations in this strain to compare expression levels and translocation in various level-of-function mutant backgrounds and development stages (embryo to adult) (**Fig. 11**). For example, the *EGL-19::GFP* animals could be used to knock-in TS1 by CRISPR-Cas9 HR like above, which could identify changes in *EGl-19* expression level and localization in TS1 animals (**Fig. 11**). Here, we show *EGL-19::GFP* expression in otherwise WT L1 animals localizes to cell membranes and specific cell types. The GFP signal was observed on the cell membrane of several head neurons, body wall muscle, and the pharynx. This result is similar to other GFP strains reported previously (Kwok et al., 2006; Lainé et al., 2014; Lee et al., 1997), while showing more specific localization to neuron cell membranes not as clearly shown and described before (Lainé et al., 2014; Lee et al., 1997). Therefore, we can conclude that *EGL-19* is expressed broadly in the L1 developmental stage, and the GFP genomic fusion with the 3' end does not seem to affect protein function or animal development.

Additionally, we assessed how several other varying level-of-function missense mutations in *egl-19* cause morphological and behavioral changes in *C. elegans* using a plate-based high-throughput recording method (Swierczek et al., 2011). Specifically, we observed differences in animal midline length, locomotion speed, and reversal duration to a mechanical tap that are consistent with previous literature (Lainé et al., 2014). Animals with GOF mutations in *egl-19* are shorter overall, while *ROF* mutations cause longer body phenotypes that can be partially restored with an endogenously expressed *egl-19cDNA* rescue transgene. These differences have been explained in part by prolonged or reduced contraction in body muscle, respectively (Lainé et al., 2014). We show here that it is also possible to modulate or restore body morphology by endogenous expression of a wild-type *egl-19cDNA* transgene. This rescue result suggests that transgenic expression of both ROF and WT *egl-19* in the same animal may partially restore intracellular calcium levels and thus body morphology, as reported previously (Lee et al., 1997). Also, we observed differences in baseline speed across all genotypes when compared to wild-type animals, but not all changes were to significance after correcting for multiple comparisons. The most severe GOF channelopathy mutant *egl-19(n2368)* was significantly slower than wild-type animals, which is likely due to its severe hypermorphic and hypercontracted phenotype limiting the animals' ability to make typical body bends required for forward locomotion, as indirectly and previously shown in a thrashing assay (Lainé et al., 2014). The opposite was observed for the second less severe GOF mutant *egl-19(ad695)* that has a similar hypercontracted (short midline length) phenotype and significantly reduced thrashing behavior (Lainé et al., 2014), suggesting that body bending might not be directly related and remains to be tested. Also, although not to significance, the average forward speed of the ROF rescue animals

was increased compared to the slower ROF mutants. This shows that although not completely rescued, changes in body morphology may be at least partially responsible for proper forward locomotion, while muscle tone and frequency of body bending should be investigated. Lastly, the duration at which animals complete a reversal behavior after mechanical tap was assessed and observed to be inversely related to forward speed, except for the most severe GOF mutation *egl-19(n2368)*. This genotype had the fastest reversal duration, whereas all other mutations were proportional to their forward speed and body length (i.e. the ROF reversal lasted in the longest, had the slowest forward speed (other than *egl-19(n2368)*, and had the longest midline). Therefore, these results indirectly suggest that the level of calcium channel function can cause proportional changes in body length, which may be responsible for defects in average forward speed and duration of reversal behavior not identified before. Electrophysiological recordings and calcium imaging in muscle of dissected *C. elegans* also showed relative changes in cellular activity (Jospin et al., 2002), where GOF animals had slower inactivation rates, and ROF mutations had decreased cellular activation (Jospin et al., 2002; Lainé et al., 2014). Taken together, the level of calcium channel (*EGL-19*) function, protein expression and localization might be responsible for changes in muscle contraction and thus additional behavioral phenotypes we further observed here in *C. elegans*.

To investigate the level of calcium channel function in neurons of intact and living *C. elegans*, we stimulated and monitored calcium activity in various level-of-function animal populations using a high-throughput microfluidic device (Larsch et al., 2013). Differences in cellular activity have also been shown for human induced Timothy syndrome type 1 neurons and heterologous

systems, but this mutation or related ones have not been directly assessed and monitored in the neurons of whole organisms. Since animals harboring the TS1 mutation by CRISPR-Cas9 HR were not directly compatible with conventional microfluidic devices (due to their small size), mixed populations of genetically balanced animals were assessed instead. Not surprisingly, no strong differences between these two populations of animals were detected, likely due to the low probability of assessing true TS1/Dnt1 animals in a mixed population, and since there was no clear effect on animal body morphology in heterozygotes (TS/+) caused by this mutation (data not shown). An attempt was made to stimulate homozygous TS1 animals using a hydrogel-based immobilization method with high-magnification fluorescence imaging (Burnett et al., 2017); however, variability in spatiotemporal stimulation delivery, low-throughput selection of TS1 homozygous animals, and indirect controls led to inconclusive results. Instead, other available GOF, ROF, and transgenic animals were assessed that may serve as human channelopathy models in general. Two strains with different GOF severities were compatible with our microfluidic device and exhibited significantly different calcium response kinetics compared to wild-type. One strain that harbors a G365R mutation in the TS2 (human G402S) loci (*egl-19(n2368)*) showed rapid response activation and inactivation kinetics, while another unrelated A906V mutation located in a voltage sensitive transmembrane segment of domain III showed significantly decreased inactivation compared to wild-type, similar to TS1 cells *in vitro*. The latter result is consistent with electrophysiological studies on dissected *C. elegans* muscle and calcium imaging (Jospin et al., 2002; Shtonda and Avery, 2005). Further, the response to diacetyl in AWA is largely responsible to *EGL-19*, since ROF animals exhibited significantly reduced (almost no) change in calcium activity response. It is worth investigating if this reduction in response is dose-dependent and

soma-specific, likewise for all other level-of-function mutations tested here. Additionally, using compounds like muscimol or other related compounds could be used to pretreat GOF animals through development, then test using microfluidics to observe any restored changes in calcium activity (Lainé et al., 2014). Although these GOF mutations are not exactly similar to TS1, their calcium activity phenotypes in neurons may be useable as models for the neurodevelopmental symptoms in this disorder.

In an attempt to compare a more subtle TS1 model compatible with our microfluidic methods, we generated a TS1 transgene expressed only in AWA neurons. This construct did not impair animal behavior or morphology (data not shown), and did not have any apparent effect on ROF calcium activity in wild-type animals. To assess whether this construct could restore function cell-specifically and yield a decreased inactivation phenotype similar to TS1 in human neurons *in vitro*, I crossed ROF mutants with animals carrying the TS1 GOF construct in AWA. This transgene did not restore calcium response function, and therefore was not appropriate to make direct comparisons in prolonged inactivation to ROF animals since their signal-to-noise ratio was low. Several possible explanations for this could be that either the TS1 transgene product is not being properly localized to the cell membrane (but is being translated since the mCherry marker is expressed), or the expression level of this transgene must be tuned appropriately *in vivo* to yield measurable effects. Interestingly, however, cell-specific expression of the *unc-2(zf35)* GOF in AWA had a significant effect on peak calcium response kinetics. So, it may still be possible to measure changes in intracellular calcium kinetics by cell-specific expression of other channelopathies or genes under these promotors.

Calcium activity in the ROF mutant showed a significant reduction in peak response and thus intracellular calcium flux. This result is also consistent with electrophysiological studies and calcium imaging in muscle of dissected ROF animals (Jospin et al., 2002), further suggesting that calcium flux may cause impaired behaviors and morphology that we and others observed and quantified previously, but not before compared in intact *C. elegans* head neurons, except *egl-19(n582)* (Larsch et al., 2015). In regard to several new TS-like mutations discovered recently, GOF and ROF-like electrophysiological recordings were recorded in what is believed to be a GOF human disorder (Boczek et al., 2015b; Ozawa et al.). These results might be consistent with our observations in neurons of intact animals, in which "summed" channel kinetic phenotypes may be a cause (Lainé et al., 2011). Moving forward, for complete characterization of each newly discovered disorder in the clinic, it would be useful to analyze the expression levels and localization of all auxiliary subunits since a combination of changes in the channel might be reason for the broad spectrum of electrophysiological phenotypes observed.

Altogether, the results described in this Chapter establish a pipeline and concept for generating and assessing human channelopathy mutations in *C. elegans* through three phenotypic tiers: behavior, morphology, and cellular activity of intact animals. Generating a variety of whole-organism animal models that mimic human disease will lead to novel hypothesis generation and methods for assessing broad and subtle phenotypes. Here, we showed that a new whole-organism TS1 model in *C. elegans* using CRISPR-Cas9 HR leads to a severe developmental arrest, while heterozygotes and balanced strains develop as wild-type, and other GOF mutations have quantifiable and significant morphological and behavioral phenotypes. Third, we identified

quantifiable differences in calcium activity in intact *C. elegans* neurons among all levels-of-function that recapitulate observations previously quantified in dissected *C. elegans* muscle, hiPSCs from TS1 patients, heterologous systems, and new cases of TS. Together, this pipeline can be followed to investigate additional channelopathy mutations for the identification of novel phenotypes at the cellular and behavioral levels in whole organisms for future genetic and pharmacological screens.

From these results, we also learned several key challenges and limitations to inspire future work. First, we found that it is possible and straightforward to generate homologous disease-causing human mutations in *C. elegans* using CRISPR-Cas9 HR. However, such targeted genes and induced mutations like those that cause TS may not act similarly in intact model systems like *C. elegans*. Currently, it remains challenging to hypothesize exact phenotypic effects that human disease-causing mutations have on model organism biology. In extreme cases, these mutations may cause severe (lethal) phenotypes, preventing the use of conventional methods to quantify relevant biological processes, like calcium activity. To this end, hiPSCs and other *in vitro* model systems remain extremely useful for evaluation of cellular activity (in the presence of therapeutic compounds) by gold-standard techniques like electrophysiology. Yet, whole-organism models provide a translational platform for investigating disease pathology in a multicellular system. Likewise, whole organisms are directly compatible with high-throughput screening technologies, while limitations in scale and cost still exist for some *in vitro* model systems. Finally, compounds that restore disease-causing phenotypes in *C. elegans* may lead to more effective treatments in humans considering off-target effects, which may not be as easily identified *in vitro*.

Chapter 3 Develop and characterize a microfluidic screening technology for the identification of short-term modulators of cellular activity *in vivo*

Abstract

High-throughput biological and chemical experiments typically use either multiwell plates or microfluidic devices to analyze numerous independent samples in a compact format. Multiwell plates are convenient for screening chemical libraries in static fluid environments, whereas microfluidic devices offer immense flexibility in flow control and dynamics. Interfacing these platforms in a simple and automated way would introduce new high-throughput experimental capabilities, such as compound screens with precise exposure timing. Whereas current approaches to integrate microfluidic devices with multiwell plates remain expensive or technically complicated, we present here a simple open-source robotic system that delivers liquids sequentially through a single connected inlet. We first characterized reliability and performance by automatically delivering 96 dye solutions to a microfluidic device. Next, we measured odor dose-response curves of *in vivo* neural activity from two sensory neuron types in dozens of living *C. elegans* in a single experiment. We then identified chemicals that suppressed optogenetically-evoked neural activity, demonstrating a functional screening platform for neural modulation in whole organisms. Lastly, we automated an 85-minute, ten-step cell staining protocol. Together, these examples show that our system can automate various protocols and accelerate experiments by economically bridging two common elements of high-throughput systems: multiwell plates and microfluidics.

Introduction

Microfluidic devices offer several advantages for biomedical research, particularly for presenting precise physical and chemical environments to cells and organisms (Albrecht and Bargmann, 2011; Bhatia and Ingber, 2014; Rothbauer et al., 2018; Sackmann et al., 2014), multiplexing experimental conditions (Albrecht and Bargmann, 2011; Cornaglia et al., 2017; Gómez-Sjöberg et al., 2007), and reducing reagent volumes for screening applications (Aubry and Lu, 2017; Cho et al., 2017; Du et al., 2016). Traditional high-throughput screening systems use multiwell plates to contain samples and chemicals in miniaturized wells and observe each condition after static long-term exposure periods, typically hours to days. For dynamic chemical delivery and monitoring, such as stimulation with brief pulses of bioactive compounds, few options exist to directly interface chemicals in multiwell plates with microfluidic devices. Current approaches include complex setups with separate inlet tubes for each well (i.e., 96 inlet tubes for a 96-well plate)5, the use of conventional liquid-handling robots to inject liquids to device inlets (Bazopoulou et al., 2017; Rane et al., 2012), and microfluidic designs that are integrated into plastic multiwell dishes (Lee et al., 2015, 2007; Ma et al., 2015; Melin and Quake, 2007; Mondal et al., 2016). These approaches are generally expensive, either due to laborious fabrication processes or to single-use cartridges operated by specialized flow control equipment. A simple yet laborious alternative is the manual transfer of an inlet tube from well to well (Larsch et al., 2013). However, any disconnection of tubing tends to introduce air bubbles due to surface tension, and these bubbles can severely disrupt fluid flow within microfluidic circuits. Rotational valves can change inlet streams without introducing bubbles, but are generally limited to 8 or 12 positions, while in-line

debubblers can remove air from tubing, but occupy relatively large fluidic volumes, and both can be expensive and difficult to clean.

In this paper, we present a robotic system that reliably and automatically transfers a single microfluidic inlet tube from one fluid reservoir to another, without introducing a bubble. In this manner, numerous liquids can be delivered sequentially into any microfluidic device. We demonstrate that this system, based on inexpensive open-source hardware and software, can completely automate: (1) the measurement of neural dose responses and optimization of chemical concentrations for robust and non-saturating responses, (2) a complex chemical screen to determine the effect of different solvents on optogenetically-activated neural responses in living nematodes, and (3) a multi-step, multi-duration cell staining protocol. In each example, the experiment was first set up by preparing a multiwell plate with desired chemicals, preparing the microfluidic device with bioassay targets (e.g. organisms or cells), then selecting the chemical exposure time course and data acquisition settings. Afterwards, all subsequent experimental activity required no user intervention. We expect that this versatile tool will expand the throughput of biological experiments that require serial delivery of multiple fluids, from neuronal imaging in living organisms to histochemical staining of cells. Further, such automation can improve results and reproducibility by minimizing human error and by simplifying the optimization of experimental protocols.

Results

A robotic platform to interface multiwell plates with microfluidic devices

The robotic system automates serial liquid delivery from standard multiwell plates to microfluidic devices by automatically raising and lowering an inlet tube into the desired well of a multiwell plate (**Fig. 15a**). It uses commercially-available parts, machined or 3D-printed brackets, and custom open-source software (**Fig. 15a**, Supplementary Figs S1, S2), keeping costs below $500. Also, the modular system mounts to a microscope for visualization and monitoring of samples contained within an integrated microfluidic device. The robot uses stepper motors to position the multiwell plate and a servo motor to raise and lower the inlet tube with sufficient force to reliably puncture plate sealing film (**Fig. 15a-c**, Supplementary Video S1). The system works with both reversibly-sealed and permanently-bonded microfluidic devices and can be adjusted for different plate configurations, such as 6-well to 384-well plates with shallow or deep wells.

To prevent a bubble from entering the robotic inlet tubing when it is raised, flow through the device is momentarily stopped by closing the outflow valve. Capillary pressure at the open end of the inlet tube can be exactly counteracted by a small hydrostatic pressure supplied from a backpressure reservoir elevated above the multiwell plate. In this pressure-balanced configuration, the inlet tube can safely lift out of a well without forward fluid flow (which would introduce a bubble into the inlet tube) or backward flow (which may transfer some inlet liquid to the next well) (**Fig. 15b-d**).

The mechanical transfer of inlet tubing from one well to another is rapid, requiring less than 2 s transition time to raise the inlet tubing, move the plate, and lower the inlet tubing into the next well (**Fig. 15e**). However, each new fluid flows sequentially through a single inlet, and therefore must flush the prior fluid from the inlet tube before reaching the microfluidic device. To minimize this switching delay, tubing was as short and narrow-bore as practical (22 cm, 250 μm inner diameter, containing about 11 μL volume). At a flowrate of 2 μL/s, about 30 s were required to completely replace the prior fluid, due to Taylor dispersion within the inlet tube (**Fig. 15e**, Supplementary Fig. S3); hence, about 5 inlet tube volumes must flow before the fluid switch is complete. To measure reliability and well-to-well fluid carryover, we monitored concentration profiles during fluid switches across a full 96-well test plate containing alternating fluorescein dye and water solutions (**Fig. 15f-h**). Using a 30 s fill delay and 2 μL/s flowrate driven by hydrostatic pressure, well-to-well carryover was 0.32% ± 0.047% S.D. across all 48 dye-to-water fluid switches. Additional wash steps reduced carryover to less than 0.02% (**Fig. 15i**).
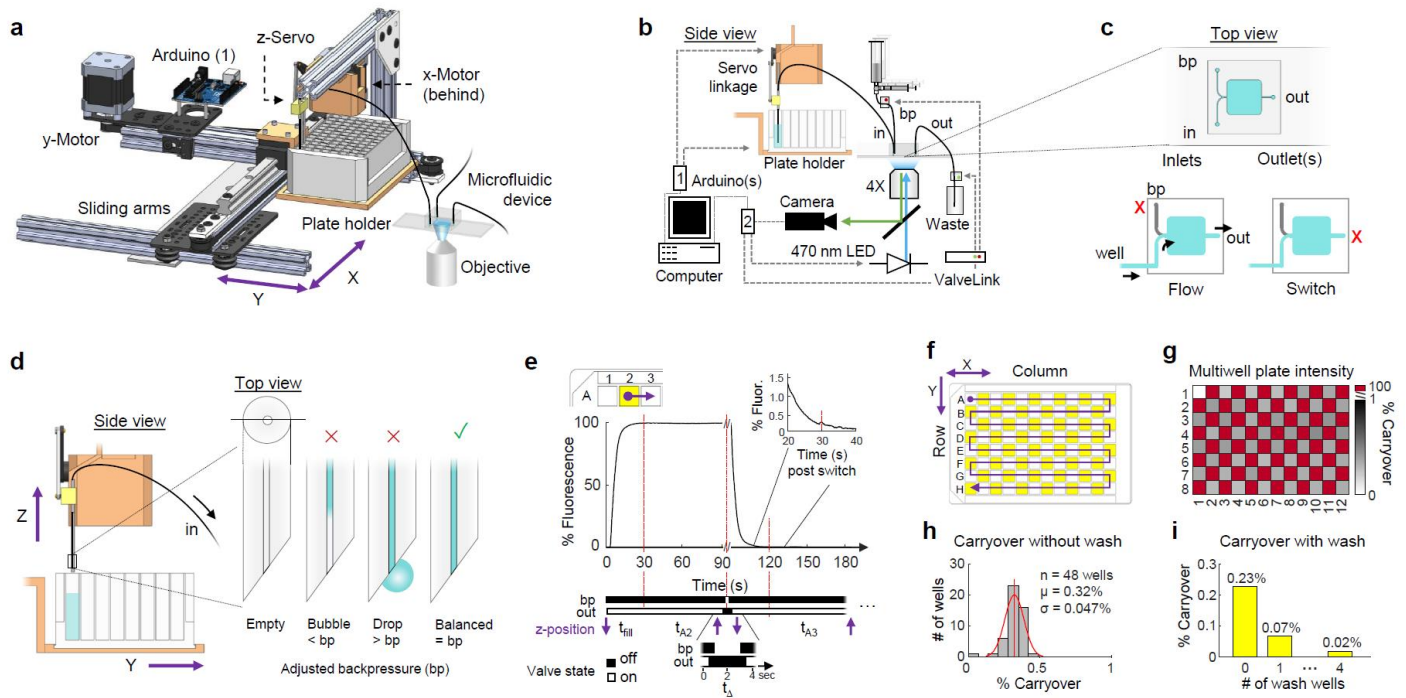
Figure 15. Robotic fluid delivery components, operation principle, and characterization of switching performance and well-to-well carryover across a 96-well plate.

a. Model of the robotic platform comprised of a multiwell plate holder with x-y motion and a servo linkage with vertical z-motion to raise and lower an inlet tube connected to a microfluidic device mounted on a microscope stage (Supplementary Video S1).
b. Control schematic of the robotic platform, microfluidic device valves, and microscope optical components. Device connections include an inlet (in) tube, backpressure (bp) reservoir, valve, and tube, and an outlet (out) valve and tube. Robotic positions are computer-controlled by Arduino (1) and all valves and microscope illumination are controlled by Arduino (2).
c. Top view of an example microfluidic device with a multiwell plate inlet (in), and backpressure (bp) port, and one waste outlet (out). Valve states (red X, closed) are illustrated below during well flow (left) and well-to-well switching (right).
d. Side view of the raised inlet tubing and magnified views demonstrating proper backpressure (bp) balance: bp too low can introduce an air bubble in the inlet tubing whereas bp too high can cause backward flow and a drop to emerge from the inlet tubing.
e. Timing of valve actuation and servo motion during well-to-well transfer and dynamics of the fluid switch monitored with fluorescein dye. Upper graphs show the time course of relative fluorescence intensity beginning with the switch from a buffer well to fluorescein at t = 0, and a switch back to buffer at t $\simeq$ 90 s. Inset shows a magnified view from 110–130 s (i.e. 20–40 s after the second tube switch). Below, corresponding actuation states of backpressure (bp) and outlet (out) valves and inlet tube z-position (purple arrows) during the short (~2 s) transition time (t$_\Delta$). Fluid switching in the microfluidic device is complete after a filling delay (t$_{fill}$, vertical red lines) dependent on flowrate and inlet tube volume.
f. Multiwell plate map showing 96 alternating buffer and fluorescein dye wells scanned in a "snake" pattern.
g. Heat map shows percent carryover without wash steps from fluorescent intensity in the microfluidic channel, calculated for each buffer well relative to the prior fluorescein well after a fill delay of 30 s.
h. Histogram of well-to-well carryover without wash steps across 48 wells, from data shown in g.
i. Sequential tubing wash steps further reduce well-to-well carryover. Data are shown using a fill delay of 30 s.

Automatic determination of chemical dose responses in C. elegans *sensory neurons*

Neural dose-response curves identify the sensitivity of neurons to a particular chemical stimulus and determine optimal working concentrations that elicit robust yet unsaturating responses. They have been manually generated in *C. elegans* by optical imaging of animals expressing a genetically-encoded calcium sensor during exposure to pulses of multiple concentrations of chemical stimuli in microfluidic devices (Chronis et al., 2007; Larsch et al., 2013). To simplify this tedious manual process, we set up a completely automated dose-response experiment by filling serially-diluted stimuli in a 96-well plate (**Fig. 16a**). About 20 young adult *C. elegans* expressing GCaMP in either the AWA or ASH chemosensory neurons were introduced into a dual-arena microfluidic device (**Fig. 16b-e**) and subjected to brief pulses of the odor diacetyl (DA) across six orders of magnitude (11.5 nM to 11.5 mM, 10^{-9} to 10^{-3} dilutions) (Supplementary Video S2). AWA chemosensory neurons showed an increase in calcium upon diacetyl exposure with an EC_{50} around 1.15 μM (10^{-7} dilution) and saturation above 11.5 μM (10^{-6} dilution) (**Fig. 16f, g** and Supplementary Fig. S4). Activity in the ASH multimodal neurons was not observed until high odor concentrations above 1.15 mM diacetyl (10^{-4} dilution) (**Fig. 16f, h**). AWA neuron responses were consistent over four repeated odor pulses, whereas ASH neurons adapted rapidly (**Fig. 16g, h**, Supplementary Fig. S4). These measurements replicated previously-reported results (Larsch et al., 2013; Taniguchi et al., 2014; Yoshida et al., 2012), and our automated experiment further revealed a negative correlation between ASH activity and AWA peak response magnitude at high odor concentrations (**Fig. 16i**) that may arise from circuit feedback (**Fig. 16j**).
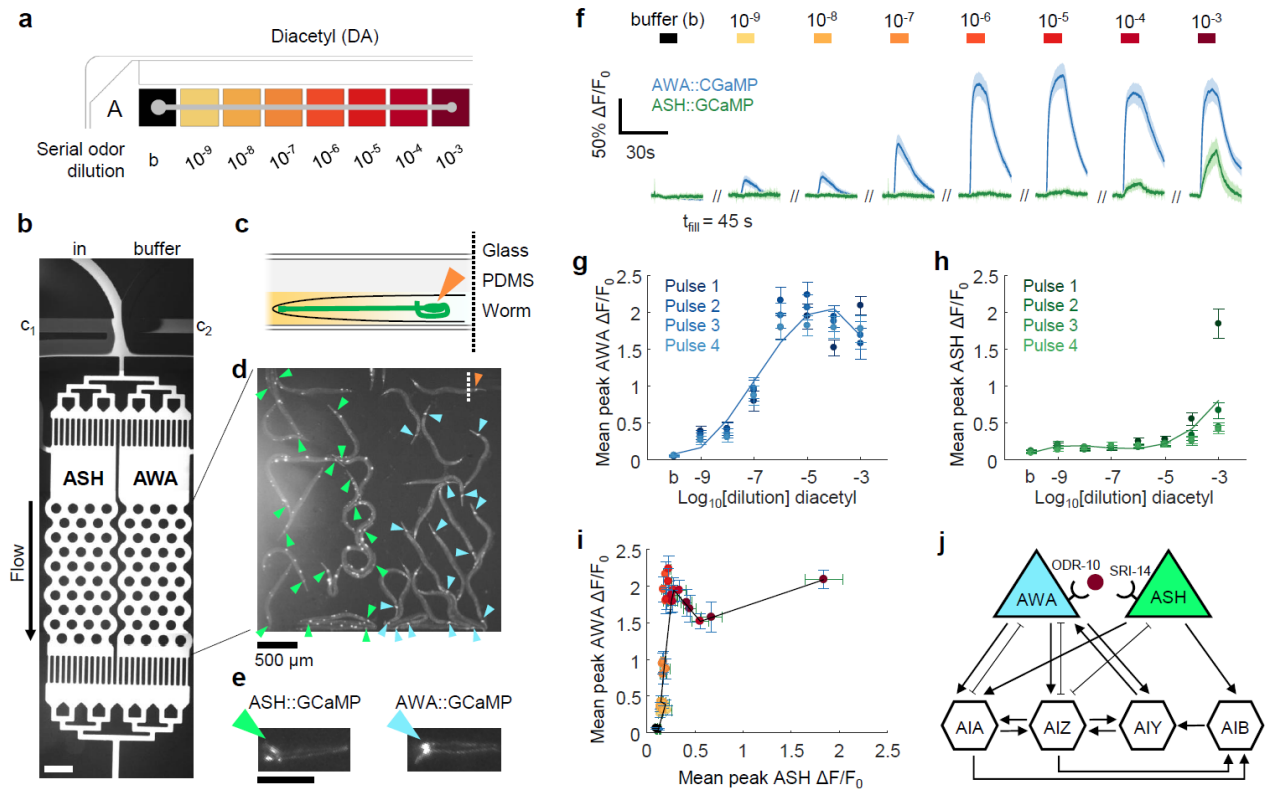
Figure 16. *Automated chemical dose response of two chemosensory neurons in* **C.** elegans *to the odor diacetyl from a single experiment.*

a. Schematic of the multiwell plate prepared with buffer (b) and serial dilutions of diacetyl odor, from 10^{-9} (11.5 nM) to 10^{-3} (11.5 mM). Gray dot indicates the first well position.

b. A reusable two-arena pulse microfluidic device with four fluidic inlets, two worm-loading ports, and an outlet. The device switches between the stimulus inlet (in), shown with high concentration fluorescein, and unlabeled buffer, depending on which of two control channels (c_1, c_2) are flowing (Supplementary Video S2). Here, c_1 flows while c_2 is closed, such that stimulus fluid flows through the animal arenas. Scale bar, 500 μm.

c. Cross-section schematic of a worm head expressing GCaMP in a single neuron in the microfluidic assembly. Orange arrow points to the fluorescent cell body (soma) as in d.

d. Wide-field (4X) fluorescent image of 36 animals expressing GCaMP in either ASH (green arrows, left) or AWA (blue arrows, right) chemosensory neurons in the device.

e. Magnified images from panel d of animals expressing GCaMP in either ASH (left) and AWA (right) chemosensory neurons. Arrow points to soma. Scale bar, 100 μm.

f. Time course and average normalized fluorescence (ΔF/F$_0$) dose response traces for AWA (blue) and ASH (green) neuron cell bodies. Four pulses (10 s each) were delivered once per minute at each increasing concentration (or buffer). Lines and shading represent mean and SEM across four pulses, n = 72 traces per concentration and neuron type.

g. Mean peak normalized calcium responses for AWA neurons across seven increasing odor steps and buffer (b). Data points show population average and SEM (n = 18) for each of four repeated pulses per concentration. Trace represents a third-degree polynomial fit of each concentration's pulse average.

h. Mean peak normalized calcium responses for ASH neurons, as described in g.

i. Mean peak normalized calcium responses of AWA plotted against ASH for each individual odor pulse. Error bars represent SEM for AWA (blue) and ASH (green), per concentration (corresponding dot color).

j. Neural network wiring diagram illustrating chemical synapses (arrows) and gap junctions (flat ends) for AWA and ASH sensory neurons and four first layer interneurons. Diacetyl is detected by different affinity receptors on each sensory neuron (Sengupta et al., 1996; Taniguchi et al., 2014).

83

An automated compound screen yields suppressors of stimulated neural activity in C. elegans

The robotic system was used to screen fourteen common solvents and carriers for their effects on optogenetically-evoked neural responses (**Fig. 17**). Each solution was prepared at two concentrations (1% and 5%) in a 96-well plate alternating with buffer control wells for 57 total solutions delivered sequentially to a microfluidic neural imaging device (**Fig. 17a**). Calcium signals were recorded from AWA chemosensory neurons of 20 young adult animals co-expressing the genetically encoded calcium sensor GCaMP2.2b and the red-shifted channelrhodopsin Chrimson in the same neuron, allowing simultaneous optical stimulation with red light and monitoring of neural calcium responses (**Fig. 17b, c**). Most light-stimulated neural responses were unaffected by <1 min exposures to each solvent concentration, compared with the buffer control response just prior (**Fig. 17d-f**, Supplementary Fig. S5). However, isopropanol, methanol, and acetonitrile significantly suppressed peak fluorescent responses at both 1% and 5% concentrations, while ethanol decreased responses only at 5% concentration. Solvent effects were transient, as returning to buffer within <1 min rapidly restored normal responses (**Fig. 17d, e, g**) in most cases, except after 5% methanol and 5% acetonitrile. Response patterns could be monitored from individual animals, allowing paired comparisons with greater statistical power, and were consistent across the population tested (**Fig. 17b, d, g**, Supplementary Fig. S5).
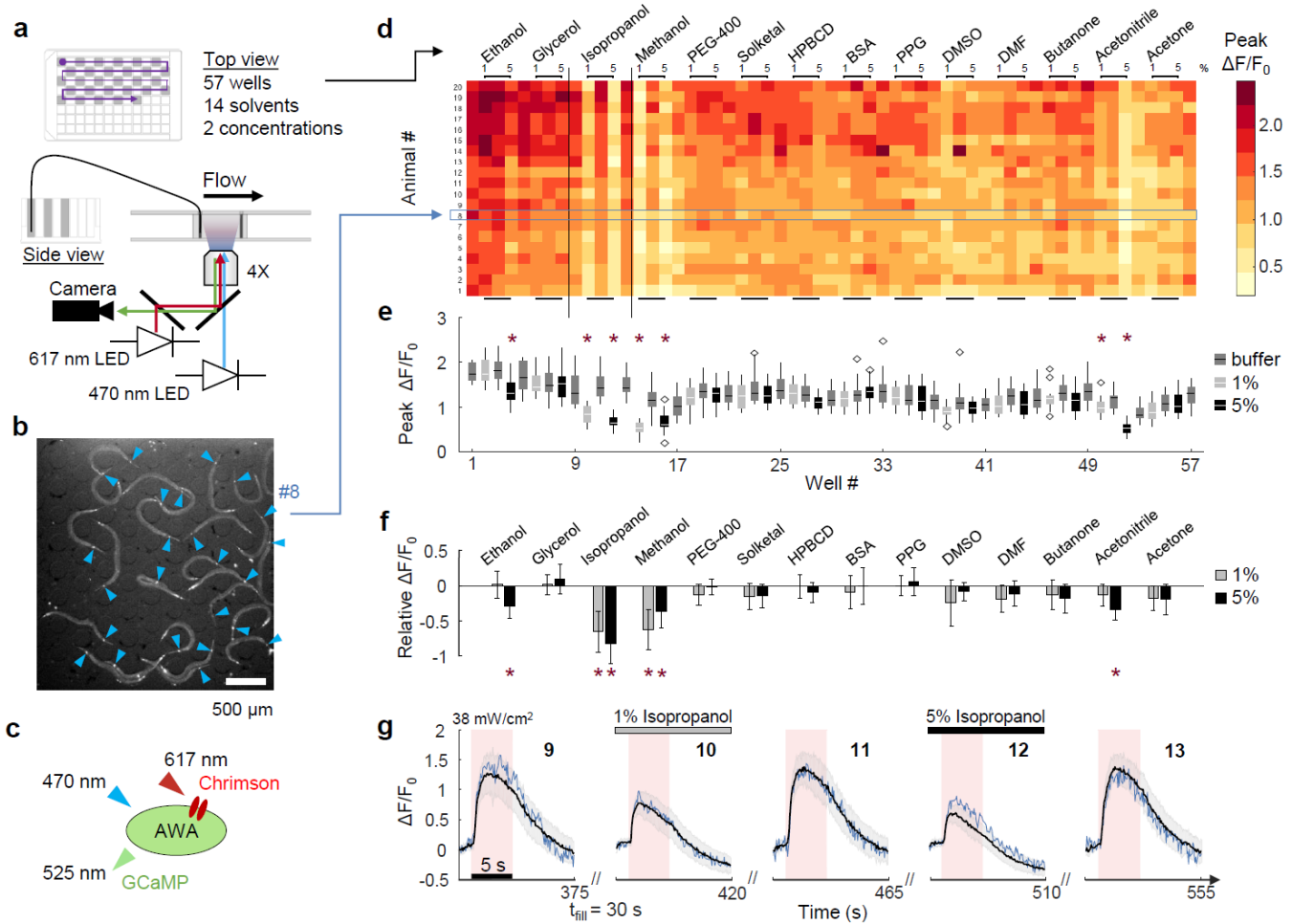
Figure 17. An automated C. elegans *solvent screen yields suppressors of optogenetically-activated neural responses.*

a. Multiwell plate map showing 57 wells containing solvents at 1% and 5% concentrations alternating with control S. Basal buffer (gray fill). Diagram below shows the optical path for simultaneous stimulation and monitoring of neural responses, *via* 470 nm blue excitation of GCaMP and green emission, and 617 nm red light stimulation of the Chrimson ion channel.

b. Wide-field 4X fluorescence image of young adult animals co-expressing GCaMP and Chrimson in the AWA sensory neurons in each animal (arrows) within a reversibly-sealed single-arena microfluidic device.

c. A schematic of excitation and emission wavelengths used for simultaneous optogenetic stimulation of AWA sensory neurons using Chrimson and recording of intracellular calcium levels with GCaMP.

d. A heat map representing 1,140 peak normalized neural responses ($\Delta F/F_0$) across 20 individual animals and 57 solutions. Horizontal blue box highlights animal #8, identified in panel b.

e. Box plot shows population average peak $\Delta F/F_0$ neural activation response for each compound. Symbols represent statistically significant mean peak differences compared to immediate prior controls (*$p < 0.001$, ANOVA repeated measures with Bonferroni correction). Boxes indicate 25th and 75th percentiles, whiskers extend to 1.5 times the interquartile range, and outliers are indicated with diamond symbols.

f. Bar graphs show the difference in mean peak $\Delta F/F_0$ response between each solvent concentration and its immediate prior buffer control. Error bars represent SD. Symbols represent statistically significant relative mean peak differences (*$p < 0.001$, paired one-sample t-tests with Bonferroni correction).

g. Example neural traces show suppression of optogenetic stimulation by isopropanol. Population average animal $\Delta F/F_0$ calcium responses (black line) to 5 s of red light stimulation are shown for wells 9 to 13 (outlined in d). Shading represents SD. Blue lines indicate responses from animal #8.

85

Solvent effects on odor vs. optogenetically-stimulated responses in C. elegans

Two fully automated independent experiments were designed to determine if there was a difference in optogenetically or odor-stimulated responses in the presence of the solvent DMF (**Fig. 18**). Three wells were prepared containing buffer, 0.1% DMF, and buffer, while animals were prepared as described in the experiment above. Individual animal responses were recorded for 15 repeated pulses of red light in the presence of buffer, then 0.1% DMF, and finally buffer, for a total of 45 repeated stimulation pulses (**Fig. 18a-b**). It was observed that the average calcium response for all 19 animals was slightly reduced after the DMF exposure and consistent across all subsequent activation pulses (red arrow, **Fig. 18c-d**). Similarly, animals expressing only expressing GCaMP in AWA were prepared in the microfluidic device, and three wells were prepared containing 1.15 μM diacetyl (DA), 1.15 μM DA in 0.1% DMF, and 1.15 μM DA. The same stimulation and recording settings were executed and calcium responses were recorded for all 15 animals. Initial habituation to the DA odor pulse was observed for the first 5-10 pulses as expected (Larsch et al., 2013, 2015), while an increase in odor response was observed on the odor pulse immediately following the last odor pulse containing DMF (red arrow, **Fig. 18e-h**). Therefore, it seems that DMF is possibly acting on the *odr-10* receptor to modulate the calcium activity response in odor-stimulated AWA chemosensory neuron, interfering with the odor molecule itself, or activating other fast-acting intracellular response and odor-detection mechanisms altogether. Repeating the same odor-stimulation experiment with another AWA-detected odor (e.g pyrazine, or 2,4,5-trimethylthiazole) would help determine if this effect is *odr-10* specific (Sengupta et al., 1996), or reflects other responsible fasting-acting intracellular mechanisms that are currently unknown.
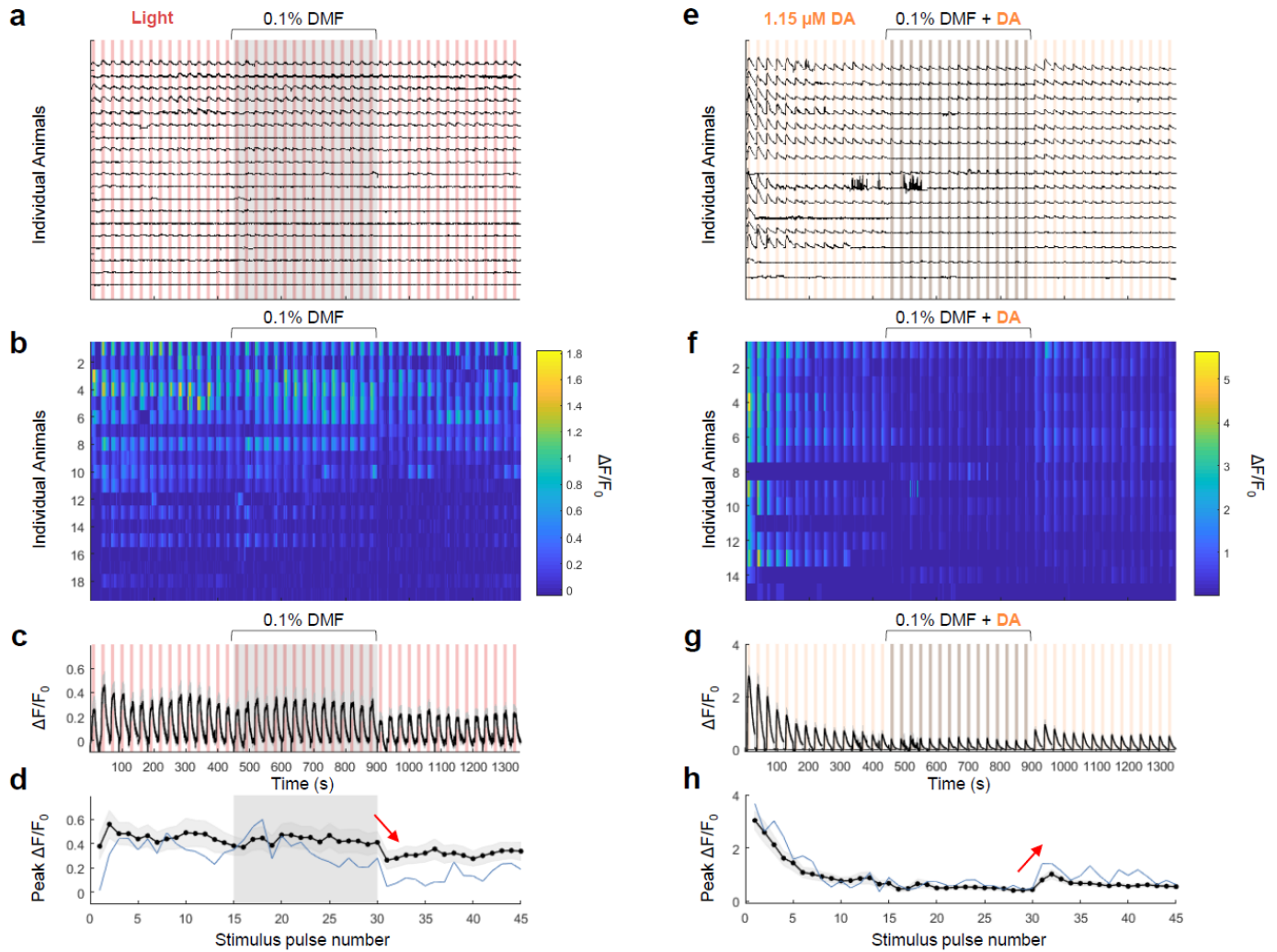
Figure 18. Solvent exposure on optogenetically- and odor-evoked calcium responses yield opposing effects.

a. Individual $\Delta F/F_0$ calcium response traces from 19 animals co-expressing Chrimson and GCaMP in the AWA chemosensory neuron, pulsed with red light for 15 s every minute, 45 times. A 0.1% DMF exposure was delivered between pulses 16-30, after which animals were re-exposed to buffer.

b. A heat map representation of individual $\Delta F/F_0$ calcium responses as shown above in a.

c. Mean $\Delta F/F_0$ calcium response trace from all individuals shown in a and b. Shading represents SEM.

d. Mean peak $\Delta F/F_0$ calcium responses from a-c across all 45 stimulus pulses. One individual animal peak response trace is shown in blue. The red arrow shows a slight decrease in mean peak response after the removal of DMF from the background solution. Shading represents SEM.

e. Individual $\Delta F/F_0$ calcium response traces from 15 animals expressing GCaMP in the AWA chemosensory neuron, pulsed with 1.15 µM diacetyl (DA) for 15 s every minute, 45 times. A 0.1% DMF + DA mix was delivered for pulses 16-30, after which animals were stimulated with just 1.15 µM diacetyl (like for the first 15 pulses).

f. A heat map representation of individual $\Delta F/F_0$ calcium responses as shown above in e.

g. Mean $\Delta F/F_0$ calcium response trace from all individuals shown in e and f. Shading represents SEM.

h. Mean peak $\Delta F/F_0$ calcium responses from e-g across all 45 stimulus pulses. One individual animal peak response trace is shown in blue. The red arrow shows a noticeable increase in mean peak response after the removal of DMF from the stimulus solution. Shading represents SEM.

Automated multi-step cell fixation and staining in a microfluidic device

Histochemical staining is often a laborious process, requiring several manual steps of fixation, washes, blocking, and labeling with visible or fluorescent probes over several hours. We used the robotic system to automate a typical cell staining procedure. Human mesenchymal stem cells (hMSCs) seeded in a microfluidic device were stained one day later by connecting the device to a multiwell plate containing ten wells filled with a sequence of staining solutions (**Fig. 19a-c**). An 85-min cell staining protocol was entered using a custom MicroManager script which controlled well position, exposure duration, and acquisition of images to monitor staining progression (Supplementary Video S3). Cells were automatically fixed in paraformaldehyde, permeabilized in Triton-X, blocked with bovine serum albumin (BSA), and stained with fluorescent phalloidin to label filamentous actin and with Hoechst to label nuclei (**Fig. 19c**). For long exposure steps (>30 min), flow through the microfluidic device was paused to prevent inlet wells from running empty and to conserve expensive reagents. Average image fluorescence increased quickly after about 15 min exposure to phalloidin (**Fig. 19d**), and high-magnification images showed actin filaments aligned within the microfluidic channel (**Fig. 19e-g**).
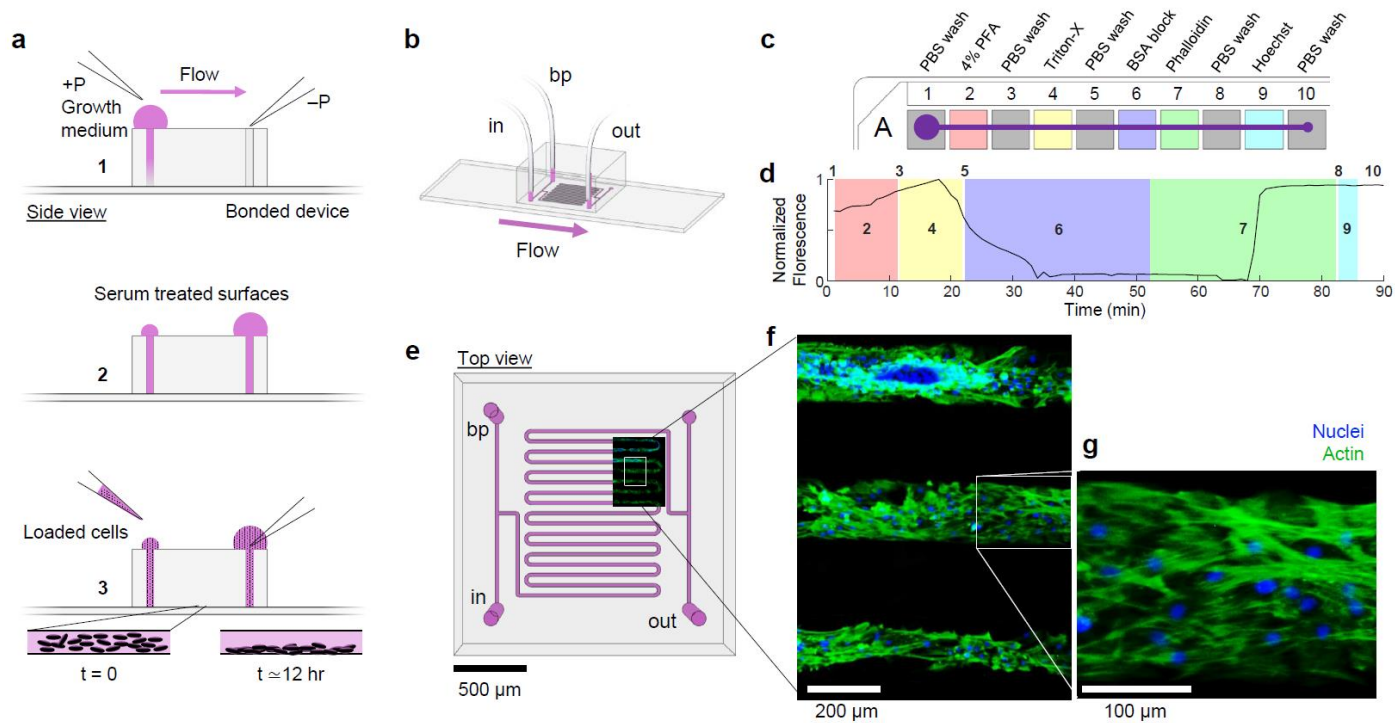
Figure 19. Automated multi-step fixation and staining of cells in microfluidic channels.

a. Side view schematic of the microfluidic cell culture preparation by treating surfaces with growth medium (1−2), then loading cells and allowing them to adhere to the glass surface overnight (3, below).
b. Schematic of the fluid inlet (in), backpressure (bp), and waste outlet (out) connections for a bonded serpentine channel microfluidic device.
c. Ten staining solutions filled in one row of a multiwell plate (A1-A10). PBS, phosphate-buffered saline. PFA, paraformaldehyde. BSA, bovine serum albumin.
d. Average fluorescence intensity monitored throughout the entire staining procedure at 1 frame per minute (Supplementary Video S3). Times during each fluid incubation step (1−10) are highlighted.
e. A top view of the serpentine channel microfluidic device design overlaid with a low magnification field of view of final stained and monitored area of cells. Inlets and outlets are labeled as in panel b.
f. A magnified area of cells from panel e in three microfluidic channels. Green, phalloidin staining of actin; and blue, Hoechst staining of nuclei.
g. A magnified area of cells from panel f showing aligned actin filaments and nuclei in a segment of one microfluidic channel.

89

Methods & Materials

Robotic system components

Two stepper motors (NEMA-17) set the x- and y-position of the multiwell plate holder, using two position limit switches to define the origin, and a servo sets the vertical z-position of inlet tubing. All actuators were controlled by an Arduino Uno R3 with two stacked motor shields (DC Motor Stepper and Servo Shield, Adafruit). The plate holder attached to a linear bearing slide rail for y-motion, which in turn traveled along two parallel V-slot linear rails (OpenBuilds) for x-motion (**Fig. 15a**, Supplementary Fig. S1). The custom multiwell plate holder was constructed from 3D-printed ABS plastic, or from aluminum to prevent sagging of a full, deep-well 96-well plate, >200 g. The inlet tube moved vertically by a servo assembly comprised of an aluminum or ABS servo mount, a servo arm, and an aluminum linkage connecting the arm to a plastic block that slides along two parallel rods. A section of hollow aluminum tubing mounted to the slider block allows insertion of replaceable Teflon inlet tubing, with a small threaded hole and set screw in the slider block securely holding the tubing in place. The inlet tubing, cut at a steep angle (~45°) at the tip, can reliably puncture a thin plastic film sealing each well on the multiwell plate (Glad Press'n Seal). A complete online computer aided design (CAD, SolidWorks 2016) of the robot is available on GitHub (albrechtLab).

C. elegans maintenance

The integrated *C. elegans* strain NZ1091 was developed by irradiation of CX16573[24] and backcrossed at least 10X. Animals were grown and maintained at 20 °C on Nematode Growth Medium (NGM) plates with OP50 *E. coli* bacteria (Brenner, 1974). For the dose response

experiment, *C. elegans* were selected as L4s the day before and tested as young adults the next day. For the chemical screen experiment, L4-stage *C. elegans* were picked and transferred to 50 µM All Trans Retinal (ATR) in OP50 *E. coli*spotted (150 µL) onto an unseeded 60 mm NGM plate 12 hrs prior to experimentation. The following strains were used:

NZ1091, kyIs587 [gpa-6p::GCaMP2.2b; unc-122p::dsRed]; kyIs5662 [odr-

7p::Chrimson:SL2:mCherry; elt-2p::mCherry], expressing GCaMP and Chrimson in

AWA neurons,

CX14887, *kyIs587* [*gpa-6*p::*GCaMP2.2b*; *unc-122*p::*dsRed*], expressing GCaMP in AWA

neurons,

CX10979, *kyEx2865* [*sra-6*p::*GCaMP3*; *unc-122*p::*GFP*], expressing GCaMP in ASH neurons.

Experimental control and automation

A suite of Arduino and MicroManager scripts automate experimental timing, serial liquid delivery patterns, stimulation controls, and image acquisition. A MicroManager graphical user interface (GUI) script enables user configuration of camera and illumination settings (exposure time, illumination pulse duration and delay, and image binning), multiwell plate positions, and timing of stimuli (Supplementary Fig. S2). These settings are transmitted *via* serial commands to two Arduino Uno microcontroller boards (**Fig. 15b**, Supplementary Fig. S2), one controlling the multiwell plate position and a second (Nobska Imaging) that sends digital pulses to control illumination and stimulation (e.g. microfluidic valves, optogenetic LED pulses, or others). With this setup, the same experiment settings (recording and stimulation) can be executed repeatedly for each well position. The robotic system can also function independently through customizable Arduino, MATLAB, or MicroManager code suites.

An Arduino program loaded on the robotic controller defines the well plate positions, motor steps per position, servo arm range, and timing of movement. Different settings allow adjustment to other well configurations (6- to 384-well plates) and plate depths (5 to 30 mm, or 300 μL to 2 mL for a 96-well plate). In its typical configuration, the Arduino code reads in serial command strings to control the plate position and tubing position (servo arm). For example, the 'homed' state (command: '0') raises the servo arm and sets the plate to well A1. The command syntax is [*wellRow*][*wellColumn*][*+ or −*], which raises the servo arm, sends the plate to the specified well, and either keeps the servo up (+) or lowers it down (−) at the final position. Commands can be strung together with a semicolon delimiter for immediate sequential execution. For example, the string 'A1-;A2-' moves the plate to well A1, lowers the servo arm and tubing ('−'), then immediately raises it again, moves to well A2, and lowers the tubing once again. The system remains in this configuration until another serial command is received (Supplementary Video S1).

For repetitive multiwell microscopy applications, two Micromanager scripts *GUI* and *RUN* can be used to coordinate robotic plate and tubing positions with fluidic valves, stimulation, and microscope image capture. *GUI* sets up the experiment parameters, and *RUN* executes them (Supplementary Fig. S2). A third script, *ROBOT*, offers manual control of multiwell plate position and valve states and can also initiate a sequence of well positions with independent durations per well (Supplementary Fig. S2). The *GUI* and *RUN* scripts were used for neural imaging (**Figs. 15-18**) and *ROBOT* for the cell staining procedure (**Fig. 19**). These scripts can be

configured to save time-stamped images and all settings metadata in a text file for automation of data analysis.

Alternatively, any program that sends serial commands can control the robotic system. For example, a MATLAB script automatically generates and transmits commands to move the plate from one well to another in a zigzag "snake" or "typewriter" pattern. Together, the Arduino code allows for fine adjustments to the robotic system, such as to configure different plate sizes and volumes, whereas MicroManager or MATLAB scripts define the sequences of well positions, timing for each experimental protocol, and data acquisition parameters. All software is available online at GitHub (albrechtLab).

Bubble-free well-to-well transfer of inlet tubing

A backpressure reservoir connected to the microfluidic device applies a small positive hydrostatic pressure relative to the multiwell plate by elevating its fluid surface a few centimeters above the fluid surfaces in the plate. During well position switching, the outflow valve is closed and the backpressure valve is opened (**Fig. 15c**). The backpressure is adjusted by raising or lowering the bp reservoir such that no bubble enters the inlet tubing (bp too low) and no droplet forms at the inlet tubing (bp too high), which could transfer a small amount fluid to the next well (**Fig. 15d**). Once the robotic system positions the inlet tube into the next well, the backpressure valve is quickly closed, the outflow valve is opened, and the next fluid begins to fill the robotic inlet tubing and flow through the microfluidic device (**Fig. 15c, e**, Supplementary Fig. S3).

93

Microfluidic device preparation

Single layer silicon master molds were designed using DraftSight and fabricated in the WPI MicroFabrication Laboratory cleanroom. Microfluidic devices were prepared from PDMS (Sylgard 184) and sealed reversibly to hydrophobic glass or permanently bonded, as previously described (Lagoy and Albrecht, 2015). Devices were permanently-bonded to standard 1 mm thick glass slides for carryover and *in vitro* experiments, and reversibly-sealed to fluorinated glass slides for *C. elegans* neural response experiments. Device designs are available by request.

Assessment of well-to-well carryover using fluorescent dye

A medium-depth 96-multiwell plate was prepared with 600 µL of water or 5 µg/mL fluorescein in alternating wells following a zigzag "snake" pattern and positioned on the robotic plate holder (**Fig. 15f**). A bonded microfluidic device with three ports was connected to inlet (in), backpressure (bp), and outlet (out) tubes, and flow was balanced by adjusting the height of the backpressure reservoir as described above. The inlet tubing was filled backwards by raising the buffer reservoir above the multiwell plate before rebalancing backpressure and inserting it into the first well. TIFF stack movies were acquired with a Hammamatsu Orca Flash 4 sCMOS camera and a 4×/0.28 NA Olympus objective mounted on an ASI RAMM microscope frame. Videos were recorded for 15 seconds per well at 10 fps with 2 × 2 binning and a 10 ms pulse of blue light (EGFP filter set, 470 nm excitation) from a Lumencor SOLA source that illuminated the fluorescein solution for each captured image frame. A 30 s fill delay was used between well switching. Mean integrated intensity was determined using ImageJ for each well in a

25 × 25 pixel region of interest at the convergence of microfluidic inlet channels, averaging the first, middle, and last frames per well to reduce noise. MATLAB was used to calculate carryover percent using these values by subtracting camera baseline (intensity of A1) from all values, then dividing the average baseline-corrected water well intensity by the immediately previous fluorescein well intensity (**Fig. 15g, h**).

To assess carryover with washing, a deep 96 well plate was prepared with 2 mL of water in each well and 2 mL of 5 µg/mL fluorescein in well A2. Data acquisition and analysis were performed as above.

Calcium imaging, optogenetic stimulation, and data analysis

Calcium imaging was performed as previously described (Larsch et al., 2013). Microfluidic neural imaging devices were modified for 4X magnification (~2.5 mm arena size) and contained one or two physically-separated arenas (**Figs. 16, 18** and **17**, respectively). Devices quickly switch the chemical environment between a stimulus inlet stream and a buffer inlet stream by opening one of two control inlets (Supplementary Video S2, **Fig. 16b**). Fluorescence microscopy was performed using an ASI RAMM microscope as described above and configured for low-magnification wide-field imaging of GCaMP fluorescence. For optogenetic activation of the Chrimson cation channel, a 617 nm 3 W LED (Mightex) was mounted beneath the RAMM stage, filtered with a 645/75 nm bandpass excitation filter, and reflected to the objective with a 590 SP dichroic which also passed green GCaMP emission light to the camera (**Fig. 17a**). For all calcium imaging experiments, neuron fluorescence was quantified using the NeuroTracker

ImageJ macro with a 6×6-pixel square for calculating integrated intensity, and custom MATLAB scripts for data aggregation, analysis and visualization. Contrast of wide-field images containing animals in the device was auto-adjusted for image print clarity using ImageJ in **Figs. 16d** and **17b**.

Statistical comparisons

IBM SPSS was used for statistical tests, and significant suppressors of neural activity (**Fig. 17d, e**) were determined using a general linear model repeated measures analysis of variance (ANOVA). Significant p-values were selected based on solvent concentrations compared to immediately prior buffer control and noted in the figure after Bonferroni's correction for multiple comparisons ($*p < 0.001$, **Fig. 17e**). Treatment effects were also assessed by one sample paired t-tests comparing the solvent response peaks minus prior buffer control peaks to a fixed zero value (no effect), yielding similar results after Bonferroni's correction ($*p < 0.001$, **Fig. 17f**).

Odor step-response in multiple C. elegans sensory neurons

Diacetyl (2,3-butanedione, Sigma) odor dilutions were prepared on the day of the experiment beginning with a 30 mL 1:1000 (10^{-3}, 11.5 mM) dilution vortexed for 1 min in paralysis buffer (S. Basal buffer without cholesterol containing 1 mM acetylcholine agonist ($-$)-tetramisole hydrochloride). Serial dilutions were prepared in 10-fold steps until 11.5 nM (10^{-9}) in a deep 2 mL glass-coated 96-well plate (WebSeal Plate+) and sealed with adhesive film (Glad Press'n Seal) (**Fig. 16a**). About twenty animals of each genotype were loaded into separate arenas and exposed for 1 hr to paralysis buffer from the buffer reservoir (**Fig. 16d**). During exposure, both

buffer and outlet valves were open, and the odor stimulus inlet tubing was blocked. After animals were immobilized, tubing was inserted into the inlet port and allowed to fill backwards by raising the buffer reservoirs above the multiwell plate to elevate backpressure (>bp, **Fig. 15d**), then returned to the balanced position (=bp). The multiwell plate was moved to position A1, and flow patterns were checked for a proper step-change stimulus by control fluorescein dye buffer pulses. Calcium imaging was performed as described above, and automated acquisition began after negative control conditions (paralysis buffer containing 100 ng/mL fluorescein) were verified to show no neural response. At each well position, animals were exposed to buffer during the programmed 45 s fill delay, then presented with four 10 s odor pulses, once per minute. Image stacks were acquired for 30 s for each odor pulse at 10 fps with 10 ms blue light excitation pulse and 2 × 2 binning. After the experiment, the glass-coated multiwell plates were washed for reuse by completely filling and rinsing with water 3X, soaking in ethanol overnight, then rinsing with water again 3X, and drying in a 65 °C oven. Inlet and outlet tubing were also reusable following a water rinse step immediately after experimentation.

Screen for solvent effects on in vivo C. elegans neural responses

Fourteen solvents were prepared in Eppendorf tubes at 1% and 5% v/v (or w/v for solids) concentrations in 1 mL paralysis buffer, vortexed for 1 min, and transferred to a medium-depth 96-multiwell plate (700 µL/well). Alternating control wells were filled with paralysis buffer (with 100 ng/mL fluorescein) to confirm baseline responses and visualize solution delivery (**Fig. 17a**). The 96-well plate was prepared 1 hr before recording and sealed with adhesive film (Glad Press'n Seal). During this time, animals were exposed to paralysis

buffer *via* the backpressure reservoir to keep them stationary during neural recording as described above. Animals were exposed to each solvent for <1 min total, including a 30 s fill delay that was programmed to sufficiently fill the tubing and microfluidic arena after each well transfer. After this delay, an immediate 15 s acquisition began at 10 fps, with 5 ms blue light (470 nm) excitation and 2×2 binning. A single 5 s red light activation stimulus (617 nm, 38 mW/cm^2) was presented from 2.5 to 7.5 s.

Microfluidic cell culture

Human mesenchymal stem cells (hMSCs, P7-P8) were grown to confluency at 37 °C with 5% CO_2 in standard growth medium (hMSCgm bullet kit, Ionza). The cells were washed, trypsinized, centrifuged, and re-suspended with fresh growth media to approximately 5×10^6 cells/mL. A cleaned and bonded PDMS device, containing a long serpentine channel, was prepared by baking at 65 °C for ~2 hrs and degassing in a vacuum desiccator for 15 min. Next, a drop of growth medium was placed over the inlet and drawn into the microfluidic channel by a hand-held pipette inserted into the outlet (**Fig. 19a**). The cell suspension was then drawn through the device in the same manner, and the device was placed in an incubator to settle and attach to the glass surface overnight. The next day, the cell-loaded device was placed on the microscope stage (at room temperature) and connected to all tubing inlets and outlets as previously described (**Fig. 19b**). The backpressure phosphate-buffered saline (PBS) solution was used to fill the robotic inlet tubing by gravity driven flow as described above before lowering it into the first multiwell plate position.

Automated cell fixation and staining

Staining solutions were prepared in PBS at 2 mL final volumes and loaded into the first 10 wells (A1-A10) of a deep (2 mL) 96-well plate (WebSeal Plate+). The solutions were 4% w/v paraformaldehyde (PFA), 0.25% v/v Triton X-100, 1% w/v bovine serum albumin (BSA), 2.5% v/v Alexa Fluor 488 (AF488) phalloidin (ThermoFisher A12379), and 0.0167% v/v Hoechst 33342 (**Fig. 19c**). At each well position, a 30 s delay was programmed to sufficiently switch from one inlet solution to the next. The staining procedure was performed in the following sequence: 30 s PBS wash, 10 min fixation in 4% PFA, 30 s PBS wash, 10 min permeabilization in 0.25% Triton X-100, 30 s PBS wash, 30 min blocking in 1% BSA, 30 min f-actin staining with 2.5% AF488 phalloidin, 30 s PBS wash, 3 min nuclear counterstain with 0.0167% Hoechst, and a final 30 s wash in PBS. A TIFF image stack of the device channels with cells was recorded at 1 frame per minute for 90 min throughout the automated staining protocol using a pulse of blue light during each acquisition (Supplementary Video S3). ImageJ was used to quantify change in green fluorescence across all 90 frames of one representative microfluidic channel (**Fig. 19d**). After staining, cells were sealed to prevent drying by applying Cytoseal to all inlets and outlets and stored at 4 °C. After staining, higher magnification images of the stained cells were obtained on an inverted Leica fluorescent microscope with FITC and DAPI filtered images overlaid using ImageJ (**Fig. 19e-g**). Contrast was auto-adjusted for image print clarity using ImageJ (**Fig. 19f-g**). The remaining staining solutions in the multiwell plate could be reused multiple times when stored at 4 °C and sealed.

Discussion

The robotic system described in this paper automates sequential delivery of different fluids from multiwell plates to microfluidic devices. Multiwell plates are easily filled manually or by liquid-handling robots, such as for large-scale screens using commercially-prepared compound libraries. After microfluidic device set-up and multiwell plate preparation, complete automation of liquid transfer spares laborious manual effort and eliminates user error, especially for large chemical screens and protocols that require multiple steps. The modular system mounts on a microscope stage for optical monitoring of the microfluidic device throughout the experiment. A custom graphical user interface provides flexibility in protocol design and timing of each chemical presentation, while automatically-generated protocol files can be saved for exact replication of complex experiments. Additionally, the robotic system is compatible with other multiwell plate formats for increased throughput (384 wells, 225 μL capacity), or longer flow durations (e.g., 48 well, 5 mL capacity; 24 wells, 10 mL capacity; 6 wells, 16.8 mL capacity).

Our robotic system compares favorably with other liquid-delivery strategies, outlined in **Table 1**. Rotational distribution valves can interface with large fluid reservoirs and are small enough to mount on a microscope stage, but are limited to 8 or 12 different inlet positions. Autosampling robots can draw liquids from large multiwell plates, but their fluid delivery is limited to the typically small volume contained within the injection needle or syringe. Compared with these commercial devices, the robotic system presented here delivered larger

volumes at faster flowrates, achieved a similarly low carryover percentage with wash steps

(<0.02%), and could be mounted on a microscope, at substantially lower cost.

Table 1. Comparison of liquid delivery systems from multiple wells or reservoirs to microfluidic devices.
Some values are not reported (n.r.) or not determined (n.d.). Mechanical switch time refers to the transfer of tubing, needle, syringe, or rotation of a valve. Fluid switch time refers to the exchange of liquid within the microfluidic device.

	Our Robotic System	**Rotary Valve**[1] (Hamilton MVP)	**HPLC Autosampler**[2] (UltiMate 3000)	**Autosampler**[3] (Aurora AS100)
Liquid delivery technique	Inlet tubing transfer	Rotary valve	Needle/syringe injection	Needle/syringe injection
Number of reservoirs	Up to 384	Up to 8 or 12	>384	Up to 1536
Reservoir volume	225 µL (384 well) 2.2 mL (96 well) 16.8 mL (6 well)	~1 mL – >1 L	10 nL – 125 µL	100 nL – 1 mL
Mechanical switch time	~2 s	~0.4 s	n.r.	n.r.
Fluid switch time (in device, at 2 µL/s)	~30 s	~30 s	not possible (max 0.03 µL/s)	n.d.
Carryover*	<0.02%	n.d.	<0.02%	n.r.
Approximate cost	<$500	$1,300	>$8,500**	$12,000
Format and size (h x w x d)	Fits on microscope stage, 19x45x31 cm³	Small unit, 10x6x10 cm³	Large frame, 36x42x51 cm³	Large frame, 16x52x58 cm³
References (use with microfluidic devices)	this work	(Larsch et al., 2013, 2015)		(Bazopoulou et al., 2017)

Notes:
 * Carryover estimate by measurement of caffeine (UltiMate 3000) or fluorescein dye (our robotic system).
 ** Cost reported for a used unit.

Instrument references:
 [1]Rotary Valve, Hamilton Company Serial Modular Valve Positioner (MVP). *OEM Liquid Handling Components*. Valve Positioner. Retrieved from: https://www.hamiltoncompany.com/products/liquid-handling-components/valve-positioner/serial-mvp on March 16, 2018.
 [2]HPLC Autosampler, Thermo Scientific Dionex UltiMate 3000 RSLCnano System. *Product Specifications*. Key Autosampler Specifications. pg. 6. Retrieved from: https://assets.thermofisher.com/TFS-Assets/CMD/Specification-Sheets/PS-70195-LC-Dionex-UltiMate-3000-RSLCnano-PS70195-EN.pdf on March 16, 2018.
 [3]Autosampler, Aurora Universal XYZ Autosampler. OEM Components. Retrieved from: http://www.aurorabiomed.com/wp-content/uploads/2014/02/OEM-autosampler.pdf on March 16, 2018.

For this system, the backpressure design is key to preventing the introduction of air bubbles, which can disrupt microfluidic flow, as the inlet tube is moved from one well to another. Balanced backpressure is readily achieved by raising or lowering a separate inlet reservoir until no air is drawn into the raised inlet tube and no droplet emerges. To implement this strategy, microfluidic devices need at least two inlets, one for drawing liquids from the multiwell plate and another to provide backpressure. Devices that already include multiple inlets need no additional backpressure inlets, such as the neural dose response experiment (**Fig. 16**), which contained a buffer reservoir that provided sufficient backpressure. While each example here used gravity-driven flow by hydrostatic pressure, the backpressure system is also compatible with vacuum or syringe-pump flow control applied from the outlet tubing.

Reliable fluid switching occurred across all wells of a 96-well plate with an average well-to-well liquid dye carryover of about 0.3% using a fill delay of 30 s, corresponding to about 5 inlet tube volumes. While sufficiently low for most experiments, carryover may be lowered further by increasing the fill delay time, increasing flow rate, or both. Adding wash steps further reduced carryover by an order of magnitude, to the level of commercial autosamplers. However, these changes may reduce overall experimental throughput by slowing fluid transitions, by lowering the available flow time per well, or reducing the number of available fluid wells per plate. For standard lab experiments, we found that the Teflon inlet tubing and glass-coated multiwell plates could be cleaned and reused repeatedly. However, particularly hydrophobic chemicals or sensitive assays may warrant the replacement of all tubing and

programming of wash steps, the use of immiscible carrier fluids, and/or extended fill delay times.

We demonstrated three types of automated experiments, each using different microfluidic device designs and different stimulation approaches, and each resulting in increased throughput and decreased manual effort. First, we measured step responses to concentrations of the odor diacetyl across six orders of magnitude in two sensory neuron types from ~40 living *C. elegans* in a single experiment, resulting in 1,152 neural calcium traces. In one experiment, our assay replicated previous results from several manual neural imaging assays (Larsch et al., 2013; Taniguchi et al., 2014; Yoshida et al., 2012), showing that at high odor concentrations above ~1 mM diacetyl, attractive AWA sensory neurons and aversive ASH neurons are simultaneously active. Since diacetyl elicits attractive behavior at moderate concentrations and aversive behavior at high concentrations, ASH signals appear to dominate the behavioral response. However, because ASH neural responses adapt rapidly while AWA responses are consistent, chemotaxis behavior is expected to be transiently aversive. Our results also revealed a negative correlation between ASH activity and AWA peak response magnitude not reported previously, suggestive of negative circuit feedback from ASH to AWA *via* indirect synaptic connectivity between these neurons. This example demonstrates the ability to pulse multiple chemicals in sequence for precisely-controlled durations, as might be required for large-scale chemical stimulation experiments.

Next, we screened a panel of commonly-used solvents and carriers for their effects on stimulated responses in sensory neurons. Most chemical libraries are stored in solvents such as DMSO for solubility and chemical stability, while some show acute suppressive effects on neurons (Lotfullina and Khazipov, 2017) and chronic exposure can lead to abnormal organism development (Maes et al., 2012). In our assay, even brief <1 min exposures of 1% and 5% methanol, isopropanol, and acetonitrile suppressed optogenetically-activated neural activity, as did 5% ethanol. Although acute solvent effects were transient, these results suggest that careful selection of solvents is prudent when screening drug libraries for neural effects. Since activation and neural response were in the same neurons, this observed suppression reflects intracellular interference by these solvents. Equally interesting would be the identification of solvent effects on synaptic communication, by monitoring post-synaptic neuron responses to pre-synaptic stimulation, and evaluating any differences in solvent sensitivity across neural (or other) cell types.

Lastly, we automated an 85 min ten-step cell staining protocol, in which each sequential chemical exposure step lasted a different duration, from 30 s to 30 mins. With a 2 mL deep 96-well plate and a typical flow rate of 2 µL/s, continuous flow lasts about 17 min per well. To achieve longer incubations, flow was paused by closing the outflow and backpressure valves, allowing for unlimited incubation duration and reduced reagent use. Alternatively, if continuous flow was necessary, the inlet could be moved to additional wells containing the same fluid. Notably, the robotic system was effective with a variety of solutions with different physical properties such as surface tension and viscosity (e.g. Triton X-100 and BSA). Further,

several important applications would be enabled by automated cell culture and sample processing as shown here. For example, immunohistochemistry with new antibodies typically requires optimization of multiple staining solution concentrations and times, including primary and secondary antibodies and blocking solutions. By automating the staining procedure and live monitoring of imaging results, protocols could be quickly optimized for maximum label specificity and contrast. Additional cell culture applications include the automatic passaging of cells, by timed exposure to buffer, trypsin, and culture medium, or the sorting and collection of specific cell types using additional outflow valves and sample collection tubes.

Together, these practical examples demonstrate the functionality and versatility of our inexpensive, open-source, and customizable platform for interfacing multiwell plates with microfluidic devices. While complex systems exist to introduce multiwell plate fluids though numerous parallel tubes to microfluidic sample chambers (Gómez-Sjöberg et al., 2007), automated serial delivery has the additional advantage of enabling the tracking of individual animal (or cell) responses across many compounds, yielding greater reliability and experimental sensitivity (Larsch et al., 2013). By automating experimental protocols with systems as presented here, the scientific bottleneck shifts to data analysis, and similar advances in automated data analysis and visualization techniques will be useful for rapid data-driven exploration, protocol optimization, and scientific discovery.

The new technology developed in this Chapter overcomes several limitations for functional compound screening in whole organisms. A previously developed high-throughput method for imaging neuronal activity in *C. elegans* keeps animals stationary during recording, which was reasoned to be required for proper quantification of calcium signals in many animals at once. Furthermore, this established microfluidic-based approach offers the ability to deliver a many solutions to animals sequentially. However, automating the delivery of compounds to biological samples in microfluidic devices posed a technical challenge. Therefore, the robotic platform described above overcomes this prior limitation, enabling short-term (seconds-minutes) exposure of compounds to animals while monitoring light-evoked calcium responses *in vivo*. Altogether, this approach enables sample immobilization, automated delivery of compounds to cells or organisms, and a functional approach for screening modulators of calcium activity. However, this method may not be suitable for screening compounds that slowly reach target sites in neurons, or require longer incubation periods to take effect. Therefore, the development of an automated large-scale method that enables long-term (hours) immobilization of whole organisms during compound exposure is needed, which I present in Chapter 4.

Chapter 4 Develop and characterize a screening method to identify compounds that modulate neural activity *in vivo* over long-term durations

Abstract

High-throughput and high-content screening (HTS and HCS, respectively) technologies are useful approaches for automatically surveying and identifying compounds that have an effect on bioactivity. Selecting the most appropriate type of screening technology depends on the sample type (cells or organisms) and relevant biological activity of interest. Human disease model cell types and whole organisms are becoming more popular in HTS and HCS for direct detection of compound effects on cellular phenotypes, organism behavior, or expression of fluorescent reporters. To screen compounds against dynamic phenotypes, like changes in intracellular calcium activity, few disease models and technologies exist and this type of screen is technically challenging for whole organisms, but it poses rewarding outcomes. Therefore, we developed a new cost-effective and open-sourced functional screening technology to identify modulators of calcium activity within whole organisms over tractable and long-term durations (>24 hrs). We used this technology to screen 640 FDA approved compounds to identify modulators of optogenetically-evoked neural activity in *C. elegans*. Of the nine primary hits, we identified felodipine and ivermectin with increasingly potent suppressive effects, as both likely direct and indirect regulators of stimulated calcium activity, respectively. We anticipate that this new dynamic high-throughput and high-content functional screening technology for whole organisms will accelerate the discovery of cellular activity modulators for the treatment of activity dependent human disorders.

Introduction

Detecting changes in cellular activity from compound exposure could elucidate novel molecular mechanisms and accelerate the discovery of treatments for activity-dependent disorders, like autism spectrum disorder, schizophrenia, and neuropathic pain (Haggarty et al., 2016; Molokanova et al., 2017). Current high-throughput screening technologies have focused primarily on the identification of compounds that affect static phenotypes (i.e. size, shape, movement) or static changes in fluorescent signals (i.e. GFP brightness) in individual populations of cells or whole organisms (Burns et al., 2006b; Kwok et al., 2006; Mondal et al., 2016; Parker et al., 2000). Meanwhile, other compound screening platforms have enabled the observation of more kinetic phenotypes, like changes in stimulated fluorescent dye signal within individual cells stimulated by perfusion techniques in the presence of various compounds (Schroeder and Neagle, 1996; Stacey et al., 2018; Virdee et al., 2017). Functional screening assays of this type enable more direct identification of compounds that affect dynamic disease-causing phenotypes, which are hallmarks of many neurological disorders (Ebert and Greenberg, 2013).

All current functional screening assays have been developed for *in vitro* culture conditions to assess the effects of compounds on cellular activity using perfusion-based stimulation. Biologically relevant cell types, like human induced pluripotent stem cells (hiPSCs), that directly mimic human disease are becoming popular for *in vitro* high-throughput functional screening provided by recent improvements in differentiation and viability at large scales (Efthymiou et al., 2014; Stacey et al., 2018). Additionally, applying compound treatments to cells in culture is straightforward, allow for direct access to the cell membrane and intracellular proteins. However,

110

challenges pertaining to maintenance and propagation of hiPSCs *in vitro* have not been completely overcome, while other biological limitations to this approach include high costs, low reproducibility, and poor assessment of off target compound effects. Also, techniques that could improve stimulation efficiency, preciseness, and throughput are not yet directly compatible at the necessary scale or have not yet been explored, like optogenetics (Molokanova et al., 2017). Therefore, additional biologically relevant samples should be further investigated that might overcome these intrinsic limitations for functional compound screening approaches.

Other biological systems overcome some of the limitations posed by *in vitro* functional screening, specifically the ease of culture, scale, and common functional imaging techniques. Screening for compounds that modulate cellular activity in whole organisms, like *C. elegans*, are an ideal approach to identify more specific drug targets, which also provides a direct translational platform for investigating mechanisms of action and genetic targets. Recent whole-animal screening technologies and methods have overcome immobilization and automation challenges (Lagoy and Albrecht, 2018; Mondal et al., 2016), but are not directly compatible with functional imaging methods or long-term incubation in chemicals, which might be required for whole-animal screens due to indirect drug access *in vivo* (Kinser and Pincus, 2017). Therefore, new simple methods that provide rapid immobilization of whole organisms, like hydrogels, can be scaled and adapted to conventional multiwell plate screening formats to serve multiple critical functions, (1) keeping animals stationary during functional imaging, and (2) passive diffusion of chemical compounds to animals over long-periods of time (Burnett et al., 2017; Dong et al., 2018).

Here, we propose a simple, versatile, and fully automated high-throughput method for screening compounds that modulate stimulated calcium activity in immobilized whole organisms over long durations. This method utilizes a rapid photo-crosslinking hydrogel that keeps animals healthy and stationary without paralytics for over 24 hours, compatible with functional calcium imaging (Burnett et al., 2017). The adaptability of the hydrogel and geometry of 384 well plates allows for simultaneous recording of ~40 embedded animals in each well, each expressing the genetically encoded calcium sensor, GCaMP, and red-shifted channelrhodposin, Chrimson, in a single neuron for dual recording and light-induced stimulation, respectively (Burnett et al., 2017; Klapoetke et al., 2014; Larsch et al., 2015). Further, this method is based on open-sourced experimental control and analysis platforms to enable rapid adaptability at economically increased scales.

We employed this method to screen 640 FDA-approved compounds and 128 controls across a genetically identical and age-synchronized population of living *C. elegans*. Using the same immobilization and screening methods, we also identified a time- and dose-dependent threshold of All-*Trans* Retinal (ATR) activity in *C. elegans*, as ATR is an essential chromophore for optogenetic experiments. Altogether, we expect that this simple and versatile method will expand the current and future possibilities for functional compound screening in biologically relevant samples to identify modulators of cellular activity with to directly investigate genetic targets and pathology.

Results

Animal distribution, immobilization, and calcium responses in 384 well plates

To screen for compounds that modulate optogenetically-evoked calcium activity in *C. elegans*, a hydrogel crosslinking procedure (Burnett et al., 2017) was adapted for encapsulation and immobilization of ~17,000 age synchronized animals at ~40 animals per well in high-content 384 well plates (**Fig. 20**). A scaled plate-based synchronization (Stiernagle, 2006) and pre-treatment of animals with All-*Trans* Retinal (ATR) protocol (Lagoy and Albrecht, 2018) was developed and modified to obtain ~17,000 ATR treated age-synchronized young adult animals in about two days (**Fig. 20a**). A liquid suspension of these animals are transferred to the multiwell plate (manually or robotically), settled to the bottom by cooling, and then all completely immobilized in less than one minute (**Fig. 20a**). The remaining 80% of the well volume can be filled with buffer or compounds at a desired concentration for all wells containing the immobilized and embedded animals (**Fig. 20a**). An automated x-y stage and custom control scripts allow for programmed screening with customized optics for dual GCaMP and Chrimson recording of animals in one well at a time (**Fig. 20b**). For all experiments described here, animals co-express GCaMP and Chrimson in the AWA chemosensory neuron as developed previously (**Fig. 20c-d**) (Lagoy and Albrecht, 2018). The distribution of animal transfer was uniform across the entire multiwell plate, with 44 animals per well on average ($\pm$ 13) (**Fig. 20d-e**). From one well containing 41 animals, a consistent red-light activated response was recorded for all individuals and an average $\Delta F/F_0$ calcium trace was calculated (**Fig. 20f**). The scale of this procedure can be adapted for different numbers of wells, treatments, and replicates per experiment.
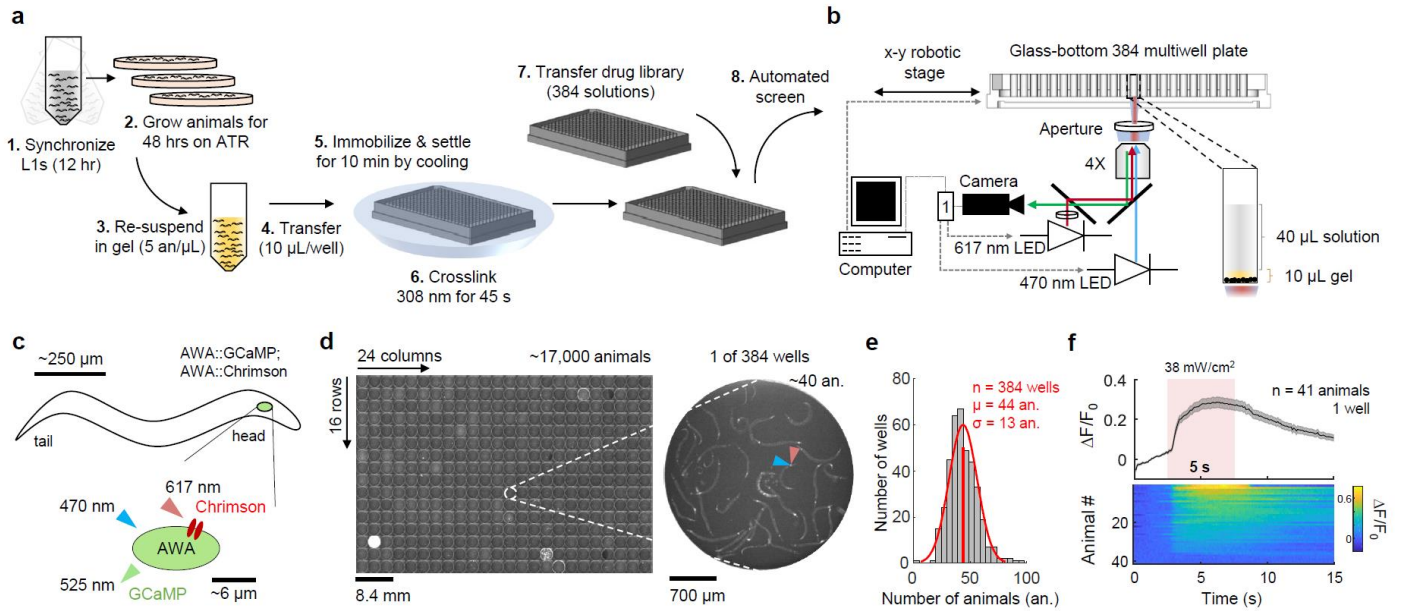
Figure 20. Method overview for automated long-term high-content screening of functional cellular activity in C. elegans.

a. Schematic of the procedure for synchronizing animals, re-suspending in gel, transferring to a 384 well plate to add compounds for automated screening.

b. The custom microscope hardware and configuration for optical recording and stimulation of individual wells containing animals. Zoom-out shows one well out of 384 that contains 20% gel with animals (10 μL), and 80% compound (40 μL).

c. Illustration of animals used for functional screening. Zoom-out shows excitation and emission wavelengths corresponding to b. Animals co-express integrated versions of Chrimson and GCaMP in the AWA chemosensory neuron.

d. A full-resolution image stitch of a 384 well plate after preparation described in a. Magnified zoom-out shows ~40 animals in a single well with excitation wavelengths (blue and red arrows) pointing at the AWA neuron of one animal.

e. Histogram distribution and normal fit of animals per well in a prepared 384 well plate shown in d. Average number of animals in each well of a 384 well plate is 44 ± 13 animals.

f. Average ΔF/F$_0$ calcium response trace of 41 wild-type animals described in c immobilized in one well, as shown in d (right). Red shading indicates light pulse stimulus. Shading represents SEM. Individual animal traces are represented on each line of the heat map below sorted in descending order by peak ΔF/F$_0$ response during stimulation.

114

Experimental control structure and data acquisition

After animal synchronization and initial plate set-up, the entire screening experiment functioned autonomously for hours to monitor up to 67,000 or more individual calcium response traces, using open-sourced software and hardware (**Fig. 21**). Two new scripts, *GUI* and *SCREEN*, were developed in MicroManager to input user-desired experimental settings and to execute them, respectively (**Fig. 21a-c**). A previously established Arduino microcontroller and scripts were used to coordinate and synchronize timing of user-selected optical stimulation parameters, illumination settings, and image acquisition (**Fig. 21a**, Nobska Imaging) (Lagoy and Albrecht, 2018). Also, seven timing and stimulation parameters required initial user input to control parameters such as the duration of GCaMP recording per well, optical stimulus power, timing during recording, and number of stimulus repeats (**Fig. 21b, d**). The same sequence of stimulation and recording was repeated for all desired number of wells, with a programmed delay between stimulation, wells, and cycles. Finally, the *SCREEN* script executed the multiwell plate position and all experimental controls input by *GUI* (**Fig. 21c-d**). For each screen experiment, experimental settings and a logged history of plate position and timing data was saved for exact experimental replicates and meta-analysis (**Fig. 21e-f**). All camera acquisition sequences were also saved with date stamped indexed filenames for proper storage and streamlined analysis.
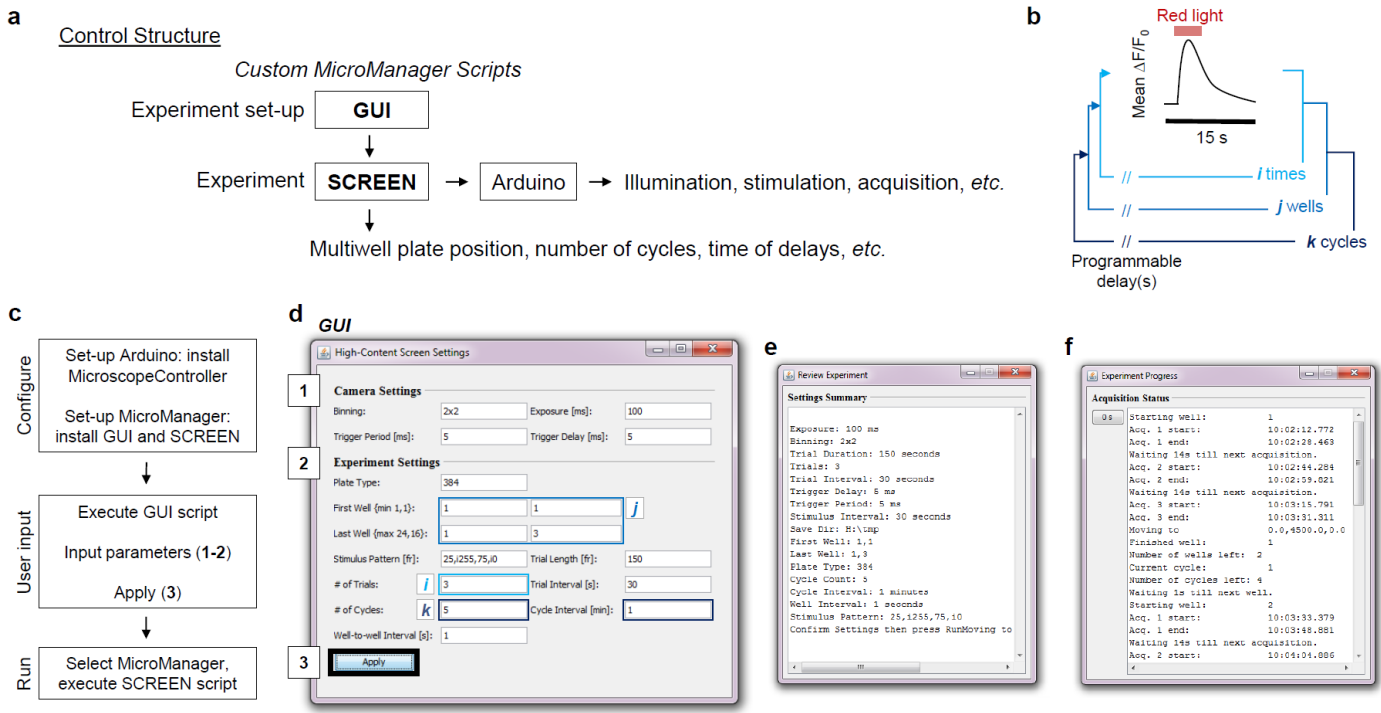
Figure 21. The custom open-source suite of MicroManager control scripts for user-defined automated experimental control.

a. Flow diagram outlining the control structure for experimental automation. Custom MicroManager scripts were developed for user input of experimental settings (GUI) before each execution (SCREEN). An Arduino microcontroller synchronizes timing of pulse stimulation and illumination, coordinated with camera execution, file saving, timing, and MicroManager x-y plate position control.

b. Each experiment requires user input of stimulus pulse length (red light duration), recording duration (15 s shown), number of repeat stimuli (i), wells to repeat (j), and well cycles to complete (k), each with programmable delay options.

c. Set-up sequence for first-time installation and execution of software. The first box shows requirements for software configuration, the second box outlines required steps for user input, and the third box describes experimental execution.

d. The *High-Content Screen Settings* GUI showing user determined (1) Camera Settings, (2) Experiment Settings, and the settings (3) Apply button. Colors correspond to control settings shown in b.

e. The *Review Experiment* window shows a preview of applied user determined variables, which is saved to the local drive experiment folder for direct experimental repeats and logged settings history.

f. The *Experiment Progress* window updates in real time throughout the experiment with current experimental parameters, like current plate position, cycle, well, *etc.* This metadata file is also saved to the experiment folder for logged history.

116

Fully- and semi-automatic analysis structure for processing all imaging data

Throughout each automated experimental duration, TIFF stacks were collected automatically using control software as described above (**Fig. 21**). Videos were stored, processed, and analyzed using either a semi-automated (blue arrow path) or completely automated method (black arrow path) with both increased data accuracy and slower analysis rate, or *vice versa*, respectively (**Fig. 22**). The semi-automated method employs a custom user-friendly ImageJ script that prompts manual selection of animal neuron positions (X,Y pixel coordinates), recorded per well and saved as separate TEXT files. The average time for manual and trained selection of neurons (at 40 animals/well) was up to ~20 wells/hour, requiring ~20 hours per 384 well plate. For automatic detection of neuron positions, an image subtraction-based method was used to gather the (X,Y) coordinate positions of neurons, or regions of the well plate that change fluorescence above a specific threshold that could be adjusted. Images were saved with auto-selected (X,Y) positions for user feedback and assessment of position quality. Once all neuron positions are recorded (manually or automatically) for each well, the position files were used to extract coordinates for automatic recording of quantification parameters (like integrated density, background intensity, *etc*.) and saved on a new line in a TEXT file for each frame of each video, for all videos per well, and all wells. Alternatively, a MATLAB script (in development, see *Future Applications*) could be used to extract additional information from each video across all frames to store all pixel values for each animal position in multiple multi-dimensional arrays. Following the blue arrow path, all processed videos were stored as TEXT files and read into MATLAB using tall tables and datastores for parallel processing, analysis, and visualization. The blue boxed flow diagram was used for all analysis in this Chapter.

Analysis Structure

384 well plate, 4 cycles, 15 s per well (10 fps), 44 animals/well

Manually select neuron positions

Experiment — Automatic data collection

Videos — MicroManager ~600 GB

Image subtraction for neuron auto-detection

Manual — Accuracy/Throughput — Automatic

High accuracy / Low-throughput

Lower accuracy / High-throughput

1-384

~ 20 hrs – 3 days (20 wells/hr)

t_{pulse} — t_0

neuronPos1-384.txt — < 1 hr

ImageJ — Processing — // — MATLAB

Import TIFFs & Pos — Import TIFFs & Pos

384 x 4 x 44 x 150
16x16

384 x 4 x

1024x1024x150 pixel values

~ 3 days — ~1 hr

Export TXT with IntDen — Load in as tall datastores — Analysis & Visualization (MATLAB) — Store InDen values in matrices

Figure 22. Flow diagram and structure of custom semi- and fully-automatic analysis software of high-content imaging data.

118

Illumination duration and All-Trans Retinal exposure methods effect baseline calcium activity

Before completing the small-molecule screen, several experimental conditions were evaluated regarding All-*Trans* Retinal exposure protocols and illumination settings (**Fig. 23-24**). Since *C. elegans* do not endogenously synthesize ATR, which is required for channelrhodopsin function (Nagel et al., 2005), the animals must be treated prior to (or during) experimentation to evoke optical responses. The treatment methods presented here enable the opportunity to soak animals in various ATR treatments, or pretreat animals on plates through development. Additionally, slight excitation spectral overlap between GCaMP and Chrimson requires specifically tuned optical properties to prevent stimulation of the Chrimson channel with blue (470 nm) light required for GCaMP monitoring. Therefore, both ATR treatment methods were examined, first with different illumination (trigger delay) settings (**Fig. 23**).

Two independent treatments of animals were either grown on 0.5 μM ATR NGM plates with food through development (48 hrs from L1 to adult age) then removed for testing, or three hours of soaking in 50 μM ATR and present through testing. Since the custom software suite enables user-desired input of illumination settings, only one parameter (trigger delay) was modified for three independent groups of each treatment (**Fig. 23a**). A trigger delay refers to the duration of the blue light pulse, while the trigger period refers to the interval of blue light pulses delivered. Both parameters are customizable to prevent photobleaching and phototoxicity, while enabling proper excitation for GCaMP emission signal. Since Chrimson activation overlaps with the blue light spectra, various trigger delay durations (2 ms, 5 ms, and 10 ms) were tested to reduce the

baseline calcium responses to various amounts of blue light without compromising signal-to-noise using a constant trigger period of 5 ms (**Fig. 23a**). One representative well of all 12 wells imaged contained ~50 animals (**Fig. 23b**). For the soaking condition, average ΔF and $\Delta F/F_0$ calcium responses showed the largest qualitative baseline response to 10 ms blue light excitation when compared to the 5 ms and 2 ms trigger delay settings, respectively (**Fig. 23c-f**). The same trend was also observed for animals grown on ATR through development (**Fig. 23g-j**). Relatedly, the signal-to-noise was largely proportional to trigger delay, yielding a higher average peak $\Delta F/F_0$ response for 10 ms, slightly lower for 5 ms, and 2 ms, respectively (**Fig. 23c, e, g, i**). It was also observed that the soaking condition caused a larger baseline response than animals pre-conditioned on plates (**Fig. 23c, e, g, i**). Therefore, this experiment yielded the selection of a trigger delay of 5 ms as most ideal for low baseline activation with little compromise to signal-to-noise and conserved ATR reagents.
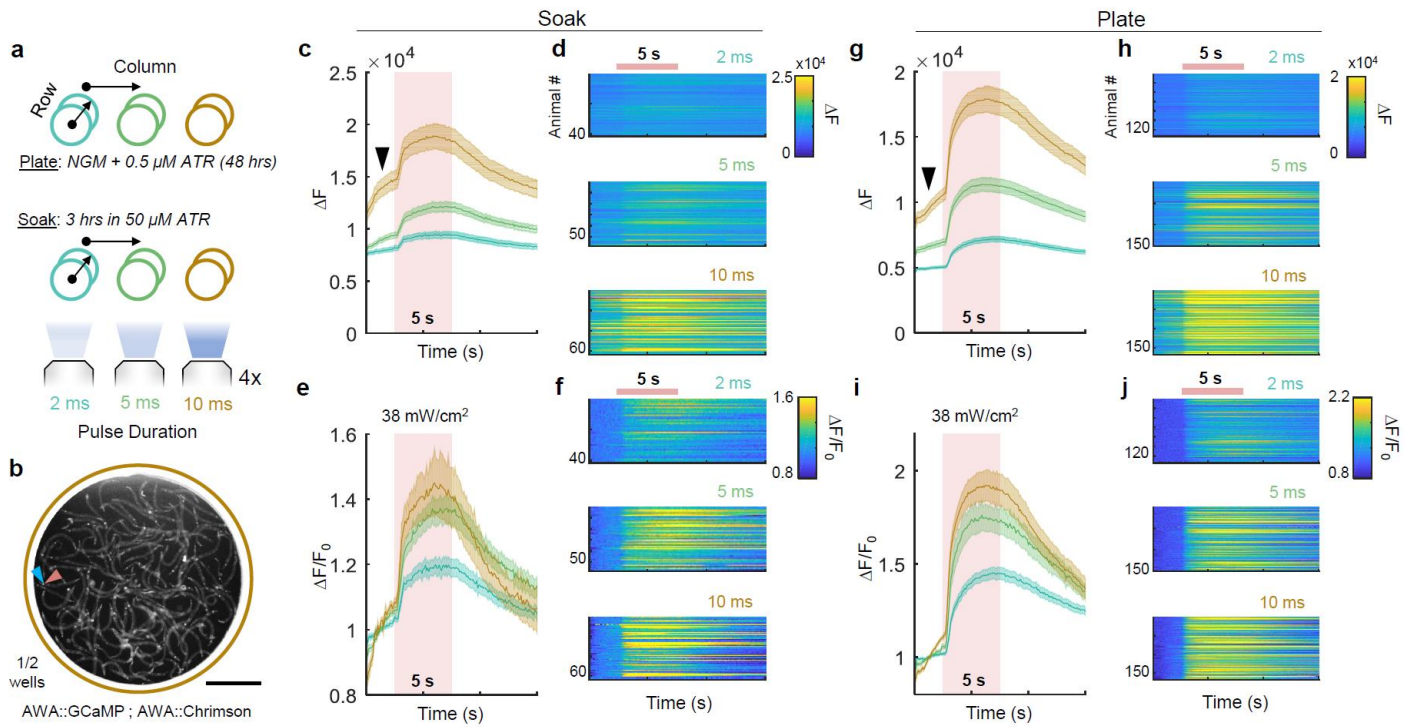
Figure 23. Characterization of All-Trans *Retinal exposure methods and effects from baseline excitation trigger delay.*

a. Multiwell plate set-up for one experiment with two well replicates (stacked circles) per trigger delay pattern (circle outline color, three different trigger delays). Animals were either raised on plates containing 0.5 µM ATR and removed for testing, or soaked in wells with 50 µM ATR for 3 hrs before testing. Semi-automated execution of data acquisition was used to deliver different trigger delays per column and treatment.

b. One representative well of immobilized animals in a well with 10 ms trigger delay. Excitation wavelength arrows point to one AWA neuron of ~50. Scale bar, 700 µm.

c. Average ΔF calcium response traces for both well replicates corresponding to column color of animals continuously soaking in 50 µM ATR for 3 hrs and throughout testing. Black arrow highlights initial response rise to longest blue light excitation trigger delay (10 ms). Shading represents SEM. Trace and shading colors correspond to trigger delay settings in a.

d. Heat maps show all individual traces from average ΔF calcium response traces from c.

e. Overlay of all average $\Delta F/F_0$ calcium response traces from c. Shading represents SEM.

f. Heat maps show all individual $\Delta F/F_0$ calcium response traces from e.

g. Average ΔF calcium response traces for both well replicates corresponding to column color of animals pre-treated on 0.5 µM ATR for 48 hrs and removed throughout testing. Black arrow highlights initial response rise to longest blue light excitation trigger delay (10 ms). Shading represents SEM. Trace and shading colors correspond to trigger delay settings in a.

h. Heat maps show all individual traces from average ΔF calcium response traces from g.

i. Overlay of all average $\Delta F/F_0$ calcium response traces from g. Shading represents SEM.

j. Heat maps show all individual $\Delta F/F_0$ calcium response traces from i.

Sensitivity of Chrimson activation is affected by ATR conditioning in C. elegans

To further qualitatively investigate the Chrimson response dynamics elicited by baseline blue light excitation in these animals for both treatment conditions in independent replicated wells as described above (soaking or plate), increasing baseline (F_0) durations (2.5 s, 5 s, 7.5 s and 10 s) before red-light stimulation were programmed using all other settings as determined previously (**Fig. 24**). Three replicates of each condition for both ATR treatments were prepared to test in one experiment (**Fig. 24a**). One representative well contained ~50 animals that each co-express GCaMP and Chrimson in the AWA neuron (**Fig. 24b-c**). As baseline durations increase, a more prominent blue-light evoked calcium response was observed for both ATR treatment conditions (**Fig. 24d-j**). This initial baseline response was consistent in magnitude and shape for all initial baseline durations; therefore, a curve fit was used to subtract the baseline response from all conditions (**Fig. 24f-g**). This resulted in normalized baseline responses, allowing for qualitative comparisons of calcium response magnitude and shape (**Fig. 24g, k**). Similar yet less prominent baseline response trends were observed for the plate treatment condition with shorter initial baseline durations, thus subtraction of the curve fit for the 10 s baseline response (red traces) resulted in somewhat negative baseline responses (**Fig. 24h-k**). Soaking treatments caused a larger baseline response, while baseline responses from animals removed from ATR after development were reduced (**Fig. 24d-k**). Therefore, from this initial characterization experiment and prior (**Fig. 23**), it was determined that a 5 ms trigger delay, 2.5 s baseline (F_0) before stimulation with plate treatment of ATR through development and removed for experimentation was ideal for screening compounds due to fewer artifacts caused by ATR and illumination parameters.
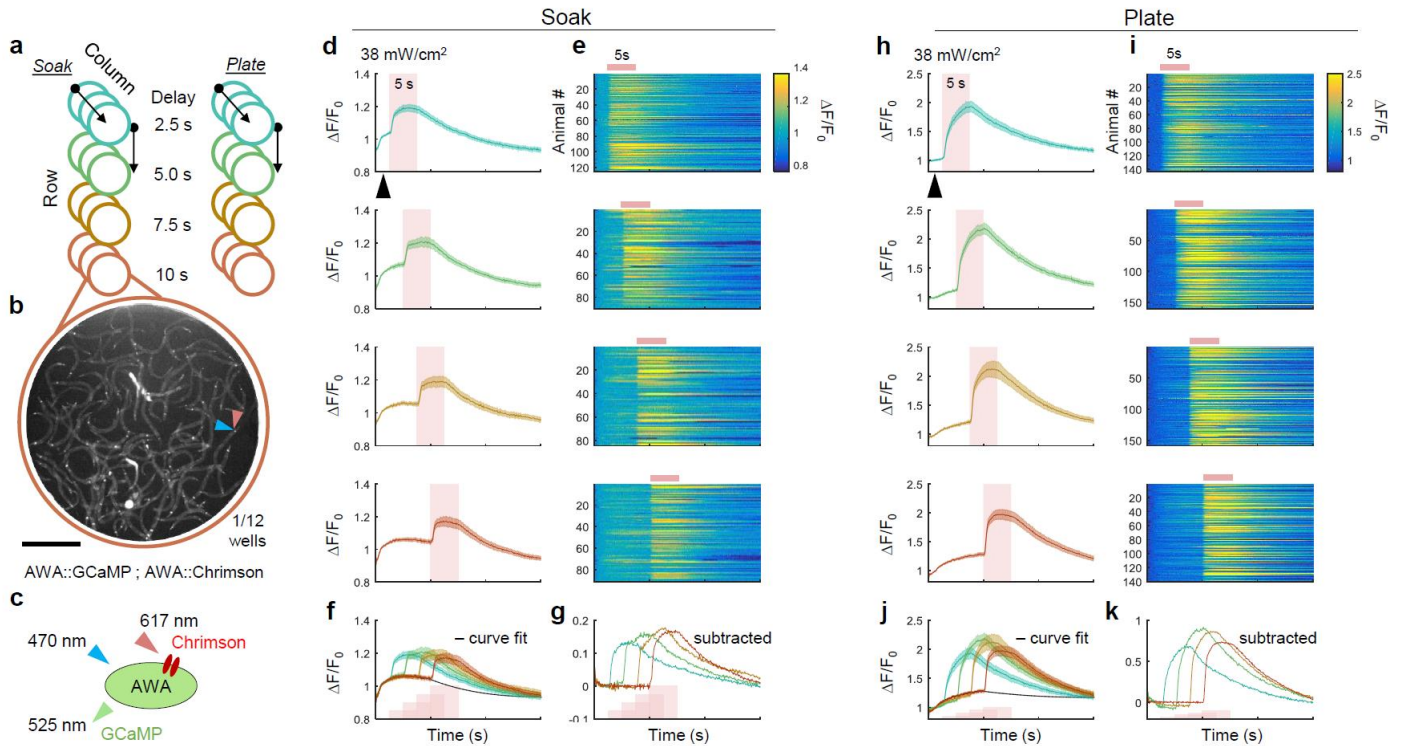
Figure 24. Characterization of All-Trans *Retinal exposure methods and effects from baseline excitation timing.*

a. Multiwell plate set-up for one experiment with three well replicates (stacked circles) per timing pattern (circle outline color, four different baseline delays). Animals were either raised on plates containing 0.5 µM ATR then removed for testing or soaked in wells with 50 µM ATR.

b. One representative well of all 24 wells from a. Excitation wavelength arrows point to the AWA neuron of ~50. Scale bar, 700 µm.

c. Excitation and emission wavelengths of GCaMP and Chrimson co-expressed in the AWA neuron monitored for these experiments.

d. Average $\Delta F/F_0$ calcium response traces for all well replicates and baseline delay conditions. Trace colors correspond to baseline delay as row color in a, for animals continuously soaking in 50 µM ATR after 3 hrs and throughout testing. Black arrow points to unideal baseline response rise to blue light excitation of Chrimson. Shading represents SEM.

e. Heat maps show individual traces corresponding to average $\Delta F/F_0$ calcium response traces shown in d.

f. Overlap of all average $\Delta F/F_0$ calcium response traces from d. A 1D data interpolation of the 10 s baseline delay is shown as the black line. Shading represents SEM.

g. Corresponding 1D data interpolation subtracted from average $\Delta F/F_0$ calcium response traces showing corrected baseline from f.

h. Average $\Delta F/F_0$ calcium response traces for all well replicates and baseline delay conditions. Trace colors correspond to baseline delay as row color in a, for animals pre-treated on 0.5 µM ATR for 48 hours and removed throughout testing. Black arrow points to low baseline response rise to blue light excitation of Chrimson. Shading represents SEM.

i. Heat maps show individual traces corresponding to average $\Delta F/F_0$ calcium response traces shown in h.

j. Overlap of all average $\Delta F/F_0$ calcium response traces from h. A 1D data interpolation of the 10 s baseline delay is shown as the black line. Shading represents SEM.

k. Corresponding 1D data interpolation subtracted from average $\Delta F/F_0$ calcium response traces showing corrected baseline from j.

123

ATR concentration yields time- and dose-dependent response thresholds

This automated immobilization method provided a platform to efficiently assess combinations of ATR treatment methods, compound exposure times, and ATR dose response comparisons (**Fig. 25**). In one experiment, 39 wells containing 13 independent replicates of ATR exposure treatments were stimulated and monitored for 24 hours, repeating each well stimulus every 20 minutes (**Fig. 25a**). This experiment yielded nearly 73,000 individual peak $\Delta F/F_0$ calcium responses (**Fig. 25b**). Two previously described ATR treatment conditions were further assessed (plate treatment or soaking, **Fig. 23-24**), with different concentrations of ATR in each well (**Fig. 25a**). Wells without ATR (—ATR) served as a negative control and showed no increase in average $\Delta F/F_0$ at each stimulation time point (**Fig. 25a-b**). Also, one ATR plate-treatment condition, then removed, and placed in buffer throughout experimentation was assessed (**Fig. 25a-b**). Three orders of magnitude of ATR concentration (0.1 µM – 100 µM) were assessed for each treatment (plate or soaking) condition (**Fig. 25a-d**). All plate-based treatment conditions approached an average peak $\Delta F/F_0$ calcium response limit after 24 hours, consistent across all conditions (**Fig. 25a-c**). For the 100 µM, 50 µM, and 10 µM soaking treatment conditions, the same average $\Delta F/F_0$ calcium response limit was reached as all plate-based treatments, albeit at different rates (**Fig. 25e**). Average $\Delta F/F_0$ calcium peak responses for 1 µM and 0.1 µM failed to reach a similar limit, as 0.1 µM treatment never elicited significantly different responses compared to the ATR negative control (—ATR) after 24 hours of compound exposure (**Fig. 25d-g**). After 24 hours, average peak $\Delta F/F_0$ calcium responses relative to the negative controls (—ATR) were similar for all plate-based treatment conditions, as well as the 100 µM and 10 µM soaking conditions (**Fig. 25f**). A dose-dependent average peak $\Delta F/F_0$ calcium response was also observed for lower

soaking concentration conditions after 24 hours (**Fig. 25f**). The curve shape for 1 µM ATR soaking after 24 hours showed a noticeable square-like on response compared to 100 µM and other high ATR concentrations (**Fig. 25d, g**). For all subsequent experiments that examine compound exposure effects on optogenetically-activated calcium responses, the plate-based treatment condition with buffer throughout experimentation (gray well treatments, **Fig. 25a**) was chosen since it allows for prolonged drug exposure effects that conserve ATR reagent to also identify compounds that directly modulate (suppress or enhance) this robust calcium response.

125
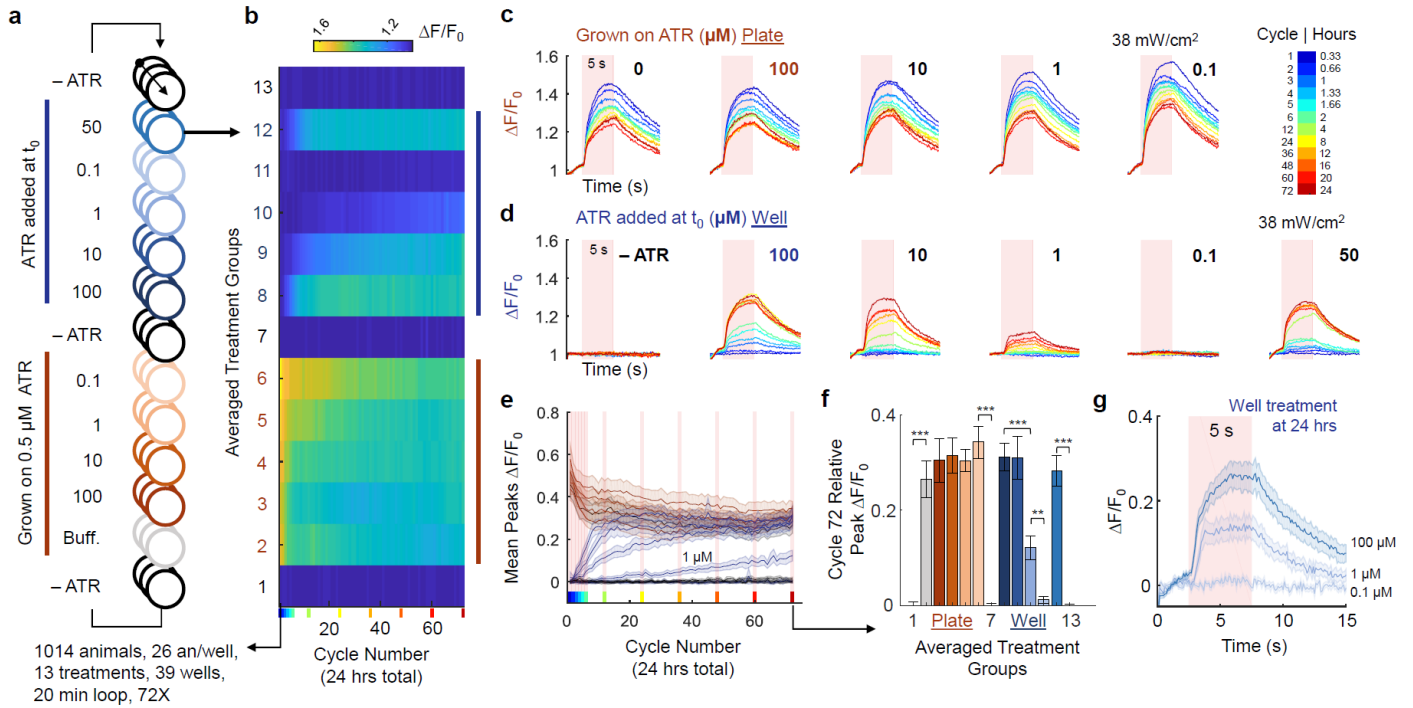
Figure 25. Automated assessment of a 24-hour time course and ATR dose response threshold for optogenetically-evoked calcium responses in C. elegans.

a. Multiwell plate schematic representing 39 independent wells, with 13 treatments and 3 technical well replicates of each condition (stacked wells). Three negative controls (– ATR) and two ATR treatment conditions across three orders of magnitude are indicated by color and labeled with treatment concentration and conditions. One stimulus per well was repeated every 20 min, 72 times lasting 24 hours total.

b. A heat map representation of average $\Delta F/F_0$ peak responses from all three row treatments corresponding to the schematic and labels in a, for 72 cycles (24 hrs total) of repeated excitation (every 20 min). The heat map represents 936 average $\Delta F/F_0$ peak data points derived from at least 73,000 total individual peak $\Delta F/F_0$ data points.

c. Average $\Delta F/F_0$ calcium response traces for all treatments corresponding to rows 2-6 in a and b, organized horizontally. The first 6 cycles (2 hours) and every 2-4 hours thereafter as indicated by the color bar (right) and x-axis in b.

d. The same layout and data representation as described in c, but corresponding to rows 7-12 in a, and b.

e. Quantification of average peak $\Delta F/F_0$ calcium responses per condition across all cycles (24 hours total). Line and shading colors represent either plate (orange) or well (blue) treatment conditions, while ATR negative controls are in black (flat curves). Trace shading represents SEM. Red shaded bars and x-axis color bar represent sampled trace time points as described in c.

f. Bar plot of relative average peak $\Delta F/F_0$ calcium responses per condition to row 1 (– ATR), consistent with well outline colors described and shown in a, for the 24 hour (72nd) time point (black arrow from e to f, and last red shading duration). Symbols represent significance after a one-way ANOVA with Bonferroni's method of correction for multiple comparisons (** $p < 0.01$, *** $p < 0.001$). Error bars represent SEM.

g. Average $\Delta F/F_0$ calcium response traces for the last cycle (72nd) at 24 hours for the well treatment condition at 100 μM, 1 μM, and 0.1 μM concentrations as labeled, corresponding to the darkest red traces in d, bar plot colors in f, and row 8, 10, and 11 in a, and b. Shading represents SEM.

126

The nemadipines antagonize optogenetically-evoked calcium responses in C. elegans over 12 hours

To determine if the *EGL-19* VGCC blocker nemadipine-A and analog nemadipine-B inhibits optogenetically-activated calcium responses in *C. elegans*, an automated dose response was performed (**Fig. 26**). In one experiment, stimulation of treatment across two orders of magnitude of each compound and two positive and negative controls with multiple technical well replicates containing 49 animals per well was repeated every 30 minutes for 12 hours (**Fig. 26a**). This single experiment yielded nearly 19,000 individual peak $\Delta F/F_0$ calcium responses (**Fig. 26b**). Average $\Delta F/F_0$ calcium response traces for all two orders of magnitude for nemadipine-A during the first three hours showed a proportional decrease in optogenetically-activated calcium responses, and reached the same response limit after all 12 hours of repeated stimulation (**Fig. 26b-d, h**). Similarly, nemadipine-B showed a proportional decrease in red-light activated calcium responses for the first three hours, with a noticeably faster decay at higher concentrations (**Fig. 26b, e-f, h**). Both positive and negative ATR controls were consistent with previous results (**Fig. 26b, g, h**). Finally, relative differences in average peak $\Delta F/F_0$ responses to negative controls at three hours showed significant differences between 10 µM nemadipine-B and 1 µM nemadipine-A, with more significant difference between higher concentrations of both compounds, exhibiting a dose-dependent effect (**Fig. 26h**). Therefore, from this single experiment, it was concluded that both higher concentrations of the nemadipines (A and B) may serve as positive drug controls for compound screening experiments.
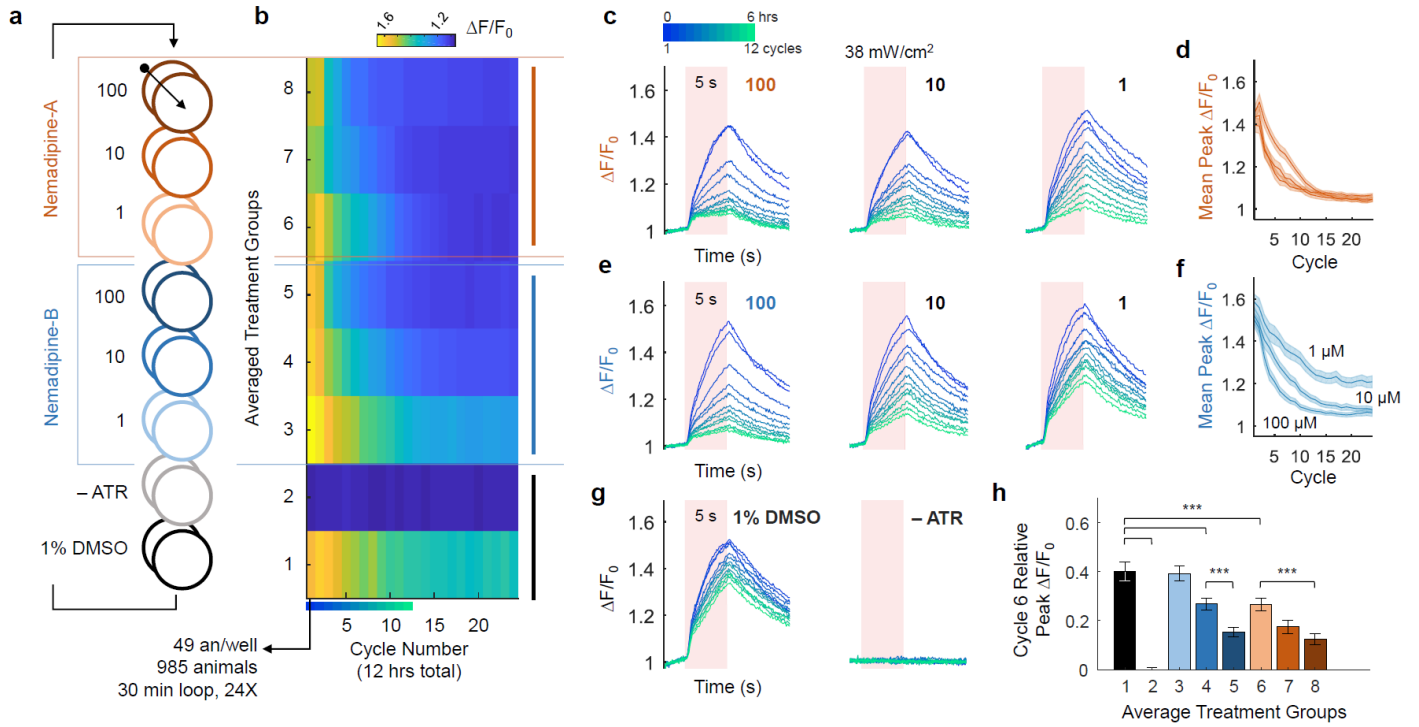
Figure 26. Automatic assessment of nemadipine dose response time course on light-evoked calcium activity in immobilized worms over 12 hours.

a. Multiwell plate schematic representing 16 wells with 8 independent treatments and two technical replicates of each condition. One stimulus per well was repeated every 30 min, 24 times, lasting 12 hours total.

b. A heat map representation of average peak $\Delta F/F_0$ calcium responses from both replicate treatment conditions corresponding to the schematic and labels in a, for 24 cycles (12 hrs total) of repeated excitation every 30 min. The heat map represents 192 average peak $\Delta F/F_0$ calcium response data points derived from nearly 19,000 total individual peak $\Delta F/F_0$ data points.

c. Average $\Delta F/F_0$ calcium response traces for all treatments corresponding to rows 6-8 in a and b, organized horizontally. The first 12 cycles (6 hours) are shown by the color bar above and x-axis in b.

d. Quantification of average peak $\Delta F/F_0$ calcium responses per concentration as visualized in b (6-8) and c across all cycles (12 hours total). Orange corresponds to nemadipine-A treatment conditions. Trace shading represents SEM.

e. Average $\Delta F/F_0$ calcium response traces for all treatments corresponding to rows 3-5 in a and b, organized horizontally. The first 12 cycles (6 hours) are shown by the color bar above and x-axis in b.

f. Quantification of average peak $\Delta F/F_0$ calcium responses per concentration as visualized in b (3-5) and e across all cycles (12 hours total). Blue corresponds to nemadipine-B treatment conditions. Trace shading represents SEM.

g. Average $\Delta F/F_0$ calcium response traces for all treatments corresponding to rows 1 and 2 in a and b, organized horizontally. The first 12 cycles (6 hours) are shown by the color bar above in c, and x-axis in b.

h. Bar plot of relative average peak $\Delta F/F_0$ calcium responses per treatment condition to row 2 in a and bar in b (− ATR). Bar colors are consistent with well outlines and treatments described and shown in a. Values are quantified for the 6th cycle (3rd hour) time point. Symbols represent significance after a one-way ANOVA with Bonferroni's method of correction for multiple comparisons (*** $p < 0.001$). Error bars represent SEM.

128

Felodipine and ivermectin suppress optogenetically-activated calcium responses in C. elegans

To validate this methodology as a functional screening platform and to identify compounds that suppress red-light activated calcium responses in *C. elegans*, 640 small molecules contained in the Lopac library were screened (**Fig. 27**). A 384 well plate was prepared with ~44 embedded animals per well at a 10 µM final concentration containing 320 FDA approved compounds from the Lopac small-molecule library. Of the remaining 64 wells, 56 contained 1% DMSO as a buffer control, four contained 100 µM nemadipine-A, and the last four contained 10 µM nemadipine-A. A 15 second video was recorded per well to monitor GCaMP, while a 5 s red-light activation pulse was delivered between 2.5 s to 7.5 s for all 384 wells. This was stimulation and recording cycle for the entire multiwell plate was repeated four times, every 6 hours. In a single experiment, this procedure yielded nearly 68,000 individual $\Delta F/F_0$ calcium response traces (**Fig. 27a-b**). This protocol was repeated for a second full 384 well plate containing the same number of controls and 320 different compounds (**Fig. 27c**). Average $\Delta F/F_0$ peak responses were calculated for each well across all four cycles of each plate to identify relative fold changes in average peak $\Delta F/F_0$ calcium responses (**Fig. 27b-d**). Additionally, average integrated $\Delta F/F_0$ curve area as fold change during the stimulation duration was calculated and similarly compared and highlighted. One compound showed a difference in relative curve area (red dot, **Fig. 27e**), but was an artifact due to noise, while most controls and other primary hits were also re-confirmed. Compounds that had fold changes larger than three standard deviations of all 1% DMSO control wells were noted (**Table 2**), while average $\Delta F/F_0$ calcium response traces for the most prominent of these changes were investigated further (**Fig. 27d-j**). Consistent between both peak and area fold change

calculations, 10 µM ivermectin and 10 µM felodipine, as well as 15/16 of the nemadapine-A (10 – 100 µM) controls were identified as positive hits for suppression of optogenetically evoked calcium activity over 18 hours (**Fig. 27d, f-k**). The average coefficient of variation (CV) for all positive drug controls across both screen plates was <6%. Specifically, the first screen plate yielded CVs of 2% and 1.61% for 10 µM and 100 µM nemadipine-A replicate wells, respectively. The second screen plate yielded slightly higher CVs of 9.35% and 8.75% for 10 µM and 100 µM nemadipine-A replicate wells, respectively. Average $\Delta F/F_0$ calcium response traces for each cycle during 10 µM felodipine exposure showed a similar significant time-dependent suppression, like 10 µM nemadipine-A, while 10 µM ivermectin resulted in a strong suppression after just 6 hours of exposure, similar to 100 µM nemadipine-A (**Fig. 27f-k**). One enhancer of optogenetically-evoked calcium activity was also identified as 10 µM parthenolide (**Fig. 28**). Additional primary hits found from this screen are listed in **Table 2**, which include several neurotransmitter receptor agonists (serotonin, dopamine, and adenosine), an inhibitor of serotonin biosynthesis, a κ-opioid agonist, and an apoptosis inducer.
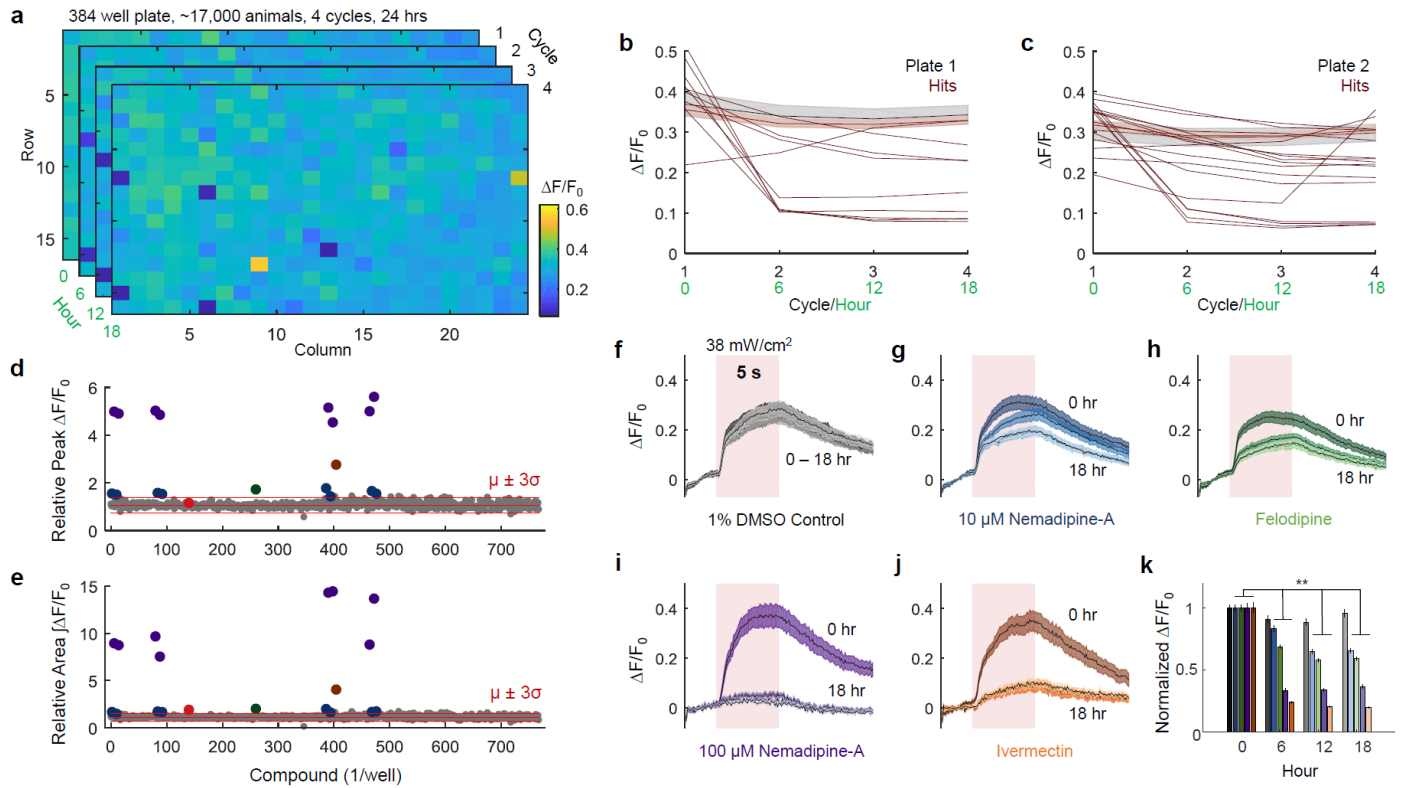
Figure 27. Identification of optogentically-evoked calcium activity suppressors by an automated long-term high-content functional screening method.

a. Four stacked heat maps representing average peak $\Delta F/F_0$ calcium responses for ~44 genetically identical animals per well of a 384 well plate at 0 hr, 6 hr, 12 hr, and 18 hr (cycle 1, 2, 3 and 4, respectively) time points. Each well contains a different compound, except for controls.

b. Average peak $\Delta F/F_0$ calcium responses for each well of the first plate screened for all cycles, grouped by either buffer controls (black line, gray shading represents SEM) or drugs (thicker red line, red shading represents SEM). Individual thin red lines represent compounds with relative peak $\Delta F/F_0$ calcium responses beyond three standard deviations from the average peak $\Delta F/F_0$ calcium response of buffer controls.

c. The same description as in b for a second independent plate screen.

d. Scatter plot of average relative peak $\Delta F/F_0$ calcium response per well, representing fold change (comparing cycle 4 to 1). nemadipine-A controls are colored purple (100 µM) or dark blue (10 µM), while other positive hits are colored green (felodipine) or dark orange (ivermectin), both at 10 µM. Red lines represent the mean $\pm$ 3 standard deviations.

e. The same description as in d for average fold change in area from integrated $\Delta F/F_0$ calcium responses. Dot colors and red lines are consistent with d. The red dot highlights a compound with significant fold change in area, not identified by relative peak quantification in d, but due to a noise artifact.

f. Overlaid average $\Delta F/F_0$ calcium response traces for all four time points from darker to lighter colored shading (0 hr – 18 hr, respectively) of 1% DMSO. Trace shading colors correspond to dots in d and represents SEM.

g. Overlaid average $\Delta F/F_0$ calcium response traces as in f for 10 µM nemadipine-A.

h. Overlaid average $\Delta F/F_0$ calcium response traces as in f for 10 µM felodipine.

i. Overlaid average $\Delta F/F_0$ calcium response traces as in f for 100 µM nemadipine-A.

j. Overlaid average $\Delta F/F_0$ calcium response traces as in f for 10 µM ivermectin.

k. Bar plot of normalized average peak $\Delta F/F_0$ calcium responses to the first cycle for all cycles, with colors corresponding to traces in f. Symbols represent significance after a two-way repeated measures mixed ANOVA with Bonferroni's method of correction for multiple comparisons (** p < 0.01). Error bars represent SEM.

131

Table 2. Primary hits identified from this functional screen of 640 FDA-approved compounds that significantly modulate optogenetically-evoked calcium activity in* C. elegans*.

Chemical name (left), biochemical and physiological action(s) (center, obtained online from Sigma-Aldrich), and chemical structure (right) are shown for each primary hit. Nemadipine-A and felodipine chemical structures were obtained from (Kwok et al., 2006), while all other structures are obtained online from Sigma-Aldrich.

Chemical Name	Biochemical/Physiological Action(s)	Chemical Structure
Nemadipine-A	A cell permeable L-type calcium channel protein inhibitor.	
Felodipine	L-type calcium channel blocker.	
Ivermectin	Positive allosteric modulator of α7 neuronal nicotinic acetylcholine receptor; also modulates glutamate-GABA-activated chloride channels.	
Chloro-APB hydrobromide	Full D_1 dopamine receptor agonist.	
S-(−)-Carbidopa	Peripheral inhibitor of L-aromatic amino acid decarboxylase.	
1-(3-Chlorophenyl)biguanide hydrochloride	Very potent 5-HT_3 serotonin receptor agonist.	
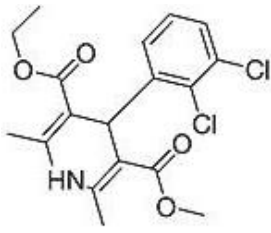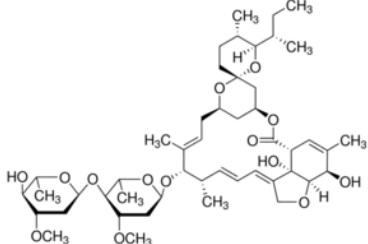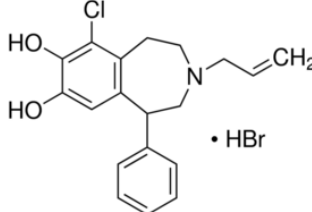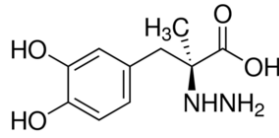
132
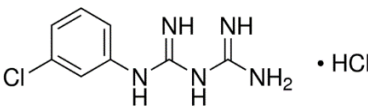
(±)-trans-U-50488 methanesulfonate salt	Selective κ-opioid receptor agonist.	
5'-(N-Ethylcarboxamido)adenosine	Potent adenosine receptor agonist with nearly equal affinity at A_1 and A_2 receptors.	
Emetine dihydrochloride hydrate	Apoptosis inducer.	
Parthenolide	Anti-inflammatory agent that inhibits NF-κB activation.	
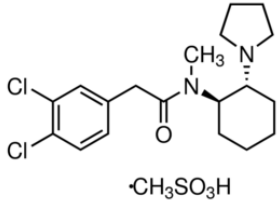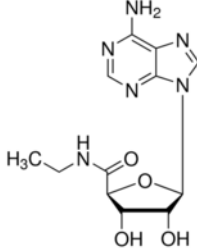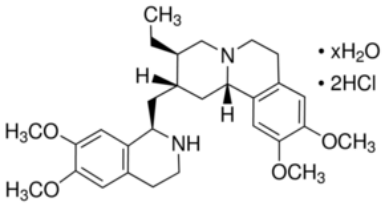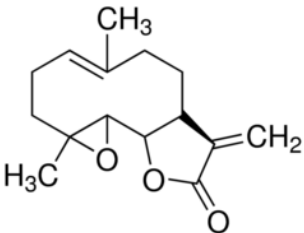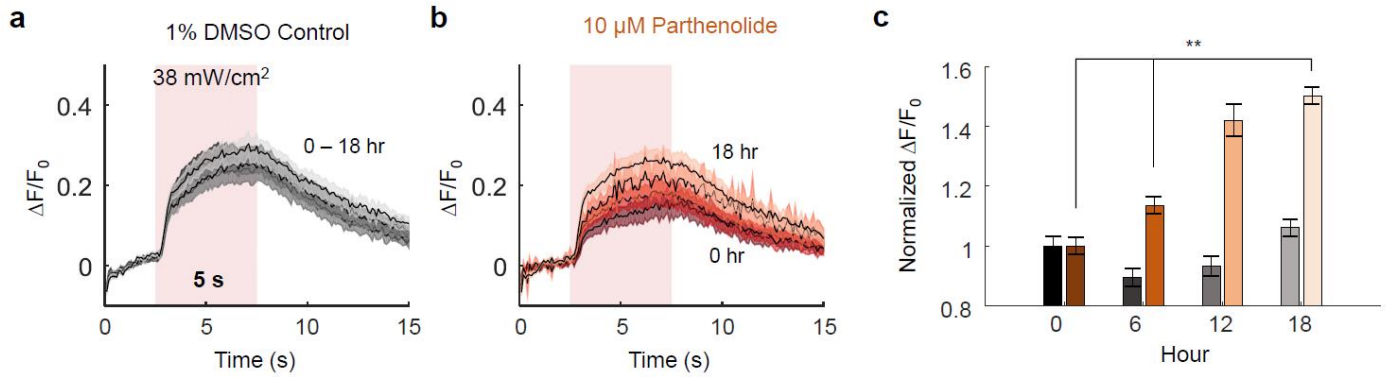
Figure 28. Parthenolide is a possible enhancer of optogenetically-evoked calcium activity in C. elegans*.*

a. The 1% DMSO buffer control shows no significant relative change in peak response over 18 hours from one representative well of the 384 well plate screen. Shading represents SEM. Darker shading colors represent early screen time points.

b. A well containing 10 μM parthenolide shows increased calcium response activity in *C. elegans*. Shading represents SEM. Darker shading colors represent early screen time points.

c. Relative changes in average peak $\Delta F/F_0$ calcium response traces over 18 hours during exposure to parthenolide shows increase in calcium activity. Symbol represents significance after a two-way repeated measures mixed ANOVA (** $p < 0.01$), showing average peak $\Delta F/F_0$ calcium response of 10 μM parthenolide treated animals at hour 18 compared to earlier hour(s) 0 and 6. Error bars represent SEM.

134

Methods & Materials

C. elegans *maintenance*

For all experiments, the integrated *C. elegans* strain NZ1091 was used. These animals were grown and maintained at 20°C on Nematode Growth Medium (NGM) plates with OP50 *E. coli* bacteria, unless otherwise stated when prepared with different ATR conditioning treatments for multiwell experiments.

NZ1091, *kyIs587* [*gpa-6*p::*GCaMP2.2b; unc-122*p::*dsRed*]; *kyIs5662* [*odr-7*p::*Chrimson:SL2:mCherry; elt-2*p::*mCherry*], expressing GCaMP and Chrimson in AWA neurons.

Synchronization of >17,000 C. elegans *on All-*Trans *Retinal or standard NGM plates*

Over 17,000 animals were synchronized by scaling standard protocol volumes and using eight 100 mm NGM plates containing gravid adults (Stiernagle, 2006). Synchronized L1s were obtained by rotating prepared eggs adjusted to ~10 animals/µL at 10 rpm in M9 solution for 12-20 hrs at 20°C. All-*Trans* Retinal (ATR) plates were prepared by re-suspending pelleted OP50 *E. coli* 5X to M9 containing a final ATR concentration of 50 µM. A 150 µL volume of this solution was seeded and spread onto each 100 mm plate immediately prior to adding 5,000 L1 synchronized animals (at ~10 animals/µL), or animals were added to standard OP50 *E. coli* seeded plates not containing ATR. Worms were grown for ~48 hours at 20°C until L4 stage, then collected by washing off plates with M9 and re-counted three times using a 5 µL sample. If needed, the final animal suspension was adjusted to ~10 animals/µL by centrifugation and resuspension in M9.

Hydrogel embedding and immobilization of animals in 384 multiwell plates

For all 384 well screening experiments, equal parts of 20% PEGDA (0.1% Irgacure) (Burnett et al., 2017)was added to a synchronized animal population in M9, resulting in ~5 an/µL, 10% PEGDA, 0.05% Irgacure, and 0.5X M9. A volume of 10 µL (containing ~40 animals) was delivered to each well of a standard high-content 384 multiwell imaging plate (Corning #4581) using a Biomek 2000 workstation (8 wells at a time), or manually transferred using a single or multichannel pipette (12 wells at a time). Both procedures used repeated mixing (4-5X) to maintain an even animal suspension during transfer (**Fig. 20a**). The animal-containing multiwell plate was cooled for 10 min at -20°C to settle animals at the bottom of the well, then immediately exposed to 308 nm UV light for cross-linked immobilization (**Fig. 20a**) (Burnett et al., 2017). Single wells can also be prepared by standard picking and transfer of animals to a final 10% gel solution (using PCR tubes), depending on experimental design and desired throughput.

Lopac drug library preparation

Aliquoted Lopac drug library plates were received from the UMMS small-molecule screening facility as 16X 96-well plates at 3 nmol of compound per well (3 µL at 1 mM in 100% DMSO), stored at -80°C until use. For a single 384 well plate screen experiment, four stock compound plates were thawed at a time and a Multidrop Combi Reagent Dispenser (ThermoScientific) was used to dilute each well of the plates to 12.5 µM compound using 240 µL autoclaved diH$_2$O. Next, 40 µL of each diluted compound was automatically mixed 4X and transferred (Biomek 2000) from the four 96 well plates to a prepared 384 well plate already containing 10 µL of worms embedded in gel, resulting in a 10 µM final concentration of compound in 1% DMSO in each well. Eight wells in the first 96 well plate were manually aspirated before liquid transfer, such that eight

nemadipine-A positive drug controls prepared as described above (four each at 10 µM and 100 µM concentrations) could be manually deposited prior to screening. This protocol allowed for screening of 384 different well preparations with 320 different compounds, 56 buffer controls (1% DMSO), and the 8 positive drug controls in one automated experiment. The remaining diluted working concentration plates were stored at -80°C for replicate use (with ~5 freeze-thaw cycles per plate). Nemadipine-A concentrations were prepared fresh or used after one thaw cycle. This protocol was repeated two times to screen eight plates containing 640 compounds from the Lopac small-molecule library, 122 1% DMSO buffer controls, and 16 nemadpine-A positive drug controls. One experiment costs <$100 ($38 for gel, $33/multiwell plate, $25/384 compounds).

Experimental control software

Animals were imaged on a commercial microscope with robotic x-y axis stage (RAMM Frame, ASI) with custom optical configurations as previously described (Lagoy and Albrecht, 2018), allowing for simultaneous blue-light excitation (GCaMP monitoring) and red-light excitation (Chrimson stimulation) through the 4X/0.28 NA wide-field imaging objective (**Fig. 20b**). The set-up was slightly modified with adjustable in-plane apertures to ensure independent optical stimulation per well. All control software was developed using MicroManager's open-source platform, as described in the *Results* (**Fig. 21**). Experimental conditions (i.e. camera settings and experimental control) are initially configured using a custom graphical user interface (*GUI*), and executed using a custom script to automate synchronized stage positioning with stimulation and recording (*SCREEN*) (**Fig. 21c-d**). Default camera settings were 100 ms exposure, 5 ms pulse, 5 ms delay, 2x2 binning, at 1024x1024 resolution, and 15 s TIFF stack movies were recorded per well with

one 5 s red light pulse (35 mW/cm^2) from 2.5 s – 7.5 s, unless otherwise noted. All experimental settings, run-time metadata, and videos are logged and saved in real-time with date and time as well as well position, cycle number, and movie number on file names for streamlined processing, indexing, and set-up of exact experimental repeats (**Fig. 21e-f**).

Software for neural signal quantification

A suite of custom ImageJ macros was developed for automated neuron selection and trace recording (aNT), or to manually select neurons (neuronPos) and then record calcium intensity in each well across all wells and cycles automatically (NT) (**Fig. 22**). The neuronPos and NT scripts were used for all results described (**Fig. 22**). Immediately after analysis, a custom ImageJ macro (oWells) was used to organize all videos for each well to their own well-labeled folders for simplified manual and automatic parsing of the large data. In both aNT and NT analysis scripts, a large 16x16 pixel square was used for measurement of integrated intensity (F$_R$), which permitted slight animal movement during unsupervised analysis (**Fig. 22**). Local background subtracted fluorescence (F) was calculated as $F = \left(F_R - F_{bg} \right)$. A single absolute minimum value from all background subtracted values (|minimum F|) was then added to each raw fluorescence value (F) to correct for all situations where negative fluorescence (-F) occurred due to background subtraction errors (**Fig. 38e**). Change in fluorescence (ΔF/F$_0$) was then calculated as $(F - F_0)/F_0$ where F$_0$ is the mean fluorescence of all time frames before stimulation, unless otherwise stated or shown. All neuron positions and raw measured values were recorded for each video and animal, saved with corresponding text file names for streamlined analysis, organized data logging, and regeneration of figures from raw files. Animal movement could be quantified using

a custom frame subtraction-based macro (anMove) in ImageJ for videos of before and after crosslinking in each well (data not shown). Neuron positions were selected using either the first video (nemadipine-A time course experiment) or last video (all other experiments) of each cycle. Another custom ImageJ macro (MWS) and FIJI Grid/Collection stitching plugin were used to stitch one frame from all full-resolution videos across a 384 well plate (24576x16384 px), which was useful for visualization and quality control.

All-Trans *Retinal exposure duration and dose response characterization in multiwell plates*

To wells of embedded animals synchronized using either ATR or non-ATR NGM plates prepared as described above, solutions of ATR at final concentrations in each well were made to 0 μM, 0.1 μM, 1 μM, 10 μM, 100 μM, or 50 μM containing 1% DMSO (**Fig. 25a**). Three replicates of each condition were set-up in adjacent wells (block form). The *GUI* script was configured to automatically stimulate and record animals in each well every 20 min for ~24 hrs (cycle 72X, 20 min cycle delay) with different initial delay timing or trigger periods as described in the *Results* (**Fig. 25a-b**). Neuron positions were manually selected then $\Delta F/F_0$ was automatically quantified (using neuronPos and NT ImageJ macros) as described previously.

Characterization of the nemadipines as positive drug controls

To wells of embedded animals, solutions were prepared to a final concentration of 1% DMSO for either 1 μM, 10 μM, or 100 μM nemadipine-A or -B (Santa Cruz Biotechnology), with 1% DMSO as the buffer control well for either ATR positive and negative ATR (– ATR) controls (**Fig. 26a**). Experimental recording was initiated and set to automatically stimulate and record animals in

each well every 30 minutes for 12 hours (cycle 24X, 30 min cycle delay) using the custom MicroManager timing and position *GUI* and *SCREEN* scripts, with otherwise default camera settings, illumination, and stimulus and recording timing durations (**Fig. 26a-b**). Neuron positions were manually selected then $\Delta F/F_0$ was automatically quantified (using neuronPos and NT ImageJ macros) as described previously.

Experimental conditions for the automated 640 small-molecule Lopac library compound screen

For each prepared 384-well plate containing multiple control conditions (56 1% DMSO buffers and 8 nemadipine-A drug controls) and 320 different compounds, 15 second TIFF stack movies (10 fps) were recorded for each well, with 1 second stage positioning delay between wells, and repeated every 257 min for ~18 hours of drug exposure (**Fig. 27a-c**). This protocol resulted in 4 videos per well at equally timed 6 hour intervals (1,536 videos per plate experiment, and 3,072 videos total for all 768 wells screened) (**Fig. 27d-e**). Default camera settings, experimental control, and plate positions were configured as described above using the *GUI* and executed using the *SCREEN* scripts. This data size accumulated to ~1 terabyte containing over 20 million neural trace data time points. When combining multiple screening plate datasets, a relative scaling factor was used to standardize for control responses (**Fig. 27d-e**).

Data processing, statistical comparisons, and visualization

All data was processed using custom developed scripts and parallel processing in MATLAB2017a to handle large (tall) data sets. MATLAB2017a was also used to perform each one-way analysis of variance (ANOVA1) with Bonferroni's method of multiple comparisons (* $p < 0.05$, ** $p < 0.01$,

*** p < 0.001) (**Fig. 25f, 26h**). Comparison bars without asterisks are the same significance level as shown immediately above for simplicity. Two-way repeated measures mixed analysis of variance with Bonferroni's method of multiple comparisons was used to compare repeated measures across more than groups (** p < 0.01) in IBM SPSS (**Fig. 27k, Fig. 28c**).

Discussion

In this Chapter, we present a new functional high-content imaging method that allows for the detection of tractable optogenetically-evoked calcium activity modulators in tens of thousands of living *C. elegans* for 24 hours. Nearly 50 immobilized and encapsulated animals in each well of a 384 well plate within a permeable hydrogel material enables the use of optogenetics for simultaneous monitoring and activation of calcium activity during exposure to a variety of compounds and small-molecules. After semi-automated plate preparation (<10 min of manual labor), this method functions autonomously using commercial hardware and custom open-sourced microscopy software to image the same animals and conditions repetitively for hours across 384 wells. The versatility of this method design and customizability in experimental control allows for both small scale optogenetic experiments over short or long durations with high temporal resolution, or large chemical screens with several time-point replicates for increased statistical power using paired sample measurements. This method is also inexpensive and efficient, costing only ~$200 to screen 768 treatments across >33,000 animals in less than one week. Additionally, custom analysis enable highly accurate, streamlined, and reproducible data, which permits the detection of new significant findings through data driven exploration.

Based on recent advances in versatile long-term immobilization techniques, our method establishes a new option for high-throughput functional screening in whole organisms. Dual monitoring and stimulation of calcium activity in biological samples over short-durations using only light is a completely orthogonal approach that offers immense flexibility in controlling and perturbing the sample environment (Burnett et al., 2017; Klapoetke et al., 2014; Larsch et al., 2015). Hydrogels offer a technically simple and versatile immobilization strategy by encapsulating animals for extended periods of time without paralytics to keep animals stationary in a static and compound-permeable environment (Burnett et al., 2017). We show here that a UV crosslinking hydrogel is adaptable for encapsulating whole organisms in a multiwell plate format with a simple and rapid total experimental set-up and immobilization time (~10 min). Animals settle and are immobilized near the glass bottom of the multiwell plate, leaving about a maximum 1.62 mm depth of gel separating the animal from added compounds. This method could be adapted for 1536 well plates, with less volume and younger developmental stages. Screening plates of this content at the same imaging resolution would increase throughput 4X and decrease overall costs.

To evaluate our method and assess a previously uncharacterized phenomenon, we assessed ATR exposure and concentration on optogenetically-activated responses in animals over 24 hours with high temporal resolution (every 20 min for 24 hours). Since *C. elegans* do not endogenously express ATR, the localization of this compound to Chrimson served as a direct measure of ATR diffusion rate and internalized functionality by the organism. We observed that it takes at least 2 hours to elicit robust optogenetically-evoked calcium responses using the highest two tested concentrations of ATR (100 µM and 50 µM). This knowledge, as well as identifying a response

limit threshold, are useful for improving ATR treatment throughput and will lead to more thoroughly controlled optogenetic experiments when using channelrhodopsins in animals that do not exogenously synthesize ATR. Since compound exposure time effects light-induced responses, these artifacts could be the source of assay variability.

In addition to identifying a minimum ATR incubation time required to elicit robust optogenetically-evoked calcium responses in *C. elegans*, we observed relative changes in Chrimson activation rates to different concentrations of ATR by a soaking exposure method. Since higher-concentrations of ATR have a lower response threshold (faster response time) that seems dose dependent, one explanation might be that more ATR molecules are present in solution and thus can be internalized by the animals and localized to Chrimson channels more rapidly. Also, with more ATR molecules present in the animal and localized to Chrimson, a larger sum of channels may be functional as protein modeling studies suggest that only one ATR molecule is required for proper rhodopsin function (Zhou et al., 2012). This idea could explain why there is a difference in response threshold timing to ATR soaking concentrations, as well as proportional sensitivities to baseline blue light activation in soaking conditions, unlike animals removed from ATR after exposure through development. Regardless, it seems that a calcium response limit is ultimately reached irrespective of ATR exposure concentration and treatment method, except for low ATR soaking concentrations which might take longer before observing such robust light-evoked responses.

Also, the rate to achieve the light-evoked calcium response threshold is likely proportional to the diffusion rate of ATR through the hydrogel matrix and permeability through the cuticle of *C. elegans*, to finally reach the Chrimson pore. Based on previous literature, an estimation of a protein diffusion coefficient (D) through PEGDA hydrogels is ~10^{-6} cm^2/s, which is proportional to the gel thickness (L) (Weber et al., 2009). When these two parameters are related together, an estimate of the diffusion time scale $t_d = L^2/D$ can be made (Weber et al., 2009). In the multiwell format, a 10 µL volume of PEGDA hydrogel in one 2.8 mm diameter well results in an estimated cylindrical thickness of ~1.6 mm. Therefore, by following these estimates and assumptions, it is likely that it takes ~2-5 hours for large proteins (>43,000 g/mol) to diffuse through the full thickness of a PEGDA hydrogel, reaching embedded animals settled at the bottom. For smaller proteins (~5,700 g/mol), the diffusion coefficient is about twice as fast (~2 $\times 10^{-6}$ cm^2/s) (Weber et al., 2009). This estimation makes sense, as optogenetically-evoked responses by ATR diffusion were observed after ~1-3 hours. Further, ATR is estimated to be markedly smaller than the protein size used to derive the previously established estimations (284 g/mol for ATR, versus 5,700 g/mol), thus ATR is hypothesized to diffuse through the hydrogel significantly faster than large proteins. By more thoroughly modeling the diffusion of a particle through this exact weight percent hydrogel and matrix uniformities, a more accurate rate of diffusion could be derived. Still, the diffusion of ATR leading to light-induced calcium responses in *C. elegans* may serve as one direct measurement strategy for deriving diffusion properties through the hydrogel. Importantly, this above model and estimation does not consider time delays involved in animal cuticle permeability and localization of the chromophore to Chrimson, which is a key consideration for reducing false negatives in compound screens using *C. elegans*.

Fortunately, there are multiple opportunities to improve the uptake of compounds and overall accumulation within *C. elegans*. Specific genes have been identified in *C. elegans* that increase the permeability of the animal cuticle, like the *bus-8* allele *e2698*. Therefore, using these animals with increased cuticle permeability for the screen may accelerate compound uptake and improve drug access to identify additional hits (Gravato-Nobre et al., 2005; Kwok et al., 2006; McCormick et al., 2013; Partridge et al., 2008). Similarly, and instead of modifying genetic backgrounds, different buffer conditions may also be used to increase cuticle permeability in *C. elegans*, yet treatments that do not severely damage the animal remain to be identified. Secondly, *C. elegans* have specific genetic mechanisms to confer resistance or help protect them against several environmental toxins (Fukushige et al., 2017; Stupp et al., 2013); therefore, screening animals with compromised detoxification pathways may also improve overall animal "druggability". If any of these genetically compromised animals are used for compound screening, it must be acknowledged that identified hits may be acting through off-target effects. Thus, follow-up analysis of primary hits using wild-type animals and quantifying drug accumulation in these genotypes may be equally important for identifying specific compound targets and related pathways.

We also found that ATR plate treatment conditions using an order of magnitude lower concentrations suggest that the uptake of ATR might be developmentally regulated since sensitivity to baseline blue light exposure was not as prominent, while robust activation is consistent overtime and reaches a steady-state peak response limit (**Fig. 25**). An additional observation from these results suggest that lower concentrations of ATR may yield a more

accurate representative measurement of membrane potential by regulating the sum of Chrimson channel functionality. This idea is derived by the calcium response traces shown by soaking in 1 µM ATR concentration (**Fig. 25d, g**), which yielded consistent square-shaped calcium response traces, typical of optogenetically-evoked current-clamp electrophysiological response recordings in this strain (Larsch et al., 2015). One possible explanation is that the fluorescent signal is more representative of voltage instead of an overabundance of calcium that could be obscuring the underlying initial cause for ion influx and cellular depolarization. To the best of our knowledge, this observation, as well as ATR concentration dependent response threshold timing was not systematically observed or measured before, and will be useful to the general field of neuroscience for more controlled and efficient assays requiring exogenous ATR exposure. Further, the significance of the steady-state response limit approached from both soaking and plate-based ATR exposure treatments is intriguing and somewhat surprising, and should be further investigated to derive biological significance that considers lack of animal nutrition, cell toxicity from repeated stimulation, and overall health-span. In light of small-molecule screening, these results also suggest that this method is capable of identifying and quantifying the effect of exogenous compound localization and concentration to internalized protein structures within *C. elegans* over tractable and long-term durations.

Since a 24 hour time period showed robust optogenetically activated calcium responses to ATR treated animals in the hydrogel, pharmacological inhibition, or channel suppression, of this robustness was further investigated. nemadipine-A and nemadipine-B (well-characterized L-type calcium channel inhibitors) were added directly to independent wells of immobilized and

encapsulated animals to specifically antagonize one source of intracellular calcium influx in *C. elegans*, the L-type voltage-gated calcium channel *egl-19*. These compounds indeed caused a strong dose dependent reduction in robustness of optogenetically-evoked calcium responses for 12 hours, compared to the buffer control, consistent with drug-induced developmental phenotypes (Kwok et al., 2006). More specifically, the level of calcium channel inhibition was observed to reach a limit at different rates for each concentration, while calcium responses were never completely eliminated until 18 hours later. The rate of inhibition seemed to approach a limit faster for nemadipine-A at all concentrations. This could be explained in part that the chemical structure for this compound has been shown to antagonize *egl-19* more specifically than its analogue due to the symmetry and location of ethyl-esters, although accumulates to a similar extent in *C. elegans* (Kwok et al., 2006). Also, nemadipine-A leads to a higher percent of severe developmental abnormalities in wild-type *C. elegans* when exposed chronically to both 100 µM and 10 µM, while developmental phenotypes were not as severely observed for animals grown on nemadipine-B for concentrations less than 100 µM (Kwok et al., 2006). However, egg laying defective phenotypes were more sensitive to lower concentrations of both nemadipine-A (0.5 µM – 1 µM) and nemadipine-B (5 µM – 10 µM) when exposed throughout development (Kwok et al., 2006). Therefore, our observed differences in calcium activity to all concentrations and both compound treatments are somewhat consistent with prior phenotype data. Altogether, these results and observations suggest that this assay is suitable for the identification of other modulators of calcium activity in *C. elegans* over tractable and long-term durations, and that nemadipine-A is an excellent positive drug control for small-molecule screening experiments, consistent with previous findings in *C. elegans*.

To demonstrate validity and scalability of this method, >33,000 animals were screened across 640 FDA approved compounds for suppressors of optogenetically-activated calcium activity in a single neuron of intact *C. elegans*. Of the hits found beyond three standard deviations from the buffer control mean (see **Table 2**), felodipine and ivermectin, as well as 15 of 16 nemadipine-A controls, demonstrated the strongest relative fold change in peak response and curve area. This initial observation led to the detection of a noticeable time-dependent inhibition of calcium activity with increasing potency for felodipine and ivermectin, respectively (**Fig. 27i, j, k**). Also, we found that a coefficient of variation across all positive drug controls was <6%, suggesting that single well replicates are suitable for identifying primary hits. Also, the three-sigma threshold estimates that there may be 6-7 false positive hits; therefore, by increasing the statistical threshold to four standard deviations from the mean would improve the confidence of identifying primary hits, and should be highly considered moving forward.

Felodipine is a dihydropyridine (DHP), similar in structure to nemadipine-A, which is a class of compounds shown to antagonize voltage-gated calcium channels in vertebrates (Tang et al., 2014). Interestingly, Kwok *et al.* (2006) reported that felodipine did not induce severe developmental effects at 25 μM in *C. elegans* as did nemadipine-A, although the compound accumulated in worms to a similar level after two hours of incubation (25 μM). A structurally modified version of felodipine screened in the library that is more similar to the symmetrical compound structure of nemadipine-A (nemadipine-B) had a stronger developmental effect on wild-type *C. elegans*. We showed that nemadipine-B seems to have a similar overall antagonistic property as nemadipine-A at 10 μM concentrations after at least 12 hours of exposure.

Therefore, this felodipine result further confirms the ability to detect specific and more subtle effects on calcium activity, and ion channels like *EGL-19*, *in vivo* using this method. This is an important finding, since the identification of compounds that target calcium channels with high specificity and fewer side effects may be more promising in the clinic.

Ivermectin is a well-known antiparasitic agent that is potently active against nematodes, arthropods, lice, and tics. It is derived from the more potent and unsafe form known as avermectin (Crump, 2017; Crump and Ōmura, 2011). This compound is currently used to treat Onchocerciasis (also known as river blindness) in humans, caused by flies infected with parasites found in remote African villages. Ivermectin interferes with worm embryogenesis and paralyzes body wall and pharyngeal muscles, which prevents reproduction and manifestation of the disease throughout the human body. This compound antagonizes glutamate-gated chloride channels (GluCl$^-$), which causes severe effects in worms by disrupting neurotransmission, but it does not cross the blood brain barrier in mammals, thus it has no effect on the human central nervous system (CNS) at low concentrations *in vivo* (Crump and Ōmura, 2011). In *C. elegans*, a high-level of resistance to this drug is facilitated by mutations in three genes, *avr-14*, *avr-15*, and *glc-1*, with some relevance of alternative resistance genes regarding permeability to the cuticle through dye filling neurons (Dent et al., 2000). It was also shown that *avr*-14, which is a GluCl$^-$ ion channel, is expressed throughout the nervous system, and in a previous small-molecule screen for broad phenotypes in *C. elegans*, ivermectin was shown to cause parental lethality at 25 μM (Kwok et al., 2006). Other indirect targets of ivermectin have also been suggested (Cully et al., 1994). Additionally, ivermectin is a large chemical, which shows that its effectiveness is

within the range of permeability to the hydrogel and worm cuticle to yield observable suppressive effects of calcium activity. To the best of our knowledge, this antagonistic observation towards calcium influx has not been reported before in *C. elegans*, but has been show *in vitro* (Samways et al., 2012), and could potentially lead to novel genetic etiology in the nervous system of nematodes, or serve as an alternative therapeutic for indirect inhibition of calcium activity for activity-dependent disorders at high-doses to be effective beyond the blood-brain barrier. Further, ivermectin was identified in a recent high-throughput screen using *C. elegans* to detect compounds that impair movement (Partridge et al., 2017). To this end, recent studies began investigating ivermectin's role on neural activity and silencing for neuropathic pain and other hyperexcitability disorders due to its highly-regarded safety at moderate concentrations (Weir et al., 2017).

Furthermore, other primary hits identified from this screen (**Table 2**) that suppressed optogenetically-evoked calcium activity in *C. elegans* include several neurotransmitter (dopamine, adenosine, and serotonin) receptor agonists, an inhibitor of serotonin biosynthesis, a κ-opioid agonist, and an apoptosis inducer. Excitingly, these compounds all have therapeutic potential for various neurological conditions, like pain and addiction (Chavkin, 2011), Parkinson's disease (Brooks, 2000), depression (Lucki, 1991), other activity-dependent disorders (Jacobson and Gao, 2006), and even cancer (Hassan et al., 2014). Although these primary hits did not have as robust suppressive effects in our screen, the relatedness of most of these compounds might suggest the specificity of potential targets capable of being identified using this method. Also, one enhancer of optogenetically-evoked calcium activity was also identified as parthenolide (**Fig.**

28), which has been previously reported to increase intracellular calcium levels *in vitro* and is involved in axon regeneration (D'Anneo et al., 2013; Gobrecht et al., 2016; Kim et al., 2012; Schneider et al., 2015). As with ivermectin and felodipine, IC_{50} values should be evaluated for these compounds to confirm effects, and examine compound effects on mutants that may be resistant to these compounds or lacking the therapeutic target.

Meanwhile, other FDA approved voltage-gated calcium channel blockers, like verapamil, nimodipine, nifedipine, nicardipine, and diltazem were not identified as positive hits in our screen. These results are also consistent with Kwok *et al.* (2006) that showed no broad phenotypic effects on *C. elegans* for all five of these FDA approved VGCC blockers at 25 μM concentrations through development. Only nimodipine was examined for uptake in worms, which did not accumulate to similar levels as the nemadipines or felodipine (Kwok et al., 2006). Therefore, it seems critical to identify treatment conditions or more "druggable" worms that will improve drug access and accumulation *in vivo*, as discussed above.

All in all, this method has proven to be a useful strategy for identifying modulators of optogenetically-evoked calcium activity in whole organisms over long-term durations. Improvements in automated data analysis as well as automation of multiwell plate preparation for screening will further reduce human labor to yield positive results more efficiently, accurately, and across more extensive drug libraries (>100,000). Furthermore, this functional screening concept and versatile method will establish new opportunities for identifying compounds that modulate dynamic cellular activity in whole organisms or cell populations. The results from these

types of screens in combination with other genetic and broad phenotype screens are expected to lead to the discovery of more specific therapeutic targets for translational studies, and ultimately the treatment of human diseases.

In addition to the results described here, there are several limitations that encourages future exploration. Foremost, the identification of methods, treatment conditions, or genetic backgrounds that improve animal druggability is critical, since several compounds did not have an effect on calcium activity, namely the VGCC blockers verapamil, nimodipine, nifedipine, nicardipine, and diltazem. Fortunately, cuticle and detoxification compromised animals can be generated to improve drug access and uptake within *C. elegans*, which should be explored and characterized further. Also, the health condition of the embedded animals should also be further characterized after prolonged compound exposure and immobilization, which may lead to more accurate claims of true *in vivo* compound effects. Finally, any primary hits that are identified from this screen should not only be confirmed using *C. elegans* through subsequent tests, but also using *in vitro* models by gold-standard electrophysiological, gene expression, and other viability assays. Then, effective compounds may proceed for translation by testing similar essential biological effects in vertebrates, which may ultimately lead to clinical trials in humans. At a minimum, we expect that this method will help accelerate and advance our understanding of fundamental genetic etiology and related compound targets involved in human neurological disease.

Chapter 5 Future Applications

This Chapter outlines and briefly discusses various future projects and ideas that are directly inferred from the results and discussions presented above. The Chapter is divided into subsections corresponding to each specific aim. Some ideas and future directions have already been attempted and has made progress, with new ideas, methods, and results described accordingly.

Evaluate and use C. elegans *channelopathy models in compound screens*

In Chapter 1, I established a pipeline for developing human channelopathy disease models in *C. elegans* by genetic manipulation of voltage-gated calcium channels, then quantified phenotypes (e.g. body morphology, forward speed, and reversal duration) and detected differences in stimulated neural calcium activity kinetics in whole-animals (**Fig. 14**). The logical next step would be to identify either compounds or genes that restore these differences in phenotype, behavior, and calcium activity (**Fig. 29**). To identify compounds that restore the altered calcium response kinetics by odor-induced stimuli, new protocols would need to be developed for treating animals with compounds prior to calcium imaging.

To restore calcium dynamics in these mutants using a compound-based approach would require careful characterization of three experimental variables: drug concentration, method of exposure, and treatment duration. One idea would be to pre-absorb compounds (~25–100 µM) on standard NGM plates, deposit age synchronized L1 animals, grow through development, then remove animals from these plates to assess changes in calcium activity using microfluidic odor-based stimulation and GCaMP recording as described in Chapter 2. A likely positive control would be to use 25 µM felodipine to assess all three phenotype levels, since we show that this compound can reduce stimulated calcium activity levels and the drug accumulates in animals without compromising body morphology. Also, nemadipine-A treatment through development on GOF animals like *egl-19(n2368)* partially restores body morphology, which would be interesting to test if these animals have restored calcium response dynamics in our system. Since other compounds may induce unwanted broad phenotypic effects, conventional microfluidic

devices may not be directly compatible. So, compound exposure time may be reduced and drug concentrations increased to treat animal stages that are directly compatible with previous quantification methods. If compound exposure is still challenging, another neuron-odor pair that is more permeable to the outside environment (like the dye filling sensory neuron ASH), or cuticle mutants, with faster absorption rates could be characterized as before and used for subsequent experiments. Importantly, odor concentrations of new odor-neuron pairs that elicit measureable changes in channel kinetics would need to be tested prior to attempting compound-effect experiments.
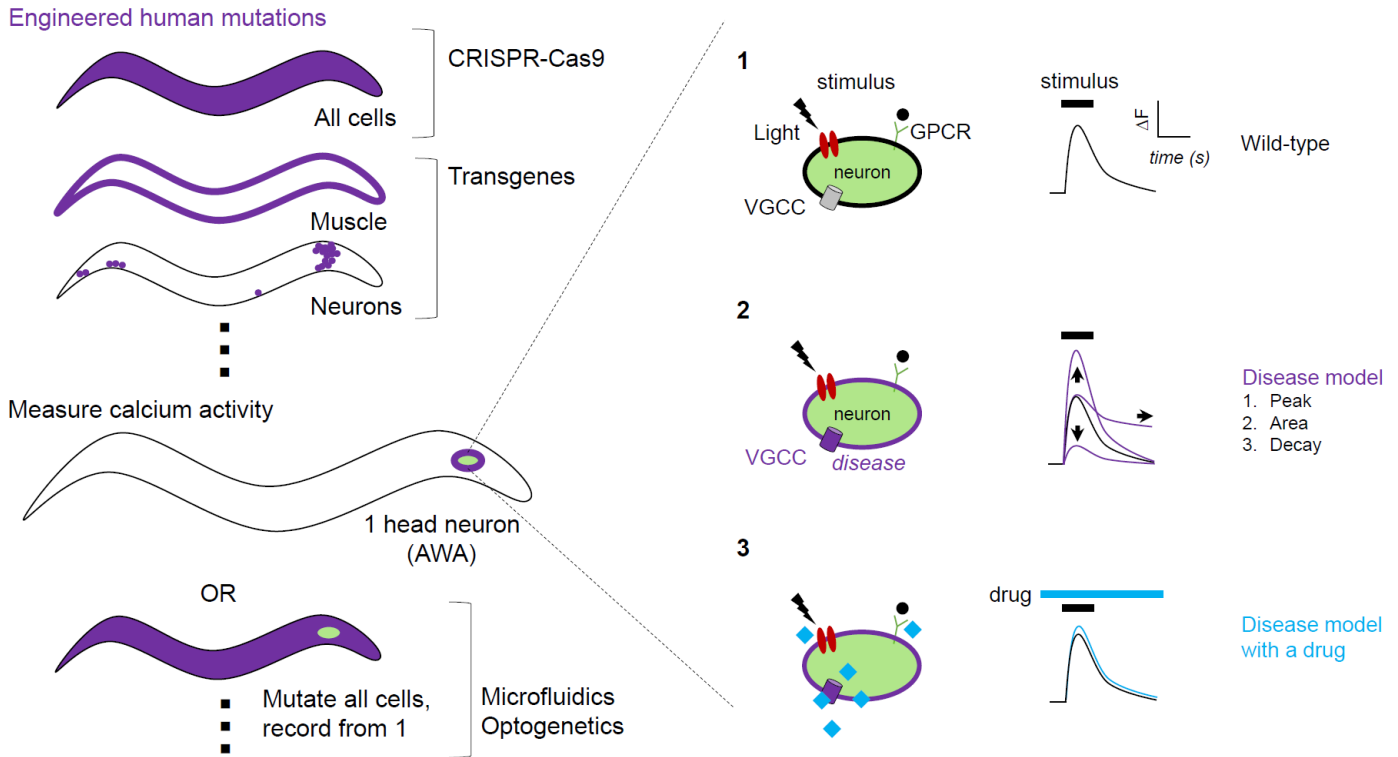
Figure 29. A model for developing and characterizing calcium channel mutants in C. elegans *for assessment of drug-induced responses.*

Manipulation of the genetic background in *C. elegans* can be accomplished through two common strategies (1) CRISPR-Cas9 based genomic engineering or (2) transgenes. CRISPR-based systems offer methods to induced genetic perturbations in every cell of the genome. Transgenes have been commonly used in *C. elegans* to express heterologous, modified, or endogenously expressed DNA in specific cell types. Unique combinations of these techniques are becoming more standard to tune and modulate gene expression through development.

1. Measuring calcium activity in single cells with different modified genomic backgrounds is possible using calcium imaging. An appropriate stimulus (odor or light) is often required to evoke a response in a corresponding cell, depolarizing the membrane and opening VGCCs, which corresponds to an increase in cellular fluorescence (ΔF) over time.
2. Monitoring ΔF in different genetic backgrounds show quantifiable differences in channel kinetics, like peak, area, and decay rate.
3. Treating animals with compounds throughout development or acutely may restore altered responses back to wild-type. These compounds may be of interest for further elucidation of genetic pathology. This model assumes that stimulation and recording methods are directly comparable to controls.

In addition to measuring compound exposure effects on odor-evoked calcium responses in *C. elegans*, follow-up work could be completed using the TS1 strain to further characterize the cause of the L1 arrest phenotype (**Fig. 8, 9**). The question still remains whether the TS1 mutation causes a non-functional *egl-19* protein (null by Pat phenotype) (Lee et al., 1997; Williams and Waterston, 1994), or if *egl-19* is indeed functional and is causing developmental arrest due to the expected decrease in channel inactivation (as in humans). Regardless, by which molecular and genetic mechanisms this may occur is likely unknown and worth investigating further. The prior thought (null) is more likely, since this phenotype resembles other hypomorphic *EGL-19* mutant alleles (as well as *pat-5*) (Williams and Waterston, 1994), and by directly antagonizing the channel pharmacologically causes the exact same severe phenotype (Kwok et al., 2006). Also, Heesun attempted to generate an *egl-19* null using CRISPR-Cas9, however a recoverable phenotype was not possible due to early on embryonic lethality also described previously (Lee et al., 1997; Williams and Waterston, 1994). Thus, it is still currently hypothesized that Pat is the null phenotype of *egl-19*, resembling a chromosomal deletion (Williams and Waterston, 1994). Further, a rescue of the TS1 phenotype would be insightful, and possible through either forward or reverse genetic approaches. Genetic suppressor and enhancer screens have already been completed for all GOF and ROF *egl-19* mutants discussed in this Chapter, so a similar approach might be worth trying for the TS1 mutant.

Another worthy idea to test the hypothesis of whether the TS1 mutation is functional or not, would be to control the regulation of *egl-19* expression at different developmental stages in *C. elegans*. A CRISPR-Cas9 auxin-degron system could be used to degrade the *EGL-19* protein tissue-

specifically (like in all neurons or muscle, or both) (Baker et al., 2016; Nishimura et al., 2009; Zhang et al., 2015). This experiment would tell us whether *egl-19* is essential in later developmental stages, and if tissue-specific degradation of *EGL-19* has an effect on behavior, morphology, or calcium activity.

Additionally, more than a dozen point mutations are known in the human version of *EGL-19* (*CACNA1C*) that cause disease (Landstrom et al., 2016), so all of these known and conserved mutations in *C. elegans* using CRISPR-Cas9 HR should be developed. It would be worth knowing if any of these mutations have the same L1 arrest phenotype, or more subtle phenotypes that are directly compatible with conventional techniques used for quantifying behavior, morphology, and calcium activity. Alternatively, new methods for stimulating and imaging cellular activity in these severe phenotypes could be developed, like using Chrimson for activation and hydrogel immobilization (Burnett et al., 2017). Depending on the results, these experiments might support the generation of transgenic animals to express GOF mutations in specific cells or using the endogenous *egl-19* promoter. Since the ROF rescue was successful by this strategy, it might be that over expression of GOF channels, or transgenic GOF expression in ROF backgrounds could yield a combination of effects with different severities, or suppressive behavioral, morphological, or activity-dependent effects that are compatible with traditional microfluidics and compound exposure experiments. Furthermore, investigation of similar effects on auxiliary subunits involved with *egl-19*, or other VGCCs in the worm could be similarly investigated: first make or select mutants, generate imaging lines, detect phenotypes, quantify behavior and calcium activity levels, attempt to restore function with genes or compounds.

Develop and characterize a microfluidic screening technology to identify acute regulators of cellular activity

The robotic platform described in Chapter 3 is versatile, and as such, we expect many interesting future uses. Since appropriate buffer conditions were previously characterized here, and a new proof-of-concept functional screening procedure was successful in identifying transient modulators, a logical next step is to screen a small-molecule library. The same experimental procedure can be set-up as explained, with a pre-determined concentration of compound in each well, either alternating with buffers, or more compact with buffer controls evenly spaced further throughout the integrated multiwell plate and/or delivery protocol. Also, the use of liquid handling robots could decrease manual labor even further for preparation of multiwell plates for integration with the microfluidic device. We expect that some compounds will have similar suppressive effects as did methanol and isopropanol in our preliminary solvent screen.

Experiments of this type will begin to generate large amounts of data, so improvements in analysis automation and data visualization would become increasingly important. Currently, for calcium imaging experiments, each acquired video for each animal requires user input and monitoring since the analysis scripts do not automatically correct for changes in neuron brightness beyond set thresholds, or correct for large animal displacements in microfluidic devices. Therefore, an analysis strategy similar to the one I developed for the plate-based high-content screen, with slight modifications for decreasing tracking errors, could be developed and employed. Streamlining this process, and by developing methods to analyze acquired data in real-time, would overcome the current data analysis bottleneck anticipated for small-molecule

screening experiments. Also, new methods for data driven exploration could improve the overall efficiency and quality of discoveries and relationships observed for each experiment. Increasingly popular platforms like D3js or MATLAB based interactive visualization toolboxes could be two potential avenues for this type of improvement to data processing. Also, multi-dimensional data relationships could be investigated by pairing different calcium response features together, like peak response, peak response time, inactivation rates, *etc.*

Another area of improvement for this method would be to further decrease carryover percent in a more efficient manner. We showed that five sequential rinsing steps reaches a carryover of 0.02% (**Fig. 15, 30**). This level of carryover may be appropriate for more sensitive compound screening, but the rate at which this percent is achieved is slow. We believe carryover is largely due to slightly high backpressure diffusion originating at the robotic inlet (>bp, **Fig. 15d**). However, =bp is critical to prevent the introduction of bubbles into the system, which could ruin experiments. Therefore, a few ideas that might accelerate this process to achieve similar results in a faster time would be to programmatically increase flow rate only during rinse wells, or use immiscible carrier fluids, like oil, to separate the serially delivered liquid compounds and bypass the biological samples. Also, development of a system that ensures proper =bp would be worthy to eliminate any chance of the introduction of bubbles. A thorough comparison of these methods with the proof-of-concept we tested here as a control might be useful (or at least worth considering) before attempting more sensitive (and expensive) drug screens as described above.
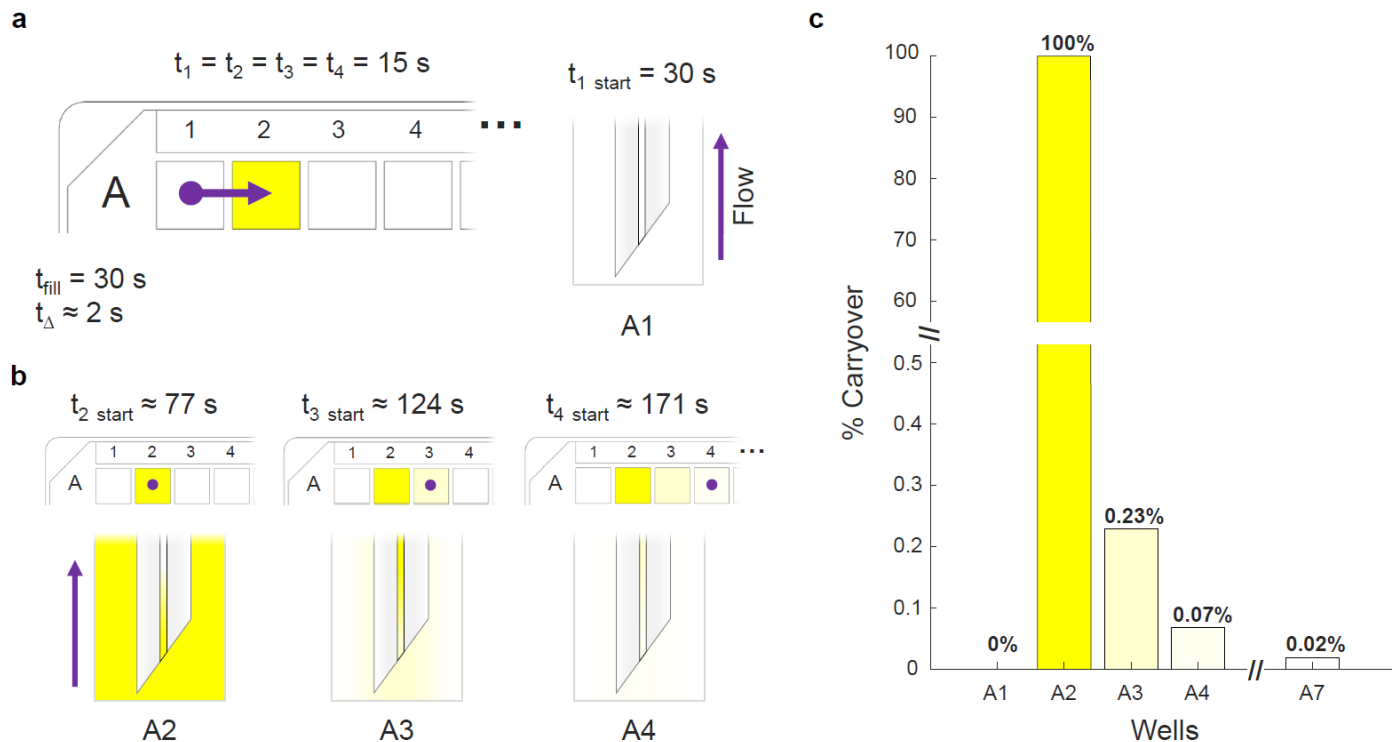
Figure 30. One method for assessment of carryover using fluorescent dye and sequential tubing wash steps.

a. Schematic of multiwell plate set-up with robotic inlet tubing position in A1 (purple dot) towards A4 at the start of an automated experiment to evaluate well-to-well carryover. A 30 s fill time between 2 s of well-to-well tubing switching and 15 s of flow through the robotic inlet and microfluidic device was programmed and acquired for each well position.

b. After the 2 s tubing switch from A1 and a subsequent tubing fill time without recording video for 30 s (t_{fill} schematic represented below) in A2 containing high-concentration fluorescein, the start of camera acquisition began (at 77 s). Subsequently, and autonomously executing the same timing conditions, a 124 second start time is initiated for camera acquisition in A3. This sequence was repeated for four more wells filled with buffer. Slight carryover is shown in each well by diffused fluorescence into the solution after the tubing enters the well (likely due to >bp).

c. Carryover percent normalized to buffer (A1) and brightness (A2). Decay in carryover percent is observed reaching ~0.02% by well A7 (a total of 5 rinse steps).

161

Develop and characterize a screen for compounds that modulate neural activity in living organisms over tractable and long-term durations

For this aim, I have already taken steps towards accomplishing several future applications that are expected to improve the overall scientific impact, as well as commercialization, and adaptability. Four general future applications of this method are enabled by its versatility (**Fig. 31**). We showed in this Chapter that it is possible to elicit and record calcium responses in the same neurons in whole, intact, living animals. Using this "same cell" approach, we were able to appropriately characterize baseline excitation conditions to more specifically elicit calcium responses to only the red light pulse. Now that optical and ATR experimental parameters and treatments have been characterized by direct observation in the same cell, we can develop strains that express Chrimson and GCaMP in different cells, assuming that these conditions are conserved. Doing so, we would be able to more directly monitor compound effects that disrupt intercellular signaling, not possible in cell based functional screens. Additionally, Chrimson could be expressed in one or more cells, while GCaMP is still recorded from one. Also, different cell types (or parts of cells, like the axon or dendrites) could be monitored or stimulated (like neuron-muscle), to identify more broadly acting effects not limited to neural circuitry. It is important to consider, however, that an intercellular approach may yield more variability in response signal, which could reduce the overall sensitivity of the method, but would still identify strong primary hits. In addition to generating new strains, the latter ideas would only require modified analysis scripts, not the method itself. New fluorescent indicators that measure voltage could also be used to detect modulators of membrane potential, or hyperpolarization of cells could be used to detect any compounds that enhance cellular activity and related biological processes.

1. Stimulate and monitor from other neurons or cell pairs and groupings.
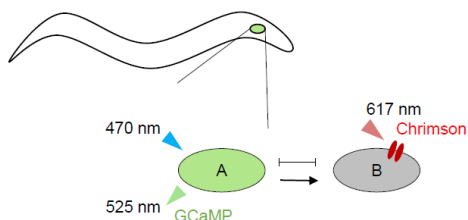
2. Screen human disease models, other organisms, *etc*.

3. Pre-treat and grow animals on plates with RNAi or compounds.
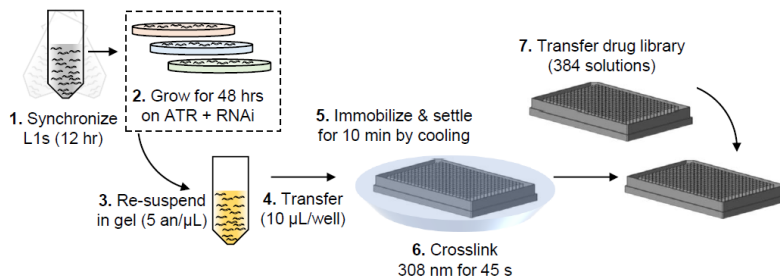
4. Analyze results in real-time and develop interactive, multi-dimensional data visualizations.
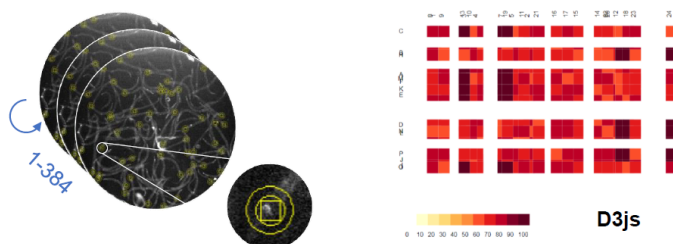
Figure 31. At least four future potential high-impact projects topics and applications using the plate-based high-content optogenetic functional screening platform.

1. Use new animal strains expressing GCaMP and Chrimson in different neurons or cell pairs (or combinations thereof) for the same Lopac screen could yield novel modulators of neural circuits (intercellular vs. intracellular).
2. Use human disease model animals to identify compounds that interact with disease-specific pathways.
3. At several animal preparation stages, different treatments could be applied through animal development. For example, RNAi might be used since animals are synchronized on standard NGM plates. Further, animals could be exposed to various compounds through development. As for project #2, conditions could be multiplexed, like combinations of RNAi and compound exposure, as well as the use of disease models for primary or secondary screens.
4. Lastly, improvements in automated data analysis (like automatic selection of neurons) would eliminate the laborious manual process (although highly accurate) of neuron position selection (left). Also, parallel data acquisition and processing would facilitate pseudo real-time data analysis for rapid identification of positive hits. Further, automatic generation of high-content interactive data visualization techniques could support data driven exploration for novel hypothesis generation and pattern identification (right).

163

Second, human disease model strains can be used to identify more specific compound effects involved in activity-dependent disorders. For example, any of the *egl-19* mutants are suitable candidates for evaluation of compound hits after completing a primary screen with wild-type, or these mutants could be used in the screen directly. Using disease model animals with similar stimulation and recording protocols described above could improve the overall impact of this new technology, which might lead to more targeted therapeutics for secondary screening assays. However, it is important to consider that some mutant strains might need adapted growth and synchronization protocols due to resulting phenotypes, like impaired or irregular developmental timing, or low brood sizes.

As a proof-of-concept for project idea #2, I generated several *egl-19* ROF and GOF mutants that co-express Chrimson and GCaMP in the same neuron studied earlier. The ROF mutants show no activation to red-light stimulus, while a rescued strain that expresses both WT and a ROF mutation shows a partially restored response (**Fig. 32**). From this experiment, we learned that *egl-19* is required for Chrimson-induced activation, and that function can be genetically restored and monitored using transgenes. Also, these light-activated responses are linked to *egl-19*, providing a starting point for elucidating compound target pathways that also suppress calcium activity. It is possible still, however, that indirect compound effects are noticeable, since we found that ivermectin suppresses calcium activity, while resistant animals could be tested to confirm these indirect target effects. Further, the ROF strain could be used to identify enhancers of calcium activity (or treatment with parthenolide), while different level-of-function strains might yield more specific effects on voltage-gated calcium channel function and related

164

pathology. As for animals co-expressing GCaMP and Chrimson in AWA with GOF *EGL-19*

backgrounds, we noticed that there might be slight differences in peak (activation) response and

inactivation kinetics during prolonged (100 s) stimulation, and worth investigating further and

quantifying using integrated versions of these strains (**Fig. 33**). The GOF experiments were

completed using microfluidics for immobilization and analysis as described in Chapter 1 (**Fig. 33**),

while the ROF and ROF rescue experiments were completed using the hydrogel immobilization

method, soaking in ATR for at least 2 hours (**Fig 32**). A standardized protocol, like NGM ATR plate

treatment of the GOF and ROF integrated strains (and ROF rescue) using the hydrogel

immobilization method in multiwell plates should be completed for higher confidence and

quantitative comparisons across these independent genotype groups, although these

preliminary data are promising. Higher-resolution imaging of these genotypes may also yield

differences in excitability from compartmentalized neural regions, explained further below (**Fig.**

34).
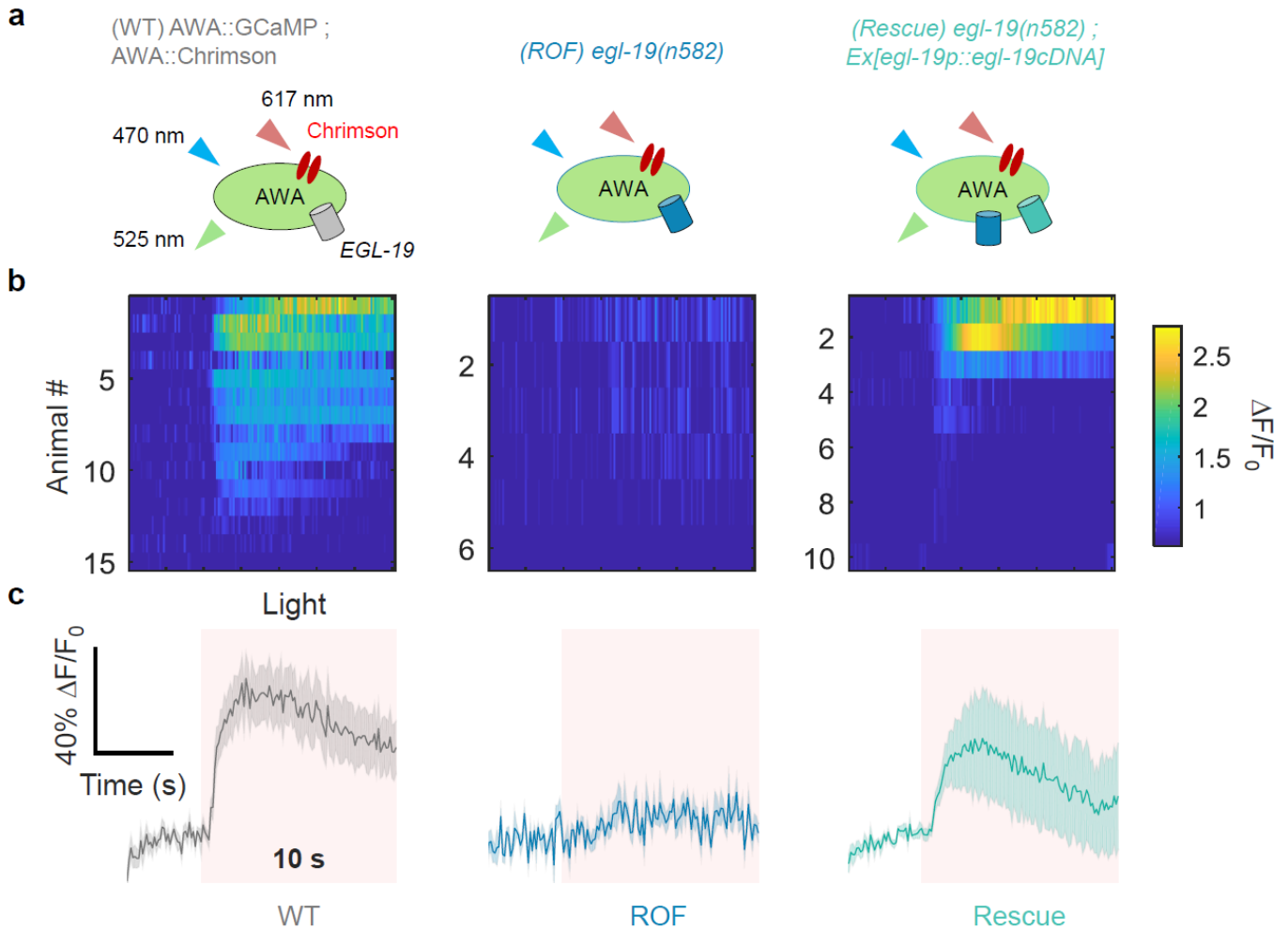
Figure 32. Chrimson-evoked calcium responses depend on the voltage-gated calcium channel EGL-19.

a. Schematics of three genotypes with wild-type (WT), a reduction-of-function background mutation (ROF), and ROF endogenous transgenic rescue all co-expressing both GCaMP and Chrimson in the AWA chemosensory neuron.

b. Heat maps represent individual animal $\Delta F/F_0$ calcium responses from one 10 second pulse of 617 nm light corresponding to the genotype schematics in a directly above. Number of animals analyzed is along the y-axis, with time along the x, corresponding to pink shading directly below in c.

c. Corresponding average $\Delta F/F_0$ calcium responses traces from the individual heat map traces as shown directly above in b and genotypes in a. Shading represents SEM.

166
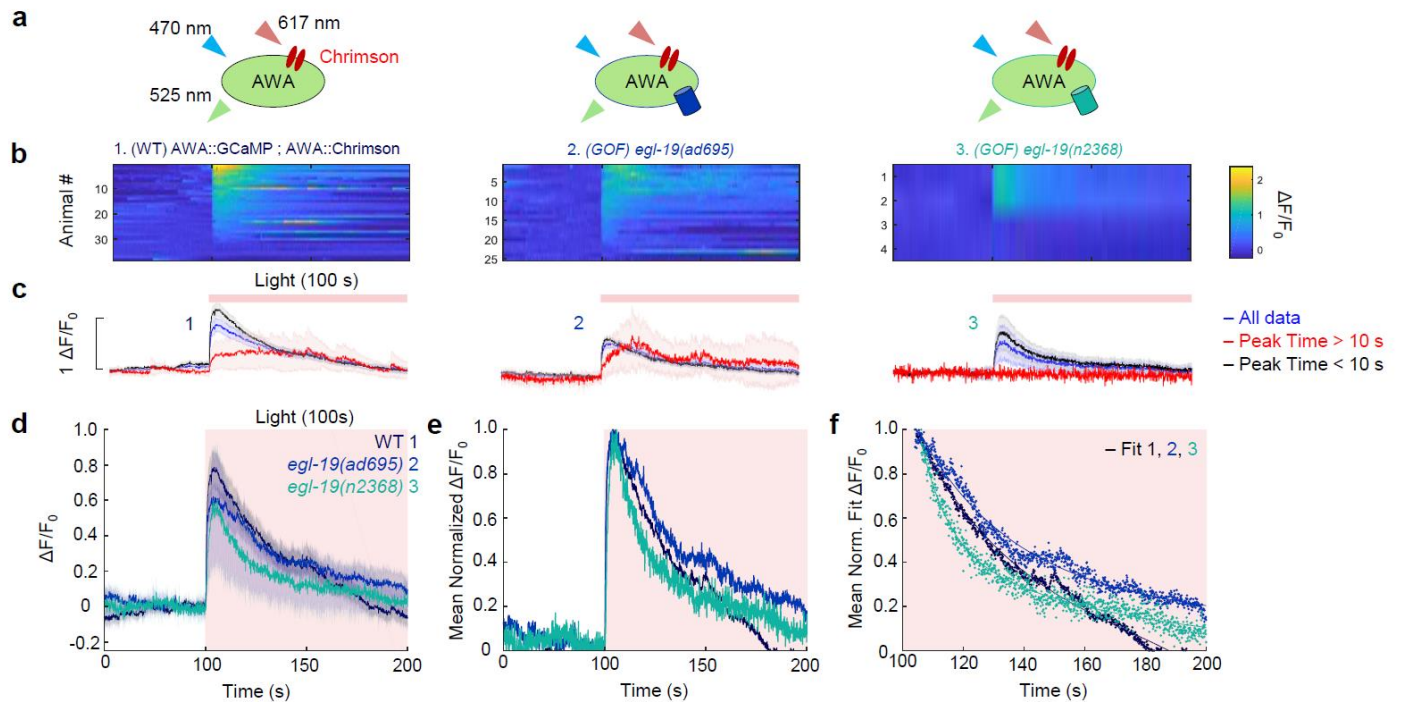
Figure 33. Chrimson-evoked calcium activity in EGL-19 GOF backgrounds have altered calcium kinetics.

a. Schematics of three genotypes with wild-type (WT), a less severe gain-of-function background mutation (GOF), and more severe GOF background mutation all co-expressing both GCaMP and Chrimson in the AWA chemosensory neuron.

b. Heat maps representing all individual calcium traces across ten independent genotypes, corresponding to labels in b, with a 100 s pulse exposure to 617 nm light (pink bar, below). Sample sizes (individual animals) are shown along the y-axis.

c. Average $\Delta F/F_0$ calcium response traces for all genotypes and data traces (blue), corresponding to individual heat maps in a. Animals that took longer than 10 s to reach their maximum peak response are averaged and shown in red. Filtered traces that do not include red traces are shown in black, and are used for all subsequent plots and quantification parameters. Corresponding trace shading represents SEM.

d. Mean $\Delta F/F_0$ calcium response traces overlaid for all genotypes corresponding to a and b show altered calcium response kinetics. Pink fill represents the presence of 100 s of 617 nm light pulse. Corresponding trace shading represents SEM.

e. Average normalized $\Delta F/F_0$ calcium response traces all genotypes from a-c. Pink fill represents presence of light stimulus.

f. Mean normalized $\Delta F/F_0$ calcium response traces from e with a second degree polynomial decay fit (thin lines) for each genotype. Pink fill represents presence of light stimulus.

From these data, it seems that an optogenetically-evoked calcium response (using Chrimson) is largely dependent on *egl-19* in *C. elegans*. So, I established a model to reason for and speculate this result, which is worth investigating further and comparing quantitatively (**Fig. 34**). Animals expressing Chrimson and GCaMP in AWA with an *egl-19* ROF background exhibit weak to no calcium response in the presence of a 617 nm light pulse (**Fig. 32**). Since these measurements were made by recording calcium activity in the cell body (soma), it is likely that *egl-19* is highly expressed in the soma of neuons (as supported by our *EGL-19::GFP* data). Due to this robust observation, I hypothesize that the two other VGCCs *cca-1* and *unc-2* are not be localized to the soma in *egl-19* ROF animals, and likely wild-type animals. Therefore, by measuring calcium responses in the axon of AWA in *egl-19* ROF backgrounds, robust calcium responses may still exist, likely due to presynaptic expression and distribution of *unc-2*, which has been reported previously in *C. elegans* sensory and motor neurons (Frøkjær-Jensen et al., 2006; Saheki and Bargmann, 2009). The CaV3 gene, *cca-1*, has not been investigated extensively in *C. elegans* neurons, but has been shown to regulate pharyngeal muscle activation (Shtonda and Avery, 2005). Thus *cca-1* might only be primarily expressed in muscle, or in dendrites of neurons, while *unc-2* is mainly in the axon, and *egl-19* in the soma. To approach this functional VGCC localization and expression concept, ROF mutations should be made for each calcium channel in *C. elegans* to determine region specific calcium responses to optogenetic activation. Likewise, fluorescently labeled VGCCs using CRISPR-Cas9 HR (like our *EGL-19::GFP* strain) would directly show localization (or co-localization) of each channel in *C. elegans*, assuming GFP or other fluorescent proteins do not effect proper membrane trafficking. Additionally, further investigation regarding the role of auxiliary subunits and *calf-1*, a calcium channel localization factor, in *C. elegans* could

help identify the role of VGCC function and molecular mechanisms involved in channel expression and regulation. These differences could also be examined, compared, and further investigated similarly using microfluidics for odor-induced calcium responses in *C. elegans* neurons, as I observed that *egl-19(n582)* dendrites in AWA respond to 1.15 µM diacetyl (results not shown), while the soma has a significantly reduced calcium response compared to wild-type (**Fig. 14**).
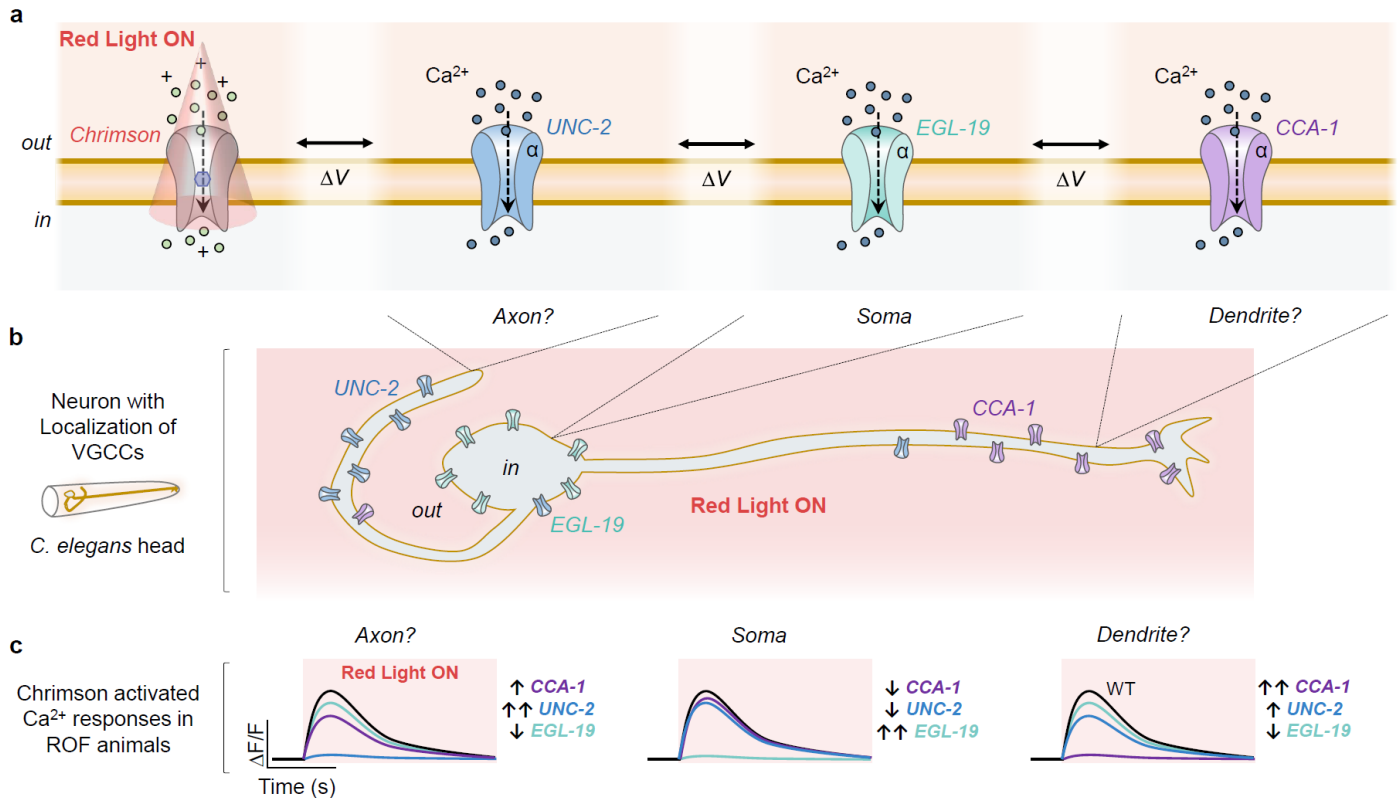
Figure 34. A model representing VGCC localization and function probed by optogenetic stimulation and recording in a single sensory neuron of C. elegans.

a. A red-light induced optogenetic response opens the Chrimson channelrhodopsin in the presence of All-*Trans* Retinal (purple shape) and generates a membrane potential due to flux of positively charged ions across the entire cell membrane. The membrane potential triggers voltage-gated ion channels to open, which may be independently localized to the axon, soma, and dendrites. From current literature and results shown here, there is reason to believe that the VGCC *UNC-2* localizes to presynaptic terminals (axon), *EGL-19* localizes to the cell body (soma), and *CCA-1* possibly localizes to dendrites or is weakly expressed throughout this sensory neuron.

b. A schematic representing a single sensory neuron (AWA) in the *C. elegans* head with hypothesized localization of VGCCs throughout the axon, soma, and dendrites (zoom-out from a).

c. Using GCaMP and Chrimson to monitor and stimulate this neuron *in vivo*, I hypothesize that a ROF *unc-2* channel is largely responsible for the calcium response in the axon. Similarly, and from my data shown above, *egl-19* is largely responsible for the calcium response in the soma. Less clear is the role of *cca-1*, which might be expressed in the dendrite, but could be functionally confirmed in a ROF mutant. Altogether, discovering where VGCCs are distributed, expressed, and function in single cells could be further investigated using this model and functional method. Also, confirming the location of VGCCs by GFP tags in single cells or throughout the organism would be another important piece of evidence to go along with functional observations.

170

Third, the multi-step protocol prior to depositing and immobilizing animals in multiwell plates for screening allows for perturbation of developmental stages and/or various pre-treatment conditions. We show that developing animals on ATR is required for eliciting light-induced calcium responses in worms; therefore, it is directly assumed that other pre-treatment conditions could be effective in altering calcium response dynamics. For example, pre-treating animals on ATR plates also containing RNAi would allow for specific knockdown of genes or genetic pathways that might have no known effect on calcium activity. Also, treating all animals on a specific compound (or compound(s)) could inhibit the function of genes or proteins prior to screening, which might lead to new multi-factor compound effects on calcium activity. Additionally, animals could be screened at different developmental stages, assuming the timing and ATR concentration effects are similar across established treatment conditions. If younger ages are used, this may allow for increased throughput due to their small size by adapting 1536 well plates, stage step size, and higher magnification optics. If similar low-magnification optics are used with these higher-content multiwell plates, then multiple wells with different treatments could be stimulated and imaged at a time with 4X throughput.

It is also possible to recover animals after being embedded in the gel from multiwell plates (**Fig. 35**). To demonstrate effective animal immobilization and recovery, one well was set up by manual picking to contain 10 μL of ~40 young adult animals, as described previously. A 10 s video was recorded before and after immobilization using a modified bright-field microscopy set-up described above, showing freely thrashing animals then restricted animal movement within the depth-of-field for fluorescent recording, respectively. The gel disk was removed by gently picking

171

out with fine tweezers and broken to release more encapsulated animals. This feature of the hydrogel is exciting, since treated and recorded individual animals can be propagated after screening to further investigate developmental effects, sequence individuals, or generate F1 progeny to test any offspring compound effects due to heritability.
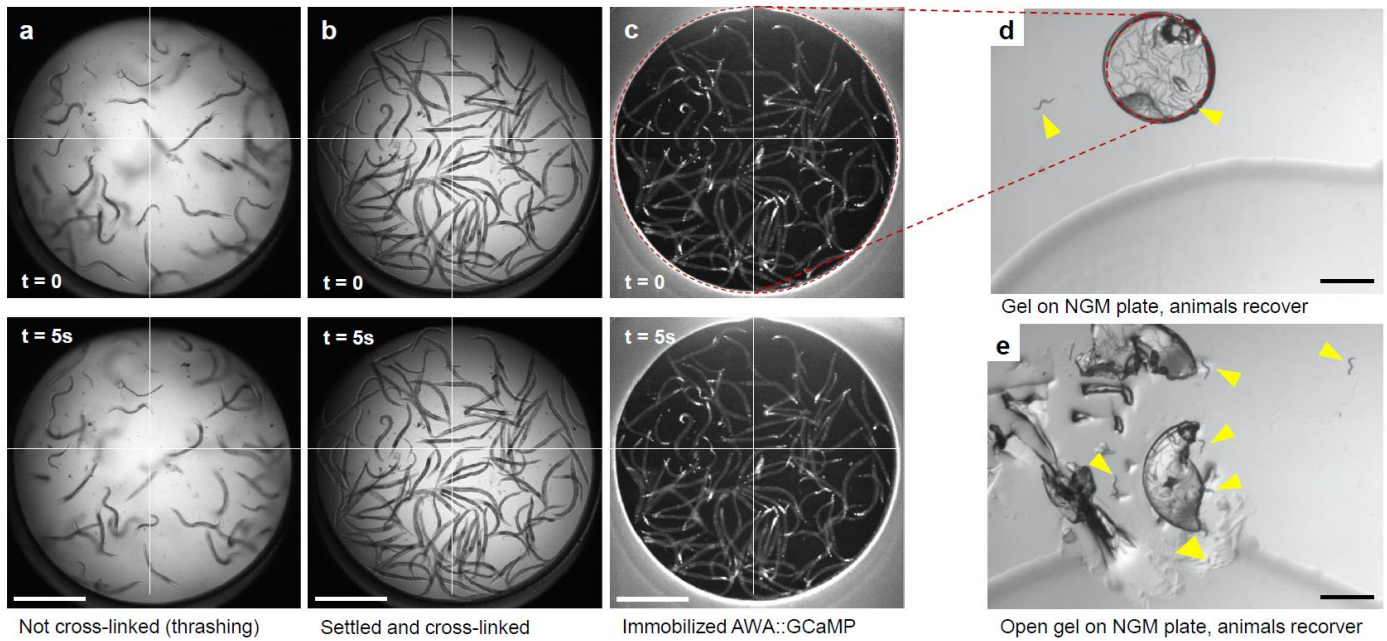
Figure 35. Immobilization of C. elegans *in one well of a 384 well plate using the hydrogel, and successful recovery of embedded animals to standard NGM plates.*

a. (above) The first frame of a 30 second bright-field video demonstrating different z-depth positions of ~40 animals in the liquid phase of the hydrogel. (below) A frame 5 seconds after the first, demonstrating relative animal movement to the overlaid grid lines to the time point above. Scale bar, 500 μm.
b. (above) The first frame of a 30 second bright-field video demonstrating uniform z-depth position of the same animals at the bottom of the well plate after settling and crosslinking. (below) A frame 5 seconds after the first, demonstrating no relative animal movement to the overlaid grid lines to the time point above. Scale bar, 700 μm.
c. (above) Same description as in b, now a fluorescent (470 nm) excitation image, shows fluorescent animal tails and AWA neurons. Scale bar, 700 μm.
d. A low magnification bright-filed image demonstrating successful removal of the gel disk from c or b on a standard NGM plate with OP50 *E. coli*. Yellow arrows represent animals that escaped the gel disk. Scale bar, 1.4 mm.
e. An image similar to d at a later time point shows a dissected gel to assist animals in escaping the hydrogel for propagation and follow-up assays. Yellow arrows show that several more animals were able to escape freely. Scale bar, 1.4 mm.

Finally, future improvements in data analysis and visualization could lead to improved efficiency of identifying and discovering hits with higher accuracy. I began working on a custom semi-automated platform for the analysis of this high-content data, with a streamlined procedure for visualizing the data, interacting with plots, and identifying hits from compound screens (**Fig. 36**). However, the processing of data could be completely automated. The only bottleneck limiting complete automation of analysis is the identification of neurons. One attempt described earlier can automatically identify neurons using an image subtraction response-threshold approach, but has low accuracy of identifying true neurons. Since this algorithm relies on changes in image (neuron object) fluorescence, the program can directly identify wells that have few animal responses (results not shown). This is an indirect way of identifying suppressor hits, which requires manual follow-up to confirm true compound effects. Therefore, developing an algorithm that can identify neurons more accurately and automatically would be useful for faster and highly accurate data processing.
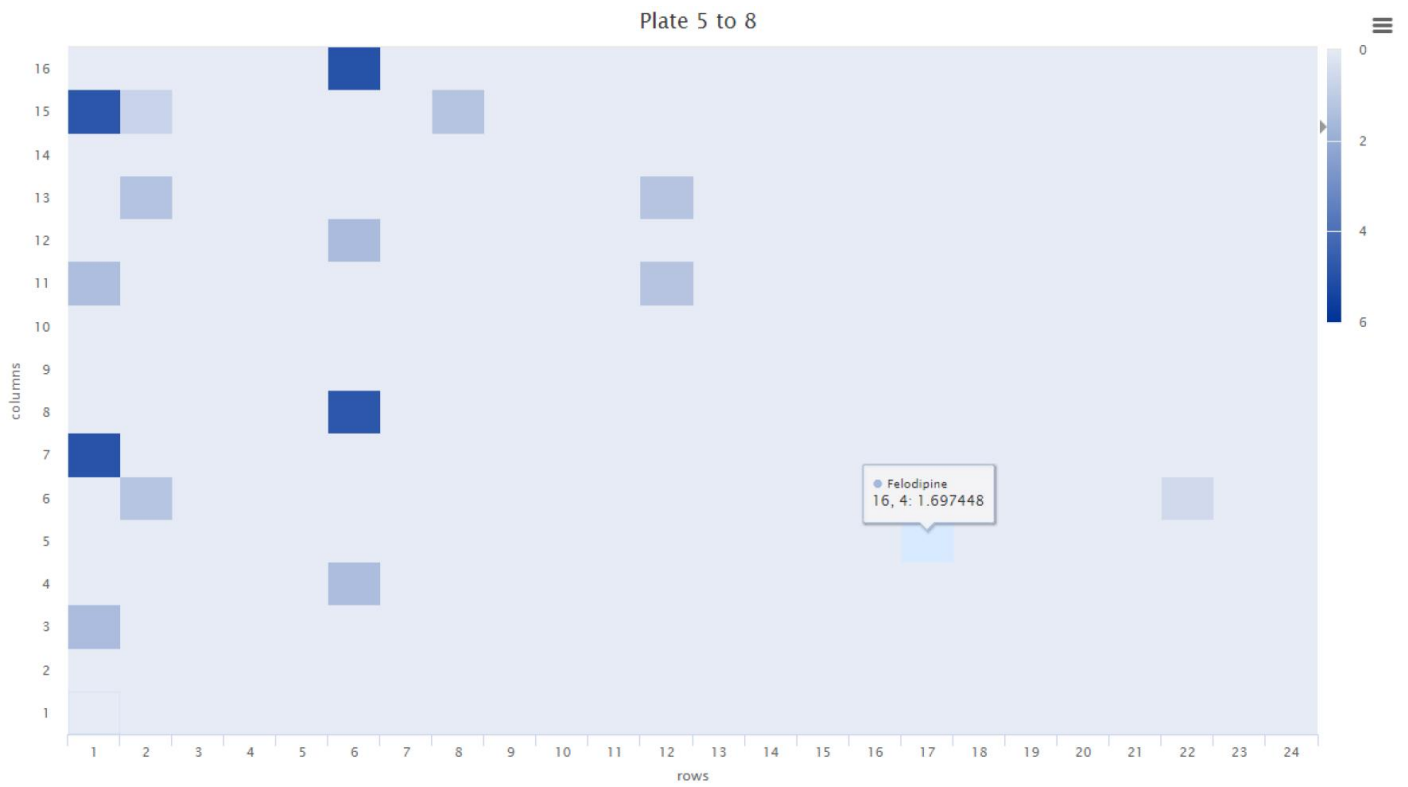
Figure 36. A MATLAB-based interactive heat map visualization for high-content screening data.

One plate from the high-content screen showing hits (dark blue) with relative fold changes greater than three standard deviations from the control mean. Darkest blue wells are 100 µM nemadipine-A treatment effects.

Secondly, improving the data analysis pipeline overall would lead to more rapid identification of hits in pseudo-real time. For example, after each image (or video frame) is acquired during experimentation, neuron positions could be identified and calcium response data points could be analyzed and collected, (both automatically) such that after each well is finished stimulation and recording, data sets are automatically available for analysis. These data sets could then be fed in an automatically updated que for processing. In other words, after each well stimulus, the data analysis pipeline is built to show results as the data is being collected. The ultimate data collection and analysis procedural goal would then be to execute the screen script and have all data analyzed and processed for the automatic discovery of hits. To begin achieving this goal, I developed a proof-of-concept analysis program in MATLAB that mimics the NT ImageJ script (**Fig. 37**). Briefly, image frames are loaded into MATLAB, and full-resolution matrices containing individual pixel values for all video frames are collected and used for calculating animal integrated density and local background. This method yields calcium response traces similar to the NT ImageJ macro. By using MATLAB for this process, parallel computing of acquired data for analysis is possible, which accelerates data processing. To compare a complete analysis of the screen dataset using ImageJ NT with MATLAB NT would require additional loops that remain to be implemented. For pseudo-real time analysis, future work would also require MATLAB to update its video processing que while data is being collected during the experiment. Alternatively, faster computer processors could reduce the delay of image analysis after the experiment is complete, which might be sufficient. However, being able to observe results while the experiment is running is ideal, such that any complications or unexpected errors could be addressed without needing to wait until the experiment is finished (saving 24 hours or more time).
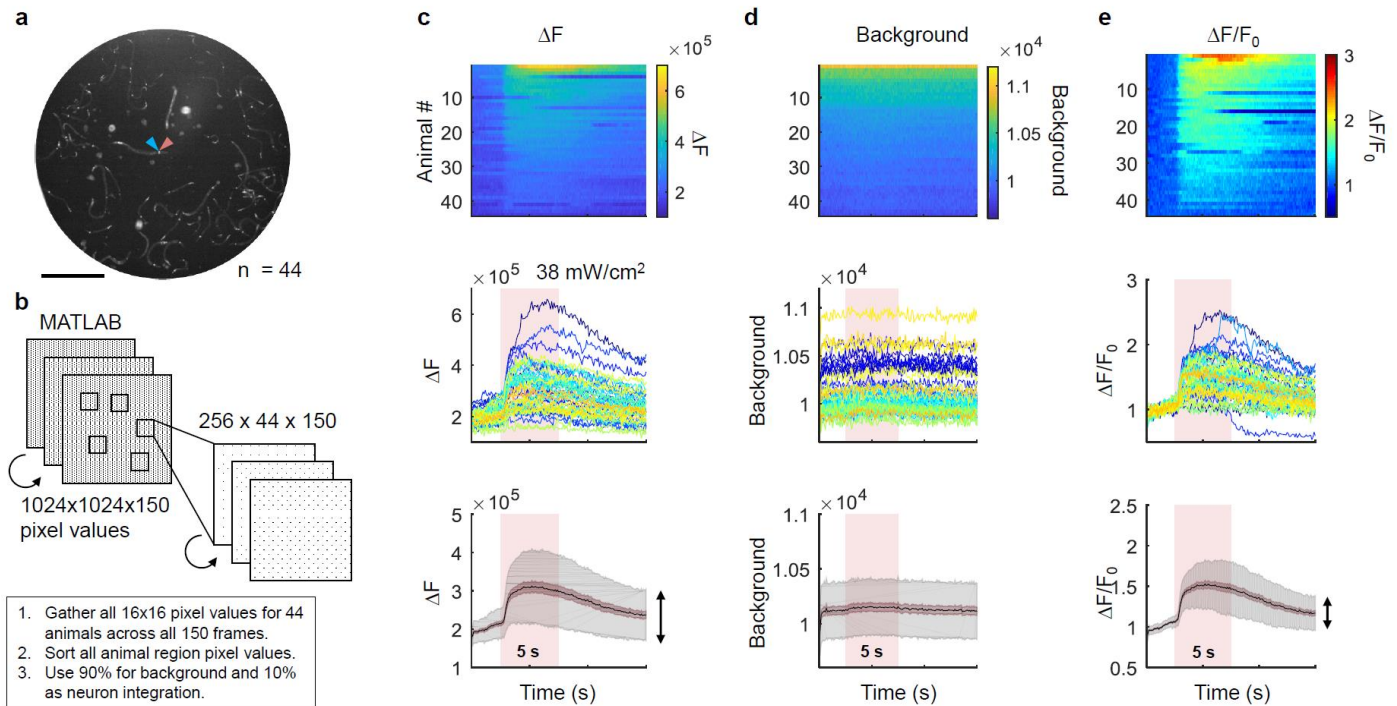
Figure 37. Development of a MATLAB NeuroTracker version with potentially improved background correction algorithm by individual animal pixel rank order for real-time data analysis.

a. One well of 384 containing 44 immobilized animals co-expressing GCaMP and Chrimson in the AWA chemosensory neuron. Arrows represent excitation wavelengths. Scale bar, 700 µm.

b. A brief overview of the MATLAB analysis pipeline for gathering all 16x16 pixel regions based on animal x-y positioning for each 150 1024x1024 pixel video frames. For one 15 s (10 fps) video with 44 animals, 6,600 sorted columns are obtained and used for calculating IntDen (10% of signal) and Background Density (90% of signal) to finally calculate ΔF, F_0, and $\Delta F/F_0$.

c. A heat map representation of ΔF, the background subtracted animal responses using an automated pixel rank order method in MATLAB, sorted in descending order by peak response during light stimulus. Individual animal traces are also shown below, and average well ΔF traces with SEM (darker red shading) and SD (gray shading).

d. A heat map representation of the 90% background for all animal positions using the automated pixel rank order method in MATLAB. Individual animal background traces are also shown below, and average background traces with SEM (darker red shading) and SD (gray shading).

e. A heat map representation of $\Delta F/F_0$ from c and d using the automated pixel rank order method in MATLAB. Individual animal traces are also shown below, and average well $\Delta F/F_0$ traces with SEM (darker red shading) and SD (gray shading). Double ended arrow highlights spread in SD for all average well traces.

Also, one feature that inspired the development of the MATLAB NT version was being able to access all raw pixel values per image frame, which was not possible using ImageJ without contacting the developers (**Fig. 38**). This was important to us while considering new methods for detecting the most accurate background fluorescence signal, which is expected to improve the accuracy of data for stronger statistical comparisons across well treatments and individual animals. Currently, background signal is estimated based on a user-desired set area around the animal's head, centered on the neural signal of interest, and scaled by the region used for calculating integrated density of the true fluorescence signal. This estimation is affected by several sources of artifact, like brightness, slight animal movement (~19–38 µm), or overlap of animals, which can generate errors (false positives and negatives), resulting in decreased accuracy of true neural signal used for comparisons (**Fig. 38d-f**). However, since ~45 animals are recorded per well, the probability of this error affecting the true signal is uniform for individual wells and across multiwell plates, allowing for comparisons between wells and treatments over time. Still, greater accuracy could be accomplished. Therefore, considering that the region used for calculating integrated density contains more pixel values than the true signal itself, which was purposely used to accommodate for slight animal movement, could be used to reduce error and improve signal accuracy. Nearly 10% of the true signal (~25 pixels, or 12x12 µm) in this box is the neuron, while the other 90% is likely background noise. So, by sorting pixel intensity values inside this box, for all animals and all video frames, a more accurate background corrected fluorescence signal based on the raw true and local background signal could be obtained. By using this method of analysis, we aim to improve standard deviation for animal averages across each well in a multiwell plate (**Fig. 37e**). Although current positive and negative controls already show

significant differences without this improvement, more sensitive detection of compounds that subtly effect peak activity or curve area, decay rate, *etc.* with streamlined real-time analysis and improved Z-score for HTS could be achieved.
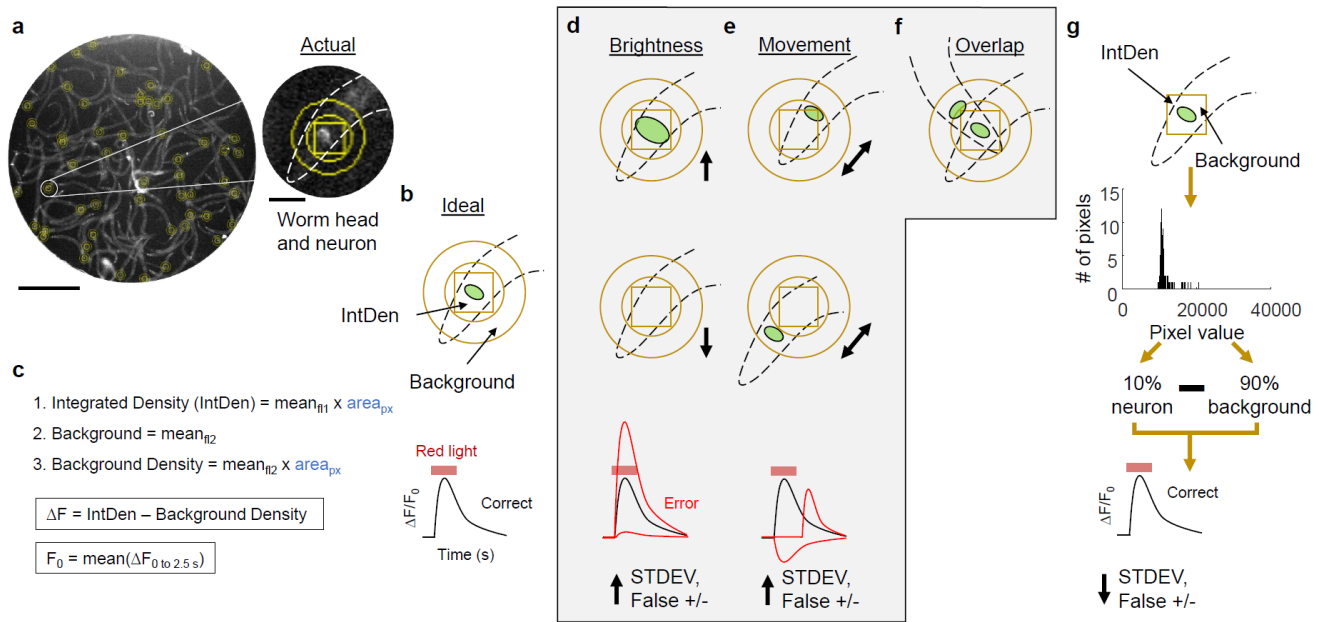
Figure 38. Important scenarios, considerations, and limits for improving automation and accuracy of neuron identification and background correction: towards a more efficient NeuroTracker analysis strategy.

a. One well of a 384 well plate showing ~40 animals expressing GCaMP in the AWA chemosensory neuron. Zoom in shows the head one animal with a 16x16 pixel box for integration of pixel intensity, and two circles forming a ring around the AWA neuron to select an average local background intensity for correction. Scale bar, 700 µm (left), 40 µm (right).

b. An ideal schematic representing the zoom-in shown in a, with arrows labeling the region for calculation of integrated density (IntDen) of the neuron position and background ($mean_{fl2}$).

c. Calculation of $\Delta F/F_0$ from the parameters show in b. Integrated density (IntDen) is the product of mean pixel intensity within the 16x16 pixel box show in b ($mean_{fl1}$) and pixel area (256) of the respective IntDen box ($area_{px}$). The local background fluorescence is calculated as the mean pixel intensity from the ring outside of the 16x16 pixel box ($mean_{fl2}$). The Background Density is calculated as the product of $mean_{fl2}$ and the $area_{px}$ for appropriate scaling. Next ΔF is calculated as the difference between IntDen and Background Density. These true values are automatically recorded and calculated for every frame of every video for every animal position recorded. After the recording of all these values is complete, F_0 is calculated as the mean of all ΔF frames before the stimulus pulse start for each animal. Finally, ΔF is the dividend and F_0 is the divisor to obtain appropriately scaled $\Delta F/F_0$ calcium response traces. Ideal mean $\Delta F/F_0$ calcium response traces during red light stimulation with no standard error or deviation of all individual $\Delta F/F_0$ animal traces is illustrated as the black trace to the right.

d. One potential cause for tracking error may result from differences in baseline neuron brightness. This artifact is possible in part to differences in GCaMP expression levels or slight differences in animal z-depth within the hydrogel. This artifact could increase standard deviation or false positives and negatives due to non-real large ΔF, or low signal to noise.

e. The large 16x16 pixel box was chosen in part to accommodate for slight movement artifacts without need to implement inefficient dynamic tracking algorithms; however, in rare cases, animals may still move outside of the box. This tracking error can result in either false negative ΔF traces, or delayed ΔF increases, leading to large standard deviations and effects on trace shape parameters.

f. A third possibility of error is that animal body overlap of two or more neurons leads to a combination of all three causes of error (inaccurate local background subtraction or movement artifacts).

g. An analysis strategy that could potentially correct for all types of error described in d-f is shown. Using the 16x16 pixel box to calculate both IntDen and Background Density is proposed. The AWA neuron is estimated to be 10% of the 256 pixels (~25 px), while the other 90% is background signal. By rank ordering the 90% background pixel intensity values for each frame for all animals and videos, a more accurate representation could be achieved, and subsequent individual ΔF, F_0, and $\Delta F/F_0$ may be more representative for each well. Additional algorithms that detect more accurate neuron pixel percentages for each frame could also improve this analysis method.

Summary of future directions and applications

In summary, each aim presented here has led to fruitful and promising applications and projects that will be beneficial to the lab and scientific community as a whole. For aim 1, human channelopathy diseases can be made in *C. elegans* to investigate severe or subtle (or combinations of) phenotypes in behavior, morphology, or calcium imaging. Depending on the results, which might be unexpected (like the TS1 mutant), follow-up genetic or compound suppressor screens could be used to identify novel pathology and therapeutic targets for human disease in these organisms. For aim 2, I developed a new method to screen for compounds that affect optogenitcally-evoked calcium activity. Since a pilot screen was useful in identifying appropriate buffer conditions, this technology is ready to screen a library of compounds in a similar manner with high statistical power using paired comparisons. For aim 3, I developed a new functional screening method for whole organisms that led to the identification of several compounds that suppress (and one that enhances) calcium activity in *C. elegans* over 18 hours of exposure at repeat time points. These primary hits should be further characterized by generating dose response curves and finding a real IC_{50} value. Due to the high-content nature of this method, data driven exploration can be developed for a more efficient functional drug screening pipeline using whole organisms, while other modifications to the protocol can simply be developed due to its versatility. Altogether, the new technologies and biology discovered here opens many different avenues of future research and development to continue to achieve our long-term goal.

181

Chapter 6 Bibliography

1. Adams, P.J., and Snutch, T.P. (2007). Calcium Channelopathies: Voltage-Gated Calcium Channels. In Calcium Signalling and Disease, (Springer, Dordrecht), pp. 215–251.
2. Ahmed, R.M., Ke, Y.D., Vucic, S., Ittner, L.M., Seeley, W., Hodges, J.R., Piguet, O., Halliday, G., and Kiernan, M.C. (2018). Physiological changes in neurodegeneration — mechanistic insights and clinical utility. Nature Reviews Neurology.
3. Ahringer, J. (2006). Reverse genetics. WormBook.
4. Akerboom, J., Chen, T.-W., Wardill, T.J., Tian, L., Marvin, J.S., Mutlu, S., Calderón, N.C., Esposti, F., Borghuis, B.G., Sun, X.R., et al. (2012). Optimization of a GCaMP calcium indicator for neural activity imaging. J Neurosci *32*, 13819–13840.
5. Akerboom, J., Carreras Calderón, N., Tian, L., Wabnig, S., Prigge, M., Tolö, J., Gordus, A., Orger, M.B., Severi, K.E., Macklin, J.J., et al. (2013). Genetically encoded calcium indicators for multi-color neural activity imaging and combination with optogenetics. Front Mol Neurosci *6*, 2.
6. Albert, P.R. (2014). Light up your life: Optogenetics for depression? J Psychiatry Neurosci *39*, 3–5.
7. Albrecht, D.R., and Bargmann, C.I. (2011). High-content behavioral analysis of Caenorhabditis elegans in precise spatiotemporal chemical environments. Nature Methods *8*, 599–605.
8. Anikeeva, P., Andalman, A.S., Witten, I., Warden, M., Goshen, I., Grosenick, L., Gunaydin, L.A., Frank, L.M., and Deisseroth, K. (2011). Optetrode: a multichannel readout for optogenetic control in freely moving mice. Nat Neurosci *15*, 163–170.
9. Ardhanareeswaran, K., Mariani, J., Coppola, G., Abyzov, A., and Vaccarino, F.M. (2017). Human induced pluripotent stem cells for modelling neurodevelopmental disorders. Nature Reviews Neurology *13*, 265–278.
10. Arnaout, R., Ferrer, T., Huisken, J., Spitzer, K., Stainier, D.Y.R., Tristani-Firouzi, M., and Chi, N.C. (2007). Zebrafish model for human long QT syndrome. PNAS *104*, 11316–11321.
11. Arribere, J.A., Bell, R.T., Fu, B.X.H., Artiles, K.L., Hartman, P.S., and Fire, A.Z. (2014). Efficient Marker-Free Recovery of Custom Genetic Modifications with CRISPR/Cas9 in Caenorhabditis elegans. Genetics *198*, 837–846.
12. Aubry, G., and Lu, H. (2017). Droplet array for screening acute behaviour response to chemicals in Caenorhabditis elegans. Lab Chip.
13. Bader, P.L., Faizi, M., Kim, L.H., Owen, S.F., Tadross, M.R., Alfa, R.W., Bett, G.C.L., Tsien, R.W., Rasmusson, R.L., and Shamloo, M. (2011). Mouse model of Timothy syndrome recapitulates triad of autistic traits. PNAS *108*, 15432–15437.
14. Baker, O., Gupta, A., Obst, M., Zhang, Y., Anastassiadis, K., Fu, J., and Stewart, A.F. (2016). RAC-tagging: Recombineering And Cas9-assisted targeting for protein tagging and conditional analyses. Scientific Reports *6*, 25529.
15. Barrett, C.F., and Tsien, R.W. (2008). The Timothy syndrome mutation differentially affects voltage- and calcium-dependent inactivation of CaV1.2 L-type calcium channels. PNAS *105*, 2157–2162.

16.	Bazopoulou, D., Chaudhury, A.R., Pantazis, A., and Chronis, N. (2017). An automated compound screening for anti-aging effects on the function of C. elegans sensory neurons. Scientific Reports *7*, 9403.

17.	Bett, G.C., Lis, A., Wersinger, S.R., Baizer, J.S., Duffey, M.E., and Rasmusson, R.L. (2012). A Mouse Model of Timothy Syndrome: a Complex Autistic Disorder Resulting from a Point Mutation in Cav1.2. N Am J Med Sci (Boston) *5*, 135–140.

18.	Bhat, S., Dao, D.T., Terrillion, C.E., Arad, M., Smith, R.J., Soldatov, N.M., and Gould, T.D. (2012). CACNA1C (Cav1.2) in the pathophysiology of psychiatric disease. Prog Neurobiol *99*, 1–14.

19.	Bhatia, S.N., and Ingber, D.E. (2014). Microfluidic organs-on-chips. Nature Biotechnology *32*, 760.

20.	Blow, N. (2007). Microfluidics: in search of a killer application.

21.	Boczek, N.J., Best, J.M., Tester, D.J., Giudicessi, J.R., Middha, S., Evans, J.M., Kamp, T.J., and Ackerman, M.J. (2013). Exome Sequencing and Systems Biology Converge to Identify Novel Mutations in the L-Type Calcium Channel, CACNA1C, Linked to Autosomal Dominant Long QT Syndrome. Circ Cardiovasc Genet *6*, 279–289.

22.	Boczek, N.J., Ye, D., Jin, F., Tester, D.J., Huseby, A., Bos, J.M., Johnson, A.J., Kanter, R., and Ackerman, M.J. (2015a). Identification and Functional Characterization of a Novel CACNA1C-Mediated Cardiac Disorder Characterized by Prolonged QT Intervals With Hypertrophic Cardiomyopathy, Congenital Heart Defects, and Sudden Cardiac Death. Circulation: Arrhythmia and Electrophysiology *8*, 1122–1132.

23.	Boczek, N.J., Miller, E.M., Ye, D., Nesterenko, V.V., Tester, D.J., Antzelevitch, C., Czosek, R.J., Ackerman, M.J., and Ware, S.M. (2015b). Novel Timothy syndrome mutation leading to increase in CACNA1C window current. Heart Rhythm *12*, 211–219.

24.	Boyden, E.S., Zhang, F., Bamberg, E., Nagel, G., and Deisseroth, K. (2005). Millisecond-timescale, genetically targeted optical control of neural activity. Nat Neurosci *8*, 1263–1268.

25.	Brenner, S. (1974). The Genetics of Caenorhabditis Elegans. Genetics *77*, 71–94.

26.	Brooks, D.J. (2000). Dopamine agonists: their role in the treatment of Parkinson's disease. Journal of Neurology, Neurosurgery & Psychiatry *68*, 685–689.

27.	Budde, T., Meuth, S., and Pape, H.-C. (2002). Calcium-dependent inactivation of neuronal calcium channels. Nature Reviews Neuroscience *3*, 873–883.

28.	Burnett, K., Edsinger, E., and Albrecht, D.R. (2017). Hydrogel encapsulation of living organisms for long-term microscopy. BioRxiv 194282.

29.	Burns, A.R., Kwok, T.C.Y., Howard, A., Houston, E., Johanson, K., Chan, A., Cutler, S.R., McCourt, P., and Roy, P.J. (2006a). High-throughput screening of small molecules for bioactivity and target identification in Caenorhabditis elegans. Nat. Protocols *1*, 1906–1914.

30.	Burns, S., Travers, J., Collins, I., Rowlands, M.G., Newbatt, Y., Thompson, N., Garrett, M.D., Workman, P., and Aherne, W. (2006b). Identification of Small-Molecule Inhibitors of Protein Kinase B (PKB/AKT) in an AlphaScreen™ High-Throughput Screen. J Biomol Screen *11*, 822–827.

31.	C. elegans Sequencing Consortium (1998). Genome sequence of the nematode C. elegans: a platform for investigating biology. Science *282*, 2012–2018.

32. Catterall, W.A. (1995). Structure and function of voltage-gated ion channels. Annu. Rev. Biochem. *64*, 493–531.

33. Catterall, W.A. (2000). Structure and regulation of voltage-gated Ca2+ channels. Annu. Rev. Cell Dev. Biol. *16*, 521–555.

34. Catterall, W.A. (2011). Voltage-Gated Calcium Channels. Cold Spring Harb Perspect Biol *3*, a003947.

35. Chalfie, M., Tu, Y., Euskirchen, G., Ward, W.W., and Prasher, D.C. (1994). Green fluorescent protein as a marker for gene expression. Science *263*, 802–805.

36. Chavkin, C. (2011). The Therapeutic Potential of κ-Opioids for Treatment of Pain and Addiction. Neuropsychopharmacology *36*, 369–370.

37. Chen, T.-W., Wardill, T.J., Sun, Y., Pulver, S.R., Renninger, S.L., Baohan, A., Schreiter, E.R., Kerr, R.A., Orger, M.B., Jayaraman, V., et al. (2013). Ultra-sensitive fluorescent proteins for imaging neuronal activity. Nature *499*, 295–300.

38. Cho, Y., Zhao, C.L., and Lu, H. (2017). Trends in high-throughput and functional neuroimaging in Caenorhabditis elegans. Wiley Interdisciplinary Reviews: Systems Biology and Medicine *9*.

39. Chronis, N., Zimmer, M., and Bargmann, C.I. (2007). Microfluidics for in vivo imaging of neuronal and behavioral activity in Caenorhabditis elegans. Nature Methods *4*, 727–731.

40. Cornaglia, M., Lehnert, T., and Gijs, M.A.M. (2017). Microfluidic systems for high-throughput and high-content screening using the nematode Caenorhabditis elegans. Lab Chip.

41. Crump, A. (2017). Ivermectin: enigmatic multifaceted 'wonder' drug continues to surprise and exceed expectations. The Journal of Antibiotics *70*, 495–505.

42. Crump, A., and Ōmura, S. (2011). Ivermectin, 'Wonder drug' from Japan: the human use perspective. Proc Jpn Acad Ser B Phys Biol Sci *87*, 13–28.

43. Cully, D.F., Vassilatis, D.K., Liu, K.K., Paress, P.S., Van der Ploeg, L.H.T., Schaeffer, J.M., and Arena, J.P. (1994). Cloning of an avermectin-sensitive glutamate-gated chloride channel from Caenorhabditis elegans. Nature *371*, 707–711.

44. D'Anneo, A., Carlisi, D., Lauricella, M., Puleio, R., Martinez, R., Bella, S.D., Marco, P.D., Emanuele, S., Fiore, R.D., Guercio, A., et al. (2013). Parthenolide generates reactive oxygen species and autophagy in MDA-MB231 cells. A soluble parthenolide analogue inhibits tumour growth and metastasis in a xenograft model of breast cancer. Cell Death & Disease *4*, e891.

45. Dent, J.A., Smith, M.M., Vassilatis, D.K., and Avery, L. (2000). The genetics of ivermectin resistance in Caenorhabditis elegans. Proc. Natl. Acad. Sci. U.S.A. *97*, 2674–2679.

46. Dick, I.E., Joshi-Mukherjee, R., Yang, W., and Yue, D.T. (2016). Arrhythmogenesis in Timothy Syndrome is associated with defects in Ca(2+)-dependent inactivation. Nat Commun *7*, 10370.

47. Dickinson, D.J., and Goldstein, B. (2016). CRISPR-Based Methods for Caenorhabditis elegans Genome Engineering. Genetics *202*, 885–901.

48. Dickinson, D.J., Ward, J.D., Reiner, D.J., and Goldstein, B. (2013). Engineering the Caenorhabditis elegans genome using Cas9-triggered homologous recombination. Nature Methods *10*, 1028–1034.

49. Dong, L., Cornaglia, M., Krishnamani, G., Zhang, J., Mouchiroud, L., Lehnert, T., Auwerx, J., and Gijs, M.A.M. (2018). Reversible and long-term immobilization in a hydrogel-microbead matrix for high-resolution imaging of Caenorhabditis elegans and other small organisms. PLOS ONE *13*, e0193989.

50. Du, G., Fang, Q., and den Toonder, J.M.J. (2016). Microfluidics for cell-based high throughput screening platforms—A review. Analytica Chimica Acta *903*, 36–50.

51. Dufendach, K.A., Giudicessi, J.R., Boczek, N.J., and Ackerman, M.J. (2013). Maternal Mosaicism Confounds the Neonatal Diagnosis of Type 1 Timothy Syndrome. Pediatrics *131*, e1991–e1995.

52. Ebert, D.H., and Greenberg, M.E. (2013). Activity-dependent neuronal signalling and autism spectrum disorder. Nature *493*, 327–337.

53. Efthymiou, A., Shaltouki, A., Steiner, J.P., Jha, B., Heman-Ackah, S.M., Swistowski, A., Zeng, X., Rao, M.S., and Malik, N. (2014). Functional Screening Assays with Neurons Generated from Pluripotent Stem Cell–Derived Neural Stem Cells. J Biomol Screen *19*, 32–43.

54. Ellis, H.M., and Horvitz, H.R. (1986). Genetic control of programmed cell death in the nematode C. elegans. Cell *44*, 817–829.

55. Faber, P.W., Alter, J.R., MacDonald, M.E., and Hart, A.C. (1999). Polyglutamine-mediated dysfunction and apoptotic death of a Caenorhabditis elegans sensory neuron. Proc. Natl. Acad. Sci. U.S.A. *96*, 179–184.

56. Felix, R. (2006). Calcium channelopathies. Neuromol Med *8*, 307–318.

57. Fire, A., Xu, S., Montgomery, M.K., Kostas, S.A., Driver, S.E., and Mello, C.C. (1998). Potent and specific genetic interference by double-stranded RNA in Caenorhabditis elegans. Nature *391*, 806–811.

58. Friedland, A.E., Tzur, Y.B., Esvelt, K.M., Colaiácovo, M.P., Church, G.M., and Calarco, J.A. (2013). Heritable genome editing in C. elegans via a CRISPR-Cas9 system. Nature Methods *10*, 741–743.

59. Fröhler, S., Kieslich, M., Langnick, C., Feldkamp, M., Opgen-Rhein, B., Berger, F., Will, J.C., and Chen, W. (2014). Exome sequencing helped the fine diagnosis of two siblings afflicted with atypical Timothy syndrome (TS2). BMC Medical Genetics *15*, 48.

60. Frøkjær-Jensen, C., Kindt, K.S., Kerr, R.A., Suzuki, H., Melnik-Martinez, K., Gerstbreih, B., Driscol, M., and Schafer, W.R. (2006). Effects of voltage-gated calcium channel subunit genes on calcium influx in cultured C. elegans mechanosensory neurons. Journal of Neurobiology *66*, 1125–1139.

61. Fukushige, T., Smith, H.E., Miwa, J., Krause, M.W., and Hanover, J.A. (2017). A Genetic Analysis of the Caenorhabditis elegans Detoxification Response. Genetics *206*, 939–952.

62. Fukuyama, M., Wang, Q., Kato, K., Ohno, S., Ding, W.-G., Toyoda, F., Itoh, H., Kimura, H., Makiyama, T., Ito, M., et al. (2014). Long QT syndrome type 8: novel CACNA1C mutations causing QT prolongation and variant phenotypes. Europace *16*, 1828–1837.

63. Gao, S., and Zhen, M. (2011). Action potentials drive body wall muscle contractions in Caenorhabditis elegans. PNAS *108*, 2557–2562.

64. Gillis, J., Burashnikov, E., Antzelevitch, C., Blaser, S., Gross, G., Turner, L., Babul-Hirji, R., and Chitayat, D. (2012). Long QT, syndactyly, joint contractures, stroke and novel CACNA1C mutation: Expanding the spectrum of Timothy syndrome. American Journal of Medical Genetics Part A *158A*, 182–187.

65. Gobrecht, P., Andreadaki, A., Diekmann, H., Heskamp, A., Leibinger, M., and Fischer, D. (2016). Promotion of Functional Nerve Regeneration by Inhibition of Microtubule Detyrosination. J. Neurosci. *36*, 3890–3902.

66. Goldin Alan L. (2006). Expression of Ion Channels in Xenopus Oocytes. Expression and Analysis of Recombinant Ion Channels.

67. Gomez-Ospina, N., Panagiotakos, G., Portmann, T., Pasca, S.P., Rabah, D., Budzillo, A., Kinet, J.P., and Dolmetsch, R.E. (2013). A Promoter in the Coding Region of the Calcium Channel Gene CACNA1C Generates the Transcription Factor CCAT. PLOS ONE *8*, e60526.

68. Gómez-Sjöberg, R., Leyrat, A.A., Pirone, D.M., Chen, C.S., and Quake, S.R. (2007). Versatile, Fully Automated, Microfluidic Cell Culture System. Anal. Chem. *79*, 8557–8563.

69. Goodman, M.B., Lindsay, T.H., Lockery, S.R., and Richmond, J.E. (2012). Electrophysiological methods for Caenorhabditis elegans neurobiology. Methods Cell Biol. *107*, 409–436.

70. Gradinaru, V., Mogri, M., Thompson, K.R., Henderson, J.M., and Deisseroth, K. (2009). Optical deconstruction of parkinsonian neural circuitry. Science *324*, 354–359.

71. Gravato-Nobre, M.J., Nicholas, H.R., Nijland, R., O'Rourke, D., Whittington, D.E., Yook, K.J., and Hodgkin, J. (2005). Multiple genes affect sensitivity of Caenorhabditis elegans to the bacterial pathogen Microbacterium nematophilum. Genetics *171*, 1033–1045.

72. Gunaydin, L.A., Grosenick, L., Finkelstein, J.C., Kauvar, I.V., Fenno, L.E., Adhikari, A., Lammel, S., Mirzabekov, J.J., Airan, R.D., Zalocusky, K.A., et al. (2014). Natural Neural Projection Dynamics Underlying Social Behavior. Cell *157*, 1535–1551.

73. Haggarty, S.J., Silva, M.C., Cross, A., Brandon, N.J., and Perlis, R.H. (2016). Advancing drug discovery for neuropsychiatric disorders using patient-specific stem cell models. Molecular and Cellular Neuroscience *73*, 104–115.

74. Hassan, M., Watari, H., AbuAlmaaty, A., Ohba, Y., and Sakuragi, N. (2014). Apoptosis and Molecular Targeting Therapy in Cancer.

75. Hatje, K., and Kollmar, M. (2013). Expansion of the mutually exclusive spliced exome in Drosophila. Nature Communications *4*, 2460.

76. Hendricks, M., Ha, H., Maffey, N., and Zhang, Y. (2012). Compartmentalized calcium dynamics in a C. elegans interneuron encode head movement. Nature *487*, 99–103.

77. Hennessey, J.A., Boczek, N.J., Jiang, Y.-H., Miller, J.D., Patrick, W., Pfeiffer, R., Sutphin, B.S., Tester, D.J., Barajas-Martinez, H., Ackerman, M.J., et al. (2014). A CACNA1C Variant Associated with Reduced Voltage-Dependent Inactivation, Increased CaV1.2 Channel Window Current, and Arrhythmogenesis. PLOS ONE *9*, e106982.

78. Heyes, S., Pratt, W.S., Rees, E., Dahimene, S., Ferron, L., Owen, M.J., and Dolphin, A.C. (2015). Genetic disruption of voltage-gated calcium channels in psychiatric and neurological disorders. Progress in Neurobiology *134*, 36–54.

79. Hillier, L.W., Marth, G.T., Quinlan, A.R., Dooling, D., Fewell, G., Barnett, D., Fox, P., Glasscock, J.I., Hickenbotham, M., Huang, W., et al. (2008). Whole-genome sequencing and variant discovery in C. elegans. Nature Methods *5*, 183–188.

80. Hori, H., Yamamoto, N., Fujii, T., Teraishi, T., Sasayama, D., Matsuo, J., Kawamoto, Y., Kinoshita, Y., Ota, M., Hattori, K., et al. (2012). Effects of the CACNA1C risk allele on neurocognition in patients with schizophrenia and healthy individuals. Scientific Reports *2*, 634.

81. Hornsten, A., Lieberthal, J., Fadia, S., Malins, R., Ha, L., Xu, X., Daigle, I., Markowitz, M., O'Connor, G., Plasterk, R., et al. (2007). APL-1, a Caenorhabditis elegans protein related to the human β-amyloid precursor protein, is essential for viability. PNAS *104*, 1971–1976.

82. Hsu, P.D., Lander, E.S., and Zhang, F. (2014). Development and Applications of CRISPR-Cas9 for Genome Engineering. Cell *157*, 1262–1278.

83. Hyman, S.E. (2008). A glimmer of light for neuropsychiatric disorders.

84. Jacobson, K.A., and Gao, Z.-G. (2006). Adenosine receptors as therapeutic targets. Nat Rev Drug Discov *5*, 247–264.

85. Jen, J.C., Ashizawa, T., Griggs, R.C., and Waters, M.F. (2016). Rare neurological channelopathies — networks to study patients, pathogenesis and treatment. Nature Reviews Neurology *12*, 195–203.

86. Jinek, M., Chylinski, K., Fonfara, I., Hauer, M., Doudna, J.A., and Charpentier, E. (2012). A Programmable Dual-RNA–Guided DNA Endonuclease in Adaptive Bacterial Immunity. Science *337*, 816–821.

87. Jorgensen, E.M., and Mango, S.E. (2002). The art and design of genetic screens: caenorhabditis elegans. Nat. Rev. Genet. *3*, 356–369.

88. Jospin, M., Jacquemond, V., Mariol, M.-C., Ségalat, L., and Allard, B. (2002). The L-type voltage-dependent Ca2+ channel EGL-19 controls body wall muscle function in Caenorhabditis elegans. J Cell Biol *159*, 337–348.

89. Kato, S., Kaplan, H.S., Schrödel, T., Skora, S., Lindsay, T.H., Yemini, E., Lockery, S., and Zimmer, M. (2015). Global Brain Dynamics Embed the Motor Command Sequence of Caenorhabditis elegans. Cell *163*, 656–669.

90. Kerr, R., Lev-Ram, V., Baird, G., Vincent, P., Tsien, R.Y., and Schafer, W.R. (2000). Optical Imaging of Calcium Transients in Neurons and Pharyngeal Muscle of C. elegans. Neuron *26*, 583–594.

91. Kim, J.-B. (2014). Channelopathies. Korean J Pediatr *57*, 1–18.

92. Kim, D.H., Kim, J., Marques, J.C., Grama, A., Hildebrand, D.G.C., Gu, W., Li, J.M., and Robson, D.N. (2017). Pan-neuronal calcium imaging with cellular resolution in freely swimming zebrafish. Nature Methods *14*, 1107–1114.

93. Kim, D.-K., Kim, T.H., and Lee, S.-J. (2016). Mechanisms of aging-related proteinopathies in Caenorhabditis elegans. Experimental & Molecular Medicine *48*, e263.

94. Kim, H., Ishidate, T., Ghanta, K.S., Seth, M., Conte, D., Shirayama, M., and Mello, C.C. (2014). A co-CRISPR strategy for efficient genome editing in Caenorhabditis elegans. Genetics *197*, 1069–1080.

95. Kim, I.H., Kim, S.W., Kim, S.H., Lee, S.O., Lee, S.T., Kim, D.-G., Lee, M.-J., and Park, W.H. (2012). Parthenolide-induced apoptosis of hepatic stellate cells and anti-fibrotic effects in an *in vivo* rat model. Experimental & Molecular Medicine *44*, 448–456.

96. Kinser, H.E., and Pincus, Z. (2017). High-throughput screening in the C. elegans nervous system. Molecular and Cellular Neuroscience *80*, 192–197.

97. Klapoetke, N.C., Murata, Y., Kim, S.S., Pulver, S.R., Birdsey-Benson, A., Cho, Y.K., Morimoto, T.K., Chuong, A.S., Carpenter, E.J., Tian, Z., et al. (2014). Independent optical excitation of distinct neural populations. Nat Meth *11*, 338–346.

98. Krey, J.F., Paşca, S.P., Shcheglovitov, A., Yazawa, M., Schwemberger, R., Rasmusson, R., and Dolmetsch, R.E. (2013). Timothy syndrome is associated with activity-dependent dendritic retraction in rodent and human neurons. Nat Neurosci *16*, 201–209.

99. Kutscher, L.M., and Shaham, S. (2014). Forward and reverse mutagenesis in C. elegans. WormBook 1–26.

100. Kwok, T. (2013). The Characterization of Nemadipine and Migrazole as Small Molecule Tools for Use in the Nematode Caenorhabditis elegans. Thesis.

101. Kwok, T.C.Y., Ricker, N., Fraser, R., Chan, A.W., Burns, A., Stanley, E.F., McCourt, P., Cutler, S.R., and Roy, P.J. (2006). A small-molecule screen in C. elegans yields a new calcium channel antagonist. Nature *441*, 91–95.

102. Lagoy, R., and Albrecht, D. (2015). Microfluidic Devices for Behavioral Analysis, Microscopy, and Neuronal Imaging in Caenorhabditis elegans. In C. Elegans, D. Biron, and G. Haspel, eds. (Humana Press), pp. 159–179.

103. Lagoy, R.C., and Albrecht, D.R. (2018). Automated fluid delivery from multiwell plates to microfluidic devices for high-throughput experiments and microscopy. Scientific Reports *8*, 6217.

104. Lainé, V., Frøkjær-Jensen, C., Couchoux, H., and Jospin, M. (2011). The α1 Subunit EGL-19, the α2/δ Subunit UNC-36, and the β Subunit CCB-1 Underlie Voltage-dependent Calcium Currents in Caenorhabditis elegans Striated Muscle. J Biol Chem *286*, 36180–36187.

105. Lainé, V., Ségor, J.R., Zhan, H., Bessereau, J.-L., and Jospin, M. (2014). Hyperactivation of L-type voltage-gated Ca2+ channels in Caenorhabditis elegans striated muscle can result from point mutations in the IS6 or the IIIS4 segment of the α1 subunit. J Exp Biol *217*, 3805–3814.

106. Landstrom, A.P., Boczek, N.J., Ye, D., Miyake, C.Y., De la Uz, C.M., Allen, H.D., Ackerman, M.J., and Kim, J.J. (2016). Novel long QT syndrome-associated missense mutation, L762F, in CACNA1C-encoded L-type calcium channel imparts a slower inactivation tau and increased sustained and window current. International Journal of Cardiology *220*, 290–298.

107. Larsch, J., Ventimiglia, D., Bargmann, C.I., and Albrecht, D.R. (2013). High-throughput imaging of neuronal activity in Caenorhabditis elegans. PNAS *110*, E4266–E4273.

108. Larsch, J., Flavell, S.W., Liu, Q., Gordus, A., Albrecht, D.R., and Bargmann, C.I. (2015). A Circuit for Gradient Climbing in C. elegans Chemotaxis. Cell Reports *12*, 1748–1760.

109. Lee, C.-Y., Chang, C.-L., Wang, Y.-N., and Fu, L.-M. (2011). Microfluidic Mixing: A Review. Int J Mol Sci *12*, 3263–3287.

110. Lee, P., Chen, C.S.Y., Gaige, T., and Hung, P.J. (2015). Automated live cell imaging of cell migration across a microfluidic-controlled chemoattractant gradient.

111. Lee, P.J., Ghorashian, N., Gaige, T.A., and Hung, P.J. (2007). Microfluidic System for Automated Cell-based Assays. JALA Charlottesv Va *12*, 363–367.

112. Lee, R.Y., Lobel, L., Hengartner, M., Horvitz, H.R., and Avery, L. (1997). Mutations in the alpha1 subunit of an L-type voltage-activated Ca2+ channel cause myotonia in Caenorhabditis elegans. EMBO J. *16*, 6066–6076.

113. Leifer, A.M., Fang-Yen, C., Gershow, M., Alkema, M.J., and Samuel, A.D.T. (2011). Optogenetic manipulation of neural activity in freely moving Caenorhabditis elegans. Nat Methods *8*, 147–152.

114. Leung, M.C.K., Williams, P.L., Benedetto, A., Au, C., Helmcke, K.J., Aschner, M., and Meyer, J.N. (2008). Caenorhabditis elegans: An Emerging Model in Biomedical and Environmental Toxicology. Toxicol. Sci. *106*, 5–28.

115. Link, C.D. (1995). Expression of human beta-amyloid peptide in transgenic Caenorhabditis elegans. Proc Natl Acad Sci U S A *92*, 9368–9372.

116. Lockery, S.R., and Goodman, M.B. (1998). Tight-seal whole-cell patch clamping of caenorhabditis elegans neurons. In Methods in Enzymology, (Academic Press), pp. 201–217.

117. Lockery, S.R., and Goodman, M.B. (2009). The Quest for Action Potentials in C. elegans Neurons Hits a Plateau. Nat Neurosci *12*, 377–378.

118. Lockery, S., Goodman, M., and Faumont, S. (2009). First report of action potentials in a C. elegans neuron is premature. Nat Neurosci *12*, 365–366.

119. Lotfullina, N., and Khazipov, R. (2017). Ethanol and the Developing Brain: Inhibition of Neuronal Activity and Neuroapoptosis. Neuroscientist 1073858417712667.

120. Lucanic, M., Garrett, T., Gill, M.S., and Lithgow, G.J. (2018). A Simple Method for High Throughput Chemical Screening in Caenorhabditis Elegans. JoVE (Journal of Visualized Experiments) e56892–e56892.

121. Lucki, I. (1991). Behavioral studies of serotonin receptor agonists as antidepressant drugs. J Clin Psychiatry *52 Suppl*, 24–31.

122. Ma, W.-Y., Hsiung, L.-C., Wang, C.-H., Chiang, C.-L., Lin, C.-H., Huang, C.-S., and Wo, A.M. (2015). A Novel 96well-formatted Micro-gap Plate Enabling Drug Response Profiling on Primary Tumour Samples. Scientific Reports *5*, 9656.

123. Maes, J., Verlooy, L., Buenafe, O.E., de Witte, P.A.M., Esguerra, C.V., and Crawford, A.D. (2012). Evaluation of 14 Organic Solvents and Carriers for Screening Applications in Zebrafish Embryos and Larvae. PLoS ONE *7*, e43850.

124. McCormick, A.V., Wheeler, J.M., Guthrie, C.R., Liachko, N.F., and Kraemer, B.C. (2013). Dopamine D2 receptor antagonism suppresses tau aggregation and neurotoxicity. Biol. Psychiatry *73*, 464–471.

125. Melin, J., and Quake, S.R. (2007). Microfluidic Large-Scale Integration: The Evolution of Design Rules for Biological Automation. Annual Review of Biophysics and Biomolecular Structure *36*, 213–231.

126. Mellem, J.E., Brockie, P.J., Madsen, D.M., and Maricq, A.V. (2008). Action Potentials Contribute to Neuronal Signaling in C. elegans. Nat Neurosci *11*, 865–867.

127. Mello, C.C., Kramer, J.M., Stinchcomb, D., and Ambros, V. (1991). Efficient gene transfer in C.elegans: extrachromosomal maintenance and integration of transforming sequences. EMBO J *10*, 3959–3970.

128. Molokanova, E., Mercola, M., and Savchenko, A. (2017). Bringing new dimensions to drug discovery screening: impact of cellular stimulation technologies. Drug Discovery Today *22*, 1045–1055.

129. Mondal, S., Hegarty, E., Martin, C., Gökçe, S.K., Ghorashian, N., and Ben-Yakar, A. (2016). Large-scale microfluidics providing high-resolution and high-throughput screening of *Caenorhabditis elegans* poly-glutamine aggregation model. Nature Communications *7*, 13023.

130. Mondal, S., Hegarty, E., Sahn, J.J., Scott, L.L., Gökçe, S.K., Martin, C., Ghorashian, N., Satarasinghe, P.N., Iyer, S., Sae-Lee, W., et al. (2018). High-Content Microfluidic Screening Platform Used To Identify σ2R/Tmem97 Binding Ligands that Reduce Age-Dependent Neurodegeneration in C. elegans SC_APP Model. ACS Chem. Neurosci.

131. Morrill, J.A., and Cannon, S.C. (1999). Effects of mutations causing hypokalaemic periodic paralysis on the skeletal muscle L-type Ca2+ channel expressed in Xenopus laevis oocytes. J Physiol *520*, 321–336.

132. Nagel, G., Ollig, D., Fuhrmann, M., Kateriya, S., Musti, A.M., Bamberg, E., and Hegemann, P. (2002). Channelrhodopsin-1: a light-gated proton channel in green algae. Science *296*, 2395–2398.

133. Nagel, G., Szellas, T., Huhn, W., Kateriya, S., Adeishvili, N., Berthold, P., Ollig, D., Hegemann, P., and Bamberg, E. (2003). Channelrhodopsin-2, a directly light-gated cation-selective membrane channel. Proc. Natl. Acad. Sci. U.S.A. *100*, 13940–13945.

134. Nagel, G., Brauner, M., Liewald, J.F., Adeishvili, N., Bamberg, E., and Gottschalk, A. (2005). Light activation of channelrhodopsin-2 in excitable cells of Caenorhabditis elegans triggers rapid behavioral responses. Curr. Biol. *15*, 2279–2284.

135. Nakai, J., Ohkura, M., and Imoto, K. (2001). A high signal-to-noise Ca2+ probe composed of a single green fluorescent protein. Nature Biotechnology *19*, 137–141.

136. NAMI (2018). Depression | NAMI: National Alliance on Mental Illness.

137. Neher, E., and Sakmann, B. (1976). Single-channel currents recorded from membrane of denervated frog muscle fibres. Nature *260*, 799–802.

138. Nguyen, J.P., Shipley, F.B., Linder, A.N., Plummer, G.S., Liu, M., Setru, S.U., Shaevitz, J.W., and Leifer, A.M. (2015). Whole-brain calcium imaging with cellular resolution in freely behaving Caenorhabditis elegans. Proc. Natl. Acad. Sci. U.S.A.

139. NIH CACNA1A (2018). CACNA1A gene. Genetics Home Reference.

140. NIH CACNA1C (2018). CACNA1C gene.

141. NIH KCNH2 (2018). KCNH2 gene.

142. NIH Timothy syndrome (2018). Timothy syndrome.

143. NIMH Mental Illness (2018). NIMH » Mental Illness.

144. Nishimura, K., Fukagawa, T., Takisawa, H., Kakimoto, T., and Kanemaki, M. (2009). An auxin-based degron system for the rapid depletion of proteins in nonplant cells. Nat Meth *6*, 917–922.

145. Ocorr, K., Reeves, N.L., Wessells, R.J., Fink, M., Chen, H.-S.V., Akasaka, T., Yasuda, S., Metzger, J.M., Giles, W., Posakony, J.W., et al. (2007). KCNQ potassium channel mutations cause cardiac arrhythmias in Drosophila that mimic the effects of aging. Proc Natl Acad Sci U S A *104*, 3943–3948.

146. O'Reilly, L.P., Luke, C.J., Perlmutter, D.H., Silverman, G.A., and Pak, S.C. (2014). C. elegans in high-throughput drug discovery. Adv Drug Deliv Rev *0*, 247–253.

147. O'Rourke, E.J., Conery, A.L., and Moy, T.I. (2009). Whole-Animal High-Throughput Screens: The C. elegans Model. In Cell-Based Assays for High-Throughput Screening, (Humana Press, Totowa, NJ), pp. 57–75.

148. Ozawa, J., Ohno, S., Saito, H., Saitoh, A., Matsuura, H., and Horie, M. A novel CACNA1C mutation identified in a patient with Timothy syndrome without syndactyly exerts both marked loss-and-gain of function effects. HeartRhythm Case Reports.

149. Pakhomov, A.G., Semenov, I., Casciola, M., and Xiao, S. (2017). Neuronal excitation and permeabilization by 200-ns pulsed electric field: An optical membrane potential study with FluoVolt dye. Biochim. Biophys. Acta *1859*, 1273–1281.

150. Paredes, R.M., Etzler, J.C., Watts, L.T., and Lechleiter, J.D. (2008). Chemical Calcium Indicators. Methods *46*, 143–151.

151. Parker, G.J., Law, T.L., Lenoch, F.J., and Bolger, R.E. (2000). Development of High Throughput Screening Assays Using Fluorescence Polarization: Nuclear Receptor-Ligand-Binding and Kinase/Phosphatase Assays. J Biomol Screen *5*, 77–88.

152. Partridge, F.A., Tearle, A.W., Gravato-Nobre, M.J., Schafer, W.R., and Hodgkin, J. (2008). The C. elegans glycosyltransferase BUS-8 has two distinct and essential roles in epidermal morphogenesis. Dev. Biol. *317*, 549–559.

153. Partridge, F.A., Brown, A.E., Buckingham, S.D., Willis, N.J., Wynne, G.M., Forman, R., Else, K.J., Morrison, A.A., Matthews, J.B., Russell, A.J., et al. (2017). An automated high-throughput system for phenotypic screening of chemical libraries on C. elegans and parasitic nematodes. Int J Parasitol Drugs Drug Resist *8*, 8–21.

154. Paşca, S.P., Portmann, T., Voineagu, I., Yazawa, M., Shcheglovitov, A., Paşca, A.M., Cord, B., Palmer, T.D., Chikahisa, S., Nishino, S., et al. (2011). Using iPSC-derived neurons to uncover cellular phenotypes associated with Timothy syndrome. Nat. Med. *17*, 1657–1662.

155. Pérez Koldenkova, V., and Nagai, T. (2013). Genetically encoded Ca2+ indicators: Properties and evaluation. Biochimica et Biophysica Acta (BBA) - Molecular Cell Research *1833*, 1787–1797.

156. Perlman, R.L. (2016). Mouse models of human disease. Evol Med Public Health *2016*, 170–176.

157. Peterka, D.S., Takahashi, H., and Yuste, R. (2011). Imaging voltage in neurons. Neuron *69*, 9–21.

158. Rajakulendran, S., Graves, T.D., Labrum, R.W., Kotzadimitriou, D., Eunson, L., Davis, M.B., Davies, R., Wood, N.W., Kullmann, D.M., Hanna, M.G., et al. (2010). Genetic and functional characterisation of the P/Q calcium channel in episodic ataxia with epilepsy. J Physiol *588*, 1905–1913.

159. Rane, T.D., Zec, H.C., and Wang, T.-H. (2012). A serial sample loading system: interfacing multiwell plates with microfluidic devices. J Lab Autom *17*, 370–377.

160. Rasband, M. N. (2010). Ion Channels and Excitable Cells. Nature Education 3(9):41.

161. Rose, M.R. (1998). Neurological channelopathies. BMJ *316*, 1104–1105.

162. Rothbauer, M., Zirath, H., and Ertl, P. (2018). Recent advances in microfluidic technologies for cell-to-cell interaction studies. Lab Chip *18*, 249–270.

163. Sackmann, E.K., Fulton, A.L., and Beebe, D.J. (2014). The present and future role of microfluidics in biomedical research. Nature *507*, 181.

164. Saheki, Y., and Bargmann, C.I. (2009). Presynaptic CaV2 calcium channel traffic requires CALF-1 and the α2δ subunit UNC-36. Nat Neurosci *12*, 1257–1265.

165. Samways, D.S.K., Khakh, B.S., and Egan, T.M. (2012). Allosteric Modulation of Ca2+ flux in Ligand-gated Cation Channel (P2X4) by Actions on Lateral Portals. J. Biol. Chem. *287*, 7594–7602.

166. San-Miguel, A., and Lu, H. (2013). Microfluidics as a tool for C. elegans research. WormBook 1–19.
167. Schafer, W.R., and Kenyon, C.J. (1995). A calcium-channel homologue required for adaptation to dopamine and serotonin in Caenorhabditis elegans. Nature *375*, 73–78.
168. Schild, L.C., and Glauser, D.A. (2015). Dual Color Neural Activation and Behavior Control with Chrimson and CoChR in Caenorhabditis elegans. Genetics *200*, 1029–1034.
169. Schneider, N., Ludwig, H., and Nick, P. (2015). Suppression of tubulin detyrosination by parthenolide recruits the plant-specific kinesin KCH to cortical microtubules. J Exp Bot *66*, 2001–2011.
170. Schobert, B., and Lanyi, J.K. (1982). Halorhodopsin is a light-driven chloride pump. J. Biol. Chem. *257*, 10306–10313.
171. Schrödel, T., Prevedel, R., Aumayr, K., Zimmer, M., and Vaziri, A. (2013). Brain-wide 3D imaging of neuronal activity in *Caenorhabditis elegans* with sculpted light. Nature Methods *10*, 1013–1020.
172. Schroeder, K.S., and Neagle, B.D. (1996). FLIPR: A New Instrument for Accurate, High Throughput Optical Screening. J Biomol Screen *1*, 75–80.
173. Schüler, C., Fischer, E., Shaltiel, L., Costa, W.S., and Gottschalk, A. (2015). Arrhythmogenic effects of mutated L-type Ca2+-channels on an optogenetically paced muscular pump in Caenorhabditis elegans. Scientific Reports *5*, 14427.
174. Schwendeman, A.R., and Shaham, S. (2016). A High-Throughput Small Molecule Screen for C. elegans Linker Cell Death Inhibitors. PLoS One *11*.
175. Senatore, A., Boone, A.N., and Spafford, J.D. (2011). Optimized Transfection Strategy for Expression and Electrophysiological Recording of Recombinant Voltage-Gated Ion Channels in HEK-293T Cells. J Vis Exp.
176. Sengupta, P., Chou, J.H., and Bargmann, C.I. (1996). odr-10 encodes a seven transmembrane domain olfactory receptor required for responses to the odorant diacetyl. Cell *84*, 899–909.
177. SfN (2018). Worldwide Neuroscience Initiatives.
178. Sharma, A., Wu, J.C., and Wu, S.M. (2013). Induced pluripotent stem cell-derived cardiomyocytes for cardiovascular disease modeling and drug screening. Stem Cell Research & Therapy *4*, 150.
179. Shtonda, B., and Avery, L. (2005). CCA-1, EGL-19 and EXP-2 currents shape action potentials in the Caenorhabditis elegans pharynx. Journal of Experimental Biology *208*, 2177–2190.
180. Smoller, J. (2013). Identification of risk loci with shared effects on five major psychiatric disorders: a genome-wide analysis. The Lancet *381*, 1371–1379.
181. Song, L., Park, S.E., Isseroff, Y., Morikawa, K., and Yazawa, M. (2017). Inhibition of CDK5 Alleviates the Cardiac Phenotypes in Timothy Syndrome. Stem Cell Reports *9*, 50–57.
182. Spillane, J., Kullmann, D.M., and Hanna, M.G. (2016). Genetic neurological channelopathies: molecular genetics and clinical phenotypes. J Neurol Neurosurg Psychiatry *87*, 37–48.
183. Splawski, I., Timothy, K.W., Sharpe, L.M., Decher, N., Kumar, P., Bloise, R., Napolitano, C., Schwartz, P.J., Joseph, R.M., Condouris, K., et al. (2004). Ca(V)1.2 calcium channel

dysfunction causes a multisystem disorder including arrhythmia and autism. Cell *119*, 19–31.

184. Splawski, I., Timothy, K.W., Decher, N., Kumar, P., Sachse, F.B., Beggs, A.H., Sanguinetti, M.C., and Keating, M.T. (2005). Severe arrhythmia disorder caused by cardiac L-type calcium channel mutations. Proc. Natl. Acad. Sci. U.S.A. *102*, 8089–8096; discussion 8086-8088.

185. Stacey, P., Wassermann, A.M., Kammonen, L., Impey, E., Wilbrey, A., and Cawkill, D. (2018). Plate-Based Phenotypic Screening for Pain Using Human iPSC-Derived Sensory Neurons. SLAS DISCOVERY: Advancing Life Sciences R&D 2472555218764678.

186. Steinlein, O.K. (2004). Genetic mechanisms that underlie epilepsy. Nature Reviews Neuroscience *5*, 400–408.

187. Stiernagle, T. (2006). Maintenance of C. elegans. WormBook.

188. Stupp, G.S., von Reuss, S.H., Izrayelit, Y., Ajredini, R., Schroeder, F.C., and Edison, A.S. (2013). Chemical detoxification of small molecules by C. elegans. ACS Chem Biol *8*, 309–313.

189. Sulston, J.E., Schierenberg, E., White, J.G., and Thomson, J.N. (1983). The embryonic cell lineage of the nematode Caenorhabditis elegans. Developmental Biology *100*, 64–119.

190. Swierczek, N.A., Giles, A.C., Rankin, C.H., and Kerr, R.A. (2011). High-Throughput Behavioral Analysis in C. elegans. Nat Methods *8*, 592–598.

191. Takahashi, K., and Yamanaka, S. (2006). Induction of Pluripotent Stem Cells from Mouse Embryonic and Adult Fibroblast Cultures by Defined Factors. Cell *126*, 663–676.

192. Tang, L., Gamal El-Din, T.M., Payandeh, J., Martinez, G.Q., Heard, T.M., Scheuer, T., Zheng, N., and Catterall, W.A. (2014). Structural basis for Ca2+ selectivity of a voltage-gated calcium channel. Nature *505*, 56–61.

193. Taniguchi, G., Uozumi, T., Kiriyama, K., Kamizaki, T., and Hirotsu, T. (2014). Screening of Odor-Receptor Pairs in Caenorhabditis elegans Reveals Different Receptors for High and Low Odor Concentrations. Sci. Signal. *7*, ra39–ra39.

194. Tian, L., Hires, S.A., Mao, T., Huber, D., Chiappe, M.E., Chalasani, S.H., Petreanu, L., Akerboom, J., McKinney, S.A., Schreiter, E.R., et al. (2009). Imaging neural activity in worms, flies and mice with improved GCaMP calcium indicators. Nat. Methods *6*, 875–881.

195. Tian, L., Hires, S.A., and Looger, L.L. (2012). Imaging Neuronal Activity with Genetically Encoded Calcium Indicators. Cold Spring Harb Protoc *2012*, pdb.top069609.

196. Towne, C., and Thompson, K.R. (2016). Overview on Research and Clinical Applications of Optogenetics. Curr Protoc Pharmacol *75*, 11.19.1-11.19.21.

197. Trent, C., Tsung, N., and Horvitz, H.R. (1983). Egg-Laying Defective Mutants of the Nematode Caenorhabditis Elegans. Genetics *104*, 619–647.

198. Tyson, and Snutch (2013). Molecular nature of voltage-gated calcium channels: structure and species comparison. Wiley Interdisciplinary Reviews: Membrane Transport and Signaling *2*, 181–206.

199. UCSF Medical Center (2018). Neurological Disorders | Conditions and Treatments | UCSF Medical Center.

200. Vann, K.T., and Xiong, Z.-G. (2016). Optogenetics for neurodegenerative diseases. Int J Physiol Pathophysiol Pharmacol *8*, 1–8.

201. Verkhratsky, A., and Parpura, V. (2014). History of Electrophysiology and the Patch Clamp. In Patch-Clamp Methods and Protocols, (Humana Press, New York, NY), pp. 1–19.

202. Virdee, J.K., Saro, G., Fouillet, A., Findlay, J., Ferreira, F., Eversden, S., O'Neill, M.J., Wolak, J., and Ursu, D. (2017). A high-throughput model for investigating neuronal function and synaptic transmission in cultured neuronal networks. Scientific Reports *7*, 14498.

203. Weber, L.M., Lopez, C.G., and Anseth, K.S. (2009). The effects of PEG hydrogel crosslinking density on protein diffusion and encapsulated islet survival and function. J Biomed Mater Res A *90*, 720–729.

204. Weir, G.A., Middleton, S.J., Clark, A.J., Daniel, T., Khovanov, N., McMahon, S.B., and Bennett, D.L. (2017). Using an engineered glutamate-gated chloride channel to silence sensory neurons and treat neuropathic pain at the source. Brain *140*, 2570–2585.

205. White, J.G., Southgate, E., Thomson, J.N., and Brenner, S. (1986). The structure of the nervous system of the nematode Caenorhabditis elegans. Phil. Trans. R. Soc. Lond. B *314*, 1–340.

206. Whitesides, G.M. (2006). The origins and the future of microfluidics.

207. WHO (2006). WHO | Neurological Disorders: Public Health Challenges.

208. Williams, B.D., and Waterston, R.H. (1994). Genes critical for muscle development and function in Caenorhabditis elegans identified through lethal mutations. The Journal of Cell Biology *124*, 475–490.

209. Yazawa, M., and Dolmetsch, R.E. (2013). Modeling Timothy Syndrome with iPS Cells. J. of Cardiovasc. Trans. Res. *6*, 1–9.

210. Yazawa, M., Hsueh, B., Jia, X., Pasca, A.M., Bernstein, J.A., Hallmayer, J., and Dolmetsch, R.E. (2011). Using induced pluripotent stem cells to investigate cardiac phenotypes in Timothy syndrome. Nature *471*, 230–234.

211. Yoshida, K., Hirotsu, T., Tagawa, T., Oda, S., Wakabayashi, T., Iino, Y., and Ishihara, T. (2012). Odour concentration-dependent olfactory preference change in *C. elegans*. Nature Communications *3*, 739.

212. Young, J.Z. (1936). Structure of Nerve Fibres and Synapses in Some Invertebrates. Cold Spring Harb Symp Quant Biol *4*, 1–6.

213. Zhang, J.-F., Ellinor, P.T., Aldrich, R.W., and Tsien, R.W. (1994). Molecular determinants of voltage-dependent inactivation in calcium channels. Nature *372*, 97–100.

214. Zhang, L., Ward, J.D., Cheng, Z., and Dernburg, A.F. (2015). The auxin-inducible degradation (AID) system enables versatile conditional protein depletion in C. elegans. Development *142*, 4374–4384.

215. Zhao, S., Cunha, C., Zhang, F., Liu, Q., Gloss, B., Deisseroth, K., Augustine, G.J., and Feng, G. (2008). Improved expression of halorhodopsin for light-induced silencing of neuronal activity. Brain Cell Biol *36*, 141–154.

216. Zhou, X.E., Melcher, K., and Xu, H.E. (2012). Structure and activation of rhodopsin. Acta Pharmacol Sin *33*, 291–299.

Chapter 7 Supplemental Information

Strains

Name	Genotype
Bargmann Lab	
CX14887	kyIs587 [gpa-6p::GCaMP2.2b, unc-122p::dsRed], Expressing GCaMP (integrated) in AWA neurons "AWA::GCaMP"
CX16573	kyIs587 [gpa-6p::GCaMP2.2b, unc-122p::dsRed]; kyEx5662 [odr-7p::Chrimson:SL2:mCherry, elt-2p::mCherry], Expressing GCaMP (integrated) and Chrimson (array) in AWA neurons "AWA::GCaMP ; AWA:Chrimson (array)"
CX8743	egl-19(n582)rf ; [egl-19p::egl-19cDNA-mChr ; coel::GFP]
CX10979	kyEx2865[sra-6p::GCaMP3; unc-122p::GFP], Expressing GCaMP in ASH neurons "ASH::GCaMP"

Alkema Lab	
QW1168	unc-2(zf35)gf ; "AWA::GCaMP"
QW1456	lin-15(n765ts) ; zfEx665[odr-7p::unc-2(zf35)gf (80ng/ul) ; lin-15 rescue] ; "AWA::GCaMP"
QW1457	lin-15(n765ts) ; zfEx666[odr-7p::unc-2(zf35)gf (80ng/ul) ; lin-15 rescue] ; "AWA::GCaMP"
-	"ASH::GCaMP" ; Ex[sra-6p::Chrimson ; elt-2p::mChr]

Albrecht Lab (Ross)	
NZ1014	[eft-3::Cas9 (50ng/uL each), pRF-4 (rol-6), unc-22 co-CRISPR gRNA], "unc-22 twitchers"
NZ1016-18, 24	unc-2(lj1) ; lin-15(n765ts) ; zfEx328[ptag168::UNC-2(R192Q) (80ng/ul) + lin-15 rescue] ; "AWA::GCaMP"
NZ1010-13, 24	unc-2(e55) ; lin-15(n765ts) ; zfEx327[ptag168::UNC-2(S218L) (80ng/ul) + lin-15 rescue] ; "AWA::GCaMP"
NZ1025,27,28	egl-19(n582)rf ; Ex[egl-19p::egl-19cDNA-mChr ; coel::GFP] ; "AWA::GCaMP"
NZ1033-37	egl-19(n582)rf ; Ex[egl-19p::egl-19cDNA-mChr ; coel::GFP] "AWA::GCaMP ; AWA:Chrimson (array)"
NZ1040-44 (4 lines)	rlEx001[elt-2::mCherry (10ng/uL) ; odr-7::egl-19(G369R)::sl2::mChr (50ng/ul)] ; "AWA::GCaMP"
NZ1045	egl-19(ad695)gf ; "AWA::GCaMP"
NZ1050	egl-19(n2368)gf ; "AWA::GCaMP"
NZ1051	egl-19(n582)rf ; "AWA::GCaMP" ; rlEx001[elt-2::mCherry ; odr-7::egl-19(G369R)::sl2::mChr]
NZ1052	egl-19(ad695)gf ; "AWA::GCaMP ; AWA::Chrimson (array)"
NZ1053	egl-19(n2368)gf ; "AWA::GCaMP ; AWA::Chrimson (array)"
NZ1055	"AWA::GCaMP" ; him-5(e1490)
Nz1059-60 (2 lines)	egl-19(G369R)gf/+ (CRISPR HR)

NZ1074-78	egl-19(G369R)/dnt1
NZ1079	egl-19(G369R)/dnt1 ; "AWA::GCaMP"
NZ1080	+/dnt1 ; "AWA::GCaMP"
NZ1081	bus-8(e2698) ; "AWA::GCaMP"
NZ1082	egl-19::GFP (CRISPR HR)
NZ1083-85 (3 lines) 4x	"AWA::GCaMP ; AWA:Chrimson (integrated)" ; him-5(e1490)
NZ1086-88 (3 lines) 10x	"AWA::GCaMP ; AWA:Chrimson (integrated)" ; him-5(e1490)
NZ1089-92	"AWA::GCaMP ; AWA:Chrimson (integrated)"
NZ1095	egl-19(n2368) ; "AWA::GCaMP ; AWA:Chrimson (integrated)"
NZ1096	egl-19(n582) ; "AWA::GCaMP ; AWA:Chrimson (integrated)"

Mello Lab	
NZ1061 (204696)	csr-1(slc)/Dnt1 ; GFP:Vbh1 (CRISPR) homozygous

Plasmids

Vector name	Construct	Use
DEST	Chrimson pDest-104 (Francis Lab, UMMS)	Gateway dest. vector
EXPR	sra-6p::Chrimson (Alkema Lab, UMMS)	Final expr. vector
EXPR	nhr-79p::Chrimson (Alkema Lab, UMMS)	Final expr. vector
Mutagenesis A	odr-3p::egl-19cDNA::sl2::CFP	Mutagenesis template
Mutagenesis B	odr-3p::egl-19cDNA(G369R)::sl2::CFP	Mutagenesis plasmid
Expression A	odr-7p::TeTx::sl2::mChr	Expression construct
Expression B	odr-7p::egl-19cDNA(G369R)::sl2::mChr	Final TS expression construct
pRB1017	(Arribere et al., 2014)	sgRNA backbone
pRF4::rol-6(su1006)	(Mello et al., 1991)	Co-injection marker
Peft-3::Cas9	(Friedland et al., 2013)	Germline endonuclease

Primers (oligomers)

Gene	Primer name	Sequence	Tm
unc-2(e55)	unc-2(e55)_forward	TGGGTTTTCACCATGATACGGA	55
unc-2(e55)	unc-2(e55)_reverse	GCGGTGATTCAGATCCATTCG	55
unc-2(lj1)	unc-2(lj1)_forward	CGAAGAAATCCAAGCGACACA	55
unc-2(lj1)	unc-2(lj1)_reverse	AACCCACAGGATGTCAGCTG	55
egl-19(n2368)	EGL-19_n2368F	TCATTCAACATGTATAGATCCAGCA	55
egl-19(n2368)	EGL-19_n2368R	ACCAGCCAATAAAATGTTTGACTTTT	55
egl-19(ad695)	EGL-19_ad695F	ATTTCACCAACGCCGTTCTT	55
egl-19(ad695)	EGL-19_ad695R	AAGTTGTGGCCATCCTTCGA	55
egl-19(n582)	EGL-19_n582F_geno	TCACGTCTGTGTTCACAGTTGA	55
egl-19(n582)	EGL-19_n582R_geno	TGTGGCCATCCTTCGAAAGT	55
egl-19(G369R)	EGL-19_TS_fwd	GTGCATTCAAATGTCAACCATC	51
egl-19(G369R)	EGL-19_TS_rev	TCGGATTGTCCATAATGTTCAG	51
-	EGL-19_TS(G406R)_anti	cgttcttttgagaattctctagacaagactcccaagaca	55
-	EGL-19_TS(G406R)_sense	tgtcttgggagtcttgtctagagaattctcaaaagaacg	55

-	gRNA10_fwd	TCTTGttgtcttgggagtcttgtc	-
-	gRNA10_rev	AAAcgacaagactcccaagacaaC	-
-	gRNA_GFP_fwd	TCTTGacccgccgaaaattcatct	-
-	gRNA_GFP_rev	AAAcagatgaattttcggcgggtC	-
egl-19(GFP)	C1F	CTACCCCATCCTCCTCCTTCTC	58
egl-19(GFP)	C1R	CCATCAGCCAACTAGACAGAG	58
egl-19(GFP)	out-CF	GGCTGACTGCTAACCAAAATCG	58